

**Search for the Rare Decay B to $\pi l+l-$
in the BaBar Experiment**

Ingrid Ofte

SLAC-R-859

Prepared for the Department of Energy
under contract number DE-AC02-76SF00515

Printed in the United States of America. Available from the National Technical Information Service, U.S. Department of Commerce, 5285 Port Royal Road, Springfield, VA 22161.

This document, and the material and data contained therein, was developed under sponsorship of the United States Government. Neither the United States nor the Department of Energy, nor the Leland Stanford Junior University, nor their employees, nor their respective contractors, subcontractors, or their employees, makes an warranty, express or implied, or assumes any liability of responsibility for accuracy, completeness or usefulness of any information, apparatus, product or process disclosed, or represents that its use will not infringe privately owned rights. Mention of any product, its manufacturer, or suppliers shall not, nor is it intended to, imply approval, disapproval, or fitness of any particular use. A royalty-free, nonexclusive right to use and disseminate same of whatsoever, is expressly reserved to the United States and the University.

Search for the rare decay $B \rightarrow \pi \ell^+ \ell^-$

in the BABAR experiment

Ingrid Ofte



Dissertation for the degree philosophiae doctor (PhD)
at the University of Bergen

December 2006

Abstract

The rare decay $B \rightarrow \pi \ell^+ \ell^-$ is the simplest manifestation of a $b \rightarrow d \ell^+ \ell^-$ flavor-changing neutral current (FCNC) process. This type of process only proceeds through penguin loop or box diagrams and is sensitive to physics at the electroweak scale. It can be used to constrain parameters of the Standard Model and its extensions. $B \rightarrow \pi \ell^+ \ell^-$ events have not yet been observed; the branching fraction is expected to be an order of magnitude smaller than the measured branching fraction for the similar $B \rightarrow K \ell^+ \ell^-$ decay.

Using 230 million $B\bar{B}$ meson pairs collected with the *BABAR* detector, we have done a search for the rare decay $B \rightarrow \pi \ell^+ \ell^-$. The data was produced in e^+e^- collision at the $\Upsilon(4S)$ resonance in the PEP-II collider between 1999 and 2004. Four exclusive B -meson decay modes have been reconstructed: $B^+ \rightarrow \pi^+ \ell^+ \ell^-$ and $B^0 \rightarrow \pi^0 \ell^+ \ell^-$, where $\ell^+ \ell^-$ is either an electron pair (e^+e^-) or a muon pair ($\mu^+\mu^-$). We find no evidence for a signal, and we obtain upper limits on the branching fractions \mathcal{B} . Assuming the isospin relation $\mathcal{B}(B^+ \rightarrow \pi^+ \ell^+ \ell^-) = 2 \times \frac{\tau_{B^+}}{\tau_{B^0}} \mathcal{B}(B^0 \rightarrow \pi^0 \ell^+ \ell^-)$, we obtain an upper limit at 90% confidence level on the the lepton-flavor-averaged branching fraction of $B \rightarrow \pi \ell^+ \ell^-$ to be

$$\mathcal{B}(B \rightarrow \pi \ell^+ \ell^-) < 9.5 \times 10^{-8} \quad \text{at 90\% C.L.}$$

We have also reconstructed two control modes $B^+ \rightarrow \pi^+ e^\pm \mu^\mp$ and $B^0 \rightarrow \pi^0 e^\pm \mu^\mp$, and we also obtain an upper limit at 90% confidence level on the lepton-flavor-violating decay $B \rightarrow \pi e \mu$ of

$$\mathcal{B}(B \rightarrow \pi e \mu) < 9.2 \times 10^{-8} \quad \text{at 90\% C.L.}$$

This is the first search for these rare decays at the current B -Factory experiments. This limit is an improvement by four orders of magnitude with respect to the the previous experimental limit, and about a factor three above Standard Model predictions.

Acknowledgments

I am grateful to all my colleagues in the *BABAR* collaboration who have contributed to planning, construction, operation and maintenance of the *BABAR* detector with which the data studied in this work was recorded. I am equally grateful to our PEP-II colleagues who have made this excellent data sample possible and for the efforts of the computing organizations that provide and support the resources needed to do *BABAR* analysis.

Further, I would like to thank a large number of physicists both at the Department of physics and technology (IFT) at the University of Bergen and at Stanford Linear Accelerator Center (SLAC), who have been fantastic colleagues, great sources of knowledge and inspiration through my years as a Ph.D. candidate.

My thesis advisor has been Professor Gerald Eigen and I am thankful for his support and encouragement in all my projects, and I have benefited strongly from our interesting physics discussions. I am grateful for his dedication and efforts in my physics analysis projects and all the time he has spent on giving me feedback on my analysis. I have also appreciated interesting discussions with Professor Bjarne Stugu, Professor Anna Lipniacka and several others at IFT.

I would also like to thank Jeff Berryhill for his guidance and help with the analysis of $B \rightarrow \pi \ell^+ \ell^-$. His systematic approach and constant focus on the the physics goals has been an inspiration to me. Thanks also to Dmitriy Kovalskiy for presenting our preliminary result at the ICHEP'06 conference. I am also grateful to all my colleagues in the Radiative Penguin Analysis Working Group and in the Review Committee who have helped develop this analysis and reviewed it. And many thanks to Jonathan Hollar for his unlimited practical advice on the physics analysis tools and for enlightening coffee break conversations.

I appreciate the opportunity granted to me by the group in Bergen, and by SLAC, to spend so much of my time at the laboratory. It was a truly great experience working closely with the detector and to familiarize myself with all the components of *BABAR* physics and analysis. And I am particularly thankful to everyone in the EMC and DIRC groups, for sharing their knowledge on detectors and detector operations. Jong Yi and Ivo Eschrich, in particular, provided lots of help

and advice with EMC operations. I am grateful to Professor Rafe Schindler for the opportunity to do the radiation sensor project and to all the people who helped and advised with this project, in particular Bernd Lewandowski, Karl Bouldin, Ivo Eschrich and Jaroslav Va'vra.

Finally, I would like to thank Anders Borgland who has been an invaluable source of encouragement, love and support, and who has also given advice and help with comprehending physics. And my most sincere thanks to my brothers Øystein and Jon Magne, my parents Ellen and Halvard and my friends for their patience with me during these years and for being so endlessly supportive and encouraging.

The research for this thesis has been supported by a grant from the Norwegian Research Council.

Ingrid Ofte

Contents

Preface	xvii
1 Theoretical and experimental motivation	1
1.1 Effective Hamiltonians for FCNC processes	4
1.2 Theoretical predictions	6
1.3 Measurable quantities	7
1.3.1 Decay rates	8
1.3.2 Ratio of decay rates	10
1.3.3 CP asymmetry	12
1.3.4 Differential decay rates	13
1.3.5 Lepton forward-backward asymmetry	13
1.3.6 Lepton-flavor violating modes	15
1.4 Summary	16
2 The <i>BABAR</i> experiment	17
2.1 The accelerator facility	17
2.2 The data sample and luminosity	18
2.3 The detector components	21
2.3.1 The silicon vertex tracker (SVT)	22
2.3.2 The drift chamber (DCH)	22
2.3.3 The Cherenkov-radiation detector (DIRC)	24
2.3.4 The electromagnetic calorimeter (EMC)	26
2.3.5 Instrumented flux return (IFR)	28
2.3.6 The <i>BABAR</i> trigger	29
2.4 Event reconstruction	30
2.4.1 Selection of tracks and neutrals	30

2.4.2	Particle identification	30
2.4.3	Data control samples	36
3	Experimental techniques	39
3.1	Event-shape variables	39
3.2	Kinematic variables	40
3.3	Plotting and fitting event distributions	41
4	Search for $B \rightarrow \pi\ell^+\ell^-$	45
4.1	Signal model and simulation samples	46
4.2	Event selection	47
4.2.1	Kinematic regions	48
4.2.2	Fisher discriminant for continuum $q\bar{q}$ suppression	50
4.2.3	Likelihood ratio for $B\bar{B}$ background suppression	51
4.2.4	Optimization of selection with Fisher and likelihood-ratio	56
4.2.5	Veto for suppression of peaking backgrounds	57
4.2.6	Multiple candidate selection	64
4.3	Data control samples	65
4.3.1	Charmonium control samples	65
4.3.2	Grand-sideband control sample	75
4.3.3	$e\mu$ control sample	85
4.4	Selection efficiencies	86
4.4.1	Lepton-identification efficiency correction	86
4.4.2	Fisher and likelihood-ratio efficiency corrections	87
4.4.3	Fully corrected signal efficiencies	87
4.4.4	Systematic effects from model dependence	88
4.5	Estimates of residual peaking background	90
4.5.1	Hadronic peaking backgrounds	90
4.5.2	Peaking backgrounds with leptons	92
4.6	Estimate of residual combinatorial background	96
4.6.1	Fits and yields in Monte-Carlo simulated data	97
4.6.2	Fits and yields in the <i>BABAR</i> data	97
4.6.3	Bias correction: toy Monte Carlo study	97
4.6.4	Background shape systematic studies	100
4.7	Results	100

4.7.1	Total number of events expected	100
4.7.2	Total number of events observed	100
4.8	Systematic uncertainties	104
4.8.1	Multiplicative systematic uncertainties	104
4.8.2	Background systematic uncertainties	106
4.9	Branching fraction upper limit	107
5	Conclusion	111
A	Beam-background detectors	123
A.1	EMC CsI(Tl)/PIN-diode Radiation Sensors	124
A.2	Preparation and assembly	125
A.3	The electronic readout	126
A.4	Calibration of the new sensors	127
A.4.1	Calibration setup	128
A.4.2	Calibration of individual sensors	129
A.4.3	Calibration of the preamplification boards	130
A.5	Radiation Dose-Rate Calculations	133
A.6	Cross-checks	137
A.6.1	Cross-check with EPICS data	138
A.6.2	Thermoluminescent dosimeter cross-check	139
A.7	Concluding remarks	141

List of Figures

1.1	Feynman diagrams of $b \rightarrow s\ell^+\ell^-$ and $b \rightarrow d\ell^+\ell^-$ in the Standard Model.	2
1.2	New-physics Feynman diagrams for the $b \rightarrow s$ transition.	3
1.3	Simulated distribution of A_{FB} as a function of q^2 for the decay $B \rightarrow K^*\ell^+\ell^-$	14
2.1	Photos of the SLAC site and the <i>BABAR</i> detector	17
2.2	Integrated luminosity at the PEP-II collider from 1999 to 2006	20
2.3	<i>BABAR</i> detector	23
2.4	DCH dE/dx with Bethe-Block curves	25
2.5	DIRC concept	26
2.6	DIRC K/π separation	27
2.7	Invariant mass of two photons ($\pi^0 \rightarrow \gamma\gamma$)	29
2.8	Electron selection efficiency	31
2.9	Effect of electron bremsstrahlung recovery on J/ψ mass reconstruction	32
2.10	Muon selection efficiency	33
2.11	Kaon selection efficiency	35
2.12	Pion selection efficiency	36
3.1	Two-dimensional fit to m_{ES} and ΔE distribution in simulated $B^+ \rightarrow \pi^+\ell^+\ell^-$ signal events	43
3.2	Two-dimensional fit to m_{ES} and ΔE distribution in off-resonance $B \rightarrow \pi e\mu$ events	43
4.1	Kinematic regions (m_{ES} vs. ΔE)	50
4.2	Distributions of input variables to the Fisher discriminant	52
4.3	Distributions of Fisher discriminants.	53
4.4	Distributions of input variables to the likelihood-ratio	55
4.5	Distributions of likelihood-ratio outputs	56
4.6	2D fits to m_{ES} and ΔE for background estimation	58

4.7	Contour plots of $S/\sqrt{S+B}$ vs. Fisher and likelihood-ratio	59
4.8	Charmonium veto regions with inclusive charmonium events	62
4.9	Charmonium veto regions with generic $B\bar{B}$ events	62
4.10	$\pi^0\pi^\pm$ invariant mass from $B^0 \rightarrow D^+(\pi^0\pi^+)\pi^-$ backgrounds (simulations)	64
4.11	Dilepton invariant mass distribution in the $B \rightarrow J/\psi\pi$ control sample	66
4.12	m_{ES} distribution in the $B \rightarrow J/\psi\pi$ control sample	67
4.13	ΔE distribution in the $B \rightarrow J/\psi\pi$ control sample	68
4.14	Pion momentum distribution in the $B \rightarrow J/\psi\pi$ control sample	70
4.15	Lepton momentum distribution in the $B \rightarrow J/\psi\pi$ control sample	70
4.16	Fisher discriminant distribution in the $B \rightarrow J/\psi\pi$ control sample	71
4.17	Likelihood-ratio in the $B \rightarrow J/\psi\pi$ control sample	71
4.18	m_{ES} , ΔE , Fisher and likelihood-ratio distributions in the $B \rightarrow J/\psi K$ control sample	72
4.19	1D fit m_{ES} in <i>BABAR</i> data to extract $B \rightarrow J/\psi K$ signal yield	73
4.20	m_{ES} and ΔE in the $B \rightarrow \psi(2S) K$ control sample	73
4.21	2D fits to m_{ES} and ΔE in <i>BABAR</i> data to extract $\mathcal{B}(B \rightarrow J/\psi\pi)$	74
4.22	2D fits to <i>BABAR</i> data for $B \rightarrow J/\psi\pi$ in the mode $B^0 \rightarrow \pi^0\mu^+\mu^-$	74
4.23a	m_{ES} distributions in sideband region (on-peak vs. $B\bar{B}$ + <i>udsc</i> samples)	77
4.23b	m_{ES} distributions in the sideband region (on-peak vs. $B\bar{B}$ + off-peak samples)	77
4.24a	ΔE distributions in sideband region (on-peak vs. $B\bar{B}$ + <i>udsc</i> samples)	78
4.24b	ΔE distributions in the sideband region (on-peak vs. $B\bar{B}$ + off-peak samples)	78
4.25a	Fisher discriminant distributions in sideband region (on-peak vs. $B\bar{B}$ + <i>udsc</i> samples)	79
4.25b	Fisher discriminant distributions in the sideband region (on-peak vs. $B\bar{B}$ + off-peak samples)	79
4.26a	Likelihood-ratio distributions in sideband region (on-peak vs. $B\bar{B}$ + <i>udsc</i> samples)	80
4.26b	Likelihood-ratio distributions in the sideband region (on-peak vs. $B\bar{B}$ + off-peak samples)	80
4.27a	$m_{\ell\ell}$ distributions in sideband region (on-peak vs. $B\bar{B}$ + <i>udsc</i> samples)	81
4.27b	$m_{\ell\ell}$ distributions in the sideband region (on-peak vs. $B\bar{B}$ + off-peak samples)	81
4.28a	Pion momentum distributions in sideband region (on-peak vs. $B\bar{B}$ + <i>udsc</i> samples)	82
4.28b	Pion momentum distributions in the sideband region (on-peak vs. $B\bar{B}$ + off-peak samples)	82

4.29a Lepton momentum distributions in sideband region (on-peak vs. $B\bar{B}$ + udsc samples)	83
4.29b Lepton momentum distributions in the sideband region (on-peak vs. $B\bar{B}$ + off-peak samples)	83
4.30a $\cos \theta_{\ell^+\ell^-}^{CM}$ distributions in sideband region (on-peak vs. $B\bar{B}$ + udsc samples) . . .	84
4.30b $\cos \theta_{\ell^+\ell^-}^{CM}$ distributions in the sideband region (on-peak vs. $B\bar{B}$ + off-peak samples)	84
4.31 Distributions of Fisher and likelihood-ratio in the $e\mu$ control sample	85
4.32 Form factor model dependence of $m_{\ell\ell}$ distribution in the $B^+ \rightarrow \pi^+e^+e^-$ mode. .	90
4.33 m_{ES} fits to extract hadronic peaking background in the signal region	92
4.34 Scatter plots of ΔE vs. m_{ES} for $B \rightarrow K^{\ell^+\ell^-}$ background events in the fit region	94
4.35 Scatter plots of ΔE vs. m_{ES} for $B \rightarrow \rho^{\ell^+\ell^-}$ background events in the fit region .	94
4.36 Scatter plots of ΔE vs. m_{ES} for $B \rightarrow K^{*\ell^+\ell^-}$ background events in the fit region	95
4.37 Scatter plots of ΔE vs. m_{ES} for inclusive J/ψ and $\psi(2S)$ background events in the fit region	95
4.38 Two-dimensional fits to <i>BABAR</i> data for the $B \rightarrow \pi e\mu$ modes	98
4.39 Scatter plots of ΔE vs. m_{ES} for <i>BABAR</i> data in the fit and signal regions	102
4.40 Two-dimensional fits to <i>BABAR</i> data for the $B \rightarrow \pi^{\ell^+\ell^-}$ modes	103
5.1 Branching-fraction upper limit vs. luminosity for $\mathcal{B}(B \rightarrow \pi^{\ell^+\ell^-})$	112
5.2 Significance vs. luminosity for $\mathcal{B}(B \rightarrow \pi^{\ell^+\ell^-})$	113
A.1 Average leakage current per diode, October 1999 through May 2002.	124
A.2 New CsI(Tl) crystal in the process of being polished.	125
A.3 Assembled background sensor	126
A.4 New sensor installed on the inner surface of the EMC forward end cap.	126
A.5 Preamplification board	127
A.6 CAMAC Beam Abort Module	127
A.7 Calibration in Co60 source well	128
A.8 Leakage current vs. radiation for new sensors biased at 30 V	130
A.9 Measured leakage current vs. radiation for old sensors biased at 30 V	132
A.10 Measured single channel output voltage of preamplification boards vs. input currents	132
A.11 Total output voltage of preamplification boards vs. sum of input currents	133
A.12 Estimated single-current output voltage vs. input current	134
A.13 Estimated total output voltage vs. sum of input currents	135

A.14 Original Pre-Amplifier Board output vs. radiation (measured) 135
A.15 Estimate of preamplification board output vs. current and radiation 137
A.16 Voltage (EMC_TOTL signal) vs. time, Nov 5, 2002 – June 30, 2003 138

List of Tables

2.1	<i>BABAR</i> data samples, 1999-2004.	21
4.1	Simulated signal and penguin background samples for the $B \rightarrow \pi\ell^+\ell^-$ analysis .	47
4.2	Simulated charmonium samples for the $B \rightarrow \pi\ell^+\ell^-$ analysis	48
4.3	Simulated generic background samples for the $B \rightarrow \pi\ell^+\ell^-$ analysis	49
4.4	Boundaries of the kinematic signal region in data	49
4.5	Optimal selection criteria for Fisher and likelihood ratio.	57
4.6	Estimates of hadronic D -modes constituting a potential background.	63
4.7	Candidate multiplicity per event	64
4.8	Yields and branching fractions extracted from fits to $B \rightarrow J/\psi\pi$ data.	69
4.9	Summary of sideband yields in <i>BABAR</i> data and Monte Carlo.	76
4.10	Summary of lepton identification efficiencies in data and Monte Carlo.	87
4.11	Summary of Fisher and likelihood-ratio efficiencies in data and Monte Carlo. . .	88
4.12	Efficiencies of $B \rightarrow \pi\ell^+\ell^-$ signal events.	89
4.13	Relative change in signal efficiencies from different form-factor models.	89
4.14	Summary of peaking background, in fit and signal regions	96
4.15	Expected (Monte Carlo) and observed (data) combinatorial background yields . .	98
4.16	Observed and bias corrected combinatorial background yields in the signal region	99
4.17	Summary of expected background with uncertainties	101
4.18	Systematics due to uncertainties in signal efficiency.	106
4.19	Results: Branching fraction upper limits	108
A.1	Calibration data from new EMC PIN-diode sensors biased at 30 V	129
A.2	Calibration data for old DCH diodes biased at 30 V.	131
A.3	Calibration data for the original preamplification board.	131
A.4	Calibration data for the spare preamplification board.	131
A.5	Mapping of radiation dose rate and voltage output from preamplification board. .	136

A.6 Summary of results from dosimeter cross-check 140

Preface

During the first half of the twentieth century, the theories of quantum mechanics and special relativity revolutionized our understanding of physics governing the very small and very fast. Through the latter half of the twentieth century, the Standard Model [1–4] for particle physics grew out of these theories and from discoveries made in particle collision experiments.

Quantum Electrodynamics (QED) [1] was developed in the 1940's, and was the first such quantum field theory to interpret light as a quantized particle (the photon) being a field excitation of the electromagnetic field. It combines quantum mechanics and special relativity, and was a success in explaining all the observed effects of atomic physics.

QED became a prototype of a local gauge field theory [5], upon which also the quantum field theory of strong interactions is modeled. The strong interaction is responsible for keeping the nucleons together in the nucleus of the atom. The early theory of the strong force, explained by Yukawa interactions between the nucleons developed in 1935 [6], models the interaction between the nucleons as a pion exchange. A yet different mechanism is responsible for the radioactive decay of the nucleus; these are due to the weak force.

Particle collision experiments followed, from fixed-target experiments from the 1950s through the 1970s, where a heavy-nucleus material was bombarded by subatomic particles, usually protons, to sophisticated high-energy physics (HEP) experiments with large linear or circular accelerators and storage rings colliding nucleons or electron positron pairs. Through the years, a zoo of new particles, “hadrons”, were discovered, most of them highly unstable elements that decay into several other particles instantaneously. Some sense of order in this chaos was introduced in the 1960's with the quark model, which postulates that the nucleons and the other hadrons which were observed in the high-energy experiments consist of quarks [7].

In the early 1970s, onto this background of quantum mechanics and special relativity and the hadron classification scheme, the Standard Model developed into a consistent theory. A quantum field theory for the strong nuclear interaction (Quantum Chromodynamics, QCD) was developed between 1960-1973 [3], and the weak nuclear interaction was unified with the electromagnetic

interaction in 1973 into the Electroweak (EW) theory [2]. This unified EW theory predicted the existence of the heavy Z^0 and W^\pm gauge bosons which were later discovered at the Super Proton Synchrotron (SPS) [8] and studied in details at the Large Electron Positron collider (LEP) [9].

The Standard Model fits very well with all observed phenomena particle physics to date. It is successful in explaining how things happen, but not so much “why”. It is unlikely to be the final theory, and leaves many questions unanswered (see *e.g.* [10]). For example, it does not explain why there are exactly three families of particles or why the charges are quantized, and the origin of particle masses is not fully understood. The masses of leptons and quarks are believed to arise from Yukawa interaction with the Higgs condensate [11], but an associated Higgs boson has not yet been seen experimentally. The Standard Model has at least 18 arbitrary parameters [12] which are determined from experiments, with 9 additional ones if we count in the neutrino masses and mixing matrix.

There are many extensions to the Standard Model. Of the most popular ones are SuperSymmetric (SUSY) [13] models which successfully combine the QCD and EW theories by describing a symmetry relation between fermions (leptons and quarks) and bosons (the “force-carrier” particles). SUSY can solve many of the unanswered questions and is a good candidate for a unified theory. However, its validity has not been established by any experimental results.

The *BABAR* experiment [14] was designed for high-precision measurements of CP violation [15] which expresses the degree of asymmetry between matter and antimatter. CP violation occurs in the Standard Model through quark mixing, and has by now been measured in many different B decay channels by both *BABAR* and Belle [16]. But CP violation and other measurable quantities may be altered by not-yet-discovered physics which is not accounted for by the Standard Model. And the search for new physics will continue with increasing energies in HEP experiments, the most imminent being the LHC experiments [17] about to come online in 2007. In the meantime, rare B decays are sensitive to presence of new physics on a higher mass scale than that of the b quark, m_b . The physics discussed in this work is related to certain rare decays of B -mesons, which due to their low rates and quantum loop structure constitute precision tests of the Standard Model as well as a testing ground for effects of physics beyond the Standard Model.

This thesis presents a search for one of these rare quantum-loop processes in which a B meson decays via the weak force into a $\pi^+\ell^+\ell^-$ final state. Chapter 1 explains in more details what is known about these physics processes today, the theoretical framework used for making predictions, and what we can learn from measuring these types of decays. Chapter 2 describes the detector and the accelerator facility which makes up the *BABAR* experiment, and which produces

and collects the B -meson data used here. In Chapter 3, the experimental techniques which are typical for this experimental setup are described, and Chapter 4 presents the analysis, control checks and results of the search for the rare radiative electroweak penguin decay $B \rightarrow \pi \ell^+ \ell^-$. Chapter 5 concludes with some thoughts on the results of the analysis, and the outlook for further studies of these decays. Appendix A describes the preparation and calibration of background radiation sensors used for protecting *BABAR* against stray radiation from the PEP-II beams.

Chapter 1

Theoretical and experimental motivation

Over the last couple of decades, a lot of attention has been focused on radiative and semileptonic penguin B -decays. The interest stems from these decays' role as a unique testing ground for physics at the electroweak scale. These penguin decays provide a laboratory for precision testing of the Standard Model [1–3] and for potentially discovering effects of new physics *beyond* it.

Experimental data from weak-interaction processes reveal that neutral Z^0 -current interactions never change the quark flavor, while the charged W^\pm -current interactions always do. The flavor-changing charged-current interaction can be understood in terms of left-handed (L) quark-fields organized in weak isospin SU(2) doublets:

$$\begin{pmatrix} u \\ d' \end{pmatrix}_L \begin{pmatrix} c \\ s' \end{pmatrix}_L \begin{pmatrix} t \\ b' \end{pmatrix}_L \quad (1.1)$$

The primed quantities are linear combinations of the mass eigenstates (d , s and b) and relate to these via the Cabibbo-Kobayashi-Maskawa (CKM) matrix [18] defined by

$$\begin{pmatrix} d' \\ s' \\ b' \end{pmatrix} = \begin{pmatrix} V_{ud} & V_{us} & V_{ub} \\ V_{cd} & V_{cs} & V_{cb} \\ V_{td} & V_{ts} & V_{tb} \end{pmatrix} \begin{pmatrix} d \\ s \\ b \end{pmatrix}. \quad (1.2)$$

where V_{ij} express the coupling strength between the quark flavors i and j . The matrix is often given in terms of the Wolfenstein parameterization [19] in which the matrix elements are given as expansions in the parameter $\lambda = |V_{us}| \approx 0.23$.

Even though flavor-changing neutral currents (FCNC) do not occur at tree level, they are allowed in higher-order processes, like penguin loop and box diagrams involving heavy virtual

particles. Examples of such loop and box diagrams are shown in figure 1.1, which depicts the electroweak decay of a B meson at the quark level. The diagrams show the amplitudes contributing to the decay $B \rightarrow \pi \ell^+ \ell^-$ if the final-state meson includes the d -quark, or the decay $B \rightarrow K \ell^+ \ell^-$ if the final-state meson includes the s -quark. These decays are the simplest manifestations of the $b \rightarrow d \ell^+ \ell^-$ and $b \rightarrow s \ell^+ \ell^-$ transitions.

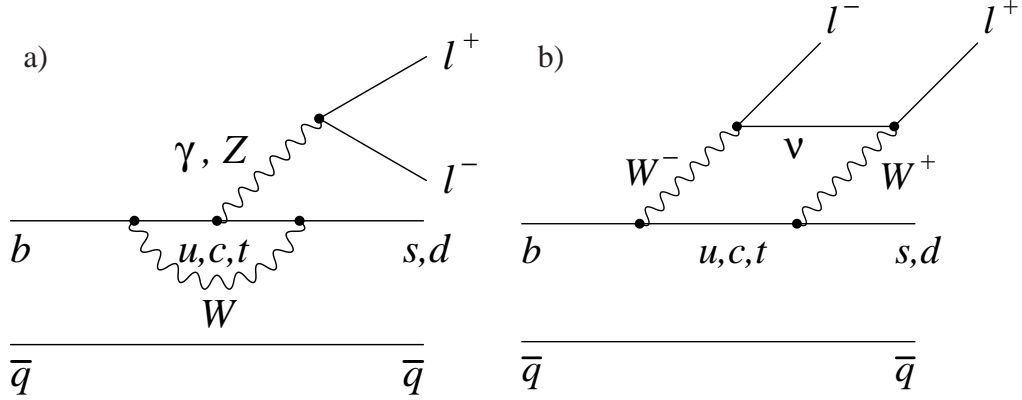


Figure 1.1: Feynman diagrams of Standard Model FCNC $b \rightarrow s \ell^+ \ell^-$ and $b \rightarrow d \ell^+ \ell^-$ transitions. Diagram a) shows the electroweak penguin process involving either a virtual photon (γ) or a virtual Z^0 , and diagram b) shows the W^\pm box diagram.

These transitions are usually called *radiative* penguin processes since the first order contributions come from what are normally radiative corrections to a tree diagram. The absence of tree diagrams for these processes results in a suppressed rate due to vertex factors, and additional suppression is caused by the GIM mechanism [20]. The type of process which is the subject of this analysis also goes under the name *semileptonic* penguins, to specify the $\ell^+ \ell^-$ final state and distinguish it from the more abundant $b \rightarrow s \gamma$ and $b \rightarrow d \gamma$ processes.

Since these decays proceed via weakly-interacting particles with virtual energies near the electroweak scale, they provide a promising means to search for effects from new flavor-changing interactions. Such effects are predicted in a wide variety of models, usually in the context of $b \rightarrow s \ell^+ \ell^-$ [21–25]. Some of these imagined new processes are depicted for the $b \rightarrow s$ transition in figure 1.2, where the loops shown involve a charged Higgs H^\pm boson or supersymmetric particles (chargino (χ^\pm) and up-type squarks ($\tilde{u}, \tilde{c}, \tilde{t}$), or gluino (\tilde{g}) or neutralino (χ^0) with down-type squarks ($\tilde{d}, \tilde{s}, \tilde{t}$)). If there exists non-trivial flavor violation in the new interactions, $b \rightarrow d \ell^+ \ell^-$ can also exhibit large observable effects, independent of the experimental constraints on $b \rightarrow s \ell^+ \ell^-$ [26, 27]. Effects of physics beyond the Standard Model may show up in the decay rates, the q^2 dependence of the decay ($q^2 = m_{\ell^+ \ell^-}^2$), in the decay angles of these decays, or they

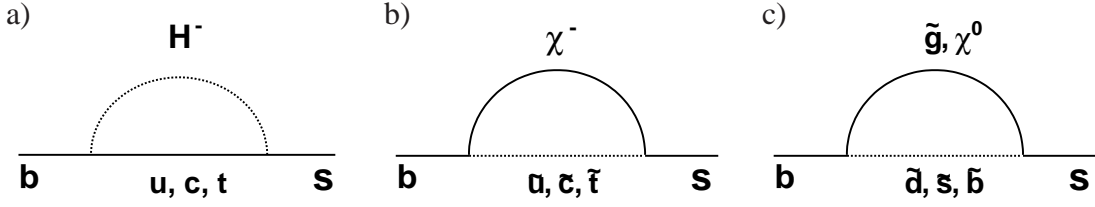


Figure 1.2: Possible new-physics Feynman diagrams for the $b \rightarrow s$ transition: a) A charged Higgs loop, b) a chargino loop with up-type squarks, c) gluino or neutralino loops with down-type squarks.

may show up as unexpected CP asymmetries [28, 29].

Even if new physics processes are not present in these decays, they are still interesting as a precision testing ground for the Standard Model at the electroweak scale. Their rates and distributions are sensitive to the top quark mass and to the CKM matrix elements.

The first evidence of a $b \rightarrow s$ penguin process was observed in 1993 by the CLEO collaboration in a signal of $B \rightarrow K^*(892)\gamma$ decays [30], which are the simplest $b \rightarrow s\gamma$ processes. CLEO was also the first to measure the inclusive $b \rightarrow s\gamma$ decay [31]. The Feynman diagram is similar to the photon penguin in figure 1.1a with the photon being real in this case. Due to angular momentum conservation, the external real photon is not allowed for a pseudoscalar meson final state (π, K) and thus the simplest $b \rightarrow s\gamma$ and $b \rightarrow d\gamma$ decays are the $B \rightarrow K^*\gamma$ and $b \rightarrow \rho\gamma$, respectively, with vector mesons (K^* and ρ) in the final states.

The decay rate for $b \rightarrow s\ell^+\ell^-$ is suppressed by another vertex coupling constant compared to $b \rightarrow s\gamma$. These rare decays have three amplitudes contributing differently at different recoil energies ($m_{\ell^+\ell^-}^2 = q^2$), thus these decays have non-trivial kinematic properties which can be predicted and measured. As early as 1987 the CLEO and ARGUS collaborations were searching for inclusive $X_s\ell^+\ell^-$ decays [32–34], where X_s is a hadronic final state originating from the s quark. These events were not observed until the large data samples of the B -Factories [35, 36] became available.

We will return to the experimental status of these decays after taking a look at the theoretical framework for understanding these processes.

1.1 Effective Hamiltonians for FCNC processes

The simple electroweak amplitude for $b \rightarrow s\ell^+\ell^-$ and $b \rightarrow d\ell^+\ell^-$ depicted in figure 1.1 is further modified by soft and hard gluon interactions between initial and final state quarks. Short-distance QCD corrections are dominant (comparable in size to the pure electroweak diagram) and these can be reliably calculated using perturbation theory. The long-distance QCD effects play a sub-dominant role because of the large mass of the B meson. Since the decay involves a single hadronic current, the non-perturbative QCD parameters can be isolated and related to the same parameters for other decays. The theoretical tool typically used is the Operator Product Expansion (OPE) [37] which separates short-distance QCD effects from long-distance QCD effects. In this framework, the effective low-energy Hamiltonian relevant to the partonic process $b \rightarrow s\ell^+\ell^-$ can be written as [23]:

$$\mathcal{H}_{\text{eff}}(b \rightarrow s\ell^+\ell^-) = -\frac{4G_F}{\sqrt{2}}V_{ts}^*V_{tb}\sum_{i=1}^{10}C_i(\mu)\mathcal{O}_i(\mu) \quad (1.3)$$

where $G_F \equiv \frac{\sqrt{2}}{8}\left(\frac{g_2}{M_W}\right)^2$ is the Fermi coupling constant and $V_{ts}^*V_{tb}$ are the CKM matrix elements which dominate for $b \rightarrow s\ell^+\ell^-$.

The operators \mathcal{O}_i describe the effective vertices and include the long-distance QCD effects, while $C_i(\mu)$ are the corresponding Wilson coefficients [37] that describe physics at short-distances (high energy scale). Both the operators and the Wilson coefficients depend on the scale at which they are calculated. However, the resulting Hamiltonian is scale independent.

The Wilson coefficients describing the short-distance QCD effects can be calculated perturbatively at some renormalization scale μ , usually in the $\overline{\text{MS}}$ scheme [38]. Their values are found by a matching procedure between the effective theory and the full Standard Model at a high energy scale $\mu \sim m_W$. At this energy scale, perturbation theory in the strong coupling $\alpha_s(\mu)$ is valid due to the asymptotic freedom property of QCD, and they can be expanded as follows [39]:

$$C_i(\mu) = C_i^{(0)}(\mu) + \frac{\alpha_s(\mu)}{4\pi}C_i^{(1)}(\mu) + \frac{\alpha_s^2(\mu)}{(4\pi)^2}C_i^{(2)}(\mu) + \mathcal{O}(\alpha_s^3) \quad (1.4)$$

Evolution of the Wilson coefficients from the high-energy scale down to the low-energy scale $\mu = m_b$, is described by the Renormalization Group Equation (RGE) [40]. In this process, contributions from W^\pm and other heavy fields are integrated out, or removed from the theory as dynamic degrees of freedom and instead contained in the initial conditions of these Wil-

¹Due to the smallness of $V_{ub}V_{us}^*$ the terms with $V_{cb}V_{cs}^*$ are $V_{tb}V_{ts}^*$ are dominating. The term $V_{cb}V_{cs}^*$ is further removed from the equation using the unitarity of the CKM matrix ($V_{tb}V_{ts}^* + V_{cb}V_{cs}^* + V_{ub}V_{us}^* = 0$)

son coefficients. At this low-energy scale, however, the presence of large logarithmic terms $\alpha_s(\mu)\ln(m_W/m_b)$ in the Wilson coefficient calculations spoils the validity of the usual perturbation series. A Renormalization Group (RG) analysis [29] allows for efficient calculation of logarithmic terms to all orders of perturbation theory. In the n 'th order of RG improved perturbation theory, the terms

$$\alpha_s^n(\mu_b) \left(\alpha_s(\mu_b) \ln \frac{\mu_W}{\mu_b} \right)^k$$

are summed to all orders of k ($k = 0, 1, 2, \dots$). The leading order (LO) corresponds to $n = 0$ in most cases. Thus, LO calculation corresponds to summing all the leading logarithmic terms of order $(\alpha_s(\mu)\ln(m_W/m_b))^k$, while at next-to-leading order (NLO), all terms of order $\alpha_s(\mu)[\alpha_s(\mu)\ln(m_W/m_b)]^k$ are summed in addition, and so on. For a detailed review of the methods, see [28, 29]. The resulting Wilson coefficients depend on α_s only via the ratio $\eta = \alpha_s(\mu_W)/\alpha_s(\mu_b)$.

The Wilson coefficients play the role of coupling constants at the FCNC vertices (operators) \mathcal{O}_i . In equation 1.3, $\mathcal{O}_1 - \mathcal{O}_6$ are four-quark operators, \mathcal{O}_7 is an electromagnetic dipole operator, \mathcal{O}_8 is a chromomagnetic operator, and \mathcal{O}_9 and \mathcal{O}_{10} are the semileptonic operators. The operator basis is defined in *e.g.* [41]. For $b \rightarrow s\ell^+\ell^-$ processes, \mathcal{O}_7 is the leading contribution of the photon penguin and \mathcal{O}_9 and \mathcal{O}_{10} are the leading contributions of the $\ell^+\ell^-$ penguin and box diagram. The operators mix under renormalization [41], thus the leading order operators receive some contributions from the other operators as well. These effects are included in the effective Wilson coefficients C_7^{eff} , C_9^{eff} and C_{10}^{eff} . Calculations of C_7^{eff} , C_9^{eff} and C_{10}^{eff} have now been performed up to next-to-next-to-leading order (NNLO) [39, 42–45].

The decays involving $b \rightarrow s\gamma$ and $b \rightarrow d\gamma$ transitions are sensitive to the Wilson coefficient C_7 . The decays involving $b \rightarrow s\ell^+\ell^-$ and $b \rightarrow d\ell^+\ell^-$ transitions are in addition sensitive to the Wilson coefficients C_9 and C_{10} .

The effective Hamiltonian for the $b \rightarrow d\ell^+\ell^-$ transition is defined by the same operators and the same Wilson coefficients that appear in equation 1.3, but here other CKM matrix elements are involved. In this case, the couplings between the external b and d quark to the u , c , and t quark loops are such that we need to include two additional terms in the Hamiltonian, and $\mathcal{H}_{\text{eff}}(b \rightarrow d\ell^+\ell^-)$ is given by [46]:

$$\begin{aligned} \mathcal{H}_{\text{eff}}(b \rightarrow d\ell^+\ell^-) = & -\frac{4G_F}{\sqrt{2}}V_{td}^*V_{tb} \left\{ \sum_{i=1}^{10} C_i(\mu)\mathcal{O}_i(\mu) \right. \\ & \left. -\lambda \{C_1(\mu)[\mathcal{O}_1^u(\mu) - \mathcal{O}_1(\mu)] + C_2(\mu)[\mathcal{O}_2^u(\mu) - \mathcal{O}_2(\mu)]\} \right\} \end{aligned} \quad (1.5)$$

where $\lambda = \frac{V_{ub}V_{ud}^*}{V_{tb}V_{td}^*}$, using the unitarity of the CKM matrix, *i.e.* $V_{tb}V_{td}^* + V_{ub}V_{ud}^* = -V_{cb}V_{cd}^*$.

1.2 Theoretical predictions

Theoretical predictions of physical observables involve calculations of matrix elements, *e.g.* $\mathcal{M} = \langle d\ell^+\ell^- | \mathcal{H}^{\text{eff}}(b \rightarrow d\ell^+\ell^-) | b \rangle$. Neglecting the d -quark mass, the QCD-corrected matrix element for the $b \rightarrow d\ell^+\ell^-$ transition is given by [47]:

$$\begin{aligned} \mathcal{M} = \frac{G_F \alpha}{2\sqrt{2}\pi} V_{td} V_{tb}^* \left\{ C_9^{\text{eff}} \bar{d} \gamma_\mu (1 - \gamma_5) b \bar{\ell} \gamma^\mu \ell + C_{10} \bar{d} \gamma_\mu (1 - \gamma_5) b \bar{\ell} \gamma^\mu \gamma_5 \ell \right. \\ \left. - 2C_7^{\text{eff}} \frac{m_b}{q^2} \bar{d} i \sigma_{\mu\nu} q^\nu (1 + \gamma_5) b \bar{\ell} \gamma^\mu \ell \right\}, \end{aligned} \quad (1.6)$$

where q^2 is the invariant dilepton mass.

Inclusive decays ($B \rightarrow X_s \ell^+ \ell^-$ and $B \rightarrow X_d \ell^+ \ell^-$) are the simplest ones from a theoretical standpoint. Here, heavy quark expansion (HQE) [48, 49] parameters can be used, and make very reliable predictions. The branching fraction of the dilepton decays are calculated as a function of $\hat{s} = q^2/m_b^2$, where q is the four-momentum transfer by the $\ell^+ \ell^-$ system, therefore $q^2 = m_{\ell^+ \ell^-}^2$ is the dilepton mass squared. m_b is the most important contribution to the theoretical uncertainty (total of $\sim 15\%$) [23]. To avoid the large uncertainty due to $m_{b,\text{pole}}^5$, it has become customary to normalize the branching fraction to experimentally measured $b \rightarrow ce\bar{\nu}$ branching fraction, thus calculating

$$\mathcal{B}_{(B \rightarrow X_s \ell^+ \ell^-)}(\hat{s}) = \frac{\mathcal{B}_{(B \rightarrow X_c e \bar{\nu})}^{\text{exp}}}{\Gamma(B \rightarrow X_c e \bar{\nu})} \frac{d\Gamma(B \rightarrow X_s \ell^+ \ell^-)}{d\hat{s}} \quad (1.7)$$

The explicit expression for the semileptonic decay width $\Gamma(B \rightarrow X_c e \bar{\nu})$ can be found in *e.g.* [39].

From an experimental point-of-view, the inclusive decays are more difficult to measure than exclusive decays. Exclusive decays have well defined kinematical properties that can be used to select the events and measure decay properties. Theoretical predictions, on the other hand, involve explicit matrix elements of the operators over meson states. The matrix elements are parameterized in terms of form factors, which are difficult to calculate precisely. These have typically had an uncertainty of 20%-30%, although continued work on improving techniques and input parameters are bringing these uncertainties down.

The form factors of the transition involving the pseudoscalar mesons $B \rightarrow \pi$ are defined in terms of the matrix elements. The matrix element describing the standard weak $B \rightarrow \pi$ current

is [50]:

$$\langle \pi(p_\pi) | \bar{u} \gamma_\mu b | B(p_B) \rangle = \left\{ (p_\pi + p_B)_\mu - \frac{m_B^2 - m_\pi^2}{q^2} q_\mu \right\} f_+^\pi(q^2) + \left\{ \frac{m_B^2 - m_\pi^2}{q^2} q_\mu \right\} f_0^\pi(q^2) \quad (1.8)$$

and the matrix element describing the $B \rightarrow \pi$ penguin current is given by:

$$\langle \pi(p_\pi) | \bar{d} \sigma_{\mu\nu} q^\nu (1 - \gamma_5) b | B(p_B) \rangle = \frac{i}{m_B + m_\pi} \{ q^2 (p_\pi + p_B)_\mu - (m_B^2 - m_\pi^2) q_\mu \} f_T^\pi(q^2, \mu), \quad (1.9)$$

where p_B and p_π are the B - and π -meson momenta, $q = p_B - p_\pi$, and m_B and m_π are the meson masses. The form factors $f_0(q^2)$ and $f_+(q^2)$ are independent of the renormalization scale μ since $\bar{u} \gamma_\mu b$ is a physical current in contrast to the the penguin current $\bar{d} \sigma_{\mu\nu} q^\nu (1 - \gamma_5) b$ [50].

In semileptonic decays the physical range in q^2 is $0 \leq q^2 \leq (m_B - m_\pi)^2$. The form factors f_+ and f_0 are relevant to $B \rightarrow \pi \ell \nu$ decays as well, while f_T only matters for the penguin decays. In this work, the signal model used for efficiency estimation uses the form-factor predictions of Ball & Zwicky [50]. This model is chosen because it includes radiative corrections and the most recent input parameters, and it calculates all the relevant $B \rightarrow \pi$ form factors $f_+^\pi(q^2)$ and $f_0^\pi(q^2)$ and $f_T^\pi(q^2)$. The calculations are done in the framework of light-cone QCD sum rules [51], which requires the final-state meson to have $E \gg \Lambda_{\text{QCD}}$, thus the calculations cover only the region $0 \text{ GeV}^2/c^4 \leq q^2 \leq 14 \text{ GeV}^4/c^4$. However, Ball & Zwicky have given a parameterization that include the main features of the analytical properties of the form factors and they extrapolate the result to cover the full physical region $0 \leq q^2 \leq (m_B - m_\pi)^2 \approx 26.4 \text{ GeV}^2/c^4$. The uncertainty due to this extrapolation is claimed to be approximately 5%. The total theoretical uncertainty at zero q^2 is now as low as 10% to 13%.

For $B \rightarrow \pi$ decays, an alternative approach exists which is to calculate form factors using lattice QCD [52]. Lattice QCD expected to give the most precise predictions in the long term, however, currently only $B \rightarrow \pi$ form factors for the standard electroweak current have been predicted. Lattice spacing constrains the calculations to $q^2 > 14 \text{ GeV}^2/c^4$, thus lattice QCD is complimentary to the the LCSR approach. Extrapolations of LCSR calculations to higher q^2 values and lattice QCD calculations to lower q^2 values have shown good agreement [53].

1.3 Measurable quantities

To tests the Standard Model and search for effects of new physics beyond it, requires observables for which there are precise theoretical predictions that can be measured with a high precision

experimentally.

1.3.1 Decay rates

Since the first observation of the $b \rightarrow s$ penguin transition by CLEO-II in 1993, when the branching fraction, \mathcal{B} , was measured based on 10 $B \rightarrow K^*(892)\gamma$ events and found to be $(4.1 \pm 1.5 \pm 0.9) \times 10^{-5}$, precision measurements have been done both of this exclusive decay as well as the inclusive decay $B \rightarrow X_s\gamma$. The world average [54] today, $\mathcal{B}(B \rightarrow K^*(892)\gamma) = (4.01 \pm 0.20) \times 10^{-5}$, is based on measurements by *BABAR* [55], Belle [56] and CLEO-II [57], in agreement with the less precise NLO Standard Model predictions (see e.g. [58, 59]).

Also the inclusive decay rate has been measured by *BABAR* [60, 61], Belle [62, 63] and CLEO-II [64, 65], and the current experimental average is [66] $\mathcal{B}(B \rightarrow X_s\gamma) = (3.55 \pm 0.26_{-0.10}^{+0.09} \pm 0.03) \times 10^{-4}$ for $E_\gamma > 1.6$ GeV. A recent result [67] based on NNLO calculations estimates $\mathcal{B}(B \rightarrow X_s\gamma) = (3.15 \pm 0.23) \times 10^{-4}$ for $E_\gamma > 1.6$ GeV. The uncertainties of the experimental results and the new theoretical results are now of the same order. The central value of the NNLO calculation is lower than earlier results from NLO calculations (see e.g. [68]), and about 1σ lower than the experimental average.

The agreement between these measurements and theoretical calculations of branching fractions of $b \rightarrow s\gamma$ transitions put constraints on new-physics parameters [23] and on the value of the Wilson coefficient C_7^{eff} , but the hint of discrepancy allows for new-physics processes in $b \rightarrow s\gamma$ transitions [69].

The $b \rightarrow s\ell^+\ell^-$ transition provide complimentary information, in particular on the Wilson coefficients C_9^{eff} and C_{10}^{eff} , and branching fraction predictions have been calculated perturbatively in QCD to NNLO [23]². The main theoretical uncertainties arise from interference with charmium production in the tree-diagram decay $B \rightarrow X_s J/\psi(\rightarrow \ell^+\ell^-)$.

The branching fraction of the exclusive decays $\mathcal{B}(B \rightarrow K\ell^+\ell^-)$ and $\mathcal{B}(B \rightarrow K^*\ell^+\ell^-)$ have recently been measured by *BABAR* [26] to be $\mathcal{B}(B \rightarrow K\ell^+\ell^-) = (0.34 \pm 0.07 \pm 0.02) \times 10^{-6}$ and $\mathcal{B}(B \rightarrow K^*\ell^+\ell^-) = (0.78_{-0.17}^{+0.19} \pm 0.11) \times 10^{-6}$, where the first errors are statistical and the last errors are systematic. These results are compatible with theoretical calculations at NNLO [23, 70], which predict $\mathcal{B}(B \rightarrow K\ell^+\ell^-) = (0.35 \pm 0.12) \times 10^{-6}$, $\mathcal{B}(B \rightarrow K^*e^+e^-) = (1.58 \pm 0.49) \times 10^{-6}$, and $\mathcal{B}(B \rightarrow K^*\mu^+\mu^-) = (1.19 \pm 0.39) \times 10^{-6}$. The hadronic uncertainties in the

²Note that the lowest-order QCD corrections to $b \rightarrow s\ell^+\ell^-$ starts at $O(\alpha_s^{-1})$, as opposed to the decay $b \rightarrow s\gamma$ where the lowest order corrections start at $O(\alpha_s^0)$. Hence, the NNLO accuracy in $B \rightarrow X_s\ell^+\ell^-$ amounts to calculating $O(\alpha_s)$ corrections, while the NNLO results mentioned for $B \rightarrow X_s\gamma$ amounts to calculating $O(\alpha_s^2)$ corrections [23].

exclusive branching fraction predictions are currently larger than the experimental uncertainties. Therefore, improved measurements of these total exclusive branching fractions will have only limited usefulness in terms of testing the Standard Model.

Predictions for inclusive decays have been computed by [23, 39, 71] to NNLO accuracy and predict $\mathcal{B}(B \rightarrow X_s e^+ e^-) = (6.89 \pm 1.01) \times 10^{-6}$ and $\mathcal{B}(B \rightarrow X_s \mu^+ \mu^-) = (4.15 \pm 0.70) \times 10^{-6}$. Various calculations of the effects of new physics have been performed, indicating possible enhancements in the branching fraction of $B \rightarrow X_s \ell^+ \ell^-$ of up to a factor of two [72] compared to Standard Model predictions. The inclusive branching fraction was first measured by Belle [35] based on 64.5 million $B\bar{B}$ -pairs: $\mathcal{B}(B \rightarrow X_s \ell^+ \ell^-) = (6.1 \pm 1.4(\text{stat.})_{1.1}^{+1.4}(\text{syst.})) \times 10^{-6}$, for $m_{\ell^+ \ell^-} > 0.2 \text{ GeV}/c^2$, and was shortly after also measured by *BABAR* [36] based on 88.9 million $B\bar{B}$ -pairs: $\mathcal{B}(B \rightarrow X_s \ell^+ \ell^-) = (5.6 \pm 1.5(\text{stat.}) \pm 0.6(\text{exp. syst.}) \pm 1.1(\text{model syst.})) \times 10^{-6}$, for $m_{\ell^+ \ell^-} > 0.2 \text{ GeV}/c^2$. Belle later updated the analysis with 152 million $B\bar{B}$ -pairs [73] and found $\mathcal{B}(B \rightarrow X_s \ell^+ \ell^-) = (4.11 \pm 0.83(\text{stat.})_{-0.81}^{+0.85}(\text{syst.})) \times 10^{-6}$, for $m_{\ell^+ \ell^-} > 0.2 \text{ GeV}/c^2$. These experimental results are most easily compared to an estimate by [74] for the combined branching fraction $\mathcal{B}(B \rightarrow X_s \ell^+ \ell^-) = (4.18 \pm 0.70) \times 10^{-6}$ for $m_{\ell^+ \ell^-} > 0.2 \text{ GeV}/c^2$. From this we see that current knowledge about the decay $B \rightarrow X_s \ell^+ \ell^-$ is limited by experimental uncertainties due to limited statistics and model dependence. Increased statistics is already available and improved measurements can be expected in the near future. The model dependence stems from the uncertainty in the $s \rightarrow X_s$ hadronization model and the fact that the experimental results to date have all used the sum-of-exclusive modes technique where the X_s hadronic system is explicitly reconstructed. A fully inclusive measurement which does not rely on explicit X_s reconstruction has not been successful so far.

The CKM-suppressed transition $b \rightarrow d$ has recently been observed by Belle [75] in the exclusive decay channels $B \rightarrow \rho\gamma$ and $B \rightarrow \omega\gamma$. With a significance of 5.1σ , they measure the combined branching fraction $\overline{\mathcal{B}}(B \rightarrow (\rho, \omega)\gamma) = (1.32_{-0.31}^{+0.34} \text{ }_{-0.09}^{+0.10}) \times 10^{-6}$, where the uncertainties are statistical and systematic. This combined branching fraction assumes the isospin relation between ρ^+ , ρ^0 and ω and is defined as

$$\overline{\mathcal{B}}(B \rightarrow (\rho, \omega)\gamma) \equiv \mathcal{B}(B^+ \rightarrow \rho^+\gamma) = 2 \frac{\tau_{B^+}}{\tau_{B^0}} \mathcal{B}(B^0 \rightarrow \rho^0\gamma) = 2 \frac{\tau_{B^+}}{\tau_{B^0}} \mathcal{B}(B^0 \rightarrow \omega\gamma)$$

BABAR has followed with a measurement [76] yielding $\mathcal{B}(B^+ \rightarrow \rho^+\gamma) = (1.06_{-0.31}^{+0.35} \pm 0.09) \times 10^{-6}$ and $\mathcal{B}(B^+ \rightarrow \rho^0\gamma) = (0.77_{-0.19}^{+0.21} \pm 0.07) \times 10^{-6}$ observing approximately 40 events in each mode. The highest significance is found from the $B^+ \rightarrow \rho^0\gamma$ mode which has a statistical significance of 5.2σ . Also here, a combined limit has been found from a combined fit

to all the modes yielding $\overline{\mathcal{B}}(B \rightarrow (\rho/\omega)\gamma) = (1.01 \pm 0.21 \pm 0.08) \times 10^{-6}$, corresponding to a statistical significance of 6.3σ . The uncertainties are statistical and systematic. The corresponding theoretical predictions are $\overline{\mathcal{B}}(B \rightarrow (\rho/\omega)\gamma) = (1.38 \pm 0.42) \times 10^{-6}$ [77].

The CKM suppressed $b \rightarrow d\ell^+\ell^-$ transition has not been measured yet. The previous search for $B \rightarrow \pi\ell^+\ell^-$ was done in 1990 by the MARKII experiment [78], which set the upper limits at 90% confidence level:

$$\mathcal{B}(B^+ \rightarrow \pi^+e^+e^-) < 3.9 \times 10^{-3}$$

$$\mathcal{B}(B^+ \rightarrow \pi^+\mu^+\mu^-) < 9.1 \times 10^{-3}$$

No search has been reported on for the $B^0 \rightarrow \pi^0\ell^+\ell^-$ modes.

In the Standard Model, the prediction for the $B \rightarrow \pi\ell^+\ell^-$ branching fraction is 3.3×10^{-8} [47]. The uncertainty in the prediction is approximately 30% with the main contribution coming from uncertainties in form-factor calculations. The branching fraction predicted is an order of magnitude smaller than the one measured for $B \rightarrow K\ell^+\ell^-$. Models beyond the Standard Model can have an observable effect on both the branching fraction as well as on *e.g.* CP asymmetries and lepton forward-backward asymmetries. Given the very small expected branching fraction, the only feasible observable with the current or future *BABAR* datasets will be the branching fraction.

Investigations have been done of how the branching fraction would be different in the framework of the general two Higgs doublet model (2HDM (model III)). In this model the branching fraction is expected to be $\mathcal{B}(B \rightarrow \pi\ell^+\ell^-) = 4.1 \times 10^{-8}$ [47]. Other physics scenarios beyond the Standard Model may possibly increase or decrease this branching fraction further, but this has not yet been explored through phenomenological calculations.

1.3.2 Ratio of decay rates

The hadronic uncertainties that currently limit the precision of theoretical predictions, typically cancel if we look at the *ratio* of branching fractions. By comparing modes with e^+e^- and $\mu^+\mu^-$ in the final state, *BABAR* has measured the ratio of branching fractions:

$$R_K \equiv \frac{\Gamma(B \rightarrow K\mu^+\mu^-)}{\Gamma(B \rightarrow Ke^+e^-)} = \frac{\mathcal{B}(B \rightarrow K\mu^+\mu^-)}{\mathcal{B}(B \rightarrow Ke^+e^-)} \quad (1.10)$$

which in the Standard Model has a very precise prediction of $R_K = 1.0000 \pm 0.0001$ [79]. While the prediction of the branching fraction is depending on fragmentation models, the prediction

of the ratio is nearly model independent, since many form-factor dependencies cancel in the ratio. This ratio may deviate from unity if particles in the loop couple differently to muons and electrons. *E.g.* if the squark in the chargino-squark loop depicted in figure 1.2b radiate a neutral Higgs boson, this Higgs boson would decay into a $\mu^+\mu^-$ pair more often than an e^+e^- pair. The predictions for R_{K^*} in the Standard Model is 0.73 ± 0.01 [79], due to the pole region for low values of q^2 . In this region the rate for electrons is higher than that for muons due to the low mass of the electrons. For q^2 above $4m_\mu^2$, the two lepton modes are expected to have nearly the same branching fraction also for $B \rightarrow K^*\ell^+\ell^-$, and $R_{K^*} = 0.991 \pm 0.002$ [79].

From the analysis of $B \rightarrow K^{(*)}\ell^+\ell^-$ events, *BABAR* found $R_K = 1.06 \pm 0.48 \pm 0.08$ [26], which is still statistics limited with only 46 signal events in the sample. Similarly, R_{K^*} over the full q^2 region was found to be $0.91 \pm 0.45 \pm 0.10$, These are based on a sample of 57 $B \rightarrow K^*\ell^+\ell^-$ events. Both results are consistent with Standard Model expectations. This is also true for the result obtained when considering only $q^2 > 0.1 \text{ GeV}^2/c^4$, which yields $R_{K^*} = 1.40 \pm 0.78 \pm 0.10$. A similar measurement of $R_\pi = \mathcal{B}(B \rightarrow \pi\mu^+\mu^-)/\mathcal{B}(B \rightarrow \pi e^+e^-)$ can be done once a significant signal of $B \rightarrow \pi\ell^+\ell^-$ events is observed.

Another interesting ratio of decay rates is the ratio of the newly discovered CKM suppressed $B \rightarrow (\rho, \omega)\gamma$ decay and the CKM allowed $B \rightarrow K^*\gamma$ decays. The ratio of the branching fractions for these two modes gives the opportunity to measure $|V_{td}/V_{ts}|$ via the relation

$$\frac{\mathcal{B}(B \rightarrow \rho\gamma)}{\mathcal{B}(B \rightarrow K^*(892)\gamma)} = \frac{|V_{td}|}{|V_{ts}|} \frac{(m_B^2 - m_\rho^2)^3}{(m_B^2 - m_{K^*}^2)^3} \left(\frac{T_1^\rho(0)}{T_1^{K^*}(0)} \right)^2 (1 + \Delta R) \quad (1.11)$$

where the ratio of $B \rightarrow K^*$ and $B \rightarrow \rho$ form-factors are well predicted ($T_1^{K^*}(0)/T_1^\rho(0) = 1.17 \pm 0.09$ [80] and ΔR is a parameter of order 10% with large uncertainty accounting for effects of weak annihilation and NLO corrections [59]. The uncertainties in $\Delta R_{\rho^+/K^{*+}}$ are rather large due to a contribution from W^+ -annihilation diagram in the $B^+ \rightarrow \rho^+\gamma$ process. To simplify the theoretical interpretation, equation 1.11 is best used with the branching fractions of the *neutral* modes only. By comparing only neutral modes, *BABAR* determines $|V_{td}/V_{ts}|_{\rho^0/K^{*0}} = (0.216_{-0.031}^{+0.029}(\text{exp.})_{-0.018}^{+0.021}(\text{theo.}))$. Using the combined branching fractions of both neutral and charged modes, *BABAR* measures $|V_{td}/V_{ts}| = (0.171_{-0.027}^{+0.018}(\text{exp.})_{-0.014}^{+0.017}(\text{theo.}))$, and Belle measures $|V_{td}/V_{ts}| = (0.199_{-0.025}^{+0.026}(\text{exp.})_{-0.015}^{+0.018}(\text{theo.}))$.

We can imagine measuring $|V_{td}/V_{ts}|$ in a similar way using the ratio $\mathcal{B}(B \rightarrow \pi\ell^+\ell^-)/\mathcal{B}(B \rightarrow K\ell^+\ell^-)$. Given that the expected branching fraction for $B \rightarrow \pi\ell^+\ell^-$ is so low, $|V_{td}/V_{ts}|$ will probably be even more firmly established by the time a $B \rightarrow \pi\ell^+\ell^-$ signal of proportions is observed. Perhaps it may be useful as a control check one day.

Recently CDF reported on a measurement of the $B_s^0\bar{B}_s^0$ oscillation frequency Δm_s [81, 82]. They measure $\Delta m_s = 17.31^{+0.33}_{-0.18} \pm 0.07 \text{ ps}^{-1}$, where the first uncertainty is statistical and the second is systematic. From this they determine $|V_{td}/V_{ts}| = (0.208^{+0.001}_{-0.002} \text{ }^{+0.008}_{-0.009})$, where the first uncertainty is experimental and the second is theoretical.

1.3.3 CP asymmetry

CP asymmetry is also measured and predicted through ratio of decay rates, with the convenient cancellation of hadronic uncertainties. The direct CP asymmetry, \mathcal{A}_{CP} , is for $B \rightarrow K^{(*)}\ell^+\ell^-$ decays defined as

$$\mathcal{A}_{CP} = \frac{\Gamma(\bar{B} \rightarrow \bar{K}^{(*)}\ell^+\ell^-) - \Gamma(B \rightarrow K^{(*)}\ell^+\ell^-)}{\Gamma(\bar{B} \rightarrow \bar{K}^{(*)}\ell^+\ell^-) + \Gamma(B \rightarrow K^{(*)}\ell^+\ell^-)} \quad (1.12)$$

This asymmetry is expected to be small in the Standard Model. The reason for this is that the loops contributing to the $b \rightarrow s\ell^+\ell^-$ transitions are proportional to $V_{tb}V_{ts}^*$, $V_{cb}V_{cs}^*$ and $V_{ub}V_{us}^*$, and the smallness of $V_{ub}V_{us}^*$ (proportional to λ^4) compared to the other two terms (proportional to λ^2 and $-\lambda^2$, respectively), combined with the unitarity of the CKM matrix ($V_{tb}V_{ts}^* + V_{cb}V_{cs}^* + V_{ub}V_{us}^* = 0$), has the consequence that $b \rightarrow s\ell^+\ell^-$ is dominated by the $V_{tb}V_{ts}^*$ -term only. Thus, the CP violation in this transition is expected to be small in the Standard Model [83].

Using the self-tagging modes reconstructed for the $B \rightarrow K^{(*)}\ell^+\ell^-$ analysis, *BABAR* measures direct CP asymmetry to be $\mathcal{A}_{CP}(B^+ \rightarrow K^+\ell^+\ell^-) = -0.07 \pm 0.22 \pm 0.02$ and $\mathcal{A}_{CP}(B \rightarrow K^*\ell^+\ell^-) = +0.03 \pm 0.23 \pm 0.03$, where the first errors are statistical and the second are systematic. The measured values in both channels are consistent with negligible direct CP asymmetry as expected by the Standard Model [84]. Using 89 million $B\bar{B}$ pairs, *BABAR* also searched for CP asymmetry in the inclusive $B \rightarrow X_s\ell^+\ell^-$ decays and found $\mathcal{A}_{CP}(B \rightarrow X_s\ell^+\ell^-) = -0.22 \pm 0.26 \pm 0.02$ [36], where the first errors are statistical and the second systematic.

The case is expected to be different for $b \rightarrow d\ell^+\ell^-$ transitions, because here the loops are proportional to $V_{td}V_{td}^*$, $V_{cb}V_{cd}^*$ and $V_{ub}V_{ud}^*$, which are all of the same order ($\sim \lambda^3$), and this introduces a considerable CP asymmetry in the partial rates [85,86]. The CP -violating difference between $b \rightarrow d\ell^+\ell^-$ and $\bar{b} \rightarrow \bar{d}\ell^+\ell^-$ is proportional to $\text{Im}(V_{ub}V_{ud}^*/(V_{td}V_{td}^*))$ and is numerically equivalent to -5% (-2%), assuming CKM parameters $\eta = 0.34$ and $\rho = 0.3(-0.3)$ [85].

The average CP asymmetry in the Standard Model has also been investigated for the partial decay rate of the exclusive $B \rightarrow (\pi, \rho)e^+e^-$ events in the region $1 \text{ GeV} < \sqrt{s} < m_{J/\psi} - 20 \text{ MeV}$ by [86]. For $B \rightarrow \pi\ell^+\ell^-$, $\mathcal{A}_{CP}^{(\pi\ell^+\ell^-)}$ is found to be between -2.2% and -6.0% depending on assumptions for the CKM matrix parameters ρ and η . The $\mathcal{A}_{CP}^{(\pi\ell^+\ell^-)}$ is almost independent of

choice of form-factor model. For $B \rightarrow \rho \ell^+ \ell^-$, $\mathcal{A}_{CP}^{(\rho \ell^+ \ell^-)}$ is approximately zero for one choice of form factors (Colangelo [87]) and between -2% and -5% based on another set of form factors (Melikhov [88, 89]).

1.3.4 Differential decay rates

Since $b \rightarrow s \ell^+ \ell^-$ and $b \rightarrow d \ell^+ \ell^-$ are three-body decays resulting from three different electroweak amplitudes, the non-trivial kinematics and angular distribution have rather precise Standard Model predictions, any of which could be modified by new physics at the electroweak scale. Measurement of these distributions, therefore, constitute tests of the Standard Model which are not currently limited by theoretical uncertainties. Predictions have been made for the differential decay rate as a function of the invariant dilepton mass, $d\Gamma(B \rightarrow X_s \ell^+ \ell^-)/d\hat{s}$, where $\hat{s} = q^2/m_b^2$ and $q^2 = m_{\ell^+ \ell^-}^2$, see e.g. [23]. Thus, it is of interest to measure the dilepton invariant mass distribution.

BABAR has measured the differential decay rate of $B \rightarrow K \ell^+ \ell^-$ and $B \rightarrow K^* \ell^+ \ell^-$ in two bins of q^2 . The low statistics does not allow for more than two bins so far. The results are generally consistent with the q^2 dependence predicted by the Standard Model.

With somewhat larger statistics than for exclusive decays, the analyses of inclusive $B \rightarrow X_s \ell^+ \ell^-$ decays have measured the differential decay rate in five bins [36]. Also these yield results which are in agreement with the Standard Model.

1.3.5 Lepton forward-backward asymmetry

Interferences between the axial-vector currents and vector currents impact the angular distribution of $b \rightarrow s \ell^+ \ell^-$ and $b \rightarrow d \ell^+ \ell^-$. For high q^2 , \mathcal{O}_9 (V) and \mathcal{O}_{10} (-A) dominate, and this leads to an effective (V-A) interaction. For low q^2 \mathcal{O}_7 (-V) dominates over \mathcal{O}_9 (V). These differences affect the angular distribution of the decay.

The forward-backward asymmetry of the lepton angle θ_ℓ as a function of q^2 , is sensitive to non-Standard Model physics. We define θ_ℓ as the angle of the positive (negative) lepton with respect to the flight direction of the \bar{B} (B) meson, measured in the dilepton rest frame [90]. The differential forward-backward asymmetry A_{FB} has a distinct pattern predicted by the Standard Model. Figure 1.3 shows a simulation of the distribution of A_{FB} for the decay $B \rightarrow K^* \ell^+ \ell^-$ by [26]. In the presence of new physics, this pattern can be altered [23, 91]. In particular, at high q^2 , the sign of A_{FB} is sensitive to the sign of the product of the Wilson coefficients C_9^{eff} and C_{10}^{eff} . In the Standard Model the sign of A_{FB} for the high q^2 region is expected to be

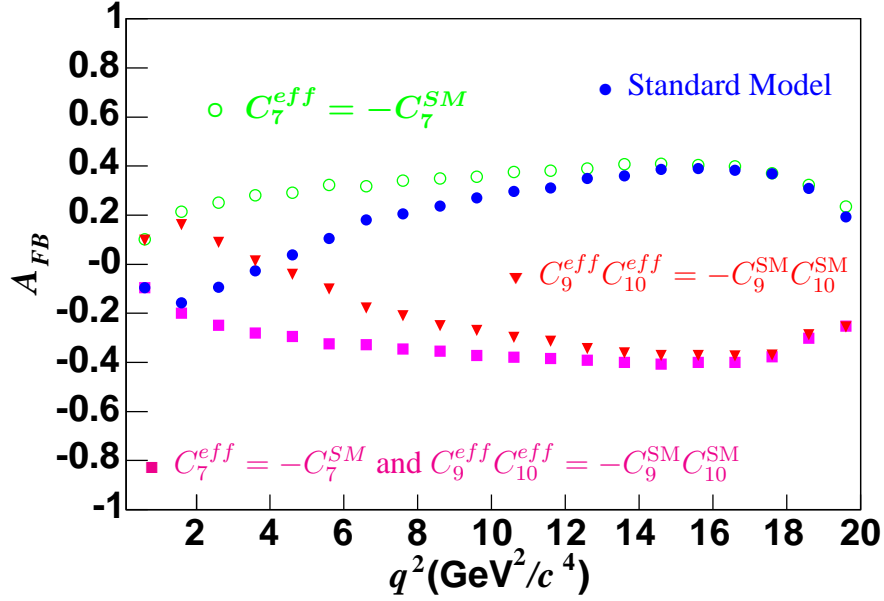


Figure 1.3: Simulated distribution of A_{FB} as a function of q^2 for the decay $B \rightarrow K^* \ell^+ \ell^-$ (by [26]). The filled circles show the Standard Model prediction. The other curves illustrate how A_{FB} is sensitive to the sign of the effective Wilson coefficients. New physics contributions may affect the effective Wilson coefficients.

positive, while it is expected to be negative for low q^2 . The cross-over point is well predicted in the Standard Model, and with enough data it can be measured. The distribution is similarly sensitive to the sign of C_7^{eff} .

Then the average lepton forward-backward asymmetry $\overline{A_{FB}}$ is defined as:

$$\overline{A_{FB}} = \frac{d\Gamma(\cos \theta_\ell > 0)/ds - d\Gamma(\cos \theta_\ell < 0)/ds}{d\Gamma(\cos \theta_\ell > 0)/ds + d\Gamma(\cos \theta_\ell < 0)/ds} \quad (1.13)$$

where $s = q^2/m_B^2$. This ratio is nearly independent of the detailed structure of the form factors.

The forward-backward asymmetry is expected to vanish for $B \rightarrow K \ell^+ \ell^-$ and $B \rightarrow \pi \ell^+ \ell^-$ because these are pseudoscalar-to-pseudoscalar decays with only one decay angle. A non-zero A_{FB} is expected for $B \rightarrow K^* \ell^+ \ell^-$ and similarly for $B \rightarrow \rho \ell^+ \ell^-$ since these are pseudoscalar-to-vector decays, with three decay angles which interfere and produce a net lepton forward-backward asymmetry. With the measured signal reported by *BABAR* and *Belle* of about 50 $B \rightarrow K \ell^+ \ell^-$ events and 70 $B \rightarrow K^* \ell^+ \ell^-$ events each, the first measurements have been made of the A_{FB} . Combining all modes with $q^2 > 0.1 \text{ GeV}^2/c^4$, *BABAR* measures $A_{FB}(B^+ \rightarrow K^+ \ell^+ \ell^-) =$

$0.15_{-0.23}^{+0.21} \pm 0.08$ [26], by a maximum likelihood fit to the distribution $\cos \theta_\ell$, which is consistent with zero as expected in the Standard Model and also in many models beyond. Combining all modes for $B \rightarrow K^* \ell^+ \ell^-$ with $q^2 > 0.1$ in a similar way, we measure $A_{FB}(B^+ \rightarrow K^+ \ell^+ \ell^-) > 0.55$ at 90% confidence level. The sample was also divided into two bins in q^2 , as the standard model predicts negative A_{FB} for $q^2 < 4$ and positive A_{FB} for $q^2 > 4$. Due to the low statistics, the bins had to be divided differently, by considering events below and above the charmonium vetoes. A large positive asymmetry, $A_{FB} = 0.72_{-0.26}^{+0.28} \pm 0.08$, is found in the high q^2 region ($q^2 > 10.24 \text{ GeV}^2/c^4$), consistent with Standard Model expectation. This disfavors new physics scenarios in which the product of C_9^{eff} and C_{10}^{eff} have opposite sign compared to the Standard Model. In the low q^2 region ($0.1 \text{ GeV}^2/c^4 < q^2 < 8.41 \text{ GeV}^2/c^4$), a lower limit of $A_{FB} > 0.19$ is set at 95% confidence level, which does not yet allow to draw any conclusions about new physics in this region.

A_{FB} for $B \rightarrow \rho \ell^+ \ell^-$ is expected to be $\approx -17\%$ [86]. The exclusive $B \rightarrow \pi \ell^+ \ell^-$ and $B \rightarrow \rho \ell^+ \ell^-$ decays have also been investigated theoretically in the general Higgs doublet model which includes effects from a neutral Higgs particles [92]. The effect from a neutral Higgs boson is expected to give sizable A_{FB} for $B \rightarrow \pi \ell^+ \ell^-$, however most significantly so for $B \rightarrow \pi \tau^+ \tau^-$. This would be a strong test of such models if they could be measured.

For $B \rightarrow \pi \ell^+ \ell^-$ and $B \rightarrow \rho \ell^+ \ell^-$, however, the rates are so small that a sample of $\sim 10^{10} - 10^{11} B\bar{B}$ mesons will be needed, and thus not likely to be studied at the current B -Factory experiments [86].

1.3.6 Lepton-flavor violating modes

In this work, the lepton-flavor violating modes $B \rightarrow \pi e \mu$ have been reconstructed for use as a control sample. In the Standard Model these decays may happen at a very low rate due to neutrino mixing. However, these rates are expected to be far below the current experimental sensitivity, and observation of such modes in the current data set would be a likely indication of physics beyond the Standard Model. Lepton-flavor violating decays have for instance been suggested through theories involving leptoquarks [25].

BABAR has searched for lepton-flavor violating decays in the $B \rightarrow K^{(*)} e \mu$ control modes and set an upper limit at 90% confidence level of $\mathcal{B}(B \rightarrow K e \mu) < 3.8 \times 10^{-8}$ and $\mathcal{B}(B \rightarrow K^* e \mu) < 51 \times 10^{-8}$.

A search by the MARK-II collaboration [78] has set an upper limit on the branching fraction $\mathcal{B}(B^+ \rightarrow \pi^+ e \mu) < 6.4 \times 10^{-3}$ at 90% confidence level. Using the reconstructed control sample of $B \rightarrow \pi e \mu$ events, we have also searched for any signal of lepton-flavor violating decays in the

analysis presented here.

1.4 Summary

With increased data samples expected within a few years, the measurement of decay angles and differential branching fractions in $B \rightarrow K^{(*)}\ell^+\ell^-$ decays can become precision measurements and put constraints on the Standard Model and models beyond it. With the branching fraction of $B \rightarrow \pi\ell^+\ell^-$ and $B \rightarrow \rho\ell^+\ell^-$ expected to be 1 – 2 orders of magnitude smaller than this, it will still be a while before differential decay rates, forward-backward asymmetries and CP asymmetries can be measured for these modes.

Chapter 2

The *BABAR* experiment

The data for this analysis has been collected by the *BABAR* detector [93] at the PEP-II collider [94, 95] at the Stanford Linear Accelerator Center (SLAC) in California, USA (figure 2.1).



Figure 2.1: Photos of the SLAC site (left) and the *BABAR* detector (right).

2.1 The accelerator facility

PEP-II is an e^+e^- asymmetric collider operating at a center-of-mass energy of 10.58 GeV, which corresponds to the mass of the $\Upsilon(4S)$ resonance. The $\Upsilon(4S)$ is a bound state of a $b\bar{b}$ quark pair which is above the mass threshold for decaying into a $B\bar{B}$ meson pair. The branching fraction

$\mathcal{B}(\Upsilon(4S) \rightarrow B\bar{B})$ is close to 100 %.

The cross-section for $e^+e^- \rightarrow b\bar{b}$ is measured from the *BABAR* data to be 1.11 nb ¹, compared to $\sigma(e^+e^- \rightarrow c\bar{c}) = 1.35 \text{ nb}$ and $\sum_{q=u,d,s} \sigma(e^+e^- \rightarrow q\bar{q}) = 2.09 \text{ nb}$. Comparing the cross-sections, we see that there is a substantial background of continuum light-quark events ($e^+e^- \rightarrow q\bar{q}$, where $q = u, d, s, c$) in the data collected *on* the $\Upsilon(4S)$ resonance. To study this background, PEP-II has run with energies below the peak of the $\Upsilon(4S)$ resonance.

In PEP-II, 9.0 GeV electrons collide with 3.1 GeV positrons, giving the center of mass a Lorentz boost of $\beta\gamma = 0.56$ in the direction of the incoming electron beam². This boost is needed in order to separate the two decaying B -meson vertices. Because the $\Upsilon(4S)$ is so close to $B\bar{B}$ -production threshold, the two B mesons are produced almost at rest in the center-of-mass frame. Due to the boost they typically move $\sim 250 \mu\text{m}$ before decaying, which is a measurable distance in the *BABAR* detector.

Due to the different beam energies, the machine needs two storage rings. The high-energy ring (HER) is used for electrons, and uses the old PEP (“Positron-Electron Project”) ring. The low-energy ring (LER) was constructed for the *BABAR* experiment and stores positrons. The rings are about 2.2 km in circumference and have hexagonal geometry with six straight segments. It further uses the powerful injection system of the linear accelerator built for the Stanford Linear Collider (completed in 1989) which injects the accelerated particles into the PEP-II beam lines. The two beams are brought to collide in Interaction Region 2 (IR-2) where the *BABAR* detector is located.

2.2 The data sample and luminosity

The purpose of the *BABAR* experiment is to study CP violation and rare B -meson decays with extremely high precision, in order to determine parameters of the Standard Model and search for effects of physics beyond it. This requires a high-statistics data sample. The e^+e^- collisions provide a clean environment in the sense that event multiplicities are low (there is on average ten tracks in a *BABAR* multihadron event) and the four-momentum of the center-of-mass frame is well defined. A high statistics sample is obtained by high *luminosity*, \mathcal{L} . Luminosity is a machine parameter relating the event rate R with the interaction cross section σ_{int} :

$$R = \mathcal{L} \cdot \sigma_{\text{int}}. \quad (2.1)$$

¹The cross-section (σ) is measured in units of *barn* (b), defined as $1 \text{ b} = 10^{-28} \text{ m}^2$. Thus a *nano barn* is $1 \text{ nb} = 10^{-37} \text{ m}^2$.

² β is the speed of the moving frame relative to the speed of light ($\beta = \frac{v}{c}$) and γ is the Lorentz factor ($\gamma = \frac{1}{\sqrt{1-\beta^2}}$).

In a symmetric collider, the luminosity is given by

$$\mathcal{L} = f \frac{n_1 n_2}{4\pi\sigma_x\sigma_y} = f \frac{n_1 n_2}{4\sqrt{\epsilon_x\beta_x^*\epsilon_y\beta_y^*}} \quad (2.2)$$

where n_1 and n_2 are the number of particles per bunch, f is the frequency of collisions, σ_x and σ_y characterize the Gaussian transverse beam profiles in the horizontal (bend) and vertical directions, and ϵ_x is the transverse emittance $\epsilon = \pi\sigma^2/\beta$, β is the amplitude function and β^* is the value of this amplitude function at the interaction point. In order to obtain high luminosity, one needs to make high-density bunches of low emittance to collide at high frequency at locations where the beam optics provide as low values of the amplitude functions as possible. At PEP-II there are collisions approximately every 4.2 ns.

The focus in designing the PEP-II collider was therefore to obtain a high instantaneous luminosity. The design luminosity of $\mathcal{L} = 3 \times 10^{33} \text{ cm}^{-2}\text{s}^{-1}$ was reached within about a year of operation. On August 16, 2006, it reached its record luminosity thus far of $12.07 \times 10^{33} \text{ cm}^{-2}\text{s}^{-1}$. A large data sample also requires efficiency of the detector in recording all the events. The *BABAR* datataking is typically 98% to 99% efficient, and averaged over all the years of data taking thus far, it has about 96% efficiency. PEP-II is typically in operation 24 hours a day and 7 days a week for several months at a time, with only short downtimes due to unforeseen problems or periodical machine development days. Each such long period of operations constitute a *run*. Since startup, there have been five runs, ranging in length from seven months for Run 3 to sixteen months for Run 5. Between each run, a shutdown of a few months accommodates machine or detector upgrades. At the end of Run 5 in August 2006, PEP-II had integrated more than $L = \int dt\mathcal{L} = 400 \text{ fb}^{-1}$ of integrated luminosity since the startup, and *BABAR* had collected more than $L = 390 \text{ fb}^{-1}$ (figure 2.2). The *integrated* luminosity has been greatly improved by the introduction of trickle injection, which involves filling the beams at a low rate during datataking so that pauses due to filling of beams are avoided.

The data sample used for this analysis consist of all good data taken from October 1999 through May 2004, corresponding to the *BABAR* datasets Run 1 through Run 4. The integrated luminosity amounts to 209 fb^{-1} of data collected on the $\Upsilon(4S)$ resonance, as well as 21.5 fb^{-1} of data collected slightly below the $\Upsilon(4S)$ resonance in order to have a data control sample consisting solely of $e^+e^- \rightarrow \text{light quark events}$. The on-resonance data sample corresponds to $230 \times 10^6 B\bar{B}$ pairs.

The sample is partitioned into several subsets (blocks) based on *BABAR* running conditions. Table 2.1 lists each subset and its $B\bar{B}$ count and integrated luminosity:

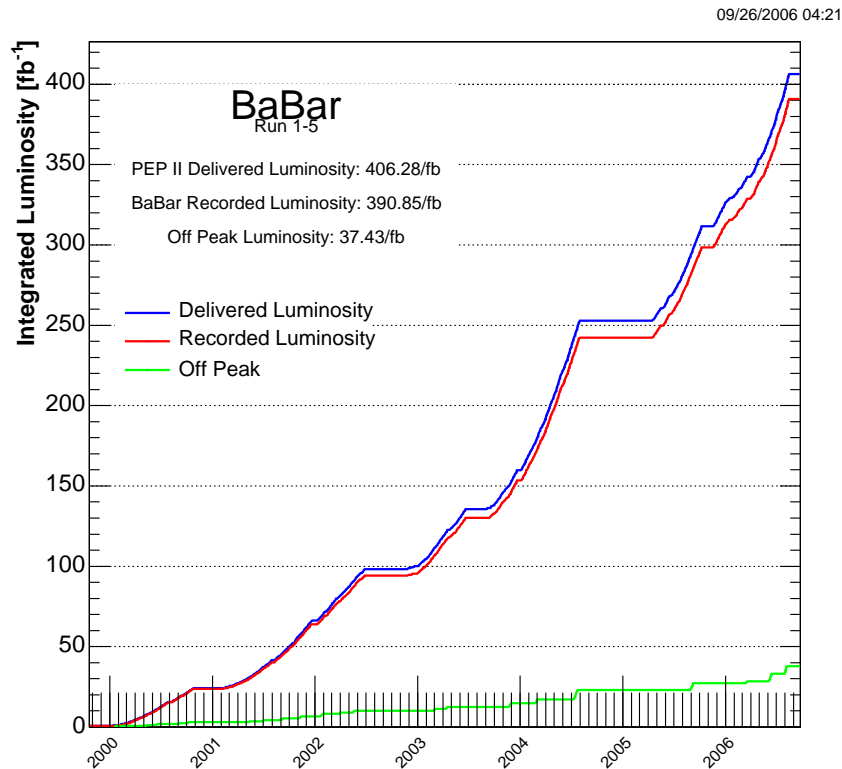


Figure 2.2: Integrated luminosity at the PEP-II collider from 1999 to 2006.

- Run 1 corresponds to data taken from October 1999 through the end of 2000, with an integrated luminosity of 19.3 fb^{-1} on-resonance. This run is further divided into two blocks, defined by different operating voltages of the DCH (see section 2.3.2):

block 1 (10.0 fb^{-1} on-resonance) had a DCH voltage of 1900 V, while

block 2 (9.3 fb^{-1} on-resonance) had a DCH voltage of 1960 V.

- Run 2 corresponds to data taken in 2001-2002, with an integrated luminosity of 59.5 fb^{-1} on-resonance. The DCH voltage at the time was 1930 V. This run has been divided into two blocks because of different muon identification performance.

In 2001, 34.6 fb^{-1} were collected on-resonance;

in 2002, 24.9 fb^{-1} were collected on-resonance.

- Run 3 corresponds to data taken in 2002-2003, with an integrated luminosity of 30.7 fb^{-1}

Run	Year	Block	Number of $B\bar{B}$ (/10 ⁶)	Integrated luminosity (fb ⁻¹)	
				On-Res.	Off-Res.
1	2000	1	10.84	10.0	0.9
1	2000	2	10.21	9.3	1.4
2	2001	1	38.80	34.6	3.7
2	2002	1	27.02	24.9	3.2
3	2003	1	33.83	30.7	2.4
4	2004	1	109.45	99.4	9.9
<i>Total</i>			230.15	208.9	21.5

Table 2.1: Number of $B\bar{B}$ decays and integrated luminosity of the 1999-2004 data sample for the various subsets of good data.

on-resonance. Like Run 4 it consists of a single block with DCH voltage of 1930 V.

- Run 4 corresponds to data taken in 2003-2004, with an integrated luminosity of 99.4 fb⁻¹ on-resonance.

The efficiencies are compared between data and simulated samples for each block independently, and any post-processing corrections are done on a block-by-block basis.

2.3 The detector components

The *BABAR* detector [93], shown in figure 2.3, surrounds the PEP-II interaction region and has five sub-detector systems at different radial distances from the beam line, each serving complementary functions in order to fully reconstruct the decay of the B -mesons and identify the decay products. The detector is constructed with a cylindrical barrel part and one end-cap on the forward and backward side. Due to the asymmetric energies and the resulting boost of the decaying particles in laboratory frame, the detector has been built in an asymmetric way. The barrel part of the detector stretches about 37 cm longer in the forward direction than in the backward direction relative to the nominal interaction point and the forward direction is equipped with more detectors, while read-out electronics and support structures are placed at the rear of the detector if possible.

The coordinate system in the lab frame is defined so that the z axis is parallel to the magnetic

field of the solenoid and in the direction of the high-energy e^- beam. The y axis points vertically upward and the x axis points horizontally, away from the center of the PEP-II ring. The origin is the nominal location of the interaction point. The real interaction point is measured on an event-by-event basis by measuring the primary vertex of the charged tracks in the event. The azimuthal angle ϕ runs from $-\pi$ to π , and the polar angle θ , between the track direction and the z axis, runs from 0 to π .

2.3.1 The silicon vertex tracker (SVT)

The silicon vertex tracker consists of five layers of 340 double-sided silicon microstrip sensors. The inner three layers are located as close as possible to the 27.9 mm radius beam pipe in order to measure the position and angle of traversing tracks with a high precision. The hit resolution in the SVT ranges from 20 μm to 40 μm . The track position and angle are of great importance for a precise reconstruction of vertices; in particular of the two decaying B mesons, but also the vertices of the B -meson decay products. The vertex resolution for a fully reconstructed B decay is 50 μm - 100 μm in the z -direction, and 100 μm - 200 μm in the $r - \phi$ direction. The two outer layers of the SVT provide further precision tracking which is especially important for the alignment of the SVT and DCH tracks. The analysis considered in this work, uses information from the B decay vertex to reduce background from incorrectly reconstructed B mesons which may have tracks originating from different B -mesons and thus different vertex positions.

The SVT is also important to identify tracks with a low transverse momentum, p_T . The SVT provides the only tracking for charged particles with $p_T < 120 \text{ GeV}/c$. One type of events relying on this information is decays involving a $D^{*\pm} \rightarrow D^0 \pi_s^\pm$, where the π_s^\pm has a low momentum (is *slow*) due to the small difference between the masses of the D^* and the D^0 mesons.

In the forward direction, the SVT cover tracks from the interaction point down to about 20° from the beam line and in the backward direction the angular coverage is down to about 30° . The angular coverage is constrained by machine (PEP-II) components.

2.3.2 The drift chamber (DCH)

The main tracking detector for *BABAR* is the 40-layer wire drift chamber, whose principle purpose is momentum measurements for charged particles. The DCH is one of the main inputs to the *BABAR* trigger. The chamber has low-mass wires and is filled with a gas mixture of about 80% helium and about 20% isobutane to minimize multiple scattering. The DCH uses a hexagonal small-cell design with individual sense wires surrounded by ground wires. The cells are

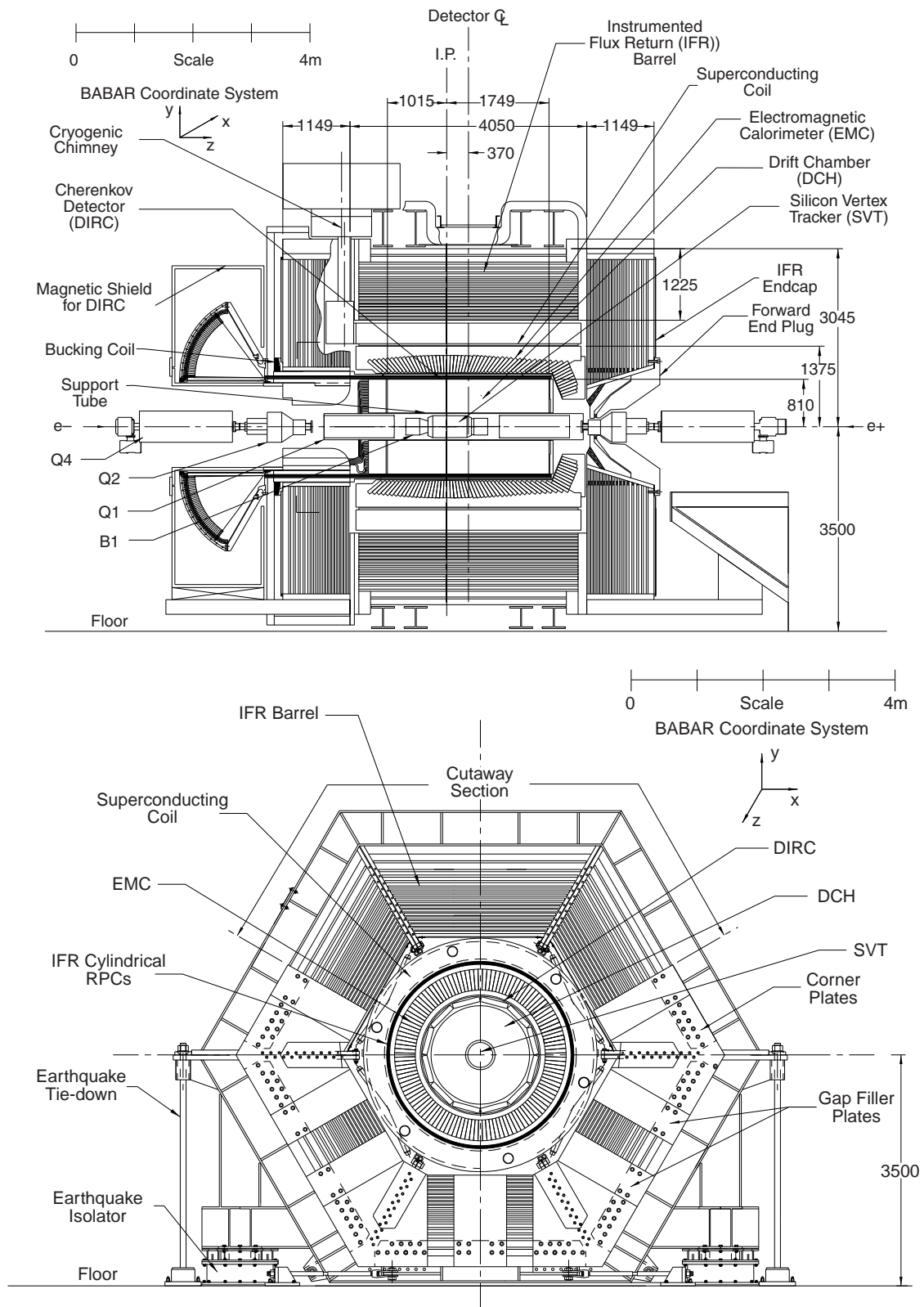


Figure 2.3: BABAR detector, side view (top) and end view (bottom).

organized in 10 superlayers of alternating axial and left- or right-stereo orientation, providing spatial coordinates with a resolution in the z -direction of $700\mu m$ [96]. The single-cell average resolution in the $x - y$ direction is $125\mu m$.

The sense wires in the DCH are currently operated at 1930 V, corresponding to an avalanche gain of $\sim 4 \times 10^4$. The design was to operate it at 1960 V, but due to continuing problems with discharges from one of the sections, the voltage was lowered to 1900 V at the start of Run 1. The damaged section was later turned off and water vapor was added to the gas mixture and after this addition no more discharges were seen.

The reconstruction of charged-particle tracks relies on information from both the SVT and the DCH. A Kalman filter algorithm [97] is used, and the trajectories of the charged particles are parameterized with 5 parameters: d_0 , ϕ_0 , ω , z_0 and $\tan \lambda$, and their associated error matrices. The parameters are measured at the point of closest approach, *poca*, to the z -axis; d_0 and z_0 are the distances of this point to the origin of the coordinate system in the $x - y$ -plane and along the z -axis, respectively. The angle ϕ_0 is the azimuth of the track, λ is the dip angle with respect to the transverse plane and $\omega = 1/p_T$ is the curvature. The track resolution is $\sigma_{z_0} = 29\mu m$, $\sigma_{d_0} = 23\mu m$, $\sigma_{\phi_0} = 0.43$ mrad, $\sigma_{\tan \lambda} = 0.53 \times 10^{-3}$ [93]. The resolution of transverse momentum has been measured using cosmic ray particles and is [96]:

$$\sigma_{p_T}/p_T = (0.45 \pm 0.03)\% + (0.13 \pm 0.01)\% \cdot p_T$$

A good resolution on the track parameters is also crucial for the quality of the Cherenkov angle reconstruction in the DIRC subsystem. The analysis presented here on $B \rightarrow \pi \ell^+ \ell^-$ relies on the Cherenkov angle reconstruction for excellent pion identification.

The DCH also provides particle identification for low-momentum tracks using the measured energy loss due to ionization (dE/dx , figure 2.4).

2.3.3 The Cherenkov-radiation detector (DIRC)

The Detector of Internally Reflected Cherenkov light (DIRC) is a ring imaging Cherenkov detector for charged-particle identification, and in particular provides separation of kaons and pions from about 500 MeV/ c up to the kinematic limit of about 4.5 GeV/ c . It consists of 144 synthetic fused silica quartz bars with a thickness of 8 cm which runs the length of the barrel part of the detector (4.9 m). When a relativistic charged particle with momentum above the Cherenkov threshold traverses the quartz bars, photons are emitted in a cone around the charged-particle trajectory, and the light is transported by total internal reflection to the rear end of the detector

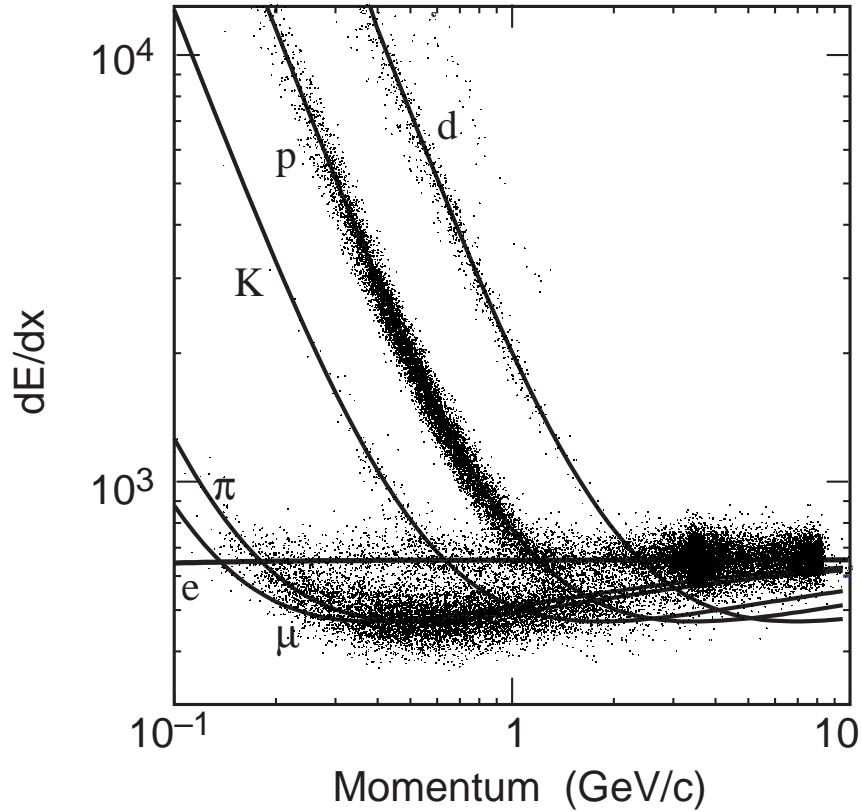


Figure 2.4: Scatter plot showing dE/dx versus momentum p in the DCH from beam background trigger data with parameterized Bethe-Block curves for different mass hypotheses.

where it is projected on to a plane of 10752 photo-multiplier-tubes (PMTs) (figure 2.5).

From the PMT measurements, an image of the Cherenkov ring (or pieces of it) is reconstructed. The radius revealing the angle of the Cherenkov cone:

$$\theta_C = \frac{1}{\beta n} \quad (2.3)$$

with $\beta = v/c$ and n is the refractive index in the medium. Since the Cherenkov angle depends on the particle velocity, the different angles at a given momentum is used to identify the charged particles (see figure 2.6).

The angular resolution of the DIRC photon detection is about 10.2 mrad, and the measured time resolution is 1.7 ns, close to the intrinsic 1.5 ns transit time spread of the PMTs. The $K\pi$ separation provided by the DIRC for tracks at 3 GeV/c is about 4.2σ , which is within 15% of the design goal [98].

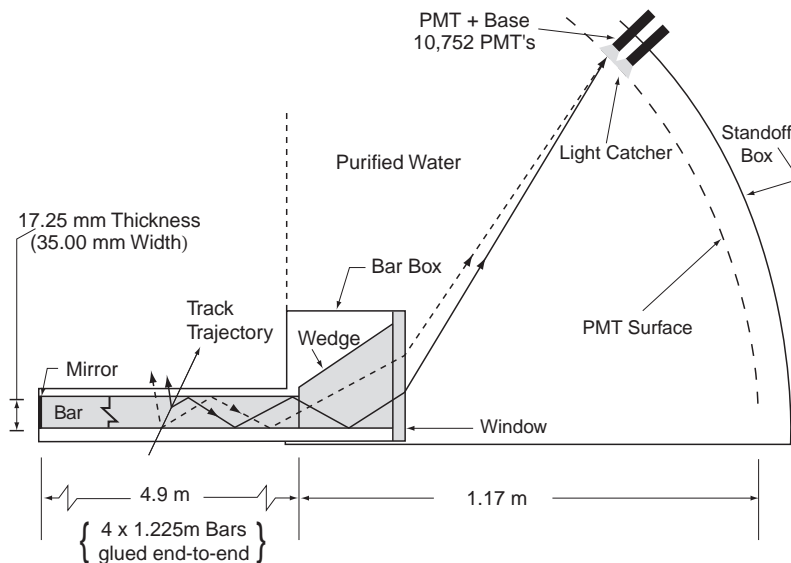


Figure 2.5: Schematic concept of the DIRC. Cherenkov light released in the silica material is guided towards the back of the detector where 10752 photo-multiplier tubes record the signals and allow for reconstruction of the characteristic Cherenkov ring images used in particle identification.

2.3.4 The electromagnetic calorimeter (EMC)

BABAR's electromagnetic calorimeter consists of 6580 CsI(Tl) scintillating crystals for measuring energy deposited by neutral and charged particles over an energy range of 20 MeV to 4 GeV. It is the only sub-detector for detecting photons and the main detector for identifying electrons. Photons and electrons interact with the scintillating material and form electromagnetic showers of photons and electron-positron pairs. The resulting shower shapes are characteristically different than for muons or hadrons which interact mainly through ionization of the material in the calorimeter. Hadrons can also interact with the nuclei of the atoms making up the crystals, although the calorimeter only amounts to less than one interaction length (λ).

An electromagnetic shower induced by electrons of more than 300 MeV typically deposits energy in more than 10 crystals, while the largest fraction of the shower is contained in 2-3 crystals.

Lateral and longitudinal shower shapes are used to separate photons and electrons from muons and charged hadrons, and from neutrons and merged $^3\pi^0$ decays as well as debris from

³ π^0 mesons where the two photons are nearly collinear in the laboratory frame and leave a single bump in the EMC.

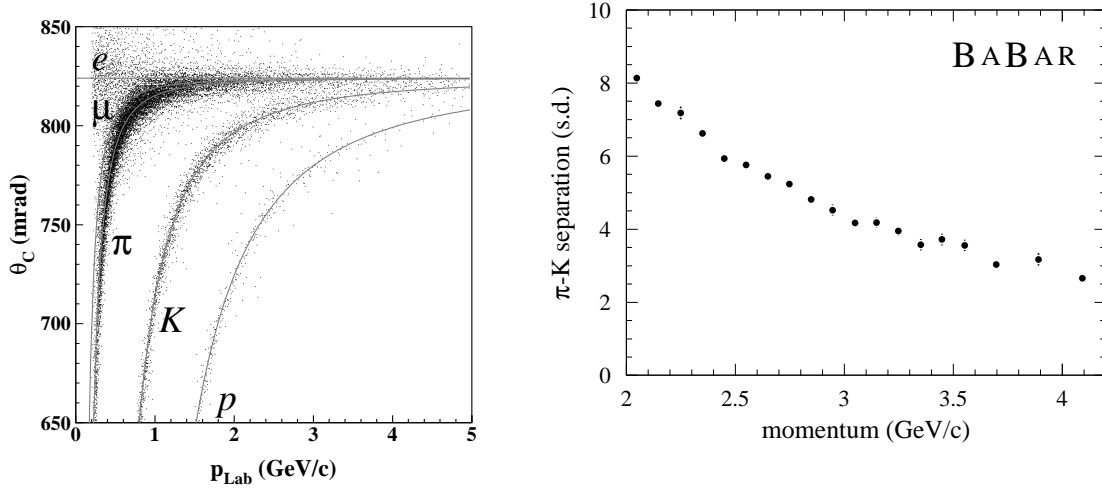


Figure 2.6: The DIRC provides K/π separation from about 500 MeV/c up to the kinematic limit of about 4.5 GeV/c.

hits of background events. Hadrons tend to have a more irregular shower shape in the EMC. The shape can be characterized by the following variables:

- The lateral moment LAT of the shower energy deposition [99], defined as $\text{LAT} = \frac{\sum_{i=3}^n E_i r_i^2}{(E_1 r_0^2 + E_2 r_0^2 + \sum_{i=3}^n E_i r_i^2)}$ where the n crystals in the EMC cluster are ranked in order of deposited energy E_i , $r_0 = 5$ cm is the average distance between crystal centers, and r_i is the radial distance of crystal i from the cluster center, which is calculated as the center of gravity with linear energy-weighting for every crystal.
- The Zernike moments A_{nm} [100] measure the irregularity of the shower shape. We use only $A_{4,2} = \sum_i^n \frac{E_i}{E_{\text{tot}}} [4(\frac{r_i}{R_0})^4 - 3(\frac{r_i}{R_0})^2] e^{-2i\phi_i}$ where r_i and ϕ_i are the radial and angular separation of crystal i with respect to the cluster center, E_{tot} is the total energy of the cluster and R_0 is a cutoff radius of 15 cm.
- For charged tracks, the longitudinal shape of the shower can be described by the distance $\Delta\phi$ between the centroid of the cluster and the extrapolation of the corresponding track at the surface of the EMC. $\Delta\phi$ typically has a wider distribution for hadron tracks than for electron tracks, and for electrons we typically have $0.0 \text{ rad} < \Delta\phi < 0.07 \text{ rad}$ [101].
- Electrons with their low mass are likely to deposit all their energy in the EMC, and can be identified from the fact that the measured E/p is close to unity. Muons and pions only

deposit ionization energy and has an E/p distribution peaking at values smaller than unity. Anti-protons interact with the detector material and yields $E/p > 1$.

The energy resolution of the EMC is measured from calibration runs with a radioactive source. These runs are typically performed once every 15-30 days and have a length of 40-60 minutes. The energy resolution is found to be [102]:

$$\frac{\sigma_E}{E} = \frac{(2.30 \pm 0.03 \pm 0.3)\%}{\sqrt[4]{E(\text{GeV})}} \oplus (1.35 \pm 0.08 \pm 0.2)\% \quad (2.4)$$

with the two terms added in quadrature. The uncertainties are statistical and systematic, where the statistical uncertainty comes from the fit and the systematic one mainly comes from uncertainties in the asymmetry of the photon E/E_{true} distribution.

The angular resolution is determined from the transverse crystal size and the distance from the interaction point:

$$\sigma_\theta = \sigma_\phi = \left(\frac{4.15 \pm 0.04 \text{mrad}}{\sqrt{E(\text{GeV})}} + (0.00 \pm 0.00) \right) \text{mrad} \quad (2.5)$$

The energy-dependent term in each of these expressions arises from fluctuations in photon statistics as well as electronics and beam-background noise. The constant term is dominant at high energies and arises from non-uniformities in light collection, shower leakage or absorption in the material between and in front of the crystals and calibration uncertainties.

The mass resolution of reconstructed π^0 mesons decaying into two photons is 6.5 MeV, illustrated by the plot in figure 2.7.

2.3.5 Instrumented flux return (IFR)

Outside of the electromagnetic calorimeter, a superconducting solenoid provides a magnetic field of 1.5 T needed to measure the charged-particle momenta. The solenoid is surrounded by steel plates which functions both as magnetic flux return and as muon detector and hadron absorber. The steel plates vary in thickness from 2 cm for the innermost plates to 10 cm for the outer plates.

The flux return is instrumented between the layers of steel, and the instrumentation used for the data sample considered here has been Resistive Plate Chambers (RPCs) [103]. There are 18 layers of steel with 19 layers of RPCs in the barrel part of the detector, and there are 18 layers of RPCs in each of the end caps. There is a total of 65 cm (four interaction lengths (λ)) of iron in the barrel and 60 cm of iron in each end-cap. During the summer of 2002 the forward end-cap

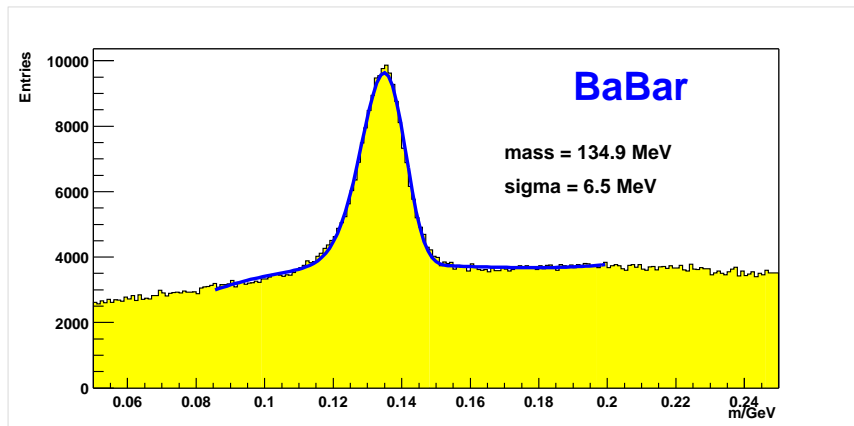


Figure 2.7: Invariant mass of two photons ($\pi^0 \rightarrow \gamma\gamma$) in hadronic events with the energy of both photons above 30 MeV and π^0 energy above 300 MeV. The solid line is a fit yielding a width of 6.5 MeV.

was increased to about six interaction lengths. There is around one interaction length before the first RPC layer. The penetration depth of a track in the IFR is used to distinguish muons from hadrons.

2.3.6 The *BABAR* trigger

The *BABAR* trigger has two levels. The first level trigger (L1) is a hardware trigger which selects physics events based on simple detector signals to reduce beam-background down to a level (2 kHz) acceptable for the software trigger (L3) which decides which events are being stored for offline processing (a few 100 Hz).

The L1 trigger decision is based on track segments from hits in the DCH, showers in the EMC and hits in the IFR. The latter is used mainly for triggering $\mu^+\mu^-$ events and cosmics, while the DCH and EMC triggers provide the main trigger inputs for *B*-physics processes.

The L3 trigger software comprises event reconstruction and classification, a set of selection filters, and monitoring. A better DCH tracking (vertex resolution) and EMC clustering filters compared to the L1 information allow for a greater rejection of beam-induced background and Bhabha events. The total trigger efficiency is required to exceed 99% for all $B\bar{B}$ events and at least 90% for other physics events.

2.4 Event reconstruction

In order to study properties of B -meson decays, the mesons are reconstructed from their decay products. These are detected as charged-particle tracks, or as clusters of energy deposits in the detector. This section describes the algorithms used in this analysis to select high-quality tracks and neutrals and to identify leptons, photons and hadrons to reconstruct the B -meson from its decay products consisting of two leptons and one pion. We also describe control samples which are used to validate the particle identification efficiencies.

2.4.1 Selection of tracks and neutrals

The tracks used as lepton candidates are required to have a distance-of-closest approach (*doca*) to the interaction point of less than 1.5 cm in the $x - y$ plane and less than 10 cm in the z -direction. The lepton tracks are further required to have a transverse momentum p_T of at least 100 MeV/ c , and to pass the quality requirement that it must have at least 12 hits in the DCH.

The requirements on hadron tracks (K^\pm , π^\pm) are similar, but to allow also low-momentum hadrons, we impose no requirement on the track's transverse-momentum and no requirement on number of DCH hits associated with the track.

Photons are reconstructed as neutral clusters in the calorimeter which are not associated with any tracks. To separate good photons from other neutral deposits in the calorimeter, we require the particle to deposit a minimum energy of 30 MeV, and require the lateral moment LAT to be less than 0.8.

2.4.2 Particle identification

This section introduces the identification algorithms used in this analysis for distinguishing the different particle species.

Electron identification

Electron candidates are identified combining information from the EMC, DIRC, and DCH. The tracks must be within the acceptance of the tracking and EMC detectors ($-0.74 \text{ rad} < \theta < 0.84 \text{ rad}$), a minimum of four crystals must be associated with the cluster resulting from the passing electron track, and the measured energy deposit should be close to the track momentum: $0.5 < E/(p \cdot c) < 1.5$. These preselection criteria separate electrons from muons. In addition, a likelihood fraction is constructed to separate electrons from hadrons by combining lateral

and longitudinal shower shapes (LAT , $\Delta\phi$) and E/p from the EMC and ionization energy loss dE/dx from the DCH. For low-momentum tracks, information from the DIRC is used as well. If at least 6 photons are expected in the Cherenkov ring image for the given track momentum, then at least 6 photon must also be measured. This ensures a reliable Cherenkov angle measurement, and also removes kaons and protons below the Cherenkov threshold. If less than 6 photons are expected for the given particle momentum, then the DIRC information is ignored, as it does not provide enough information. If the track passes this selection, the Cherenkov angle is taken into account for the likelihood fraction.

Overall, the selection efficiency from this algorithm is between 92% to 95% as shown in figure 2.8. The misidentification rate of pions is less than 0.2%. Kaons and protons with momentum below 500 MeV/c have selected at a rate of 2% – 10%, however, tracks with such a low momentum are rarely used.

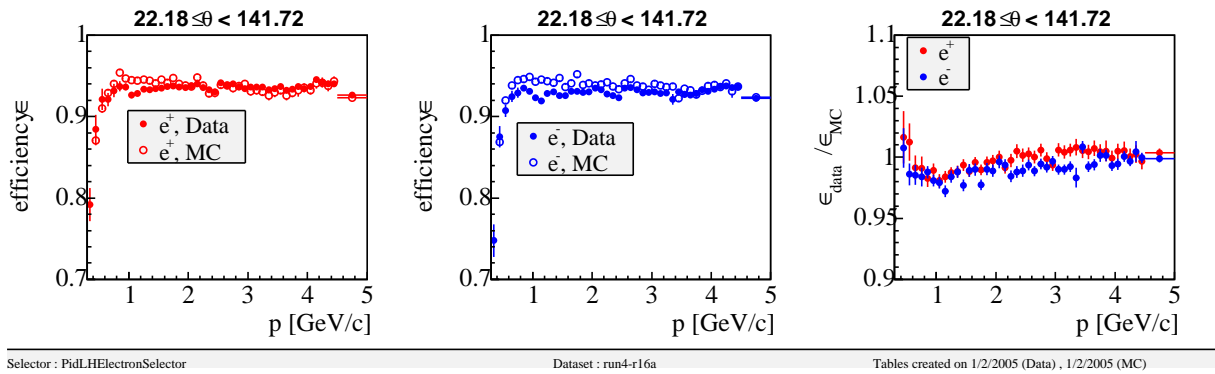


Figure 2.8: Electron selection efficiency as a function of momentum in Monte Carlo and data $e^+e^- \rightarrow e^+e^-\gamma$ control sample. The left plot shows the efficiency of e^+ in data (points) and in Monte Carlo (open circles), the middle plot shows the same for e^- , and the right plot shows the ratio of efficiencies in data and Monte Carlo for e^+ and e^- tracks.

Electron bremsstrahlung recovery

When ultra-relativistic particles get deflected by the field surrounding an atomic nuclei, they emit photons to conserve four-momentum. For the energies relevant to *BABAR* data, only the electrons (due to their small mass) display any measurable amount of this Bremsstrahlung effect [104].

We attempt to recover the original electron energy by combining the electron candidates with nearby photons, *i.e.* the photon must lie within an angular region in the polar angle θ of:

$$|\theta_e - \theta_\gamma| < 35 \text{ mrad}$$

and within the following region in the azimuth angle φ :

$$\begin{aligned} \varphi_0^{e^-} - 50 \text{ mrad} < \varphi_\gamma < \varphi_{\text{cent.}}^{e^-} \text{ for } e^-, \\ \varphi_{\text{cent.}}^{e^+} < \varphi_\gamma < \varphi_0^{e^+} + 50 \text{ mrad for } e^+ \end{aligned}$$

Here, (θ_0, φ_0) is the initial direction of the electron track, evaluated at the interaction point, and $(\theta_{\text{cent.}}, \varphi_{\text{cent.}})$ is the centroid position of the associated calorimetric shower. Only photons with an energy $E_\gamma > 0.030$ GeV are considered, and it also has to pass the quality criteria of $0.0001 < LAT_\gamma < 0.80$ and $Zernike(42) < 0.25$.

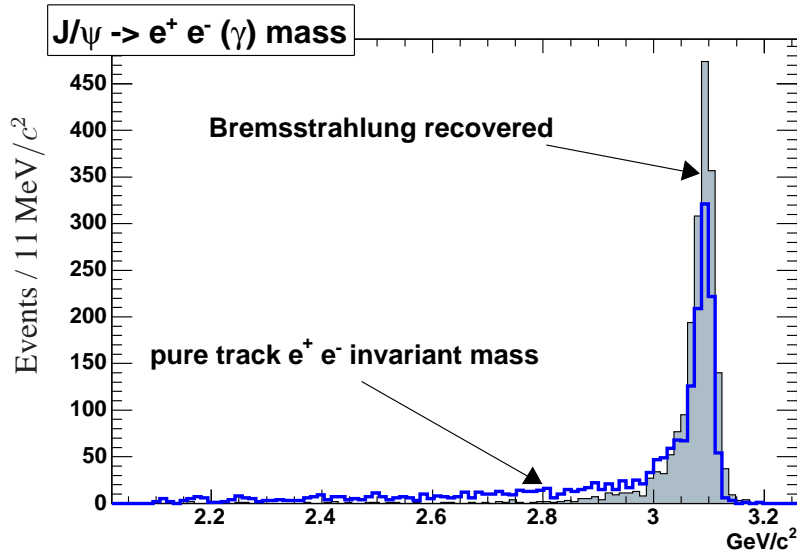


Figure 2.9: e^+e^- invariant mass with and without bremsstrahlung recovery. The distributions contain Monte Carlo simulations of $B \rightarrow J/\psi K$ events.

Muon identification

Muons are identified by their penetration depth in the IFR and energy E_{cal} deposited in the EMC. The latter is effective in removing electrons from the sample, while information from the IFR is mainly used to distinguish between muons and hadrons.

Muons are generally the particle which travels through the most material, while hadrons are stopped in the iron plates to a greater extent. Thus the penetration depth $N_\lambda^{\text{meas.}}$ (in units of interaction lengths) and its deviation ΔN_λ from expectation for a μ -track are useful parameters.

The hits in the IFR are matched to the track extrapolation from the DCH, and a goodness-of-fit parameter $\chi_{\text{match}}^2/d.o.f.$ is used to reduce background from neutral hadrons in close proximity with another track.

Similarly, a parameter T_C describes the continuity of the track and is used for tracks in the forward end cap and the boundary between barrel and forward end-cap. This is to guard against artificially large number of interaction lengths due to random hits from beam background in close proximity with a pion track.

Hits in the IFR cluster are parameterized by a third-order polynomial fit in three dimensions, and the goodness-of-fit $\chi^2_{\text{fit}}/d.o.f.$ can be used to suppress hits from beam-background events.

The average multiplicity \bar{m} of hit strips per layer as well as its standard deviation $\sigma_{\bar{m}}$ is also used to remove events with random beam background.

All of this information is combined into a neural network algorithm which gives a continuous output variable between 0 (background-like) and 1 (signal-like). Different levels of muon efficiency and hadron rejection can be achieved by changing the neural network output values. The selection used here is rather tight, and has a muon efficiency of about 70% for momenta higher than 1.5 GeV/c, which is the momentum needed for a charged particle to reach the IFR detector. The mis-identification rate for pions using this selection, is about 3%. Misidentification of kaons are generally lower than that of pions, with the exception of kaons with momentum larger than 4.0 GeV/c. The muon efficiency as a function of particle momentum is shown in figure 2.10.

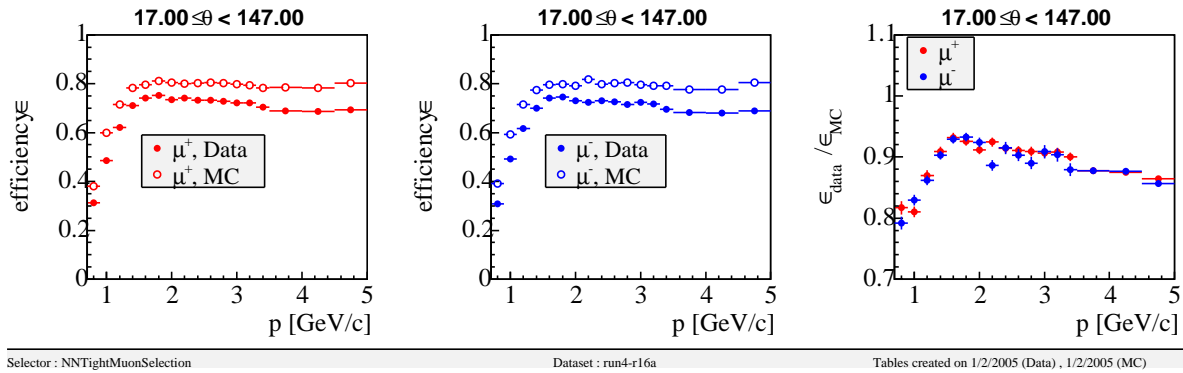


Figure 2.10: Muon selection efficiency as a function of momentum in Monte Carlo and data $e^+e^- \rightarrow \mu^+\mu^-\gamma$ control sample. The left plot shows the efficiency of μ^+ in data (points) and in Monte Carlo (open circles), the middle plot shows the same for μ^- , and the right plot shows the ratio of efficiencies in data and Monte Carlo for μ^+ and μ^- tracks. As can be seen from the left and middle plots, the muon efficiency turns on for particle momenta of 0.7 GeV/c which is the threshold momentum for a track to reach the IFR detector. The efficiency is slightly overestimated in the Monte Carlo simulations for particle momenta between 0.7 GeV/c and 1.5 GeV/c, as is seen from the right plot.

A *loose* muon selection is also used for a hadronic control sample for the $B \rightarrow \pi\ell^+\ell^-$ analysis (Chapter 4). This has a looser selection criterion on the neural-network output which

gives a muon identification efficiency of nearly 90%, and a mis-identification rate of pions and kaons of 8% and $1 - 2\%$, respectively.

Charged kaons

The identification of charged kaons combine information from the SVT, DCH and the DIRC into a likelihood fraction. For each charged track, a likelihood is calculated for each particle hypothesis. The total likelihood is the product of likelihoods:

$$L = L_{DIRC} \cdot L_{DCH} \cdot L_{SVT}. \quad (2.6)$$

We require that the fraction of likelihoods of being a kaon over that of being a pion is high ($L_{kaon}/L_{pion} > 0.9$ or a momentum-dependent requirement if the momentum is larger than 2.5 GeV/ c), and at the same time that the fraction of likelihoods of being a kaon over that of being a proton is high. Here the requirement is less strict ($L_{kaon}/L_{proton} > 0.20$, also here with a momentum dependent requirement for tracks with $p > 2.5$ GeV/ c). In addition, the track must not be identified as an electron, unless its momentum is less than 40 MeV/ c .

For the likelihoods from the SVT and DCH, the measured dE/dx is compared against the expected dE/dx from the Bethe-Bloch parameterization. The DCH likelihood is calculated based on a Gaussian probability-density function, and the SVT likelihood is calculated based on a Bifurcated Gaussian probability-density-function. The likelihood from the DIRC is based on the Cherenkov angle, the number of photons and the track quality.

The efficiency of the kaon selection is more than 80% for most of the momentum spectrum (see figure 2.11), with a mis-identification rate from pions and muons of a few percent, the largest being $\sim 5\%$ for tracks with momentum $p > 3.5$ GeV/ c . The kaon identification for particle momenta below 0.7 GeV/ c relies mainly on dE/dx measurements in the DCH. For $p > 0.7$ GeV/ c , the kaon identification relies on the DIRC.

Charged pions (π^\pm)

The charged pion π^\pm candidates are selected based on the same likelihood structure used for selecting charged kaons, only here the requirements are that $L_{kaon}/L_{pion} < 0.2$ and that $L_{proton}/L_{pion} < 0.5$. Again, the track is required to fail the electron identification criteria.

The efficiency of the pion identification is highest for the low-momentum tracks, 80% to 90% efficient for most of the kinematic region used here, then dropping off a bit for the highest-momentum tracks (see figure 2.12). Kaon mis-identification rates are between 2% and 10%, with

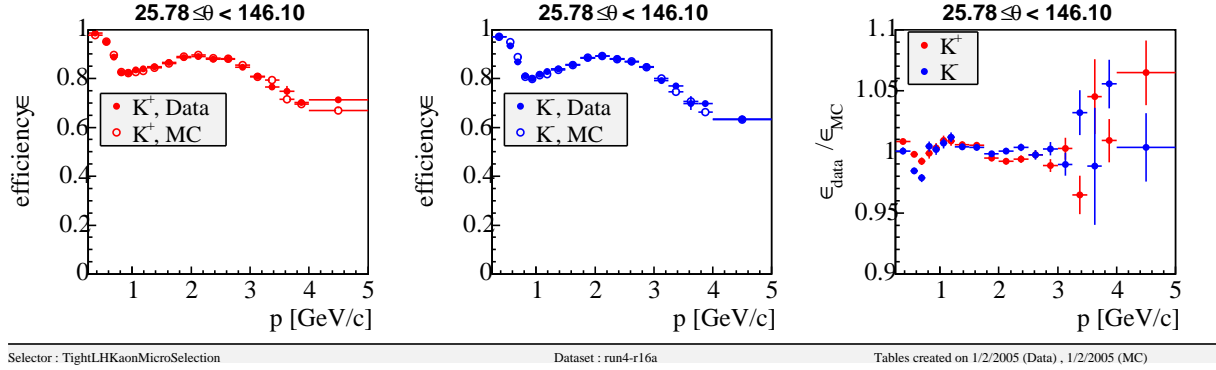


Figure 2.11: Kaon selection efficiency as a function of momentum in Monte Carlo (MC) and data $D^{*+} \rightarrow D^0\pi_s^+$, $D^0 \rightarrow K\pi$ control sample. The left plot shows the efficiency of K^+ in data (points) and in Monte Carlo (open circles), the middle plot shows the same for K^- , and the right plot shows the ratio of efficiencies in data and Monte Carlo for K^+ and K^- tracks. Kaon identification for particle momenta below 0.7 GeV/c relies on dE/dx measurements in the DCH. For $p > 0.7$ GeV/c, the kaon identification relies on the DIRC. The right plot shows a dip in the data/MC ratio due to incorrect modeling of the transition region in the Monte Carlo.

a misidentification rate from muons of about 40%. The pion identification for particle momenta below 1.1 GeV/c relies mainly on dE/dx measurements in the DCH. For $p \approx 0.7$ GeV/c, kaons become visible in the DIRC, and above this momentum, the dE/dx measurement in the DCH loses its discriminating power and kaon/pion separation relies mainly on the DIRC detector.

Neutral pions (π^0)

We construct π^0 candidates from two neutral clusters in the EMC consistent with two photons. π^0 candidates are required to satisfy the following requirements:

- $0.115 \text{ GeV} < m_{\pi^0} < 0.150 \text{ GeV}$

Here m_{π^0} , the invariant mass of the two photons, is calculated at the $\gamma\gamma$ origin, which is taken to be the $\ell^+\ell^-$ vertex position.

- $0.050 \text{ GeV} < E_\gamma < 10.0 \text{ GeV}$
- $0.0 < LAT_\gamma < 0.80$

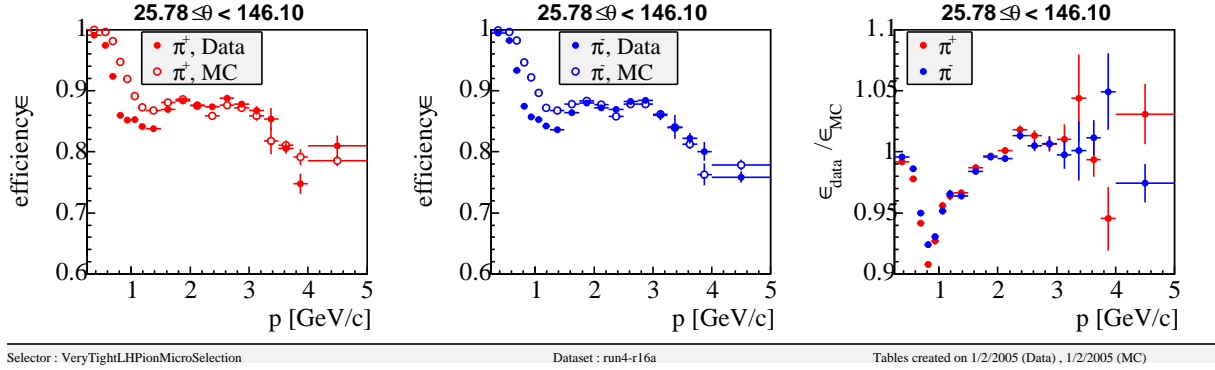


Figure 2.12: Pion selection efficiency as a function of momentum in Monte Carlo (MC) and data $D^{*+} \rightarrow D^0 \pi_s^+$, $D^0 \rightarrow K \pi$ control sample. The left plot shows the efficiency of π^+ in data (points) and in Monte Carlo (open circles), the middle plot shows the same for π^- , and the right plot shows the ratio of efficiencies in data and Monte Carlo for π^+ and π^- tracks. A dip is seen in the data/MC ratio in the right plot for particle momenta $p \approx 0.9$ GeV/c due to imperfect modeling in the Monte Carlo of the region where pion/kaon separation transitions from relying on the DCH and to relying on the DIRC.

2.4.3 Data control samples

With the very large dataset collected by *BABAR* the precision of the measurements is high, and small differences between the Monte Carlo (MC) simulated events and real data events can have a measurable impact on the physics results.

Tuning and performance studies of particle identification is done with high-purity data control samples:

- Muon identification, as well as muon contamination to other particle selectors, is studied in a control sample of $e^+e^- \rightarrow \mu^+\mu^-\gamma$ events, selected by requiring exactly two oppositely-charged tracks and one photon consistent with the four-momentum of the incoming electron and positron. Muon identification criteria are applied to one of the tracks and the efficiency of the criteria can be tested by applying it to the other track. Since this is a three-body decay, the muon efficiency can be measured over a wide range of momenta.
- Identification of charged kaons and pions are checked with a control sample of $D^{*+} \rightarrow D^0 \pi_s^+$, which is selected from its signature of a slow (low-momentum) pion and small mass difference $\Delta m_{(D^{*+} - D^0)}$. The D^0 decays into a K^- and a π^+ , and its decay products can be used as control sample for kaons and pions. This data sample is also used to check pion efficiency by the kaon selection and vice versa, as well as kaon efficiency by lepton

selectors.

- Pion contamination in the electron and muon selection is checked with a control sample of $e^+e^- \rightarrow \tau^+\tau^-$ events where one of the taus decay into a 3 particles (3-prong decay) ($\tau^- \rightarrow \pi^-\pi^+\pi^-\nu_\tau$) and the other decay is a more common ($\sim 85\%$) 1-prong decay with one charged particle and at least one neutrino.
- Electron efficiency, as well as electron contamination to other particle identification algorithms, is studied in a control sample of radiative Bhabha events ($e^+e^- \rightarrow e^+e^-\gamma$). Similar to the muon control sample, these events are selected by requiring exactly two oppositely-charged tracks and a photon with total energy and momentum consistent with the incident particles. The highest-momentum track is identified as an electron via its E/p , and the other track is used to study the selection efficiency.

Using these control samples, identification efficiencies are determined for each particle selection algorithm for each particle type, and in the Monte Carlo, the particle ID efficiency is adjusted to match the data. The measured efficiencies are stored in look-up-tables which hold the identification efficiencies for each run block in different bins of particle momentum, ϕ and θ .

The control samples typically consist of low-multiplicity events, and an additional correction is done here to check the efficiencies in multihadron events. For this we use charmonium control samples, which have the same final states as signal. This procedure is described in section 4.4.

All simulated events are thus corrected for data–MC differences at several levels:

- Particle identification differences are studied in data control samples and simulations of the same processes, and high-precision correction by data/MC ratios are found for all charged particles as a function of particle momentum and direction. Each identified track has been corrected according to this procedure.
- Particle identification is also studied in event types similar to signal by using charmonium control samples. A correction is applied for the total efficiency per block.
- Relative differences between the tracking efficiencies in data and Monte Carlo is found from comparing tracks detected in the SVT and the DCH detectors. Systematic uncertainties on this method is obtained from studying a control sample of 3-1 prong $\tau\bar{\tau}$ decays. Events with K_S^0 decays provide an additional control sample for tracks with a vertex displaced from the interaction point. Tracking efficiencies have been studied in the data and

in Monte Carlo, and correction factors applied according to momentum and direction for all tracks with quality criteria applied.

- π^0 efficiencies are studied in data and Monte Carlo using a control sample of $\tau\bar{\tau}$ events and measuring the double ratio $\frac{(\tau\rightarrow\rho)_{data}/(\tau\rightarrow\rho)_{MC}}{(\tau\rightarrow\pi)_{data}/(\tau\rightarrow\pi)_{mc}}$. Momentum-dependent weights have been applied to events containing π^0 candidates.

Chapter 3

Experimental techniques

The experimental setup of *BABAR* and PEP-II is such that kinematic features of the events can be used to distinguish between signal and background. This chapter introduces some of the most common quantities typically used in *BABAR* analyses, and which are used in the analysis described in the next chapter.

3.1 Event-shape variables

With PEP-II beam energies of 10.58 GeV, just above threshold for $B\bar{B}$ production, the two B -mesons are produced almost at rest in the center-of-mass frame. Therefore, the decay particles from the two B mesons are isotropically distributed. This is not the case, however, for the light-quark background which makes up about 2/3 of the events at 10.58 GeV. Events with $e^+e^- \rightarrow q\bar{q}$, where $q = u, d, s, c$, produce lighter meson decay products with higher momentum, and this makes the event shapes more jet-like.

A set of variables describing the event shape is commonly used in HEP analyses (see *e.g.* [105]). Unless stated otherwise, these are always defined in the center-of-mass frame. The variables considered in this analysis (plots can be seen in section 4.2.2) are the following:

- *Fox Wolfram moments* [106], defined as

$$H_l = \frac{1}{E_{\text{vis}}^2} \sum_i \sum_j |\vec{p}_i| |\vec{p}_j| P_l(\cos\theta_{ij}), \quad (3.1)$$

where E_{vis} is the total visible energy of the event, \vec{p}_i and \vec{p}_j are the momenta of particles i and j , and θ_{ij} is the angle between the momenta of particle i and j . P_l is the Legendre [107]

polynomial of order l . In this work, only the ratio of second to zeroth Fox-Wolfram moments is used:

$$R_2 = \frac{H_2}{H_0}. \quad (3.2)$$

The distribution of R_2 is close to zero for a perfectly isotropic event and close to 1 for a perfectly back-to-back two-jet event. Thus, at the $\Upsilon(4S)$ resonance, B decays tend to have a distribution around 0.2 while continuum events tend to peak around 0.7 in this variable.

- *Thrust*: The quantity thrust T is defined by [108]:

$$T = \max_{|\vec{n}|=1} \frac{\sum_i |\vec{n} \cdot \vec{p}_i|}{\sum_i |\vec{p}_i|} \quad (3.3)$$

and the thrust axis is given by the \vec{n} vector for which the maximum is attained. The value range is $1/2 \leq T \leq 1$, with a 2-jet event corresponding to $T \approx 1$ and an isotropic event to $T \approx 1/2$.

The direction of the thrust axis can also be used to separate the jet-like continuum events from the isotropic $B\bar{B}$ events. In this analysis, we define an angle θ_{thrust} as the angle between the thrust axis of the reconstructed B and the thrust axis of the remaining particles in the event. $|\cos \theta_{\text{thrust}}|$ has a uniform distribution in signal $B\bar{B}$ events because B -decays do not have a well defined thrust axis. However, $|\cos \theta_{\text{thrust}}|$ peaks around 1 for continuum events, since the thrust axes of the two jets are back-to-back.

- *Legendre moments*: The i -th moment L_i is defined by $L_i = \sum_j |p_j^*| |\cos(\theta_j^*)|^i$, where the p_j^* are the center-of-mass momenta of all particles not used in reconstructing the signal B candidate, and the angle θ_j^* is between the particle's momentum and the thrust axis of the signal B . For signal $B\bar{B}$ events, the distribution is peaked around zero, while for continuum events the distribution of L_2/L_0 is around 0.6.

3.2 Kinematic variables

The PEP-II beam energies are known to a high precision [93]. The mean energies of the two beams, $E_{\text{beam}}^* = (E_{e^+}^* + E_{e^-}^*)/2$, where the asterisk indicates the center-of-mass frame, are calculated from the total magnetic bending strength and the average deviations of the accelerating frequencies from their central values. The spread in the measured beam energy is $\sigma_{E_{\text{beam}}^*} = 2.6 \text{ MeV}$.

We can compare the energy E_B of the reconstructed B meson with the well-known beam energy:

$$\Delta E = E_B^* - E_{\text{beam}}^* \quad (3.4)$$

If the B -meson is correctly reconstructed this quantity will be zero. The spread in this quantity is dominated by the spread in E_B^* which is typically 20 MeV.

Another useful kinematic quantity is the energy-substituted mass:

$$m_{ES} = \sqrt{E_{\text{beam}}^{*2} - |\vec{p}_B^*|^2} \quad (3.5)$$

where \vec{p}_B^* is the B -meson momentum in the center-of-mass frame reconstructed from the B -meson decay products. For a correctly reconstructed B meson, this quantity is equal to the nominal B mass, m_B . The spread in m_{ES} is dominated by the spread in beam energy.

These two kinematic variables span a two-dimensional plane which is used to select signal B -meson decays. Correctly reconstructed B -mesons occupies a small signal region in this plane which is used to search for signal events. Events outside of this region are useful for studying properties of background events.

3.3 Plotting and fitting event distributions

These and other kinematic variables are used to isolate the signal events. The tool typically used to plot the variables is the ROOT analysis framework [109]. The signal and background distributions in the $m_{ES}-\Delta E$ plane are modeled by fitting a probability-density-function (PDF) to the data points in this plane. The tool used here for fitting PDFs to the distribution is RooFit [110].

The signal shape is parameterized in both m_{ES} and ΔE by a Gaussian function plus a radiative tail described by an exponential power function, commonly referred to as a Crystal Ball lineshape [111]. This takes the form

$$f(x) \propto \begin{cases} \exp(-\frac{(x-\bar{x})^2}{2\sigma^2}) & ; (x-\bar{x})/\sigma > \alpha \\ A \times (B - \frac{x-\bar{x}}{\sigma})^{-n} & ; (x-\bar{x})/\sigma \leq \alpha \end{cases}, \quad (3.6)$$

where $A \equiv (\frac{n}{|\alpha|})^n \times \exp(-|\alpha|^2/2)$ and $B \equiv \frac{n}{|\alpha|} - |\alpha|$. The variables \bar{x} and σ are the Gaussian peak and width, and α and n are the point at which the function transitions to the power function and the exponent of the power function, respectively. A plot of simulated Monte Carlo $B^+ \rightarrow \pi^+ \ell^+ \ell^-$ signal events fitted with the described PDF is shown in figure 3.1. The fit to the signal distributions are used to determine the width of the signal region and to evaluate signal in the

charmonium control samples (section 4.3.1).

The combinatorial background shape is parameterized by an Argus threshold function [112] in m_{ES} :

$$f(m_{\text{ES}}) = m_{\text{ES}} \sqrt{1 - \left(\frac{m_{\text{ES}}^2}{E_b^2}\right)^2} \exp[-\zeta(1 - \left(\frac{m_{\text{ES}}^2}{E_b^2}\right)^2)], \quad (3.7)$$

where ζ is a fit parameter and $E_b = E_{\text{beam}}^*$ as introduced earlier. The combinatorial background shape in ΔE is parameterized by an exponential function or a first-order polynomial function.

For evaluating the combinatorial background in two dimensions ($m_{\text{ES}}-\Delta E$) we use a probability-density-function which is a product of an Argus function in m_{ES} and an exponential in ΔE :

$$f(\Delta E, m_{\text{ES}}) = N e^{s\Delta E} \cdot m_{\text{ES}} \sqrt{1 - \frac{m_{\text{ES}}^2}{E_b^2}} e^{-\xi(1 - \frac{m_{\text{ES}}^2}{E_b^2})}, \quad (3.8)$$

where N is a normalization factor, and s and ξ are free parameters determined in the fit to the data. Figure 3.2 shows events from a background control sample consisting of off-resonance events reconstructed in the $B \rightarrow \pi e \mu$ reconstruction mode. The plot shows the projections of the fitted PDF onto the m_{ES} and ΔE distributions.

For systematic studies we also use a more general form for the background shape (equation 3.8), where the Argus slope, ξ , is allowed to be a function of ΔE

$$\xi = \xi(\Delta E) = \xi_0 + \xi_1 \Delta E + \frac{1}{2} \xi_2 \Delta E^2. \quad (3.9)$$

where ξ_i are correlation parameters.

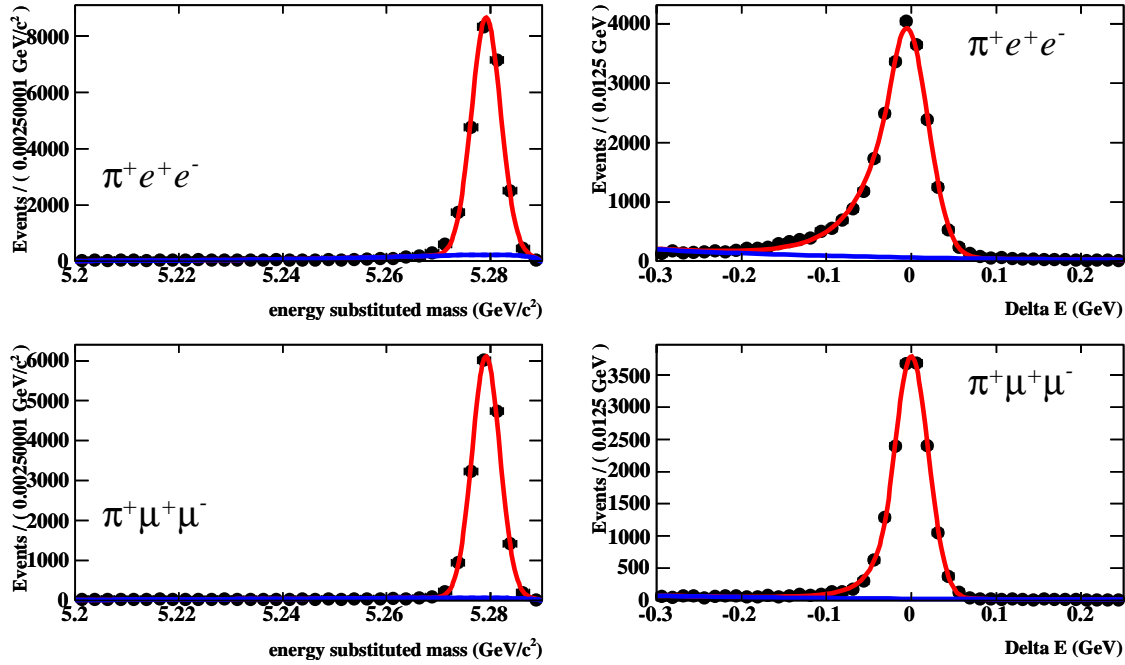


Figure 3.1: Projections of two-dimensional fit to m_{ES} and ΔE distribution in simulated $B^+ \rightarrow \pi^+ \ell^+ \ell^-$ signal events. The signal distributions in m_{ES} and in ΔE have been fitted to a Crystal Ball lineshape (equation 3.6).

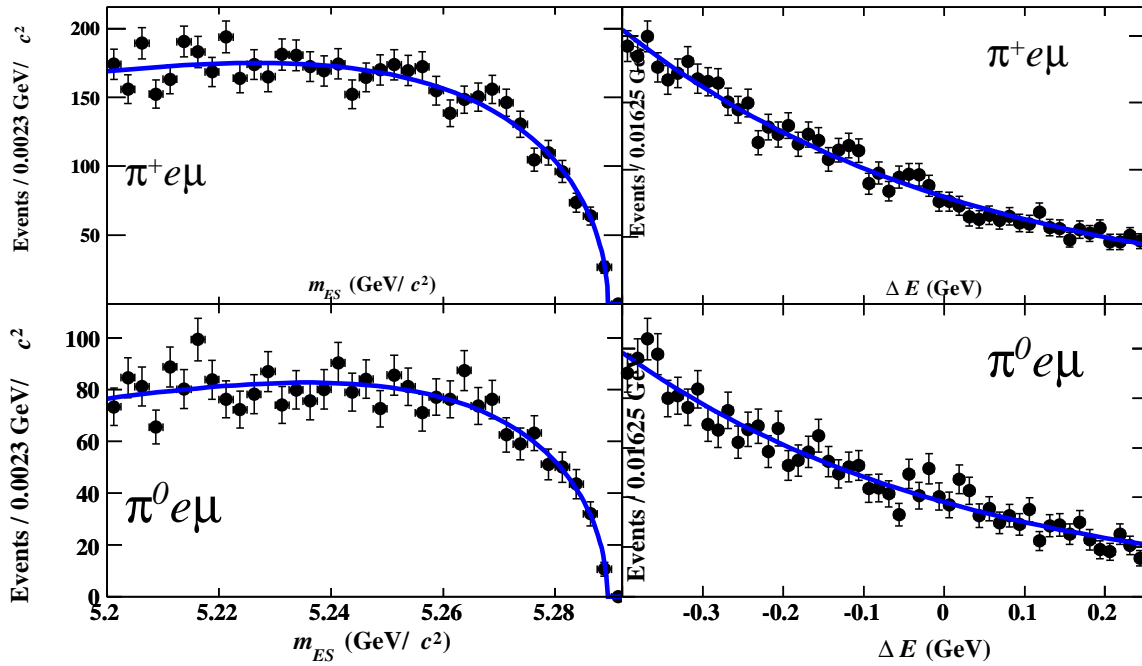


Figure 3.2: Projections of two-dimensional fit to m_{ES} and ΔE distribution in a background control sample of off-resonance events reconstructed in the $B \rightarrow \pi e \mu$ modes. The background distributions have been fitted to a product of an Argus function in m_{ES} and an exponential function in ΔE (equation 3.8).

Chapter 4

Search for $B \rightarrow \pi \ell^+ \ell^-$

If the Standard Model prediction [47] is correct, we expect that around 22 $B \rightarrow \pi \ell^+ \ell^-$ events (summing over lepton flavor and pion isospin) may have been produced in the data collected during *BABAR* Run 1–4. It is tempting to start looking for these events and try to measure a branching fraction, which could be altered with respect to Standard Model expectations in the case of new physics. The main challenge experimentally is that we search for a very rare decay mode, with large abundance of pions and leptons in background events from both other $B\bar{B}$ events and continuum events. In addition, we expect a signal-like background component from the CKM favored $B \rightarrow K \ell^+ \ell^-$ decay which will be impossible to remove completely. However, the excellent K – π separation provided by the DIRC subdetector reduce these backgrounds to a very low level.

The basic technique is to reconstruct the decay of the B meson from all the final state particles. The lepton pairs considered are e^+e^- , $\mu^+\mu^-$, and $e^\pm\mu^\mp$, with the latter combination primarily serving as a background control sample. The mesons reconstructed in $B \rightarrow \pi \ell^+ \ell^-$ modes are π^\pm and π^0 . To reduce background, strict particle identification is required, a multivariate discrimination technique is used to separate signal from combinatorial backgrounds, and direct vetoes are used to remove “peaking” backgrounds which have the same shapes as signal in the variables used to extract the signal.

The signal yield is extracted by counting events in the kinematic signal region. The combinatorial background is estimated from an extended unbinned maximum likelihood fit of the m_{ES} sideband, which is then extrapolated into the signal region. Background which peaks in the signal region is estimated from simulated sources and, in the case of hadronic B decays, from data control samples. Independent control samples in *BABAR* data are used extensively to verify the efficiency of the signal selection, to estimate the performance of the multivariate discriminants,

to estimate peaking backgrounds, and to test the fit technique.

This is a “blind analysis” [113], in the sense that the B candidates in *BABAR* data that are to be included in the signal extraction procedure are not examined until the event selection has been finalized.

4.1 Signal model and simulation samples

The signal efficiency and characteristics are determined using a sample of Monte Carlo simulations of $B \rightarrow \pi \ell^+ \ell^-$ events. The signal decay kinematics follow the modeling of Ali *et al* [23], and $B \rightarrow \pi$ form-factors are based on Ball & Zwicky [50, 114, 115]. The simulated samples are modeled with a full detector simulation based on GEANT4 [116] with the event generator EvtGen [117].

To study background yields and characteristics, a large number of B -meson decay channels have been studied with simulated events:

- The decays $B \rightarrow J/\psi \pi$ and $B \rightarrow \psi(2S) \pi$, with $J/\psi \rightarrow \ell^+ \ell^-$ and $\psi(2S) \rightarrow \ell^+ \ell^-$, have the exact same final states as the $B \rightarrow \pi \ell^+ \ell^-$ decay. The amplitudes of these decays also interfere with the penguin amplitude and make the theoretical predictions difficult in certain regions of $m_{\ell^+ \ell^-}$. These Monte Carlo samples are used to study rejection of this class of background.
- Simulations of the penguin decays $B \rightarrow K^{(*)} \ell^+ \ell^-$ and the charmonium modes $B \rightarrow J/\psi K$ and $B \rightarrow \psi(2S) K$, models the background from the more abundant signal-like events where a kaon passes the pion selection.
- Generic $B\bar{B}$ and continuum events model the combinatorial background and are used to optimize the event selection.
- A large number of samples modeling exclusive B -meson decays have been investigated to consider potential peaking background modes, *e.g.* $B^+ \rightarrow \bar{D}^0 (\rightarrow K^+ \pi^-) \pi^+$.

The only simulated data samples which directly affect the final branching fraction upper limit are the signal samples from which the signal efficiencies are obtained, and certain types of peaking background processes. The shapes and level of non-peaking combinatorial backgrounds are determined directly from the *BABAR* data.

Tables 4.1 – 4.3 list the samples of simulated events used in the study of signal and background characteristics.

Process	\mathcal{B}	$\delta\mathcal{B}/\mathcal{B}$ (%)	Ref.	Events	Number of $\Upsilon(4S)$ (/10 ⁹)	Data/MC (/10 ⁻³)
$B^+ \rightarrow \pi^+ e^+ e^-$	3.3×10^{-8}	30	[47]	232000	7031	0.033
$B^0 \rightarrow \pi^0 e^+ e^-$	1.65×10^{-8}	30	[47]	232000	14061	0.016
$B^+ \rightarrow \pi^+ \mu^+ \mu^-$	3.3×10^{-8}	30	[47]	234000	7091	0.032
$B^0 \rightarrow \pi^0 \mu^+ \mu^-$	1.65×10^{-8}	30	[47]	230000	13939	0.017
$B^+ \rightarrow \rho^+ e^+ e^-$	6.0×10^{-8}	30	[47]	234000	3900	0.059
$B^0 \rightarrow \rho^0 e^+ e^-$	3.0×10^{-8}	30	[47]	234000	7800	0.030
$B^+ \rightarrow \rho^+ \mu^+ \mu^-$	6.0×10^{-8}	30	[47]	232000	3867	0.060
$B^0 \rightarrow \rho^0 \mu^+ \mu^-$	3.0×10^{-8}	30	[47]	232000	7734	0.030
$B^+ \rightarrow K^+ e^+ e^-$	3.4×10^{-7}	29	[26]	268000	788	0.29
$B^0 \rightarrow K^0 e^+ e^-$	3.4×10^{-7}	29	[26]	580000	1706	0.14
$B^+ \rightarrow K^+ \mu^+ \mu^-$	3.4×10^{-7}	29	[26]	268000	788	0.29
$B^0 \rightarrow K^0 \mu^+ \mu^-$	3.4×10^{-7}	29	[26]	578000	1700	0.14
$B \rightarrow K^* e^+ e^-$	7.8×10^{-7}	38.5	[26]	580000	744	0.31
$B^0 \rightarrow K^{*0} e^+ e^-$	7.8×10^{-7}	38.5	[26]	576000	738	0.31
$B \rightarrow K^* \mu^+ \mu^-$	7.8×10^{-7}	38.5	[26]	578000	741	0.31
$B^0 \rightarrow K^{*0} \mu^+ \mu^-$	7.8×10^{-7}	38.5	[26]	582000	746	0.31

Table 4.1: Samples of simulated signal ($B \rightarrow \pi \ell^+ \ell^-$) and penguin background events used in this analysis. The number of events and effective number of $\Upsilon(4S)$ decays (and branching fraction assumptions) in the simulations are given, along with the ratio of the number of $\Upsilon(4S)$ decays in the data to the effective number of simulated events.

4.2 Event selection

The $B^+ \rightarrow \pi^+ \ell^+ \ell^-$ events are selected from three charged-particle tracks and $B^0 \rightarrow \pi^0 \ell^+ \ell^-$ events are selected from two charged-particle tracks and two photons if the event is kinematically consistent with originating from a B meson.

We require two oppositely-charged lepton candidates ($\ell = e, \mu$) in the combinations $e^+ e^-$, $\mu^+ \mu^-$ or $e^\pm \mu^\mp$. The leptons are identified using particle identification criteria described in section 2.4.2. Electron candidates are required to have a momentum $p_e > 0.3$ GeV/ c ; muon candidates are required to have momentum $p_\mu > 0.7$ GeV/ c . Lepton pairs with at least one electron with a low invariant mass, $m_{\ell^+ \ell^-}$, are considered consistent with coming from photon conversions ($\gamma \rightarrow e^+ e^-$), and these events are vetoed if $m_{\ell^+ \ell^-} < 0.03$ GeV/ c^2 . The lepton pairs are combined with a pion (either a π^\pm track or a π^0 meson decaying to $\gamma\gamma$). The charged-pion identification and neutral pion reconstruction are both described in section 2.4.2.

Process	\mathcal{B}	$\delta\mathcal{B}/\mathcal{B}$ (%)	Ref.	Events	Number of $\Upsilon(4S)$ (/10 ⁶)	Data/MC (/10 ⁻³)
$B^+ \rightarrow J/\psi\pi^+$	4.8×10^{-5}	12.5	[54]			
$J/\psi \rightarrow \ell^+\ell^-$	11.8%	1.7		127000	22422	10.3
$B^0 \rightarrow J/\psi\pi^0$	2.2×10^{-5}	18.2	[54]			
$J/\psi \rightarrow \ell^+\ell^-$	11.8%	1.7		814000	317374	0.73
$\pi^0 \rightarrow \gamma\gamma$	98.798%					
$B^+ \rightarrow J/\psi K^+$	9.9×10^{-4}	4.04	[54]			
$J/\psi \rightarrow \ell^+\ell^-$	11.8%	1.7		169000	1447	159
$B^+ \rightarrow \psi(2S)\pi^+$	3.0×10^{-5}		[118]			
$\psi(2S) \rightarrow \ell^+\ell^-$	1.47%	7.2		88800	201361	1.1
$B^0 \rightarrow \psi(2S)\pi^0$	1.5×10^{-5}		[118]			
$\psi(2S) \rightarrow \ell^+\ell^-$	1.47%	7.2				
$\pi^0 \rightarrow \gamma\gamma$	98.798%			88200	404866	0.57
$B^+ \rightarrow \psi(2S)K^+$	6.8×10^{-4}	5.9	[54]			
$\psi(2S) \rightarrow \ell^+\ell^-$	1.47%	7.2		50100	5012	45.9

Table 4.2: Samples of simulated charmonium events used in this analysis. The number of events simulated and the effective number of $\Upsilon(4S)$ decays (and branching fraction assumptions) are given, along with the ratio of the number of $\Upsilon(4S)$ decays in the data to the effective number of simulated events. Similar-sized samples are also used of B meson decays to charmonium and ρ and K^* final states.

This section describes the event selection and background rejection for the $B \rightarrow \pi\ell^+\ell^-$ modes in detail. Events selected as $B \rightarrow \pi e\mu$ are considered a control sample of the penguin modes, and the event selection for these modes is not optimized separately. The selection criteria used for these modes are summarized in section 4.3.3

4.2.1 Kinematic regions

Using the kinematic variables m_{ES} and ΔE defined in section 3.2, we define three kinematic regions to evaluate signal and background (see figure 4.1):

- **The signal region** is defined as a $\pm 2\sigma$ region around of the mean values in m_{ES} and ΔE , where σ is the standard deviation of the signal distributions. m_{ES} is expected to peak at the mass of the B -meson, while ΔE is expected to peak at zero for correctly reconstructed signal events. For Monte Carlo simulated samples, the standard deviations $\sigma_{m_{ES}}$ and $\sigma_{\Delta E}$

Process	σ	\mathcal{B}	Events	Number of $\Upsilon(4S)$ (/10 ⁶)	Data/MC (/10 ⁻³)
Generic B^+B^-	1.11 nb	50%	584.1	1168.0	0.20
Generic $\overline{B^0}B^0$	1.11 nb	50%	540.7	1081.4	0.21
Continuum $c\bar{c}$	1.35 nb		425.6		0.66
Continuum $u\bar{u}/d\bar{d}/s\bar{s}$	2.04 nb		677.1		0.62

Table 4.3: Samples of simulated generic $B\overline{B}$ and $e^+e^- \rightarrow q\bar{q}$ ($q = u, d, s, c$) continuum events used in this analysis. The number of events and effective number of $\Upsilon(4S)$ decays (and branching fraction assumptions) in the simulations are given, along with the ratio of the number of $\Upsilon(4S)$ decays in the data to the effective number of simulated events.

are obtained from fits to the signal Monte Carlo samples; for defining the regions in data, both the mean and the standard deviations are determined from fits to the $B \rightarrow J/\psi \pi$ data control samples. The values defining the boundaries in data are given in table 4.4. The data events in the signal region are not inspected until the event selection criteria are finalized and background expectations have been determined.

mode	m_{ES} low [GeV/ c^2]	m_{ES} high [GeV/ c^2]	ΔE low [MeV]	ΔE high [MeV]
$B^+ \rightarrow \pi^+ e^+ e^-$	5.2748	5.2847	-53.6	37.4
$B^0 \rightarrow \pi^0 e^+ e^-$	5.2767	5.2839	-115.0	82.5
$B^+ \rightarrow \pi^+ \mu^+ \mu^-$	5.2749	5.2847	-42.0	35.0
$B^0 \rightarrow \pi^0 \mu^+ \mu^-$	5.2764	5.2836	-87.4	68.0

Table 4.4: Boundary values defining the signal region for each $B \rightarrow \pi \ell^+ \ell^-$ mode. The boundaries used in the $B^+ \rightarrow \pi^+ e \mu$ and $B^0 \rightarrow \pi^0 e \mu$ modes are the same as for the $B^+ \rightarrow \pi^+ e^+ e^-$ and $B^0 \rightarrow \pi^0 e^+ e^-$ modes, respectively.

- **The fit region** includes the signal region as well as a sideband in m_{ES} and ΔE wide enough to fit the combinatorial background distributions to determine background normalizations and shapes. This region also remains hidden until the event selection criteria are finalized. Events in this region are inspected and compared to expectations before the signal region is investigated. For all modes, the fit region is defined by

- $m_{\text{ES}} > 5.2 \text{ GeV}/c^2$ and
- $|\Delta E| < 0.25 \text{ GeV}$.

- **The grand sideband region** is a very broad region surrounding the fit region and is disjoint from the fit region. The sideband region is dominated by combinatorial background and is used to isolate background-like events for further study and for comparison with simulated background events. The sideband region is defined by

- $5.0 \text{ GeV}/c^2 < m_{ES} < 5.3 \text{ GeV}/c^2$
- $|\Delta E| < 0.50 \text{ GeV}$
- and *not* in the fit region.

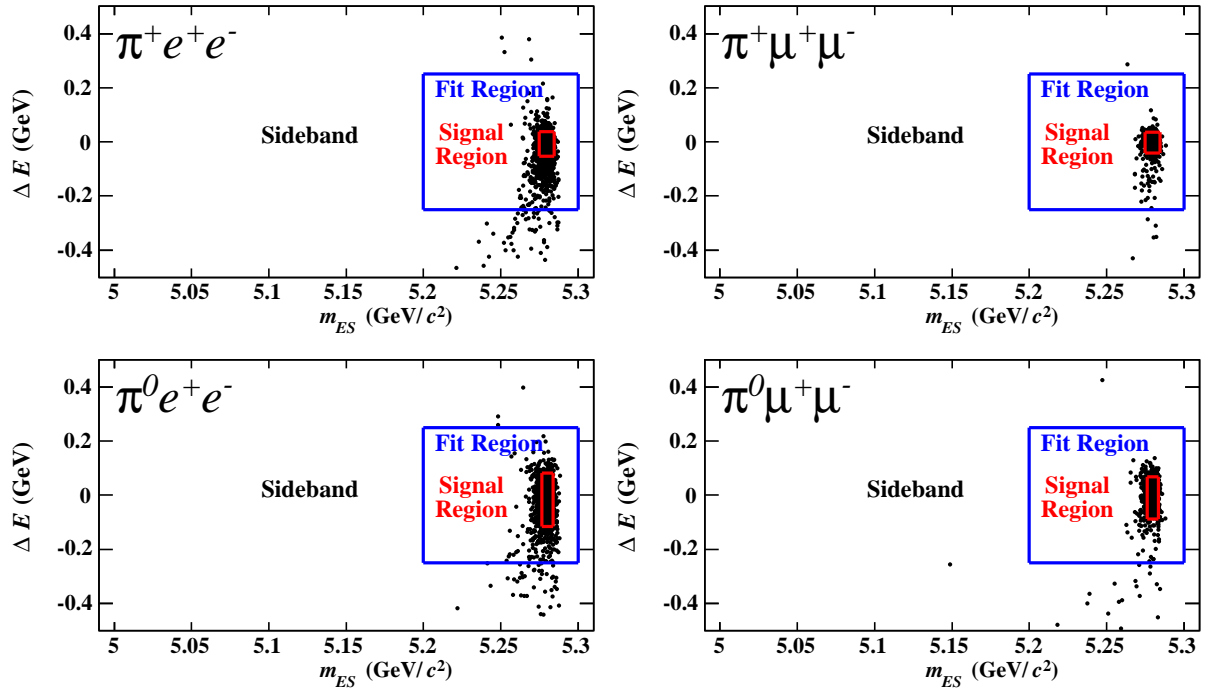


Figure 4.1: The three regions of m_{ES} and ΔE used to analyze $B \rightarrow \pi\ell^+\ell^-$ candidates. The boundaries of the signal region are defined as $\pm 2\sigma$ relative to the mean of the signal distributions, where σ is the standard deviation of the signal distribution for each of the modes. The fit region is a larger region which also includes the signal region. The sideband region outside the fit region contains only background events. The points are simulated $B \rightarrow \pi\ell^+\ell^-$ events.

4.2.2 Fisher discriminant for continuum $q\bar{q}$ suppression

To suppress background from continuum $u\bar{u}/d\bar{d}/s\bar{s}$ and $c\bar{c}$ events, we use a Fisher discriminant [119] composed of selected event shape variables. Figure 4.2 show distributions of these in

Monte Carlo signal events and in off-resonance data events. The following quantities have been used:

- The ratio of Fox-Wolfram [106] moments $R_2 = H_2/H_0$, as defined in section 3.1. The moments are computed with all charged and neutral particles in the event. The distribution of R_2 peaks around 0.2 for signal events and 0.7 for background events. In figure 4.2a, a preliminary selection of $B\bar{B}$ events has already removed most events with $R_2 > 0.5$.
- The value $|\cos \theta_B|$, where θ_B is the angle between the B candidate's momentum and the beam axis in the center-of-mass frame. For correctly reconstructed signal events, this angle is distributed as $\sin^2 \theta_B$, while for incorrectly reconstructed events in the continuum background, the distribution is uniform, as seen in figure 4.2b.
- The value $|\cos \theta_{\text{thrust}}|$, where θ_{thrust} is the angle between the thrust axis of the reconstructed B and that of the remaining particles in the event. As seen in figure 4.2c, this has a uniform distribution for signal events and peaks near 1 for continuum background.
- The ratio of Legendre moments L_2/L_0 , computed from all particles not used in reconstructing the signal B candidate with respect to the thrust axis of the signal B . As seen in figure 4.2d, these have a signal distribution around zero and a background distribution at positive values. Due to a preliminary selection of $R_2 > 0.5$, the background distribution of this variable has already been truncated.

A Fisher discriminant is a linear combination of discriminating variables which projects the discriminating power onto a single one-dimensional quantity. We define the Fisher discriminant, \mathcal{F} , as:

$$\mathcal{F} = c_0 + c_1 \cdot R_2 + c_2 \cdot \cos \theta_B + c_3 \cdot \cos \theta_{\text{thrust}} + c_4 \cdot L_2/L_0 \quad (4.1)$$

The Fisher discriminant coefficients, c_1 , c_2 , c_3 and c_4 are determined independently for each mode so as to maximize the discriminating power. The first coefficient, c_0 , is defined so that the signal distribution of \mathcal{F} has mean value zero.

The distributions of the output Fisher discriminants are shown in figure 4.3 for simulated signal events and for off-resonance data events. An independent selection is chosen for each mode (see section 4.2.4).

4.2.3 Likelihood ratio for $B\bar{B}$ background suppression

To suppress backgrounds from non-signal $B\bar{B}$ events, we define a likelihood ratio from four quantities. For each of these variables, we construct a probability-density-functions (PDF) for

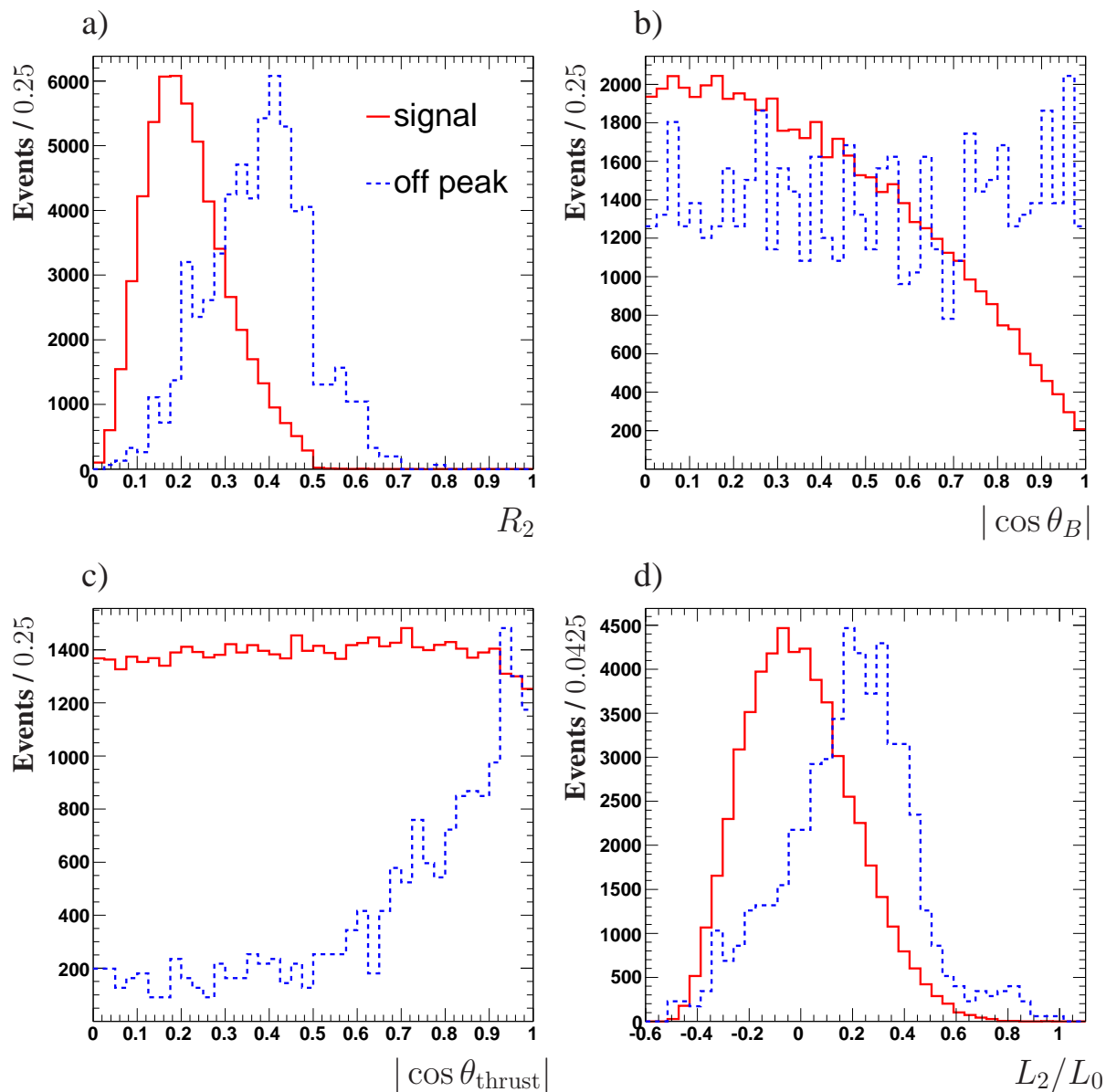


Figure 4.2: Distributions of input variables for the Fisher discriminant for $B^0 \rightarrow \pi^0 e^+ e^-$ events in the signal Monte Carlo (solid line) and off-resonance data (dashed line). The input variables are a) R_2 , b) $|\cos \theta_B|$, c) $|\cos \theta_{\text{thrust}}|$ and d) L_2/L_0 ,

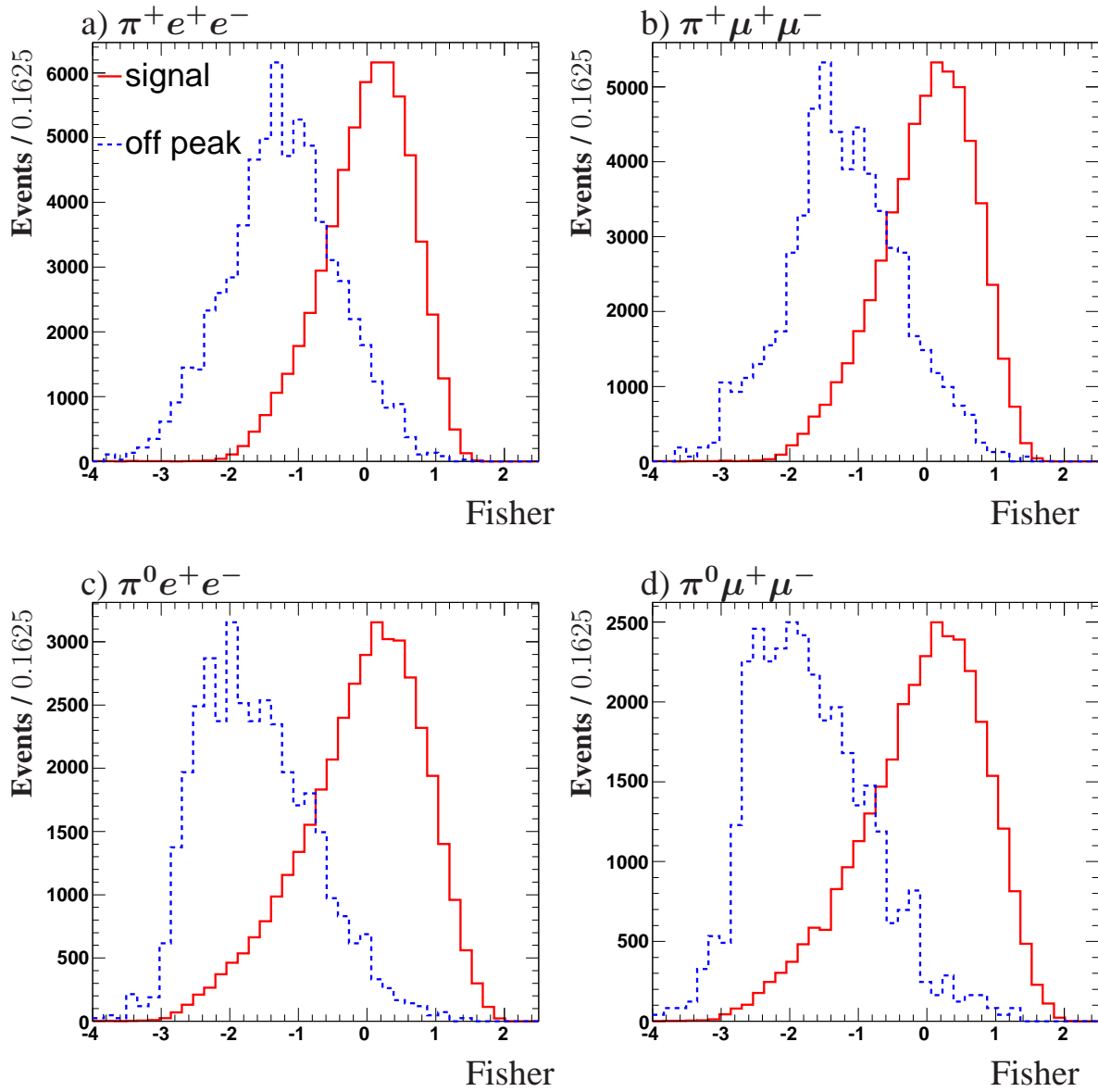


Figure 4.3: Distributions of Fisher discriminants for a) $B^+ \rightarrow \pi^+e^+e^-$, b) $B^0 \rightarrow \pi^0e^+e^-$, c) $B^+ \rightarrow \pi^+\mu^+\mu^-$ and d) $B^0 \rightarrow \pi^0\mu^+\mu^-$ events from signal Monte Carlo (solid line) and off-resonance data (dashed line).

signal and background ($B\bar{B}$) distribution. The PDFs are fitted to simulated $B \rightarrow \pi \ell^+ \ell^-$ signal events and generic $B\bar{B}$ events for each mode individually. These distributions and best-fit PDFs are shown in figure 4.4. The quantities used are:

- The missing energy in the event, computed from all charged and neutral particles in the event. If all particles in the event are detected, signal events will have no measured missing energy. Leptons in $B\bar{B}$ background typically stems from semileptonic decays, and these events have a measurable missing energy. The distributions are parameterized by a sum of two Gaussian functions, and can be seen in figure 4.4a.
- The logarithm of the vertex probability of the B candidate. In correctly reconstructed signal events the tracks should all originate from the same vertex and the vertex fit should give a high vertex probability. For random combinations of particles, the vertex point will have a lower probability than signal events. The distributions are described by the sum of an exponential function and a first-order polynomial and can be seen in figure 4.4b.
- The logarithm of the vertex probability of the two leptons. The same arguments as previous point apply here as well. The distributions are described by the sum of an exponential function and a first-order polynomial and can be seen in figure 4.4c.
- The value $\cos \theta_B$, where θ_B is the angle between the B candidate's momentum and the beam axis in the center-of-mass frame. For correctly reconstructed signal events, this angle is distributed as $\sin^2 \theta_B = (1 - \cos^2 \theta_B)$, and is parameterized by a second-order polynomial. For incorrectly reconstructed events in the $B\bar{B}$ background, the distribution is uniform. As seen in figure 4.4d, a component of the $B\bar{B}$ background has a $(1 - \cos \theta_B)$ distribution as well. Thus, also a linear term is allowed for the background parameterization.

From these PDFs we construct a likelihood (\mathcal{L}) ratio:

$$\mathcal{L} \text{ ratio} = \frac{\text{signal } \mathcal{L}}{\text{signal } \mathcal{L} + B\bar{B} \mathcal{L}} \quad (4.2)$$

where

$$\begin{aligned} \text{signal } \mathcal{L} &= \prod_i \mathcal{P}df_i^{(S)} \\ &= \mathcal{P}df_{E_{\text{miss}}}^{(S)} \cdot \mathcal{P}df_{\text{llVtx}}^{(S)} \cdot \mathcal{P}df_{\text{BVtx}}^{(S)} \cdot \mathcal{P}df_{\cos \theta_B}^{(S)} \end{aligned} \quad (4.3)$$

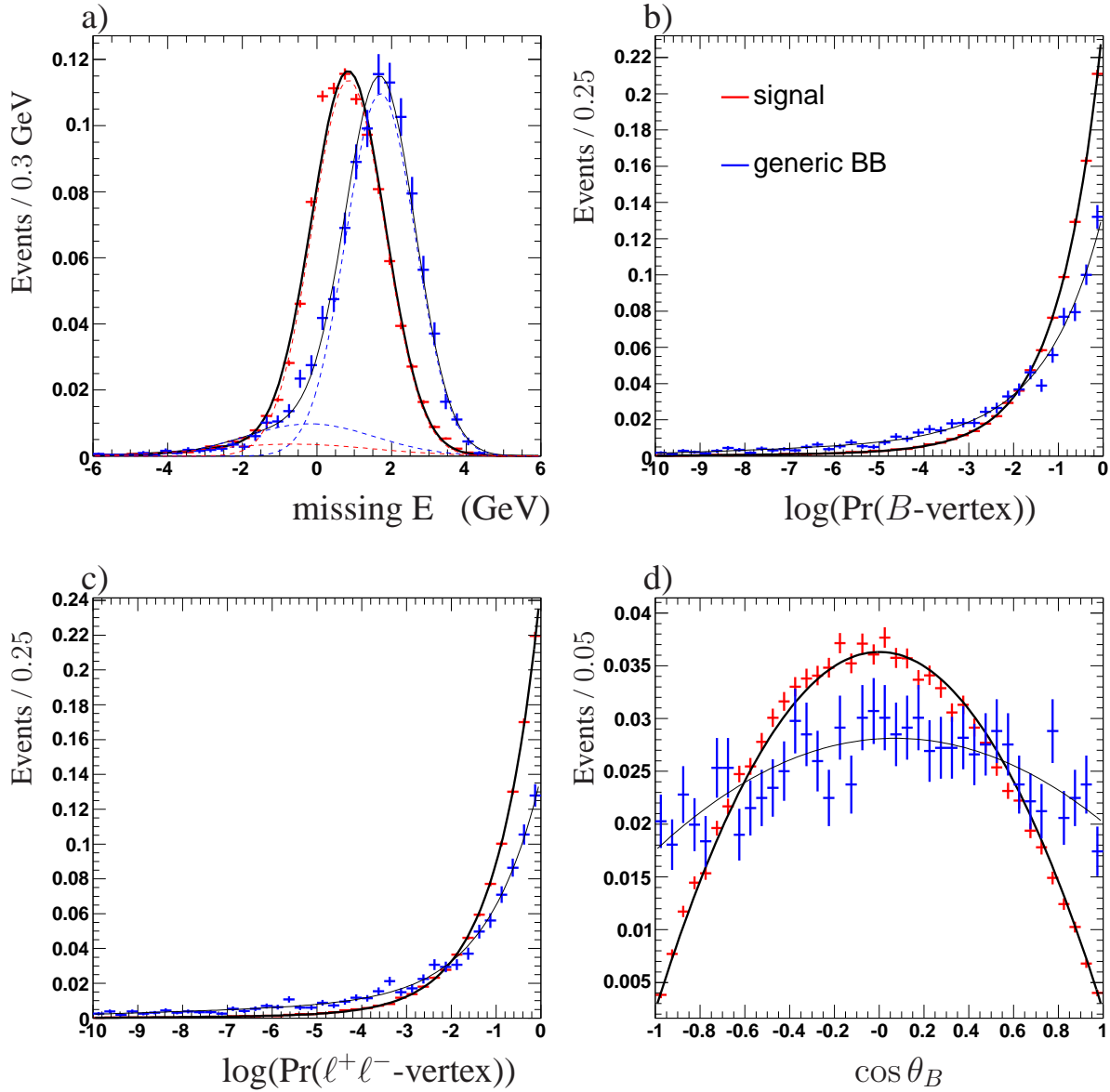


Figure 4.4: Distributions of input variables to the likelihood ratio for $B^+ \rightarrow \pi^+ \mu^+ \mu^-$ events in signal Monte Carlo (thick line) and $B\bar{B}$ Monte Carlo (thin line): a) missing energy in the event, b) logarithm of the B -vertex probability, c) logarithm of the $\ell^+ \ell^-$ -vertex probability, and d) $\cos \theta_B$. The dashed lines in figure a) show the contributions of the individual Gaussian components.

where $\mathcal{P}df^{(S)}$ is the probability-density-function for the signal distribution of variable i . The background likelihood ratio is defined similarly from PDFs obtained from distributions in the $B\bar{B}$ Monte Carlo samples.

The distributions of the output likelihood ratio are shown in figure 4.5. For signal-like events this ratio will approach 1, for $B\bar{B}$ -like events it will approach 0. An independent cut value is chosen for each mode (see section 4.2.4).

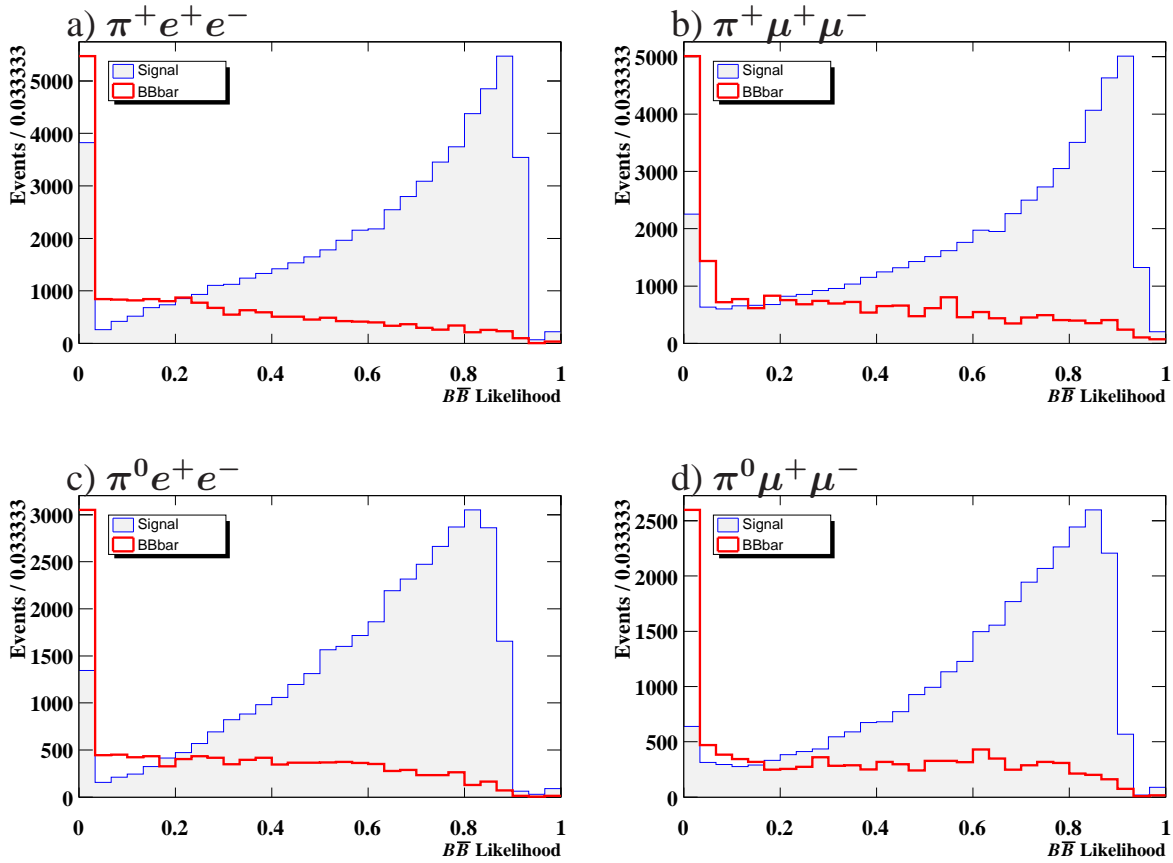


Figure 4.5: Distributions of likelihood-ratio outputs for a) $B^+ \rightarrow \pi^+ e^+ e^-$, b) $B^0 \rightarrow \pi^0 e^+ e^-$, c) $B^+ \rightarrow \pi^+ \mu^+ \mu^-$ and d) $B^0 \rightarrow \pi^0 \mu^+ \mu^-$ events from signal Monte Carlo (solid histogram) and $B\bar{B}$ Monte Carlo (thick line).

4.2.4 Optimization of selection with Fisher and likelihood-ratio

To reduce the combinatorial background, we select events which have large values for the Fisher discriminant and \mathcal{L} -ratio outputs. The optimization is done for \mathcal{F} and likelihood-ratio selection

criteria simultaneously. For each reconstruction mode, the optimal selection criteria is chosen such that it maximizes $S/\sqrt{S+B}$, where S and B are the signal and background yields expected in the signal region.

The signal yield, S , is determined from counting simulated signal events in the signal region, and the background yield, B , is determined from a two-dimensional extended unbinned maximum likelihood fit to simulated generic $B\bar{B}$ and continuum events in the $m_{ES} - \Delta E$ plane. The background fit function is a product of an Argus threshold function [112] in m_{ES} and a first-order polynomial in ΔE . Figure 4.6 shows projections onto m_{ES} and ΔE of the Monte Carlo simulated events and best-fit functions in the fit region for events selected as $B^+ \rightarrow \pi^+ e^+ e^-$.

The simulation samples are normalized to the luminosity of the *BABAR* dataset to be analyzed (209 fb^{-1}), and for the signal estimation, we assume Standard Model branching fractions as suggested in [47].

Figure 4.7 shows a contour plot of $S/\sqrt{S+B}$ as a function of Fisher and likelihood-ratio criteria for each of the four penguin modes.

mode	$\mathcal{F} >$	$\mathcal{L} \text{ ratio} >$	efficiency	S yield	B yield	$S/\sqrt{S+B}$
$B^+ \rightarrow \pi^+ e^+ e^-$	-0.1	0.5	7.2%	0.54	0.97	0.43
$B^0 \rightarrow \pi^0 e^+ e^-$	0.1	0.4	5.7%	0.22	0.92	0.21
$B^+ \rightarrow \pi^+ \mu^+ \mu^-$	0.1	0.4	4.7%	0.37	0.77	0.34
$B^0 \rightarrow \pi^0 \mu^+ \mu^-$	0.2	0.5	3.1%	0.13	0.58	0.14

Table 4.5: Optimal selection criteria for the Fisher discriminant (\mathcal{F}) and the likelihood (\mathcal{L}) ratio, as well as signal efficiencies, signal (S) and background (B) yield estimates and significance after sideband scaling and efficiency corrections.

4.2.5 Vetoes for suppression of peaking backgrounds

This section describes a series of vetoes that are used to suppress peaking backgrounds. These are events where a B meson decays into the same or similar final states as signal event. Therefore, the events resemble our signal in that they populate the same kinematic region of the m_{ES} and ΔE plane. Some peaking backgrounds are easy to veto because they contain narrow resonances. The resonances we veto are

- $J/\psi \rightarrow \ell^+ \ell^-$ and $\psi(2S) \rightarrow \ell^+ \ell^-$:

These come primarily from $B \rightarrow J/\psi \pi$ or $B \rightarrow \psi(2S) \pi$ events, but also from the more copious $B^+ \rightarrow J/\psi K^+$ and $B^+ \rightarrow \psi(2S) K^+$ modes, where the kaon passes the pion selection.

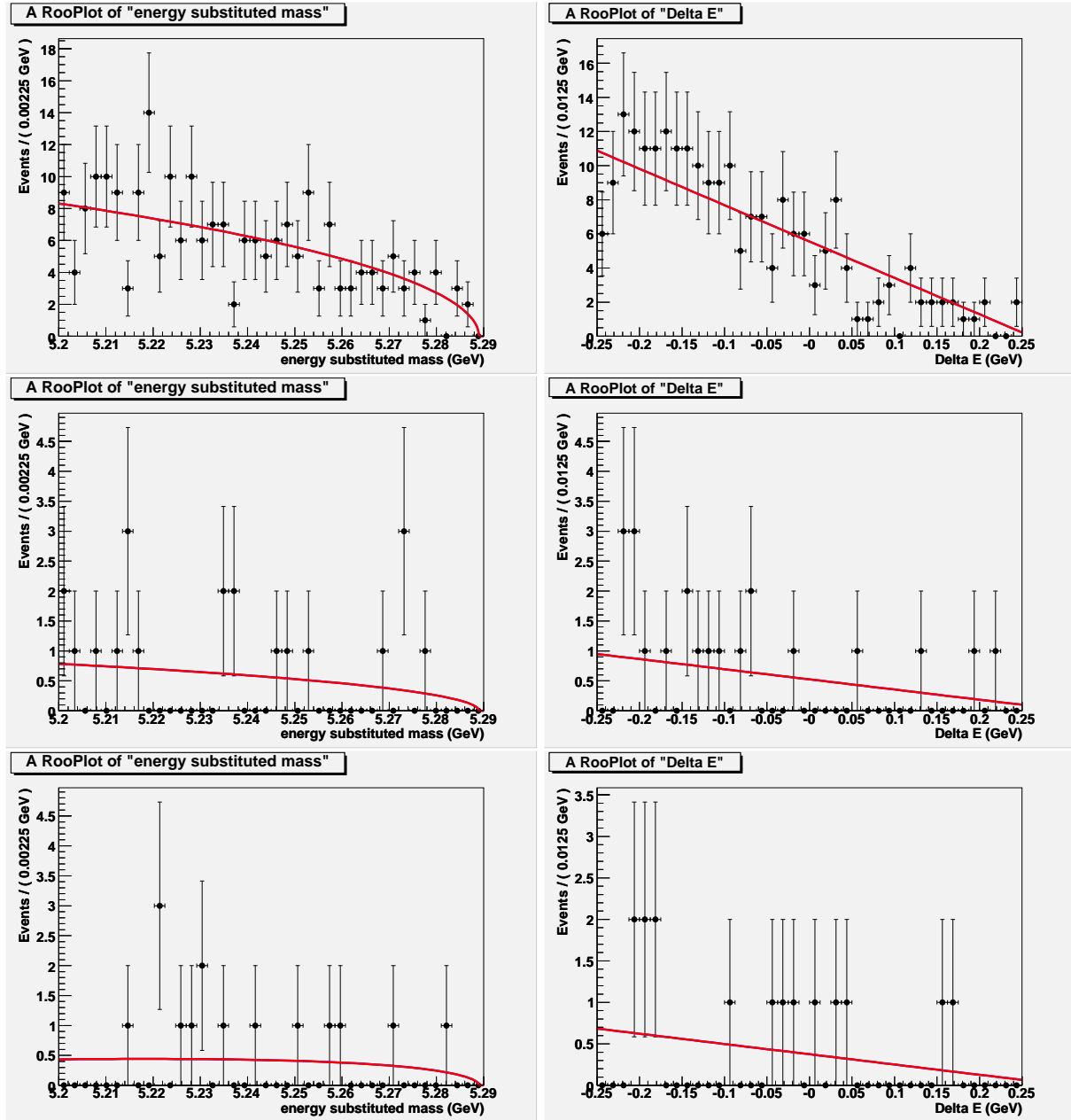


Figure 4.6: Projections of m_{ES} (left plots) and ΔE (right plots) for two-dimensional fits for $B^+ \rightarrow \pi^+ e^+ e^-$ to Monte Carlo simulated background samples: $B\bar{B}$ (top), $c\bar{c}$ (middle) and $u\bar{u}/d\bar{d}/s\bar{s}$ (bottom).

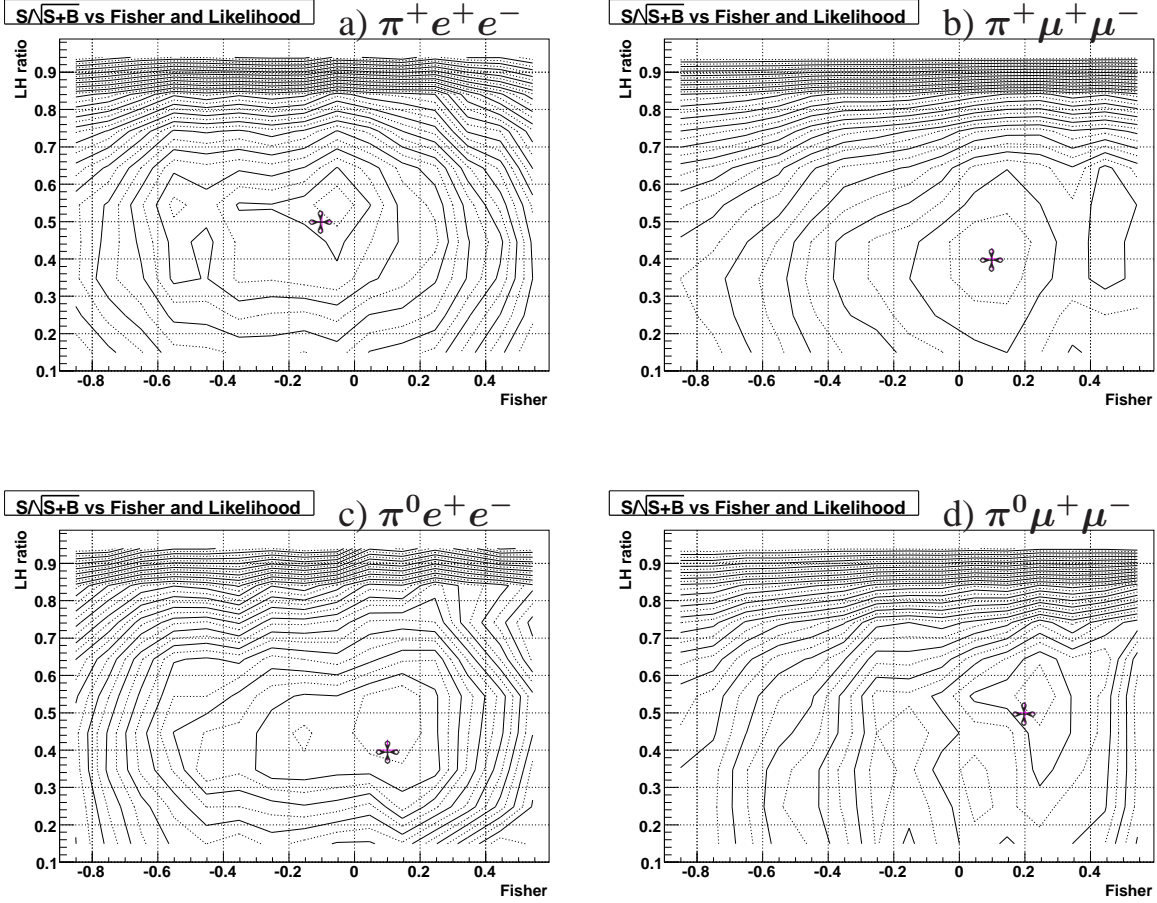


Figure 4.7: Contour plots of $S/\sqrt{S+B}$ vs. Fisher and likelihood (LH) ratio for a) $B^+ \rightarrow \pi^+ e^+ e^-$, b) $B^+ \rightarrow \pi^+ \mu^+ \mu^-$, c) $B^0 \rightarrow \pi^0 e^+ e^-$, d) $B^0 \rightarrow \pi^0 \mu^+ \mu^-$. A marker indicates the optimal selection criteria, which are also given in table 4.5.

- $D^0 \rightarrow \pi^- \pi^+$, $D^+ \rightarrow \pi^0 \pi^+$, $D^0 \rightarrow K^- \pi^+$ and $D^+ \rightarrow \pi^0 K^+$:

The D mesons are produced in the decays $B \rightarrow D\pi$ or $B \rightarrow DK$ where hadrons are misidentified as muons. The $D^+ \rightarrow \pi^0 K^+$ decay is doubly Cabibbo suppressed, but we veto it anyway.

Charmonium vetoes

Events with a charmonium meson decaying into a pair of leptons have sharp peaks in $m_{\ell^+ \ell^-}$ and are simple to remove. We veto events with $m_{\ell^+ \ell^-}$ consistent with a J/ψ or a $\psi(2S)$, which are the two most dominating charmonium resonances.

Complications arise due to bremsstrahlung of electrons and misidentification of tracks, pri-

marily kaons. If electrons from a J/ψ lose energy due to bremsstrahlung and the photon(s) are not recovered by the bremsstrahlung recovery procedure, then the measured invariant mass will be smaller than expected for a J/ψ meson and the ΔE will be decreased correspondingly. To account for this effect, we make the veto dependent on ΔE of the reconstructed B candidate, as illustrated in figures 4.8 and 4.9. The veto regions are defined in a similar way as was done in [26]. Since bremsstrahlung also occurs for muons, albeit to a lesser extent, we also make the veto ΔE -dependent for the muon modes. If the event contains a kaon mis-identified as a pion, then the ΔE will be reduced due to the incorrect mass assumption. We have increased the width of the ΔE -dependent veto correspondingly in order to remove the small background from $B \rightarrow J/\psi K$ (and $B \rightarrow \psi(2S)K$) event. This reduces the efficiency somewhat, but we have put emphasis on removing as much peaking background as possible.

For electron modes, the J/ψ veto region is the union of the following three regions in the $\Delta E - m_{\ell\ell}$ plane:

- $2.90 \text{ GeV}/c^2 < m_{\ell\ell} < 3.20 \text{ GeV}/c^2$
- for $m_{\ell\ell} > 3.20 \text{ GeV}/c^2$, a band in the $\Delta E - m_{\ell\ell}$ plane defined by

$$1.11c^2 \times m_{\ell\ell}(\text{GeV}/c^2) - 3.67 \text{ GeV} < \Delta E < 1.00c^2 \times m_{\ell\ell}(\text{GeV}/c^2) - 2.875 \text{ GeV}$$

- for $m_{\ell\ell} < 2.90 \text{ GeV}/c^2$, a triangle in the $\Delta E - m_{\ell\ell}$ plane defined by

$$\Delta E < 1.00c^2 \times m_{\ell\ell}(\text{GeV}/c^2) - 2.875 \text{ GeV}$$

For muon modes, the J/ψ veto region is the union of the following three regions in the $\Delta E - m_{\ell\ell}$ plane:

- $3.00 \text{ GeV}/c^2 < m_{\ell\ell} < 3.20 \text{ GeV}/c^2$
- for $m_{\ell\ell} > 3.20 \text{ GeV}/c^2$, a band in the $\Delta E - m_{\ell\ell}$ plane defined by

$$1.11c^2 \times m_{\ell\ell}(\text{GeV}/c^2) - 3.614 \text{ GeV} < \Delta E < 1.00c^2 \times m_{\ell\ell}(\text{GeV}/c^2) - 2.925 \text{ GeV}$$

- for $m_{\ell\ell} < 3.00 \text{ GeV}/c^2$, a triangle in the $\Delta E - m_{\ell\ell}$ plane defined by

$$\Delta E < 1.11c^2 \times m_{\ell\ell}(\text{GeV}/c^2) - 3.31 \text{ GeV}$$

The $\psi(2S)$ veto region is defined the same way for electrons and muons, but wider for π^0 modes than for π^\pm modes. For $\pi^\pm\ell^+\ell^-$, we veto the union of the following three regions in the $\Delta E - m_{\ell\ell}$ plane:

- $3.60 \text{ GeV}/c^2 < m_{\ell\ell} < 3.75 \text{ GeV}/c^2$
- for $m_{\ell\ell} > 3.75 \text{ GeV}/c^2$, a band in the $\Delta E - m_{\ell\ell}$ plane defined by

$$1.11c^2 \times m_{\ell\ell}(\text{GeV}/c^2) - 4.305 \text{ GeV} < \Delta E < 1.00c^2 \times m_{\ell\ell}(\text{GeV}/c^2) - 3.525 \text{ GeV}$$

- for $m_{\ell\ell} < 3.60 \text{ GeV}/c^2$, a triangle in the $\Delta E - m_{\ell\ell}$ plane defined by

$$\Delta E < 1.00c^2 \times m_{\ell\ell}(\text{GeV}/c^2) - 3.525 \text{ GeV}$$

For $\pi^0\ell^+\ell^-$, we veto the union of the following three regions in the $\Delta E - m_{\ell\ell}$ plane:

- $3.60 \text{ GeV}/c^2 < m_{\ell\ell} < 3.75 \text{ GeV}/c^2$
- for $m_{\ell\ell} > 3.75 \text{ GeV}/c^2$, a band in the $\Delta E - m_{\ell\ell}$ plane defined by

$$1.11c^2 \times m_{\ell\ell}(\text{GeV}/c^2) - 4.194 \text{ GeV} < \Delta E < 1.00c^2 \times m_{\ell\ell}(\text{GeV}/c^2) - 3.525 \text{ GeV}$$

- for $m_{\ell\ell} < 3.60 \text{ GeV}/c^2$, a triangle in the $\Delta E - m_{\ell\ell}$ plane defined by

$$\Delta E < 1.00c^2 \times m_{\ell\ell}(\text{GeV}/c^2) - 3.525 \text{ GeV}$$

There is an additional charmonium veto imposed on the electron modes for those events which escape the vetoes described above. If a photon which does not arise from electron bremsstrahlung is incorrectly recovered by the bremsstrahlung-recovery algorithm, it could escape the veto on $m_{\ell\ell}$ mass. We reduce this possibility by requiring that also the invariant mass of the two electrons *without* bremsstrahlung recovery does not lie in the regions $2.90 \text{ GeV}/c^2 < m_{\ell\ell} < 3.20 \text{ GeV}/c^2$ and $3.60 \text{ GeV}/c^2 < m_{\ell\ell} < 3.75 \text{ GeV}/c^2$.

Vetoes against $B \rightarrow D\pi$ backgrounds

B -meson decays to $D\pi$ and DK where $D \rightarrow \pi\pi$ or $D \rightarrow K\pi$ may peak in the signal region if both tracks reconstructed as leptons are really misidentified hadrons. Table 4.6 gives an overview of the $B \rightarrow Dh$ modes that may contribute and which are being vetoed.

The event is vetoed if either the $\ell^+\ell^-$ combination or the $\pi\ell$ combination is consistent with originating from a D when the tracks are given $\pi\pi$ or $K\pi$ hypotheses. The selection differs according to modes:

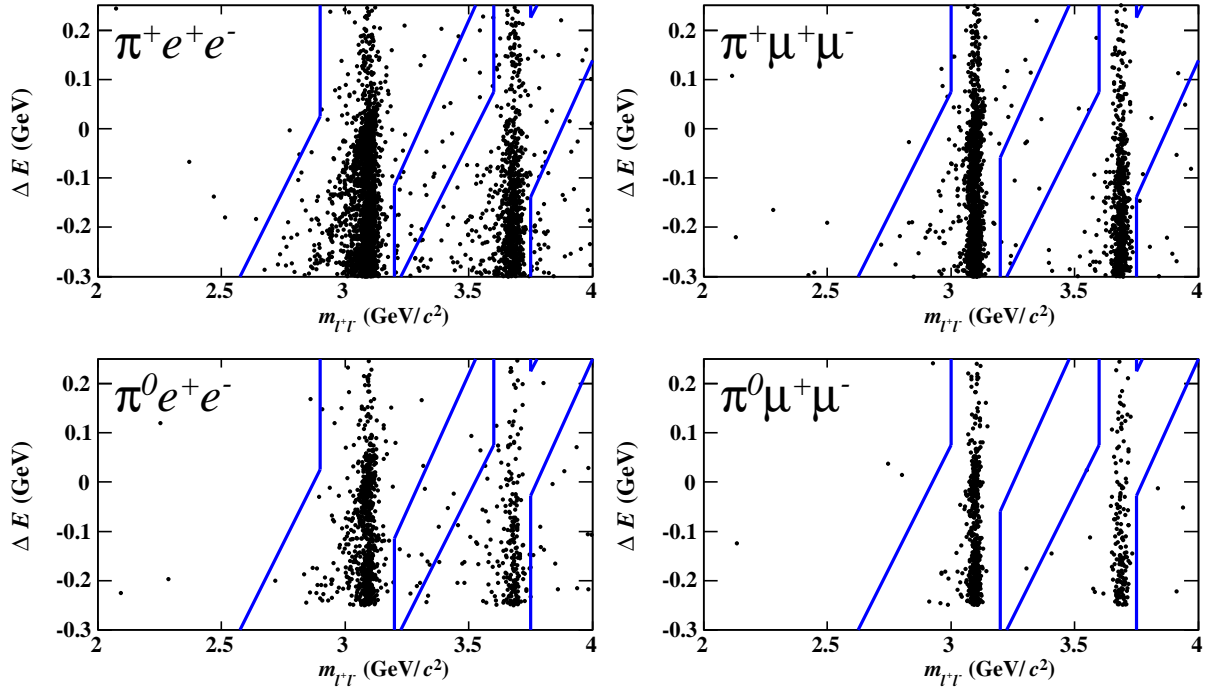


Figure 4.8: Veto regions in the plane spanned by $m_{\ell^+\ell^-}$ and ΔE are indicated by lines for each of the four reconstruction modes. The dots corresponds to simulated inclusive $B \rightarrow J/\psi X$ and $B \rightarrow \psi(2S)X$ events (X signifies any addition particles).

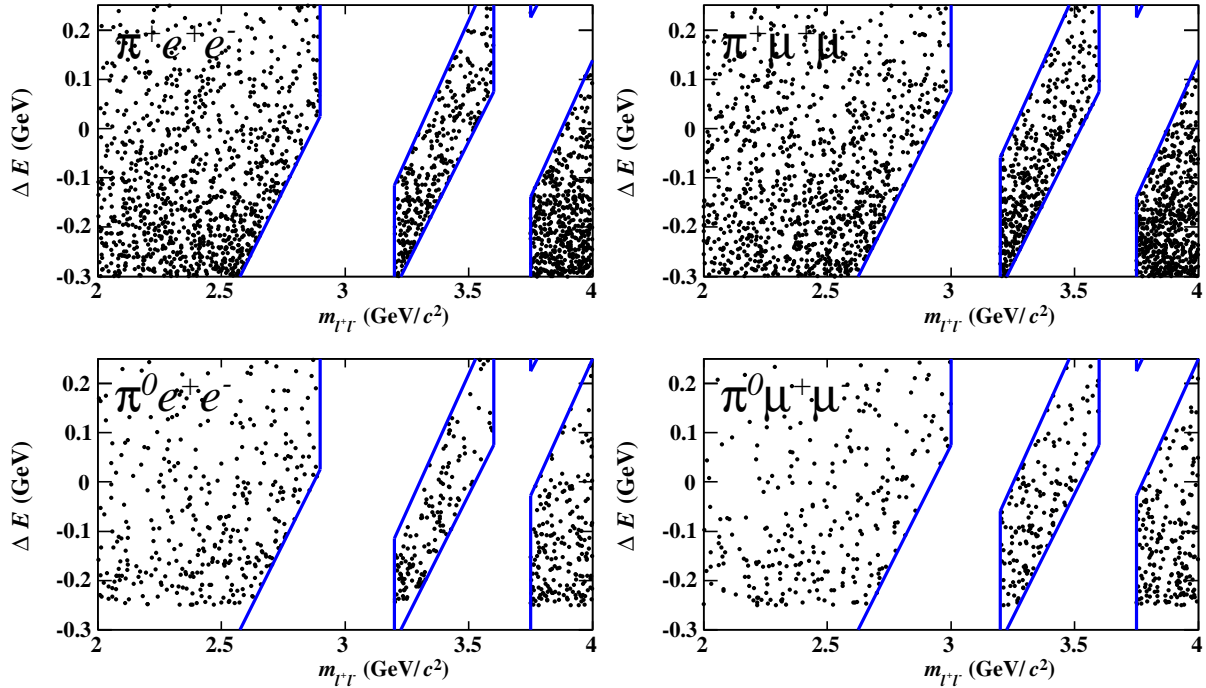


Figure 4.9: Veto regions in the plane spanned by $m_{\ell^+\ell^-}$ and ΔE are indicated by lines for each of the four reconstruction modes. The dots corresponds to simulated generic $B\bar{B}$ events and here events in the charmonium veto region have been removed.

Process	$\mathcal{B}(B \rightarrow Dh) \times$ $\mathcal{B}(D \rightarrow hh)$	Effective $\mathcal{B}(B \rightarrow hhh)$	events expected (Run1-4)
$B^- \rightarrow D^0 \pi^-$	$(4.91 \pm 0.21) \times 10^{-3} \times$		
$D^0 \rightarrow \pi^- \pi^+$	$(1.38 \pm 0.05) \times 10^{-3}$	$(6.78 \pm 0.38) \times 10^{-6}$	1560 ± 87
$D^0 \rightarrow K^- \pi^+$	$(3.81 \pm 0.09) \times 10^{-2}$	$(1.87 \pm 0.09) \times 10^{-4}$	43055 ± 2072
$B^- \rightarrow D^0 K^-$	$(3.7 \pm 0.6) \times 10^{-4} \times$		
$D^0 \rightarrow \pi^- \pi^+$	$(1.38 \pm 0.05) \times 10^{-3}$	$(5.11 \pm 0.85) \times 10^{-7}$	117 ± 19
$D^0 \rightarrow K^- \pi^+$	$(3.81 \pm 0.09) \times 10^{-2}$	$(1.41 \pm 0.23) \times 10^{-5}$	3245 ± 529
$B^0 \rightarrow D^0 \pi^0$	$(2.91 \pm 0.28) \times 10^{-4} \times$		
$D^0 \rightarrow \pi^- \pi^+$	$(1.38 \pm 0.05) \times 10^{-3}$	$(4.016 \pm 0.41) \times 10^{-7}$	92 ± 9
$D^0 \rightarrow K^- \pi^+$	$(3.81 \pm 0.09) \times 10^{-2}$	$(1.11 \pm 0.11) \times 10^{-5}$	2552 ± 280
$B^0 \rightarrow D^- \pi^+$	$(2.87 \pm 0.19) \times 10^{-3} \times$		
$D^- \rightarrow \pi^- \pi^0$	$(1.33 \pm 0.22) \times 10^{-3}$	$(3.82 \pm) \times 10^{-6}$	878 ± 156
$D^- \rightarrow K^- \pi^0$	$< 4.2 \times 10^{-4}$	$< 1.2 \times 10^{-6}$	< 276
$B^0 \rightarrow D^- K^+$	$(2.0 \pm 0.6) \times 10^{-4} \times$		
$D^- \rightarrow \pi^- \pi^0$	$(1.33 \pm 0.22) \times 10^{-3}$	$(2.66 \pm 0.91) \times 10^{-7}$	61 ± 21
$D^- \rightarrow K^- \pi^0$	$< 4.2 \times 10^{-4}$	$< 8.4 \times 10^{-8}$	< 19

Table 4.6: Estimate on how many hadronic events with D mesons are *produced* in the Run 1–4 data sample. Here $h = \pi$ or K . These modes are expected to peak in m_{ES} and ΔE and will be vetoed. Estimates are based on branching fraction expectations from [54].

- In the $B^+ \rightarrow \pi^+ e^+ e^-$ and $B^0 \rightarrow \pi^0 e^+ e^-$ modes, we do not veto D events, since the rate of hadrons passing the electron selection is very low.
- In the $B^+ \rightarrow \pi^+ \mu^+ \mu^-$ we veto events which have two opposite-charge tracks with an invariant mass within the range $1.84 \text{ MeV}/c^2 - 1.89 \text{ MeV}/c^2$. We consider the following particle combinations and mass hypotheses:

$\ell^+ \ell^-$ assuming $\pi^+ \pi^-$, $K^+ \pi^-$ (if $B^+ \rightarrow \pi^+ \ell^+ \ell^-$) or $\pi^+ K^-$ (if $B^- \rightarrow \pi^- \ell^+ \ell^-$), and
 $\pi^+ \ell^-$ assuming $\pi^+ \pi^-$ or $K^+ \pi^-$.

- In the mode $B^0 \rightarrow \pi^0 \mu^+ \mu^-$ (figure 4.10) we veto events where the invariant mass of the neutral pion and any of the leptons is in the range $1.79 \text{ MeV}/c^2 - 1.94 \text{ MeV}/c^2$ when assigning either m_{π^\pm} or m_{K^\pm} mass hypotheses to the lepton tracks:

$\pi^0 \ell^+$ assuming $\pi^0 \pi^+$ or $\pi^0 K^+$
 $\pi^0 \ell^-$ assuming $\pi^0 \pi^-$ or $\pi^0 K^-$

If an event falls into any of these categories, it is removed by the D veto.

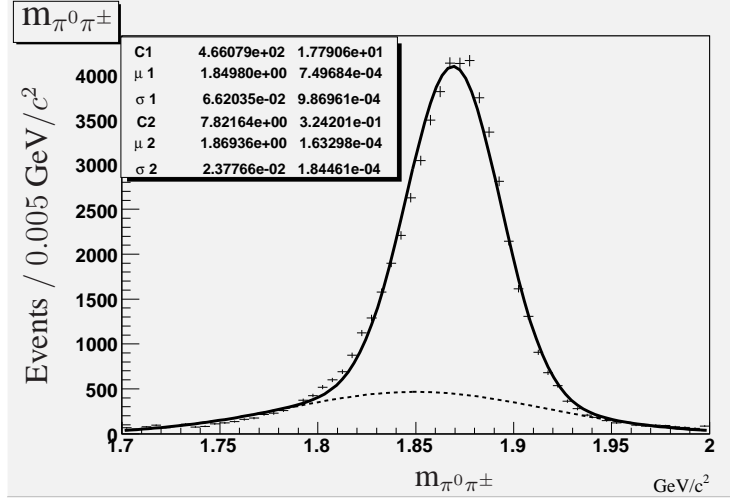


Figure 4.10: $\pi^0\pi^\pm$ invariant mass for simulated $B^0 \rightarrow D^+(\pi^0\pi^+)\pi^-$ events reconstructed as $B^0 \rightarrow \pi^0\ell^+\ell^-$ with a pion misidentified as a lepton. A sum of two Gaussian PDFs has been fitted to the distribution.

4.2.6 Multiple candidate selection

If more than one B candidate remains after all the selection criteria have been applied, one is selected based on:

- For $B^+ \rightarrow \pi^+\ell^+\ell^-$: the candidate which has the π^\pm with most SVT hits
- For $B^0 \rightarrow \pi^0\ell^+\ell^-$: the first candidate which appears in the ntuple (effectively a random choice).

Table 4.7 lists the average number of B candidates selected in simulated signal events.

Mode	Candidates/event
$B \rightarrow \pi e^+ e^-$	1.13
$B^0 \rightarrow \pi^0 e^+ e^-$	1.35
$B \rightarrow \pi \mu^+ \mu^-$	1.15
$B^0 \rightarrow \pi^0 \mu^+ \mu^-$	1.59
$B \rightarrow \pi e \mu$	1.06
$B^0 \rightarrow \pi^0 e \mu$	1.04

Table 4.7: Mean number of signal candidates per event for signal Monte Carlo events passing all selection criteria except the multiple candidate selection.

4.3 Data control samples

Control samples in the data are used to verify that the simulated samples are correctly representing the data.

The vetoed peaking-background events constitute a useful set of independent control samples. In particular, the charmonium samples are high-statistics samples with the same kinematics as signal events in particular regions of q^2 . Control samples of $J/\psi \rightarrow \ell^+\ell^-$ events are the largest samples. These describe individual particle momenta over a large range, but is naturally limited to a narrow region of $q^2 = m_{\ell^+\ell^-}$. The smaller sample consisting of $\psi(2S) \rightarrow \ell^+\ell^-$ events is a control sample for a higher q^2 -region.

The J/ψ control samples are used to study the signal efficiency, signal shapes and to verify the analysis by measuring the $B \rightarrow J/\psi \pi$ branching fraction.

Hadronic peaking background are evaluated using a sample of $B \rightarrow \pi\mu h$ events, where one track is identified as a pion, one track is *loosely* identified as a muon, as described in section 2.4.2, and the third track is not identified as any particular hadron. The loose muon selection has a rather large fraction of mis-identified pions and kaons, and provide a suitable data sample for this study. All tracks are also required to fail the electron selection, and all tracks except the loose “muon” are required to fail the muon selection. This selects a sample of predominantly hadronic events consisting of $B \rightarrow \pi\pi\pi$ and $B \rightarrow K\pi\pi$.

Background control samples are used to cross-check the background estimates based on continuum and $B\bar{B}$ simulated samples. The final background estimate is done using the *BABAR* data in the fit region, but the optimization is done with simulated samples.

4.3.1 Charmonium control samples

A J/ψ control sample is constructed by selecting events which belong kinematically to the signal region, and which satisfy all of the other requirements, except that they are required to *fail* the J/ψ veto. Three different selections of J/ψ samples have been used for different purposes.

The $B \rightarrow J/\psi \pi$ control sample

This sample is the one with events most similar to $B \rightarrow \pi\ell^+\ell^-$ signal events. Like for the $B^+ \rightarrow \pi^+\ell^+\ell^-$ selection, the selection of $B^+ \rightarrow J/\psi\pi^+$ will contain a non-negligible background component from the more abundant $B^+ \rightarrow J/\psi K^+$ events where the kaon fails rejection by the pion selection. Also other background sources have been studied. For low values of ΔE there are contributions from $B \rightarrow J/\psi \rho$ and $B \rightarrow J/\psi K^*$ as well.

Using this sample we compare various distributions of data and Monte Carlo simulated events to check that the level of agreement is acceptable. Figures 4.11-4.17 show the distributions of $m_{\ell^+\ell^-}$, m_{ES} , ΔE , π and ℓ momenta as well as the outputs of the Fisher discriminant and the likelihood-ratio in the *BABAR* data and Monte Carlo simulations. Also the input quantities to the latter two discriminants were checked and were showing good agreement between data and Monte Carlo. The statistics of this sample is limited, so this is not a precision test. To achieve the best possible statistics in the simulation sample, a cocktail of $B \rightarrow J/\psi \pi$, $B \rightarrow J/\psi K$ and inclusive $B \rightarrow J/\psi X$ are used. In the plots, the Monte Carlo distributions are drawn with two sets of error bands: the total uncertainty (light gray) obtained from summing in quadrature the Monte Carlo statistical uncertainty and the branching fraction systematic uncertainty, and the Monte Carlo statistical uncertainty only (dark gray). All the distributions show that the data is well described by Monte Carlo simulations.

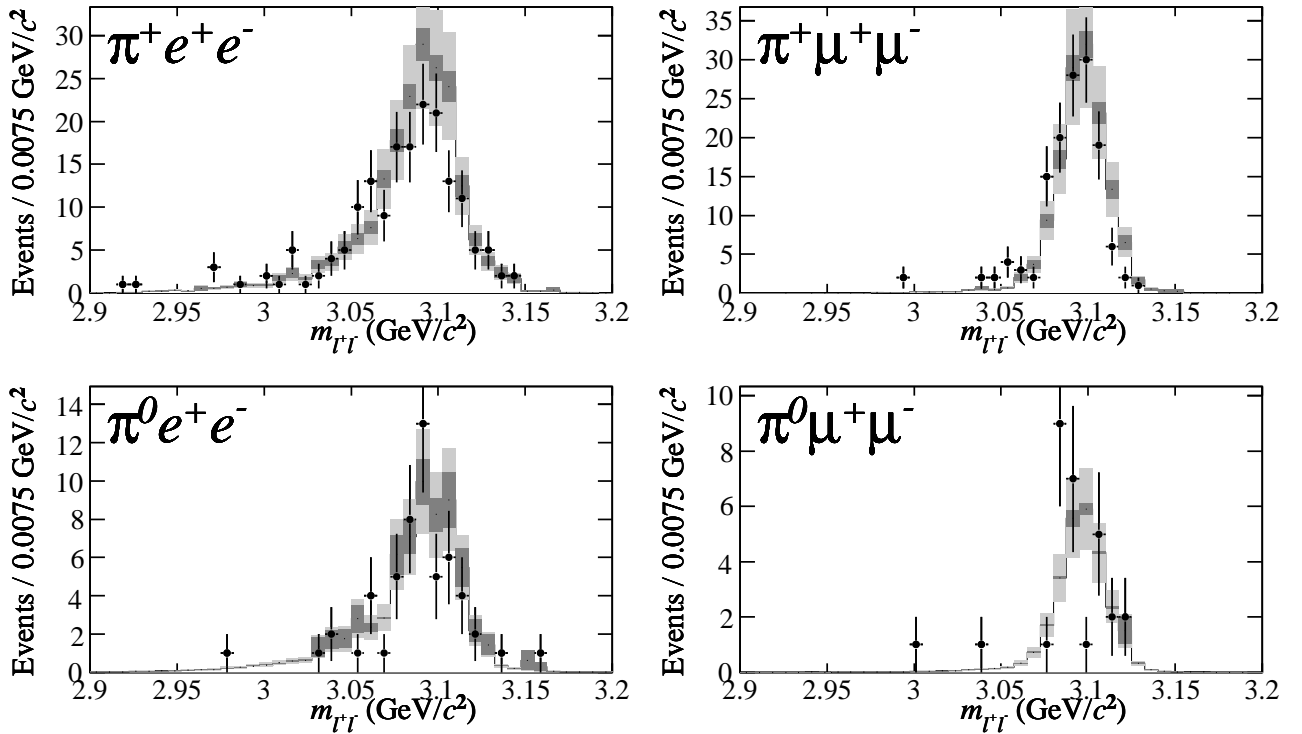


Figure 4.11: Distributions of the dilepton invariant mass in the $B \rightarrow J/\psi \pi$ control samples for the four B reconstruction modes. The points with error bars are on-resonance data events, and the gray histograms are simulated events, with statistical and systematic uncertainties shown in the dark and light gray bands, respectively.

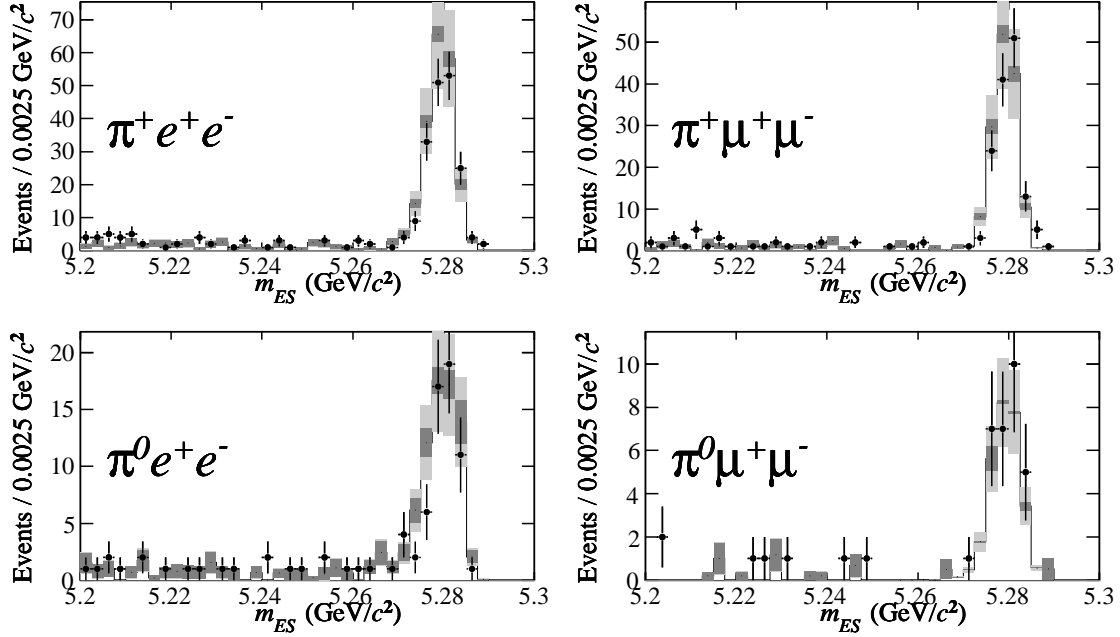


Figure 4.12: Distributions of m_{ES} in the $B \rightarrow J/\psi \pi$ control samples for the four B reconstruction modes. The points with error bars are on-resonance data events, and the gray histograms are simulated events, with statistical and systematic uncertainties shown in the dark and light gray bands, respectively.

The $B^\pm \rightarrow J/\psi K^\pm$ control sample

A larger sample is obtained by replacing the pion identification with kaon identification. $B^\pm \rightarrow J/\psi K^\pm$ events are more abundant than $B^\pm \rightarrow J/\psi \pi^\pm$. Due to the incorrect mass hypothesis (m_{π^\pm}) assigned to the K^\pm track, the reconstructed energy E_B is lower than expected for $B^\pm \rightarrow \pi^\pm \ell^+ \ell^-$ decays, thus ΔE is shifted by about -70 MeV.

This sample gives a high-statistics comparison of the signal shapes. Figure 4.18 shows comparisons of data and Monte Carlo events using distributions of m_{ES} , ΔE , the Fisher discriminant and the likelihood ratio. The level of agreement is found to be satisfactory.

The “ $K\ell^+\ell^-$ ” $B^\pm \rightarrow J/\psi K^\pm$ control sample

The sample of $B^\pm \rightarrow J/\psi K^\pm$ events can be improved by reconstructing the events as $B \rightarrow K\ell^+\ell^-$, thereby obtaining a ΔE distribution which is centered at zero and has a reduced width. For this, we use the event selection developed for the $B \rightarrow K\ell^+\ell^-$ analysis [26], and also here with the J/ψ vetoes reversed. The purity of this sample is very high. Figure 4.19 shows the m_{ES}

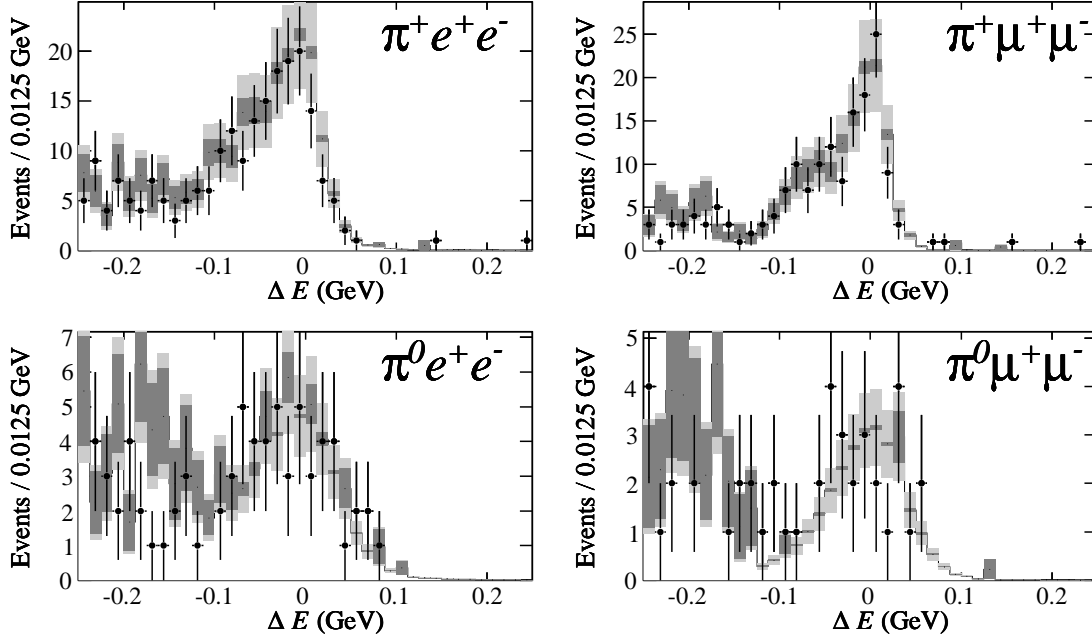


Figure 4.13: Distributions of ΔE in the $B \rightarrow J/\psi\pi$ control samples for the four B reconstruction modes. The points with error bars are on-resonance data events, and the gray histograms are simulated events, with statistical and systematic uncertainties shown in the dark and light gray bands, respectively.

fit on the full on-resonance data sample.

This control sample is used for studying the efficiencies of the lepton identification, the Fisher discriminant criteria and the likelihood-ratio criteria in $BABAR$ data and Monte Carlo simulations. The results of this study is described in section 4.4.

The $B^\pm \rightarrow \psi(2S)K^\pm$ control sample

Events that are removed by the $\psi(2S)$ vetoes also constitute a control sample which checks the signal efficiencies at somewhat higher q^2 than what events with J/ψ do. The branching fraction of $B \rightarrow \psi(2S)\pi$ is expected to be small [118], and with the combined branching fraction of $\psi(2S) \rightarrow (e^+e^-)$ or $(\mu^+\mu^-)$ being only $(14.65 \pm 1.05) \times 10^{-3}$ [54], these events are not useful as a control sample.

Instead we select $B^\pm \rightarrow \psi(2S)(\rightarrow \ell^+\ell^-)K^\pm$ events by applying kaon identification to the hadron track and reverting the $\psi(2S)$ veto. Figure 4.20 shows the distributions of m_{ES} and ΔE in this data sample compared to Monte Carlo simulated events.

Mode	Yield	Eff. (%)	$\mathcal{B}/10^{-6}$	PDG $\mathcal{B}/10^{-6}$
$B^+ \rightarrow \pi^+ e^+ e^-$	108 ± 14	18.2	44 ± 6	48 ± 6
$B^+ \rightarrow \pi^+ \mu^+ \mu^-$	89 ± 11	12.2	54 ± 7	48 ± 6
$B^+ \rightarrow \pi^+ \ell^+ \ell^-$			48 ± 4	48 ± 6
$B^0 \rightarrow \pi^0 e^+ e^-$	54 ± 9	16.0	25 ± 4	22 ± 4
$B^0 \rightarrow \pi^0 \mu^+ \mu^-$	28 ± 6	8.7	24 ± 5	22 ± 4
$B^0 \rightarrow \pi^0 \ell^+ \ell^-$			24 ± 3	22 ± 4

Table 4.8: $B \rightarrow J/\psi \pi$ yields and branching fractions from the fits of *BABAR* data. Combined branching fractions are computed from the least-squares weighted average; all uncertainties are statistical only.

$B \rightarrow J/\psi \pi$ branching fraction measurement

Using the $B \rightarrow J/\psi \pi$ control sample, we measure the branching fractions $\mathcal{B}(B \rightarrow J/\psi \pi)$ as a crosscheck for the $B \rightarrow \pi \ell^+ \ell^-$ analysis. The branching fractions are computed from yields extracted by a two-dimensional extended unbinned maximum likelihood to events in the fit region for four final states.

The signal shape is parameterized in both m_{ES} and ΔE by a Gaussian function plus a radiative tail described by an exponential power function, as described in section 3.3.

In the charged modes, a signal-like component for $B^+ \rightarrow J/\psi K^+$ is included, with the mean of ΔE offset by about -70 MeV. The shape parameter for this peaking background component has been fixed to values obtained from the $B^+ \rightarrow J/\psi K^+$ control sample.

The combinatorial background shape is parameterized by an Argus threshold function [112] in m_{ES} , as described in section 3.3.

Figure 4.21 shows projections of the data and best-fit probability density function for the reconstruction mode $B^+ \rightarrow J/\psi \pi^+$ with $J/\psi \rightarrow e^+ e^-$. The background from $B^+ \rightarrow J/\psi K^+$ events is clearly visible in figure 4.21b, and a dashed line indicates the fit component for these events. Figure 4.22 shows projections from a similar fit to the events selected as $B^0 \rightarrow J/\psi \pi^0$, with $J/\psi \rightarrow \mu^+ \mu^-$.

Table 4.8 summarizes the $B \rightarrow J/\psi \pi$ signal yields obtained from these fits, the signal efficiencies obtained from studying simulated $B \rightarrow J/\psi \pi$ signal events and the corresponding branching fractions in the *BABAR* data. The measured branching fractions are consistent with the world average [54] for these decays.

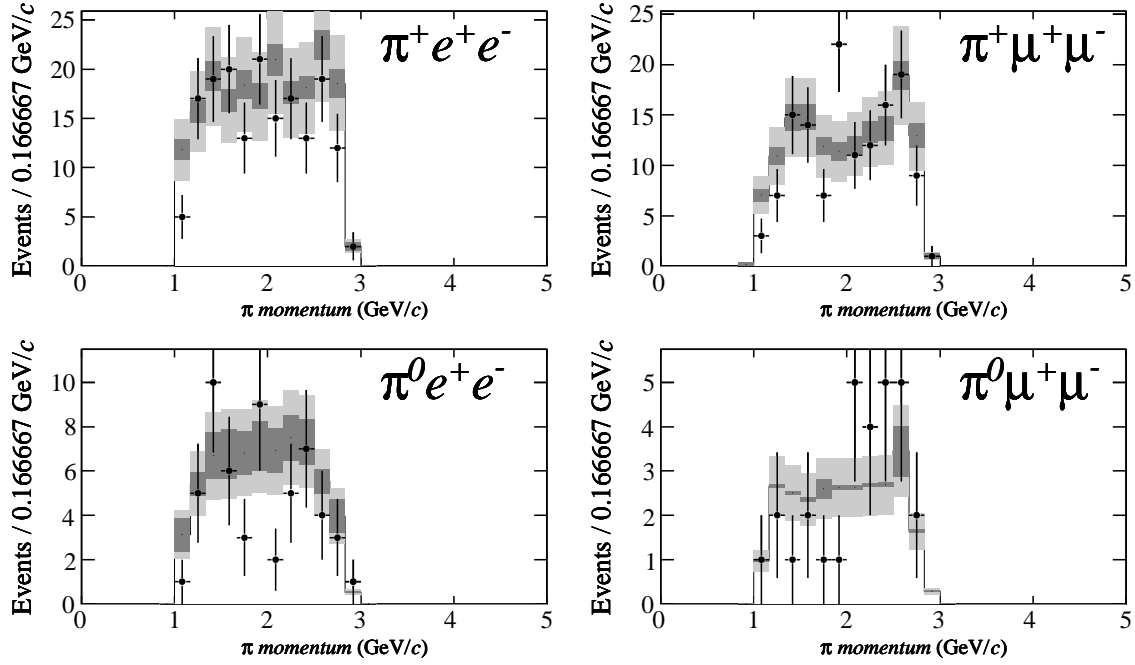


Figure 4.14: Distributions of the pion momenta in the $B \rightarrow J/\psi \pi$ control samples for the four B reconstruction modes. The points with error bars are on-resonance data events, and the gray histograms are simulated events, with statistical and systematic uncertainties shown in the dark and light gray bands, respectively.

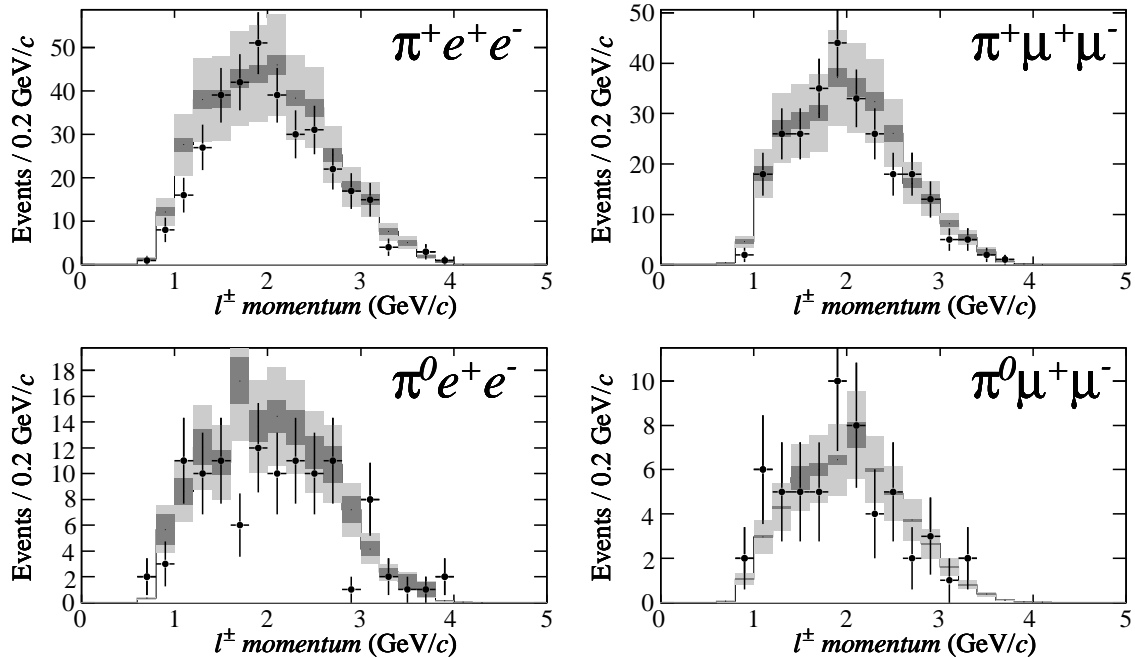


Figure 4.15: Distributions of the lepton momenta in the $B \rightarrow J/\psi \pi$ control samples for the four B reconstruction modes. The points with error bars are on-resonance data events, and the gray histograms are simulated events, with statistical and systematic uncertainties shown in the dark and light gray bands, respectively.

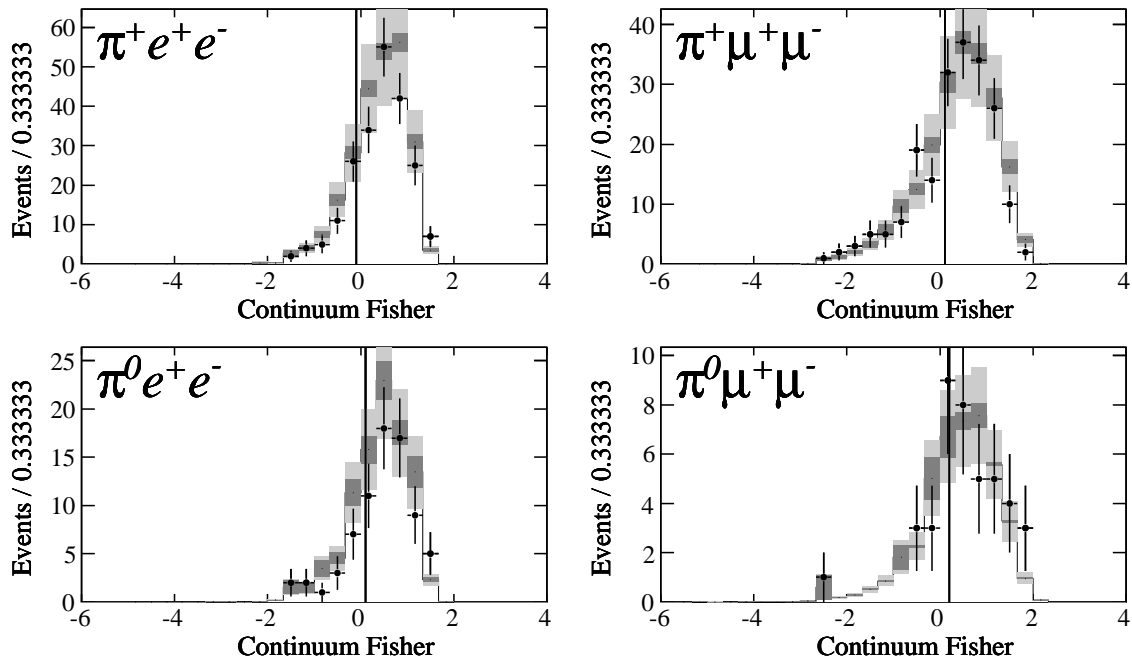


Figure 4.16: Distributions of the Fisher discriminant in the $B \rightarrow J/\psi\pi$ control samples for the four B reconstruction modes. The vertical line indicates the optimal Fisher selection (keeping events to the right of the line), although this selection has not been used in making this plot. The points with error bars are on-resonance data events, and the gray histograms are simulated events, with statistical and systematic uncertainties shown in the dark and light gray bands, respectively.

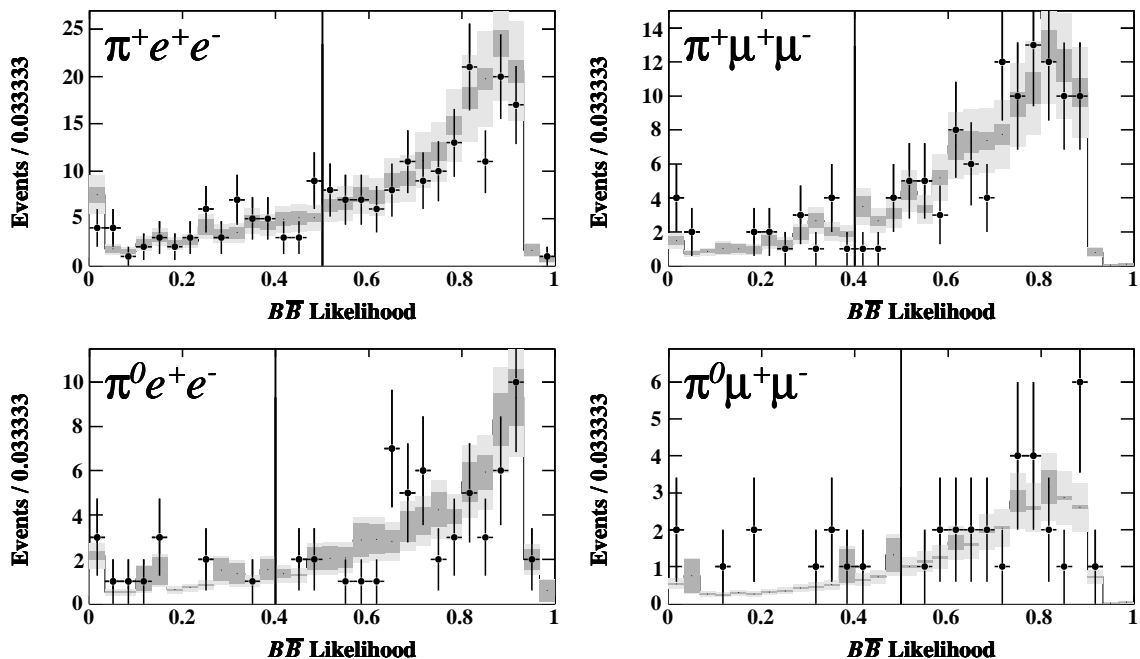


Figure 4.17: Distributions of the likelihood ratio in the $B \rightarrow J/\psi\pi$ control samples for the four B reconstruction modes. The vertical line indicates the optimal likelihood-ratio selection (keeping events to the right of the line), although this selection has not been used in making this plot. The points with error bars are on-resonance data events, and the gray histograms are simulated events, with statistical and systematic uncertainties shown in the dark and light gray bands, respectively.

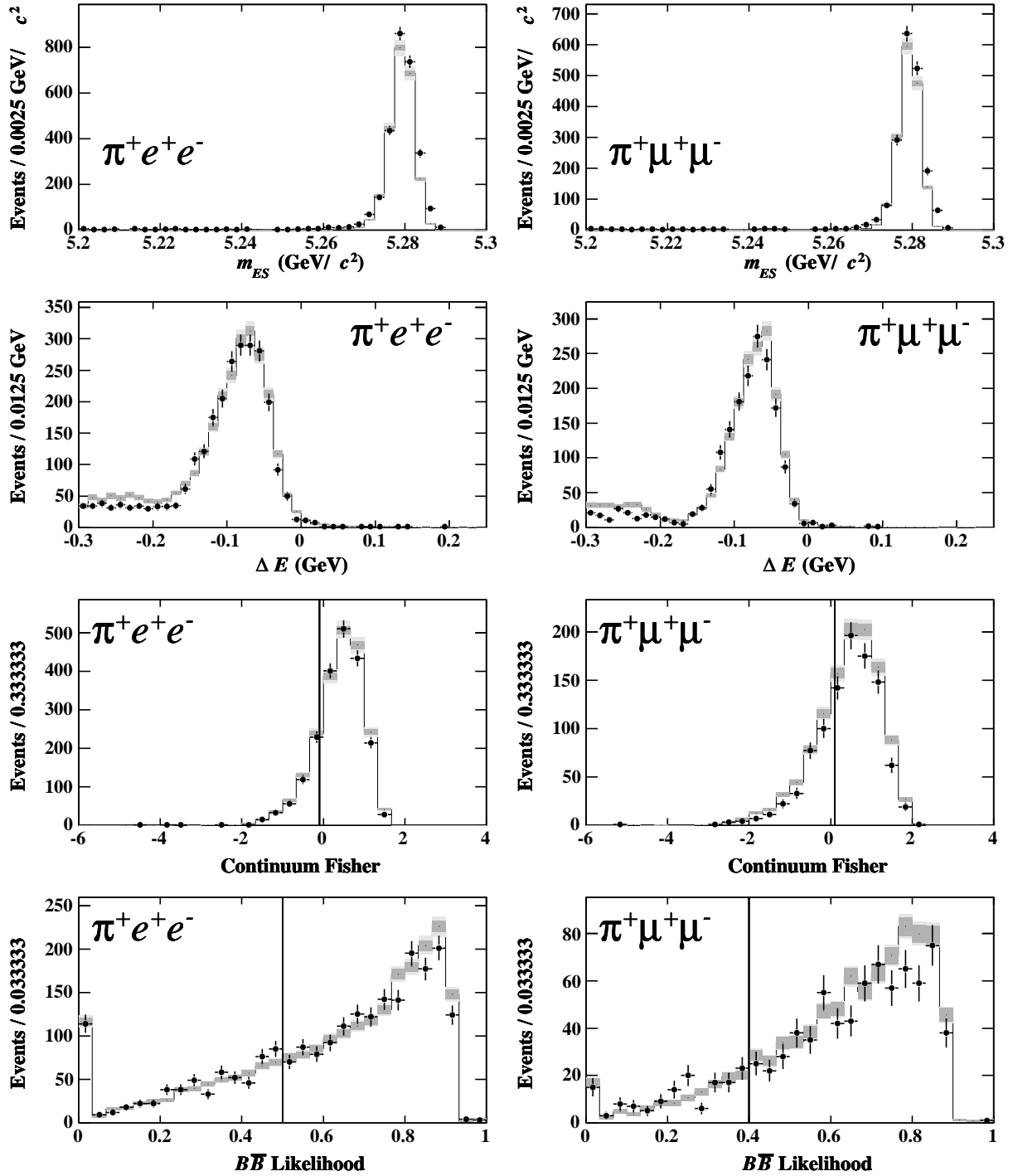


Figure 4.18: Distributions of m_{ES} , ΔE , Fisher discriminant and likelihood ratio in the $B \rightarrow J/\psi K$ control samples for *BABAR* data (points) and Monte Carlo (histograms) for the charged- B reconstruction modes. The lines in the third- and fourth-row plots indicate the optimal Fisher and likelihood ratio selections, respectively (events to the right of the line are selected).

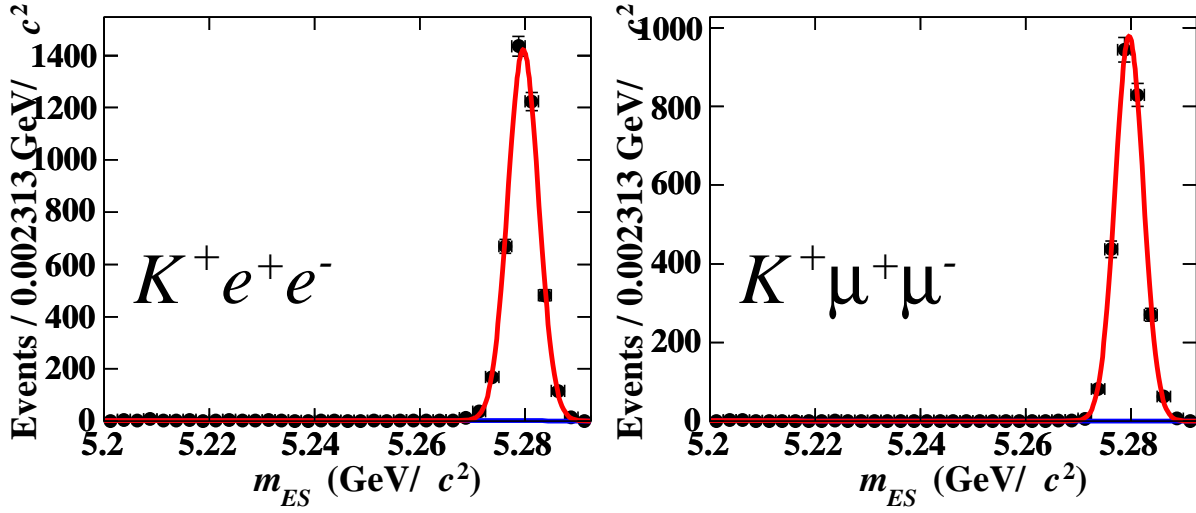


Figure 4.19: Fit to the m_{ES} distributions in on-resonance data, for the $B \rightarrow J/\psi K$ control samples. These fits are used to extract the yields and efficiencies of the $B \rightarrow J/\psi K$ control sample for the lepton ID efficiency study.

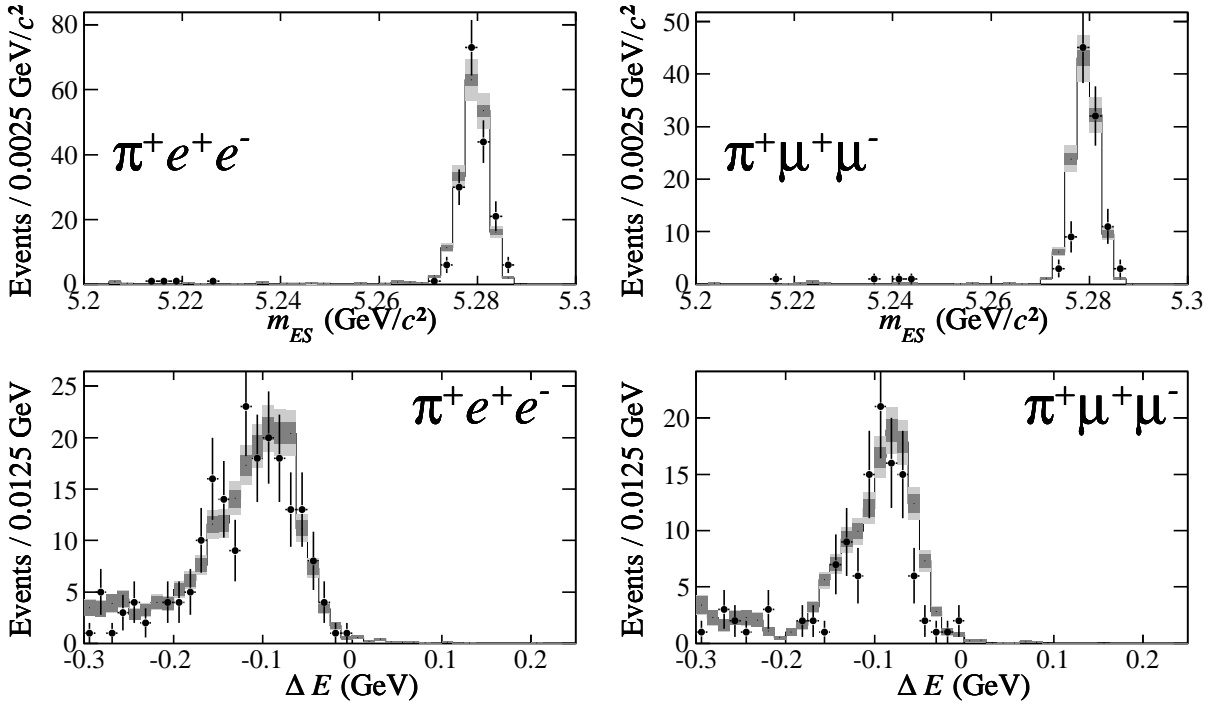


Figure 4.20: m_{ES} and ΔE distributions in the $B \rightarrow \psi(2S) K$ control samples for the charged- B reconstruction modes. The points with error bars are on-resonance data events, and the gray histograms are simulated events, with statistical and systematic uncertainties shown in the dark and light gray bands, respectively.

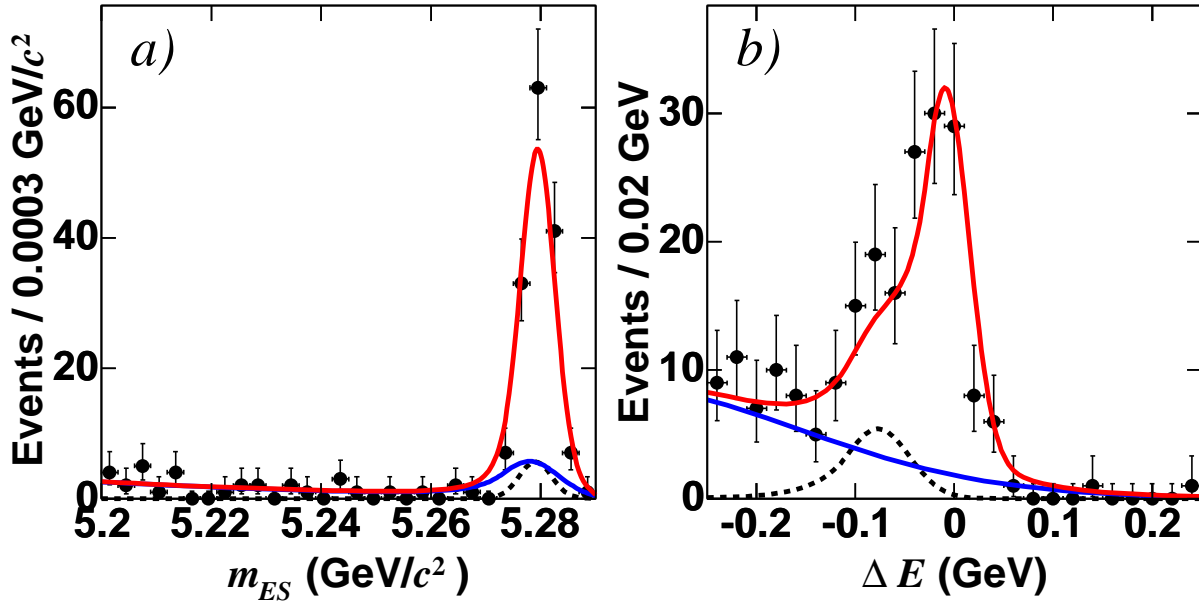


Figure 4.21: Projections of (a) m_{ES} and (b) ΔE from a two-dimensional fit to *BABAR* data for $B \rightarrow J/\psi \pi$ in the mode $B^+ \rightarrow \pi^+ e^+ e^-$. The dashed line is the $B \rightarrow J/\psi K$ component, the blue line is the sum of the this and the combinatorial components, and the red line is the sum of all components.

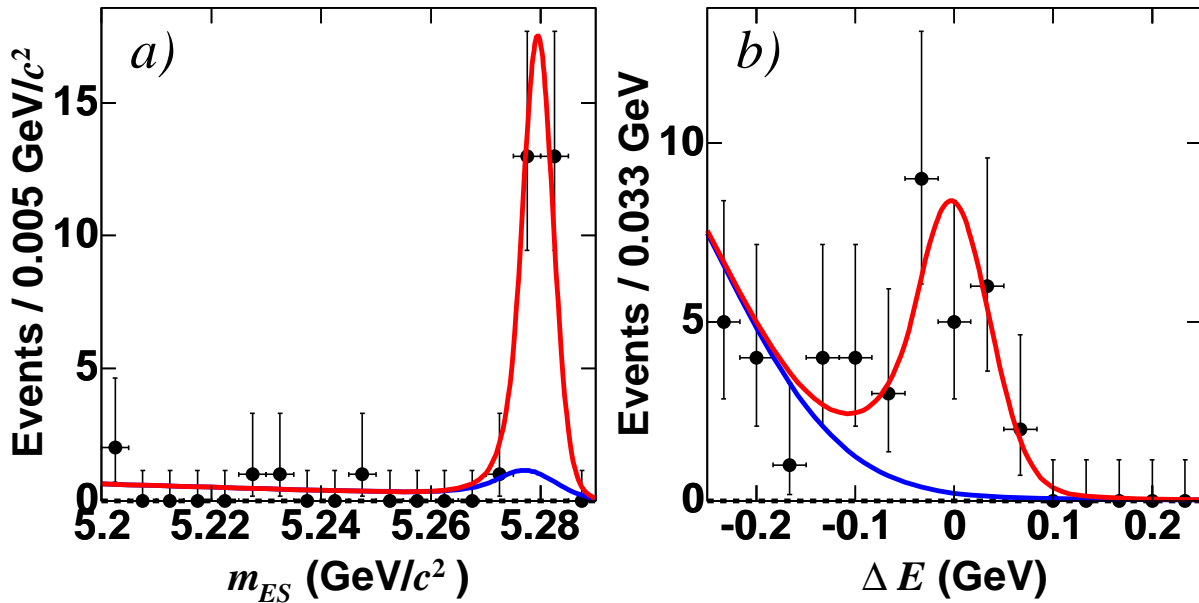


Figure 4.22: Projections of (a) m_{ES} and (b) ΔE from a two-dimensional fit to *BABAR* data for $B \rightarrow J/\psi \pi$ in the mode $B^0 \rightarrow \pi^0 \mu^+ \mu^-$. The blue line is the sum of the feed-down and combinatorial components, and the red line is the sum of all components.

4.3.2 Grand-sideband control sample

In order to understand our combinatorial background sources, *BABAR* data in the grand sideband region are compared with the sum of predicted yields in Monte Carlo-generated generic $\overline{B^0B^0}$, B^+B^- , uds and $c\bar{c}$ samples; each subsample in this sum is scaled independently to the corresponding on-resonance data luminosity. Figures 4.23a-4.30a show the distribution of kinematical variables in on-resonance data and the combined generic $B\overline{B}$ and continuum Monte Carlo sample. The continuum fraction of the total is shown in a gray histogram.

Simulations compare well with data for the $B \rightarrow \pi\mu^+\mu^-$ channels, but for the $B \rightarrow \pi e^+e^-$ channels there are substantially more events in the data than in the Monte Carlo samples. The events causing the discrepancy tend to have low pion momentum (figure 4.28a) and large lepton-lepton opening angle (figure 4.30a). We believe this discrepancy results from two-photon processes which are not modeled in the *BABAR* Monte Carlo. Two-photon interactions occur when an electron and a positron at high energies and in close proximity emit a pair of virtual photons which interact electromagnetically to produce a pair of fermions, *i.e.* $(e^+e^-) \rightarrow (e^+e^-)\gamma\gamma \rightarrow (e^+e^-)(ff)$, where the fermions, f , can be either leptons or quarks turning into hadrons. Usually, the original electron and positron retain their momenta and high energies and escape detection, while the two fermions have low momenta and balanced transverse momenta. If the virtual photons are hard enough, one or both of the e^+ and e^- can scatter into the detector, along with the fermions, and these are most likely the events seen as an excess of events in the data. No such excess of events is seen in the $\mu^+\mu^-$ channels.

The belief that the discrepancy is due to two-photon events is further strengthened by the observation that these are non- $\mathcal{Y}(4S)$ events. When replacing the continuum-Monte Carlo sample with the off-resonance data sample, the overall normalization of the histograms agree. This is seen in figures 4.23b-4.30b, where on-resonance data are compared with the sum of $B\overline{B}$ -Monte Carlo and off-resonance samples. The contribution from off-resonance data is shown separately.

Since the discrepancy is more pronounced for the lower values of m_{ES} (figure 4.23a) and reasonably small in the fit region these events are not further studied or removed. In the end, the relative normalization of the combinatorial background will be floating in the fit, hence it is not essential to the signal extraction that the normalization is modeled precisely by the simulation. However, the generic Monte Carlo is used to determine selection criteria for the Fisher discriminant and likelihood-ratio. Therefore, for this purpose we scale the generic Monte Carlo samples to match the on-resonance data, with scale factors determined from comparison with sideband and off-resonance data.

The scaling factors are determined separately for $B\overline{B}$ and continuum Monte Carlo:

- $B\bar{B}$ -Monte Carlo scaling factors are determined from the ratio of on-resonance data yields to the sum of $B\bar{B}$ -Monte Carlo and off-resonance data yields in the *grand sideband region*.
- Continuum-Monte Carlo scaling factors are determined from the ratio of off-resonance data yields to the continuum-Monte Carlo yields in the *fit region plus the ΔE sidebands*. Here, ΔE sideband is defined as outside the fit region in ΔE but within the fit region in m_{ES} .

Table 4.9 summarizes the luminosity-scaled yields used to determine the scaling factors for generic Monte Carlo samples.

Mode	MC Yield	Data Yield	Data/MC
Continuum MC and off-resonance yields in the ΔE -sideband and fit region			
$B^+ \rightarrow \pi^+ e^+ e^-$	48 ± 6	136 ± 36	$(285 \pm 83)\%$
$B^0 \rightarrow \pi^0 e^+ e^-$	19 ± 3	58 ± 24	$(312 \pm 140)\%$
$B^+ \rightarrow \pi^+ \mu^+ \mu^-$	88 ± 7	87 ± 29	$(100 \pm 34)\%$
$B^0 \rightarrow \pi^0 \mu^+ \mu^-$	35 ± 5	39 ± 19	$(111 \pm 57)\%$
$B^+ \rightarrow \pi^+ e \mu$	225 ± 12	165 ± 40	$(73 \pm 18)\%$
$B^0 \rightarrow \pi^0 e \mu$	54 ± 6	58 ± 24	$(108 \pm 46)\%$
$B\bar{B}$ MC + off-resonance and on-resonance yields in the grand sideband region			
$B^+ \rightarrow \pi^+ e^+ e^-$	1402 ± 90	1296 ± 36	$(92 \pm 6)\%$
$B^0 \rightarrow \pi^0 e^+ e^-$	732 ± 62	729 ± 27	$(100 \pm 9)\%$
$B^+ \rightarrow \pi^+ \mu^+ \mu^-$	965 ± 54	862 ± 29	$(89 \pm 6)\%$
$B^0 \rightarrow \pi^0 \mu^+ \mu^-$	356 ± 38	322 ± 18	$(90 \pm 11)\%$
$B^+ \rightarrow \pi^+ e \mu$	2115 ± 79	1976 ± 44	$(93 \pm 4)\%$
$B^0 \rightarrow \pi^0 e \mu$	824 ± 46	819 ± 29	$(99 \pm 7)\%$

Table 4.9: Comparison of the sample yields to determine sideband data/MC scale factors for generic Monte Carlo simulated samples. The total yields have been scaled to 209 fb^{-1} .

As a cross-check, data/MC ratios were also obtained for different sub-regions of the m_{ES} - ΔE plane. The ratios were all in agreement within errors.

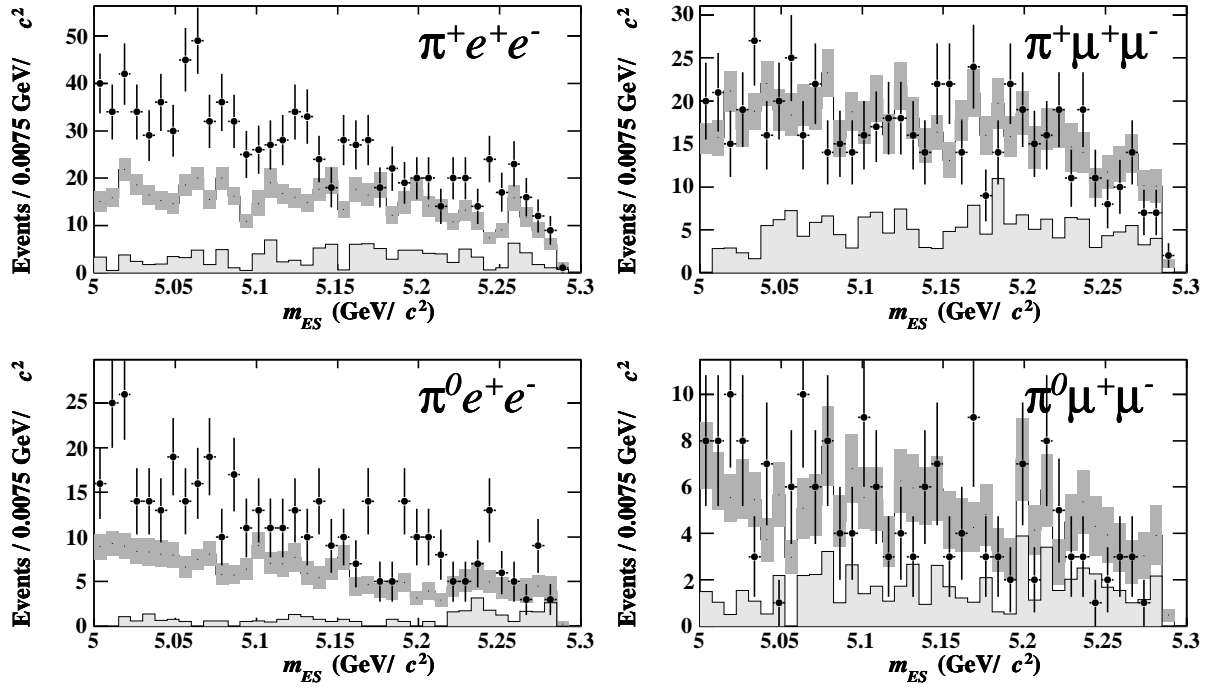


Figure 4.23a: Distributions in m_{ES} of events in the upper and lower sidebands of ΔE . On-resonance data (points) and generic ($B\bar{B} + u\bar{u}/d\bar{d}/s\bar{s}/c\bar{c}$) Monte Carlo (histograms). The light gray histograms show the contribution from $u\bar{u}/d\bar{d}/s\bar{s}/c\bar{c}$ events.

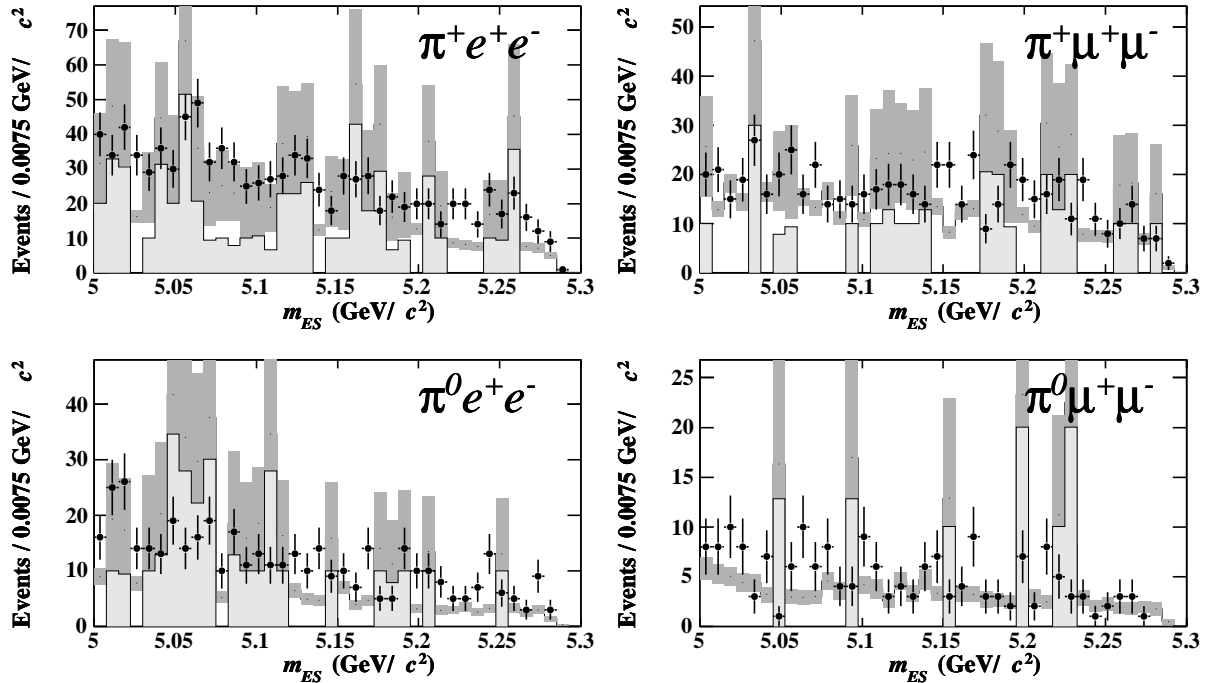


Figure 4.23b: Distributions in m_{ES} of events in the upper and lower sidebands of ΔE . On-resonance data (points) and the sum of generic $B\bar{B}$ Monte Carlo and off-resonance data (histograms). The light gray histograms show the contribution from off-resonance events.

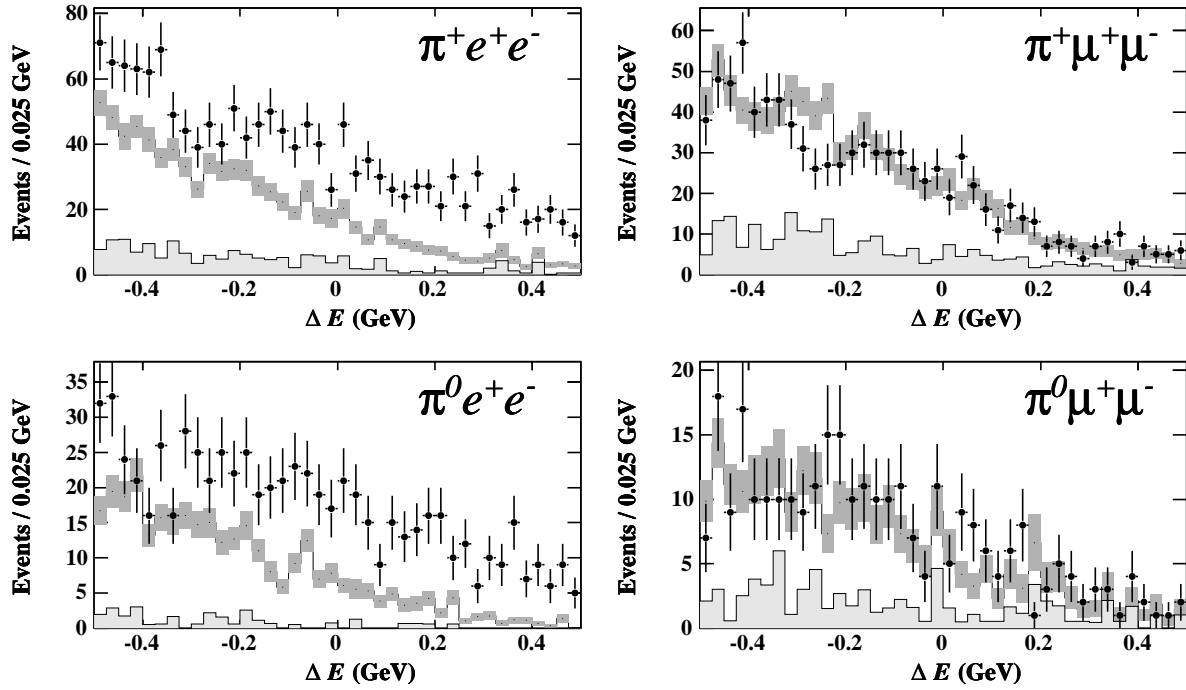


Figure 4.24a: Distributions in ΔE of events in the lower sideband of m_{ES} . On-resonance data (points) and generic ($B\bar{B} + u\bar{u}/d\bar{d}/s\bar{s}/c\bar{c}$) Monte Carlo (histograms). The light gray histograms show the contribution from $u\bar{u}/d\bar{d}/s\bar{s}/c\bar{c}$ events.

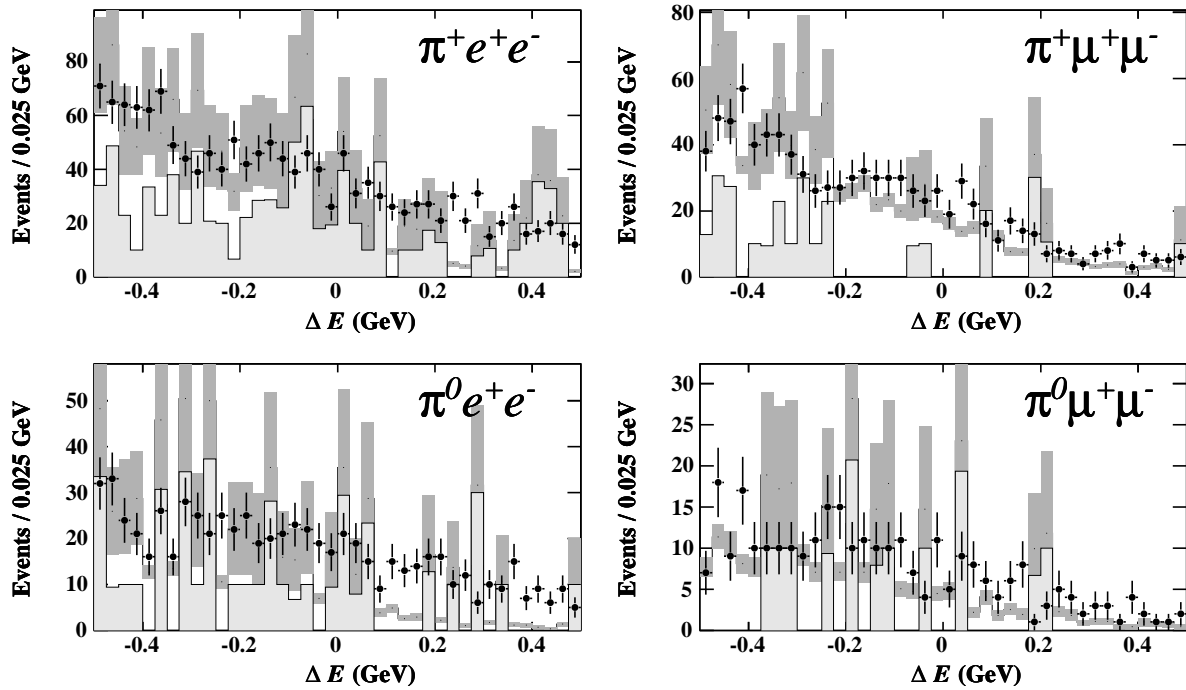


Figure 4.24b: Distributions in ΔE of events in the lower sideband of m_{ES} . On-resonance data (points) and the sum of generic $B\bar{B}$ Monte Carlo and off-resonance data (histograms). The light gray histograms show the contribution from off-resonance events.

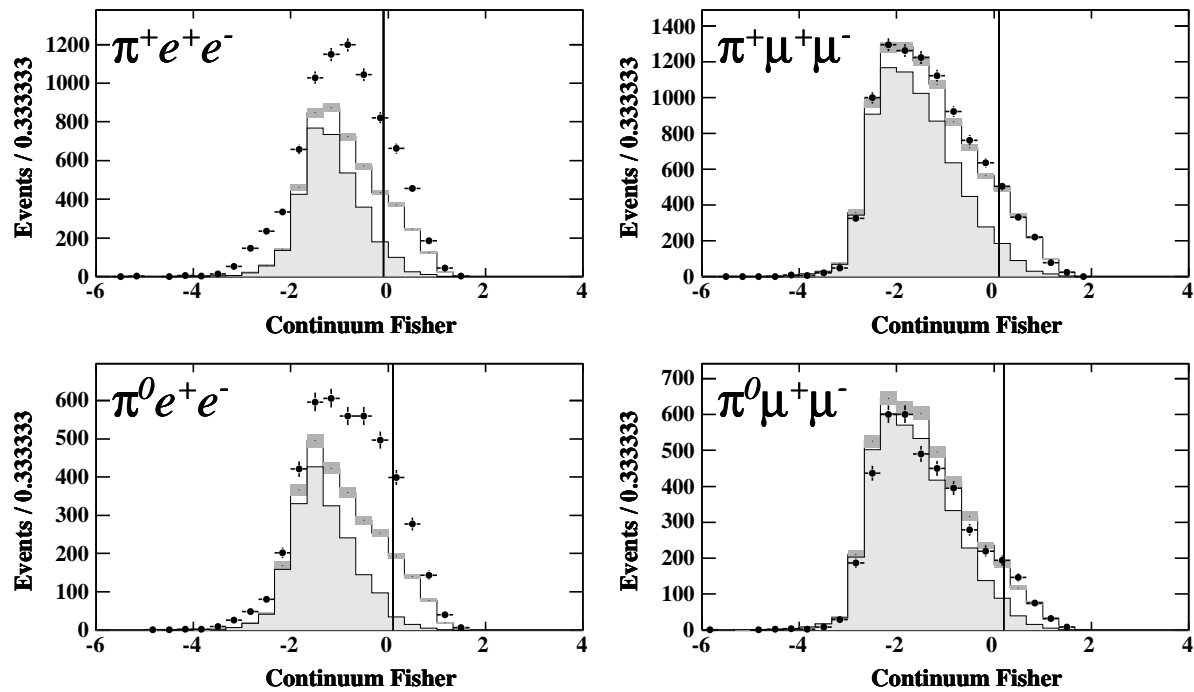


Figure 4.25a: Distributions in the Fisher discriminant of events in the grand sideband. On-resonance data (points) and generic ($B\bar{B} + u\bar{u}/d\bar{d}/s\bar{s}/c\bar{c}$) Monte Carlo (histograms). The light gray histograms show the contribution from $u\bar{u}/d\bar{d}/s\bar{s}/c\bar{c}$ events. The vertical line indicates the optimal lower value for making a selection in the Fisher discriminant.

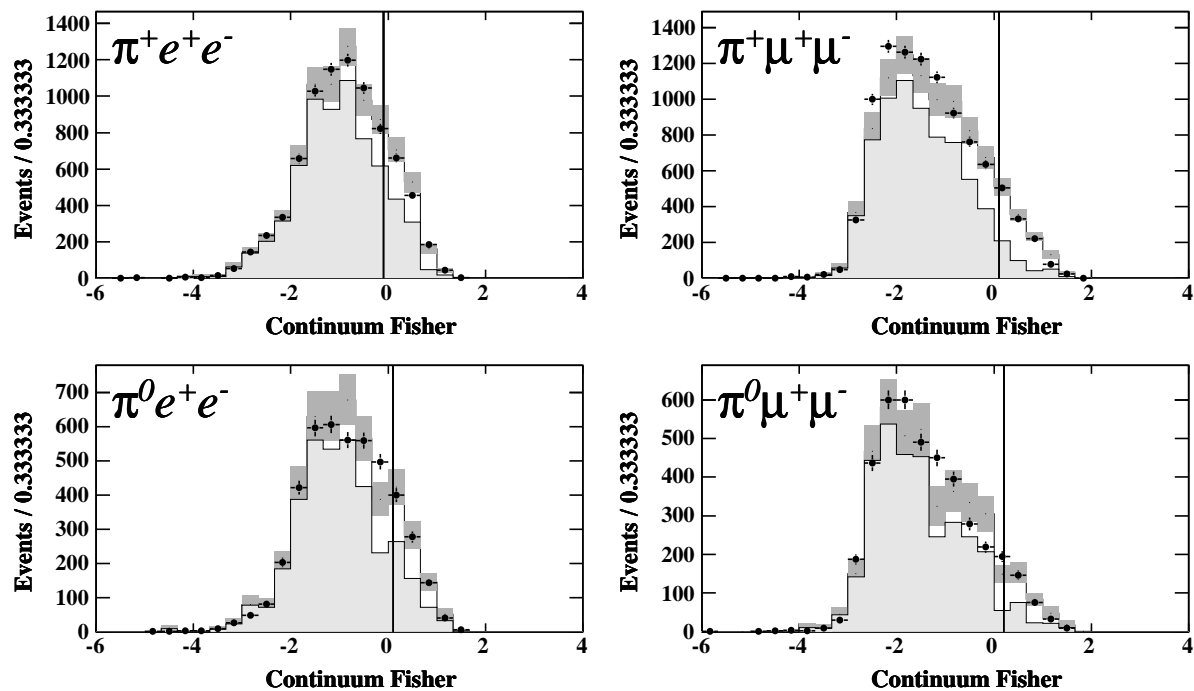


Figure 4.25b: Distributions in the Fisher discriminant of events in the grand sideband. On-resonance data (points) and the sum of generic $B\bar{B}$ Monte Carlo and off-resonance data (histograms). The light gray histograms show the contribution from off-resonance events. The vertical line indicates the optimal lower value for making a selection in the Fisher discriminant.

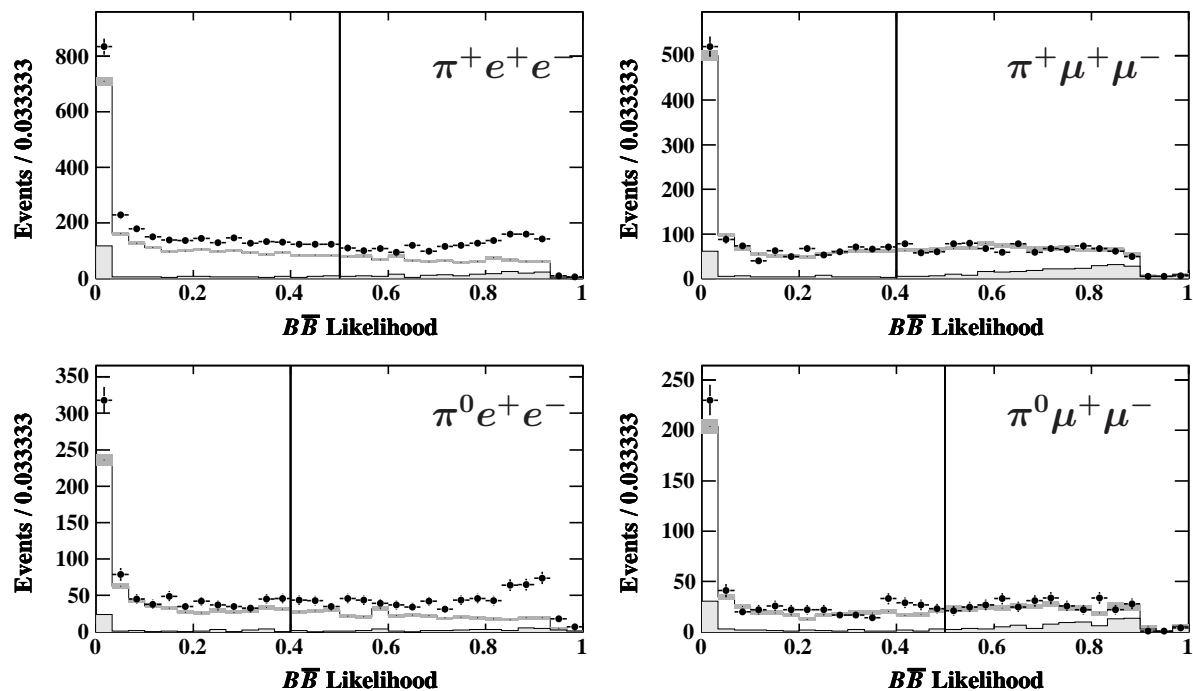


Figure 4.26a: Distributions in the likelihood ratio of events in the grand sideband. On-resonance data (points) and generic ($B\bar{B} + u\bar{u}/d\bar{d}/s\bar{s}/c\bar{c}$) Monte Carlo (histograms). The light gray histograms show the contribution from $u\bar{u}/d\bar{d}/s\bar{s}/c\bar{c}$ events. The vertical line indicates the optimal lower value for making a selection in the likelihood ratio.

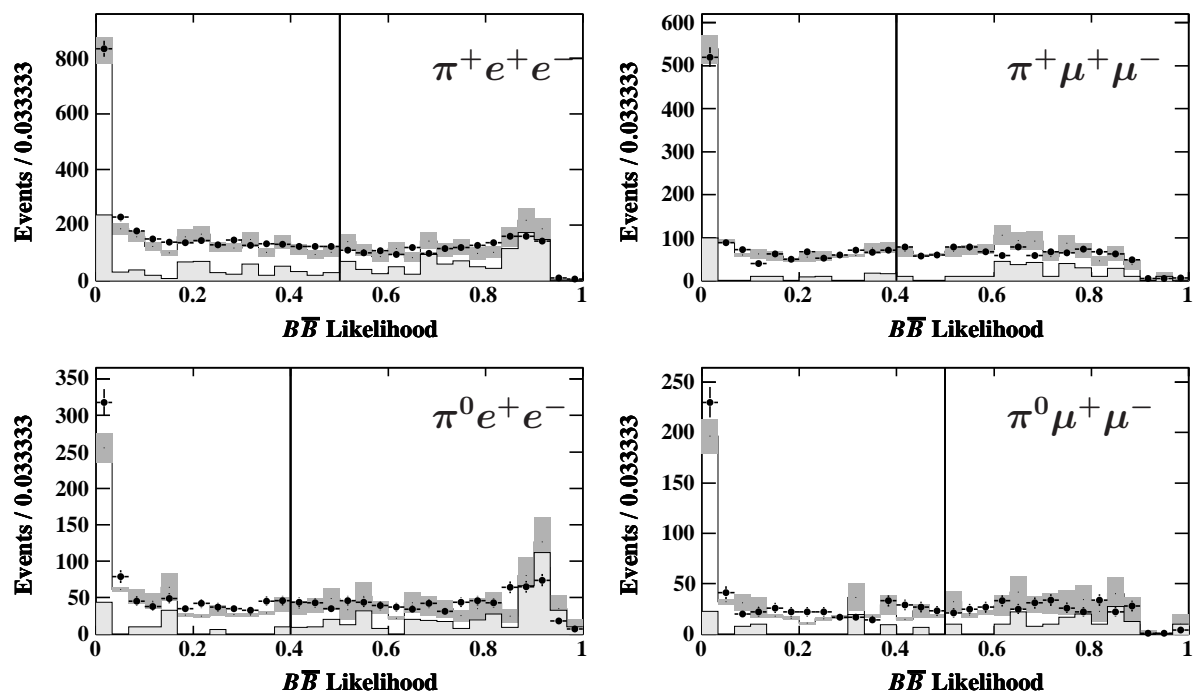


Figure 4.26b: Distributions in the likelihood ratio of events in the grand sideband. On-resonance data (points) and the sum of generic $B\bar{B}$ Monte Carlo and off-resonance data (histograms). The light gray histograms show the contribution from off-resonance events. The vertical line indicates the optimal lower value for making a selection in the likelihood ratio.

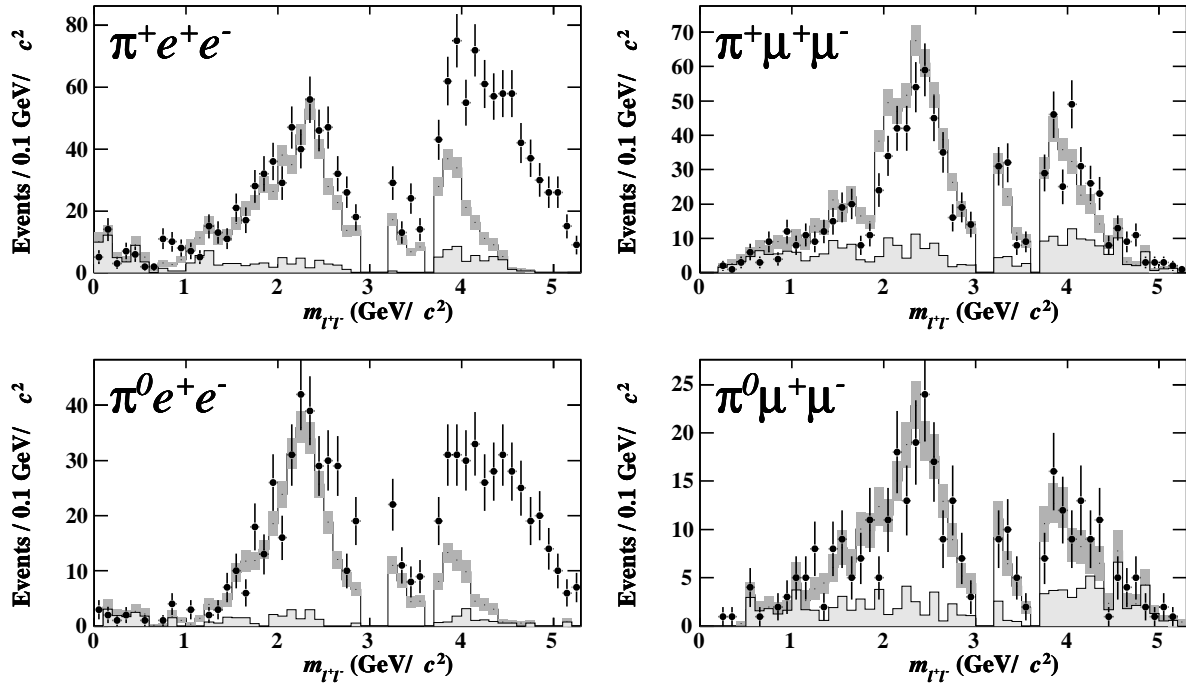


Figure 4.27a: Distributions in dilepton invariant mass, $m_{\ell^+\ell^-}$, of events in the grand sideband. On-resonance data (points) and generic $(B\bar{B} + u\bar{u}/d\bar{d}/s\bar{s}/c\bar{c})$ Monte Carlo (histograms). The light gray histograms show the contribution from $u\bar{u}/d\bar{d}/s\bar{s}/c\bar{c}$ events.

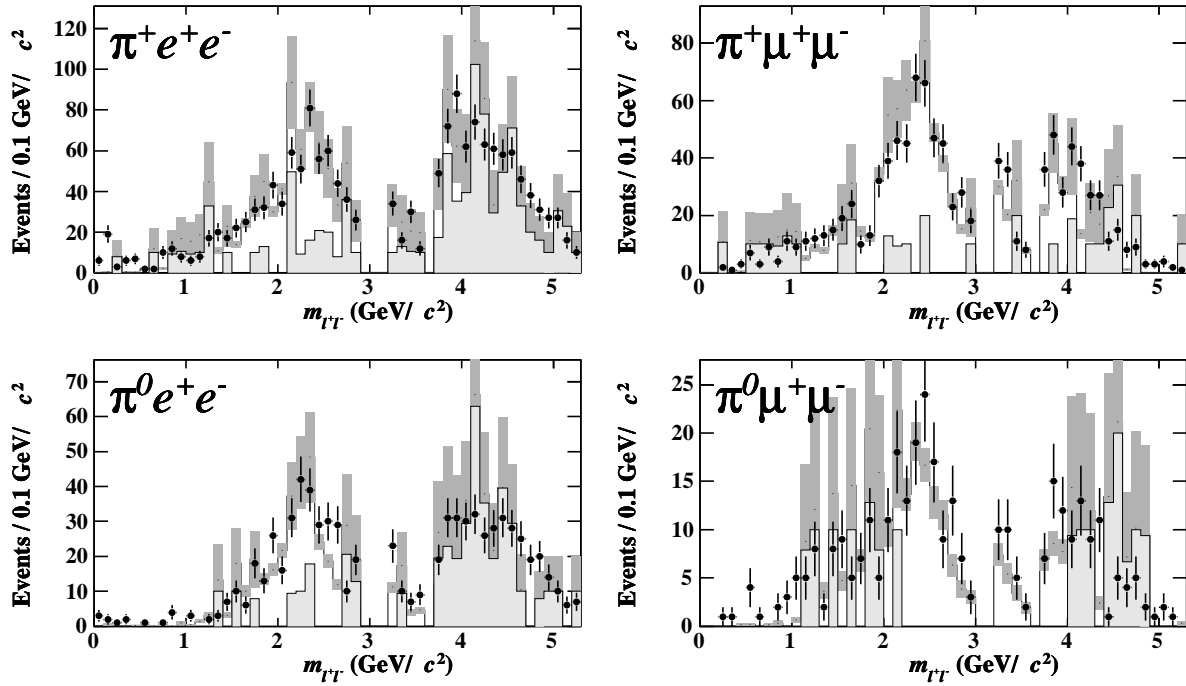


Figure 4.27b: Distributions in dilepton invariant mass, $m_{\ell^+\ell^-}$, of events in the grand sideband. On-resonance data (points) and the sum of generic $B\bar{B}$ Monte Carlo and off-resonance data (histograms). The light gray histograms show the contribution from off-resonance events.

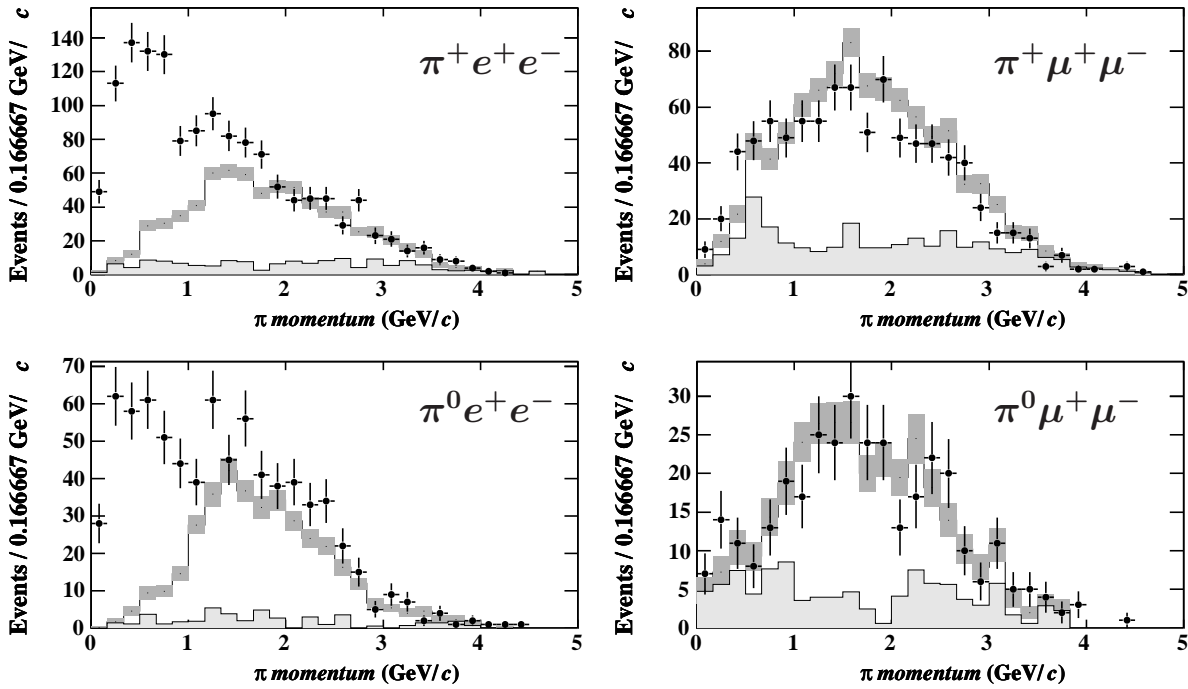


Figure 4.28a: Distributions in pion momentum, p_π , of events in the grand sideband. On-resonance data (points) and generic ($B\bar{B} + u\bar{u}/d\bar{d}/s\bar{s}/c\bar{c}$) Monte Carlo (histograms). The light gray histograms show the contribution from $u\bar{u}/d\bar{d}/s\bar{s}/c\bar{c}$ events.

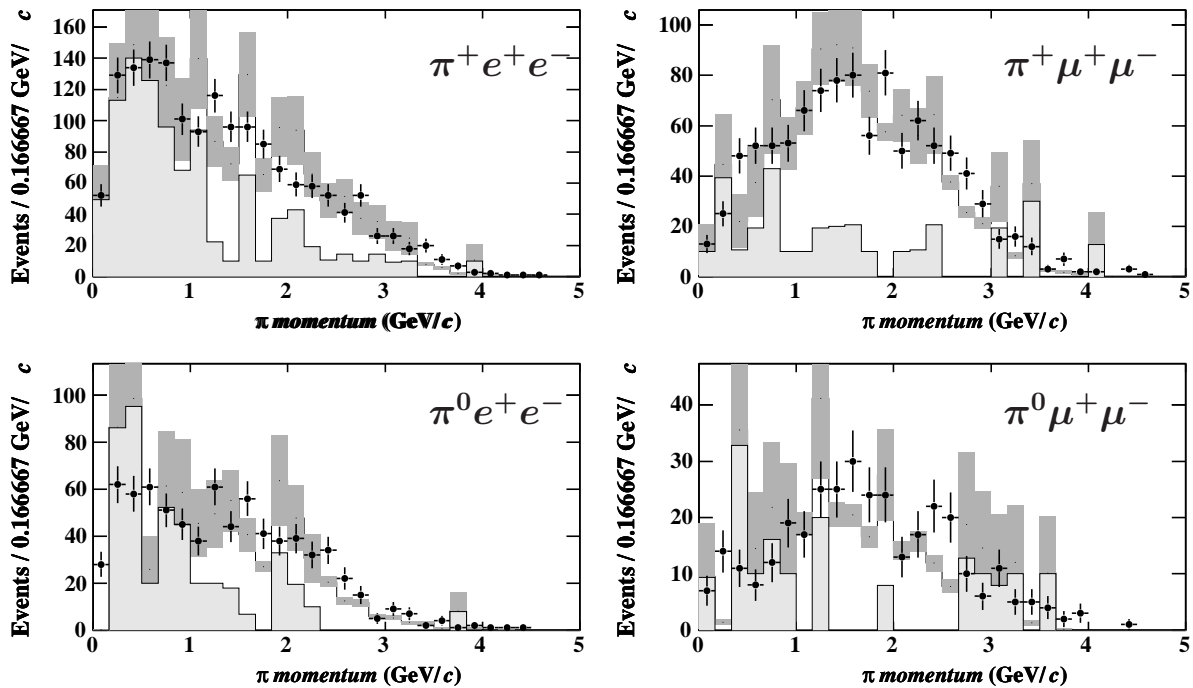


Figure 4.28b: Distributions in pion momentum, p_π , of events in the grand sideband. On-resonance data (points) and the sum of generic $B\bar{B}$ Monte Carlo and off-resonance data (histograms). The light gray histograms show the contribution from off-resonance events.

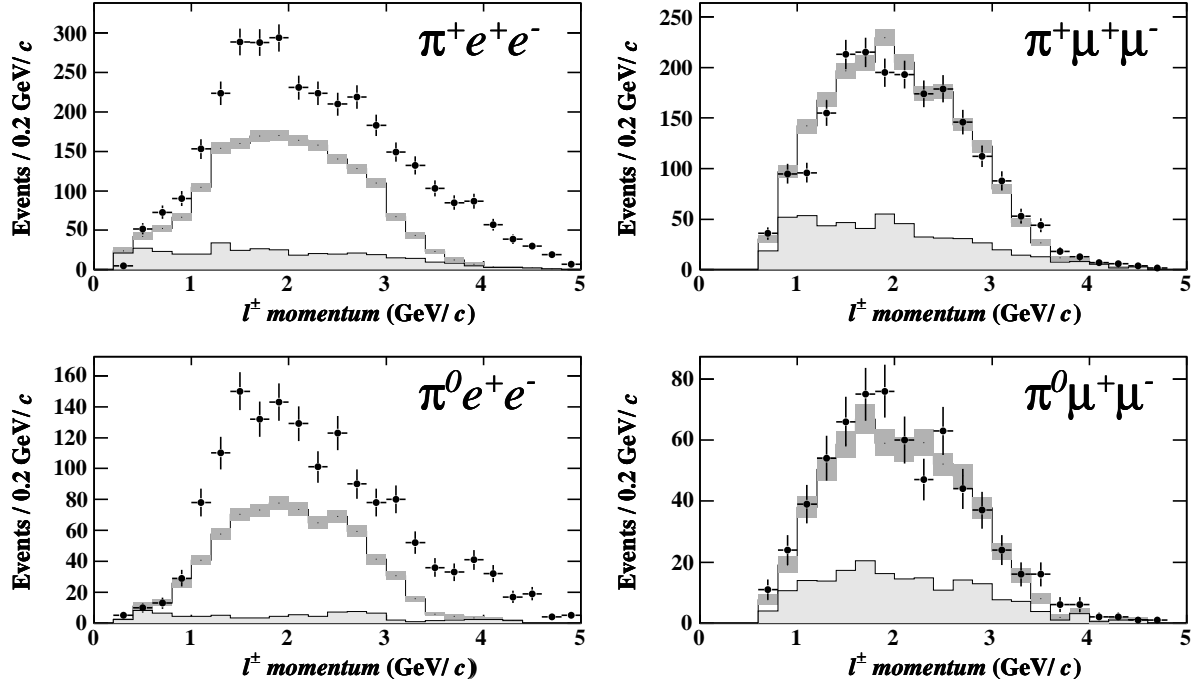


Figure 4.29a: Distributions in lepton momentum, p_ℓ , of events in the grand sideband. On-resonance data (points) and generic ($B\bar{B} + u\bar{u}/d\bar{d}/s\bar{s}/c\bar{c}$) Monte Carlo (histograms). The light gray histograms show the contribution from $u\bar{u}/d\bar{d}/s\bar{s}/c\bar{c}$ events.

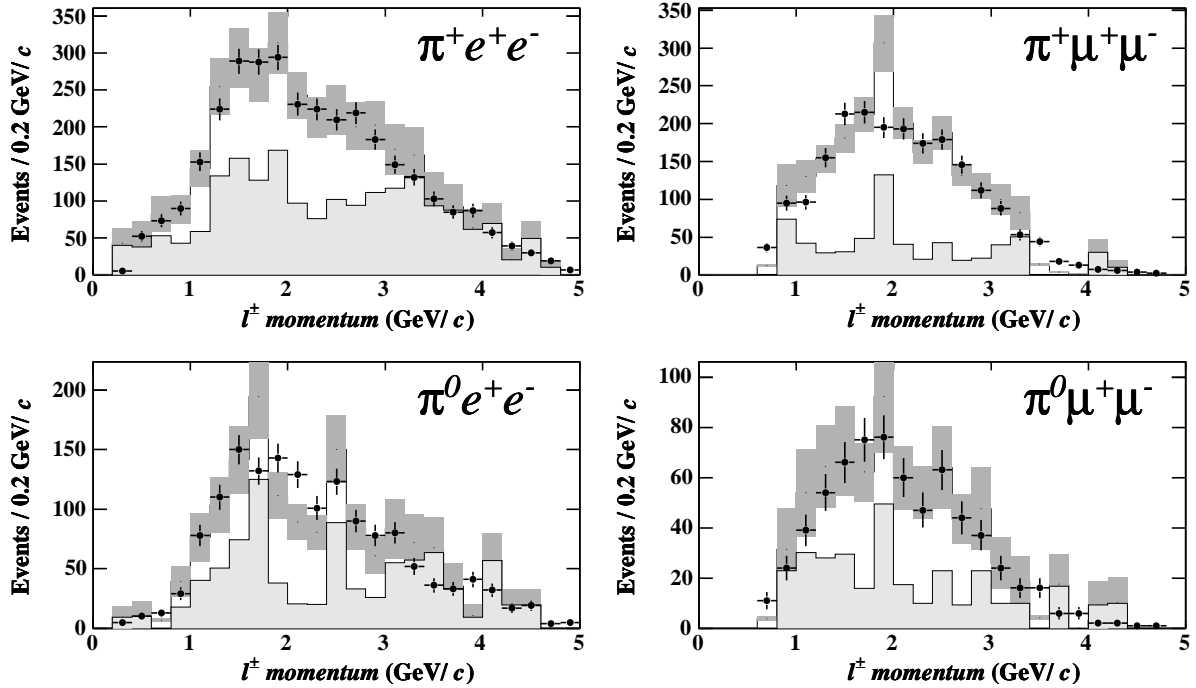


Figure 4.29b: Distributions in lepton momentum, p_ℓ , of events in the grand sideband. On-resonance data (points) and the sum of generic $B\bar{B}$ Monte Carlo and off-resonance data (histograms). The light gray histograms show the contribution from off-resonance events.

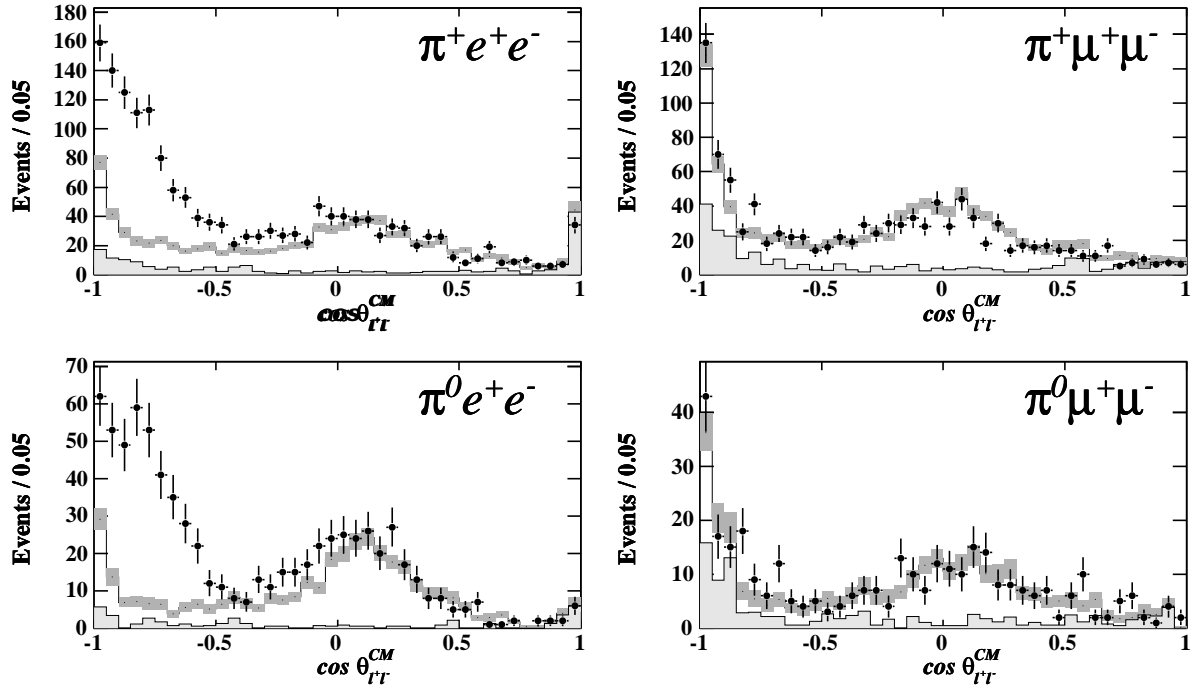


Figure 4.30a: Distributions in $\cos \theta_{\ell^+ \ell^-}^{CM}$, the angle between the two leptons in the center-of-mass frame, of events in the grand sideband. On-resonance data (points) and generic ($B\bar{B} + u\bar{u}/d\bar{d}/s\bar{s}/c\bar{c}$) Monte Carlo (histograms). The light gray histograms show the contribution from $u\bar{u}/d\bar{d}/s\bar{s}/c\bar{c}$ events.

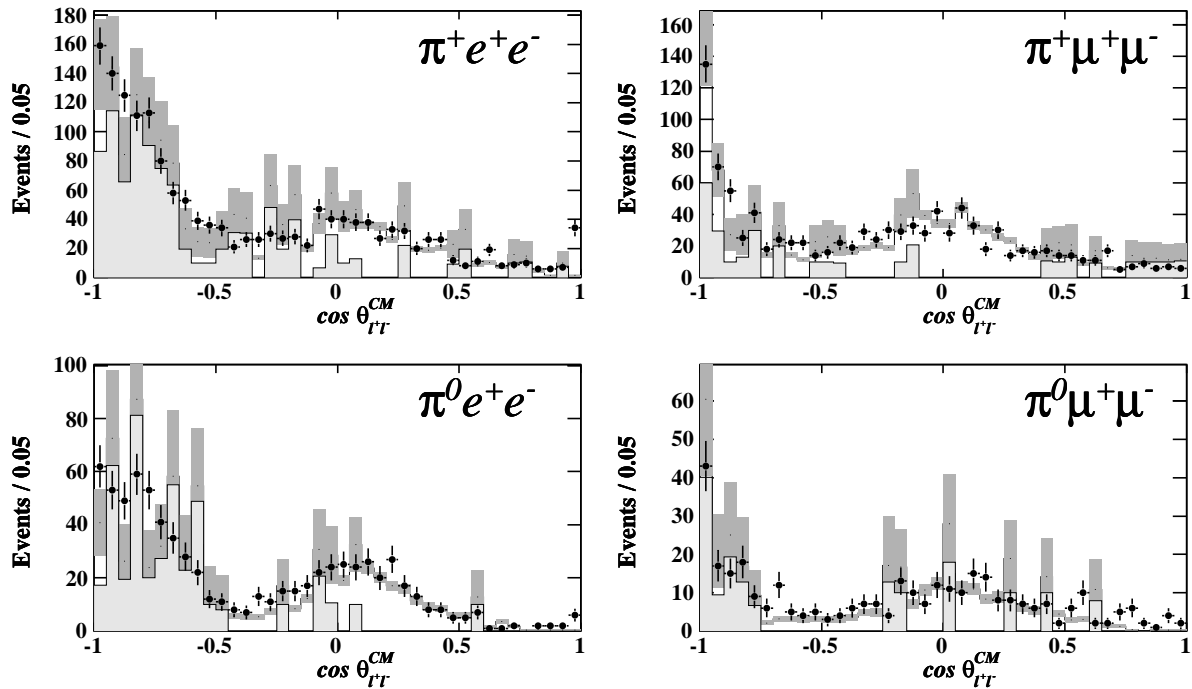


Figure 4.30b: Distributions in $\cos \theta_{\ell^+ \ell^-}^{CM}$, the angle between the two leptons in the center-of-mass frame, of events in the grand sideband. On-resonance data (points) and the sum of generic $B\bar{B}$ Monte Carlo and off-resonance data (histograms). The light gray histograms show the contribution from off-resonance events.

4.3.3 $e\mu$ control sample

An additional cross-check on the data–MC agreement for combinatorial background is provided by the $e\mu$ control sample.

For selecting $B^+ \rightarrow \pi^+ e\mu$ and $B^0 \rightarrow \pi^0 e\mu$ events, we use the same selection criteria as the $B \rightarrow \pi e^+ e^-$ mode and $B^0 \rightarrow \pi^0 e^+ e^-$ mode, respectively, with one exception: the vetoes against of $B \rightarrow D\pi$ background (section 4.2.5) is implemented as for the $B^+ \rightarrow \pi^+ \mu^+ \mu^-$ and $B^0 \rightarrow \pi^0 \mu^+ \mu^-$ modes.

No peaking structures are expected in the $e\mu$ reconstruction modes, but the vetoes of peaking backgrounds, *e.g.* $B \rightarrow J/\psi\pi$ and $B \rightarrow D\pi$, are used to eliminate these background processes in cases where one of the muons are misidentified as an electron, or vice versa.

Figure 4.31 shows a comparison of Fisher and likelihood-ratio distributions for on-resonance $e\mu$ data in the fit region (points with error bars) and total generic Monte Carlo samples (gray bands). The input variables were also investigated, and data–MC agreement is good in all of these distributions.

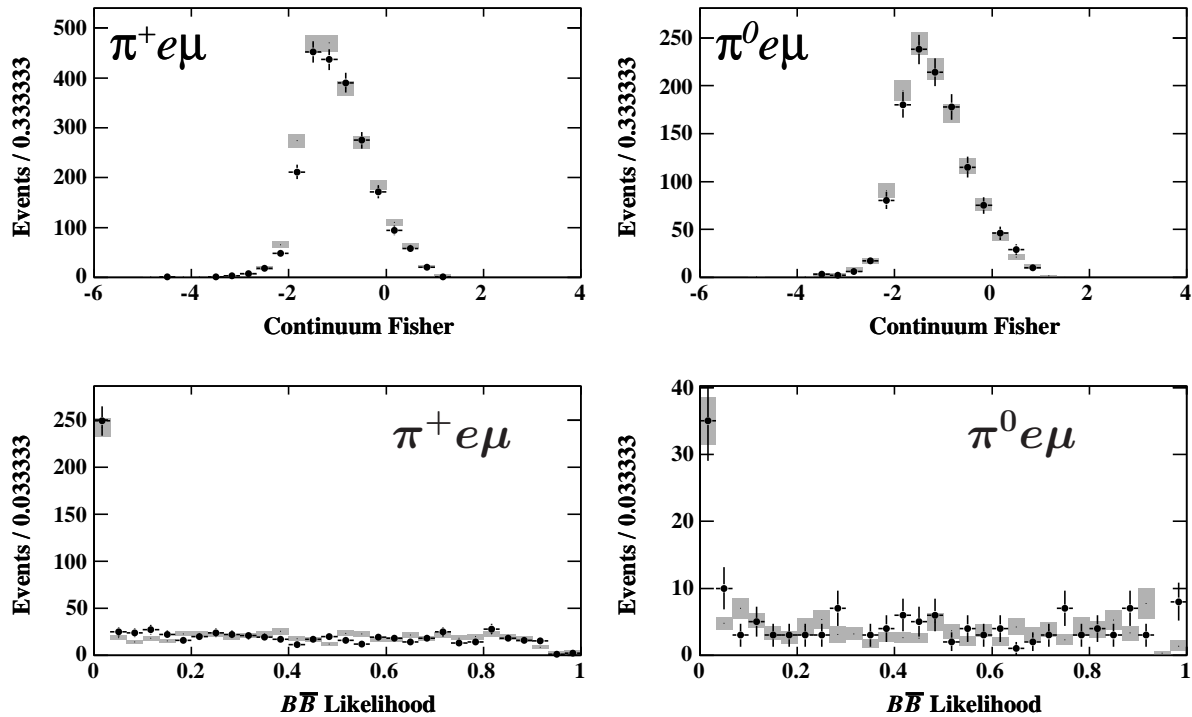


Figure 4.31: Distributions of Fisher and likelihood-ratio for $e\mu$ control sample events in the fit region.

4.4 Selection efficiencies

The efficiency calculation is based on signal Monte Carlo samples (large samples of simulated $B \rightarrow \pi\ell^+\ell^-$ and $B \rightarrow \pi e^\pm\mu^\mp$ events). Some corrections have already been applied for differences between data and Monte Carlo performance of tracking and particle identification. These corrections are based on low-multiplicity samples described in section 2.4.3. Due to detector response differences, efficiencies may be different for $B\bar{B}$ events where we typically have ten charged tracks and many neutral particles.

In order to correct for any additional efficiency discrepancy in data and Monte Carlo, we compare the efficiencies of individual selection criteria using the $B \rightarrow J/\psi K$ control sample introduced in section 4.3.1. This sample has nearly no background and high statistics. The measured data/MC efficiency differences are used as correction factors when evaluating the signal efficiency from simulated signal. The uncertainties in these ratios are used to bound systematic uncertainties on the signal efficiency.

4.4.1 Lepton-identification efficiency correction

To check the efficiency of the lepton identification, we select $B \rightarrow J/\psi K$ events kinematically, but with only one lepton identified. By applying signal-region ΔE selection and fitting the distribution in m_{ES} with a signal PDF and a background PDF, we obtain the signal yield corresponding to the signal region. Figure 4.19 shows the data selected with both leptons identified.

The efficiency is calculated the same way in data and Monte Carlo, by measuring the number of events where both leptons pass particle identification, versus events where one of the leptons fail the particle identification.

The measured efficiencies in data and Monte Carlo as well as the measured data/MC-ratios are summarized in table 4.10 for electron and muon identification. The electron identification is $(92.0 \pm 0.3)\%$ efficient in the data and $(92.9 \pm 0.1)\%$ efficient in Monte Carlo, which gives a correction factor for an e^+e^- pair of 0.983 ± 0.007 . The muon identification is $(67.5 \pm 0.6)\%$ efficient in the data and $(69.2 \pm 0.2)\%$ efficient in Monte Carlo, which gives a correction factor for a $\mu^+\mu^-$ pair of 0.947 ± 0.019 . The uncertainties in the correction factors are assigned as systematic uncertainties in the signal efficiencies.

Lepton ID	Data Efficiency	MC Efficiency	$C = (Data/MC)^2$
Electron	$(92.0 \pm 0.3)\%$	$(92.9 \pm 0.1)\%$	$(98.3 \pm 0.7)\%$
Muon	$(67.5 \pm 0.6)\%$	$(69.2 \pm 0.2)\%$	$(94.7 \pm 1.9)\%$

Table 4.10: Identification efficiencies for electrons and muons in data and Monte Carlo (MC). The table also lists the correction factor, C , used to correct the efficiency of lepton pairs in Monte Carlo.

4.4.2 Fisher and likelihood-ratio efficiency corrections

Since the selections by Fisher discriminant and likelihood-ratio are optimized individually for each mode, it seems natural to determine the efficiencies from $B^+ \rightarrow J/\psi \pi^+$ and $B^0 \rightarrow J/\psi \pi^0$ events. However, these control samples are not very large, and this would lead to an unnecessarily large systematic uncertainty. We therefore chose to use $B^+ \rightarrow J/\psi K^+$ events, since these have the same topology and cover nearly the same kinematic region as $B \rightarrow J/\psi \pi$ events.

Thus, we use the selection of $B^\pm \rightarrow K^\pm \ell^+ \ell^-$ events as described in section 4.3.1, but define the Fisher discriminant and the likelihood ratio as they are defined for the $B \rightarrow \pi \ell^+ \ell^-$ selection modes. This procedure is justified because the input quantities to the Fisher discriminant and likelihood-ratio do not depend directly on the final state particles, with the exception of the B vertex probability. For $B^0 \rightarrow \pi^0 \ell^+ \ell^-$, the latter is approximated by the $\ell^+ \ell^-$ vertex probability.

Table 4.11 tabulates the measured efficiencies and ratios of the selections based on the Fisher discriminant and the likelihood ratio in data and Monte Carlo. The efficiency of each selection criterion has been measured with and without the other criterion applied. Within uncertainties, the measured data/MC ratios agree between the two methods, with the exception of data/MC for Fisher selection efficiencies in the $B \rightarrow \pi \mu^+ \mu^-$ modes, where the two data/MC measurements still agree within 2σ . The data/MC ratios are all close to 1.0, and overall the efficiency is measured to be a little higher in Monte Carlo than in data. We correct the signal efficiency by the data/MC ratio obtained from measuring the efficiency of the combined Fisher and likelihood-ratio criteria.

4.4.3 Fully corrected signal efficiencies

After all corrections have been applied, the signal efficiencies in the fit region and in the signal region are given in table 4.12.

Mode	Data Efficiency	MC Efficiency	$C = (Data/MC)$
Fisher efficiencies for events that pass the likelihood selection:			
$B^+ \rightarrow \pi^+ e^+ e^-$	$(82.1 \pm 0.7)\%$	$(82.0 \pm 0.3)\%$	$(100.1 \pm 0.9)\%$
$B^0 \rightarrow \pi^0 e^+ e^-$	$(71.5 \pm 0.8)\%$	$(72.4 \pm 0.2)\%$	$(98.8 \pm 1.1)\%$
$B^+ \rightarrow \pi^+ \mu^+ \mu^-$	$(69.8 \pm 0.9)\%$	$(69.2 \pm 0.4)\%$	$(100.9 \pm 1.5)\%$
$B^0 \rightarrow \pi^0 \mu^+ \mu^-$	$(66.4 \pm 1.0)\%$	$(65.2 \pm 0.4)\%$	$(101.8 \pm 1.7)\%$
Fisher efficiencies independent of likelihood selection:			
$B^+ \rightarrow \pi^+ e^+ e^-$	$(79.3 \pm 0.6)\%$	$(79.2 \pm 0.3)\%$	$(100.1 \pm 0.8)\%$
$B^0 \rightarrow \pi^0 e^+ e^-$	$(69.0 \pm 0.7)\%$	$(70.3 \pm 0.3)\%$	$(98.0 \pm 1.1)\%$
$B^+ \rightarrow \pi^+ \mu^+ \mu^-$	$(66.8 \pm 0.9)\%$	$(67.4 \pm 0.4)\%$	$(99.1 \pm 1.4)\%$
$B^0 \rightarrow \pi^0 \mu^+ \mu^-$	$(63.3 \pm 0.9)\%$	$(63.2 \pm 0.4)\%$	$(100.2 \pm 1.5)\%$
Likelihood efficiencies for events that pass the Fisher selection:			
$B^+ \rightarrow \pi^+ e^+ e^-$	$(70.6 \pm 0.8)\%$	$(72.0 \pm 0.3)\%$	$(98.2 \pm 1.2)\%$
$B^0 \rightarrow \pi^0 e^+ e^-$	$(80.8 \pm 0.7)\%$	$(82.0 \pm 0.3)\%$	$(98.5 \pm 0.9)\%$
$B^+ \rightarrow \pi^+ \mu^+ \mu^-$	$(81.7 \pm 0.9)\%$	$(85.3 \pm 0.3)\%$	$(95.8 \pm 1.1)\%$
$B^0 \rightarrow \pi^0 \mu^+ \mu^-$	$(76.8 \pm 0.9)\%$	$(80.3 \pm 0.4)\%$	$(95.6 \pm 1.3)\%$
Likelihood efficiencies independent of Fisher selection:			
$B^+ \rightarrow \pi^+ e^+ e^-$	$(68.2 \pm 0.7)\%$	$(69.5 \pm 0.3)\%$	$(98.2 \pm 1.1)\%$
$B^0 \rightarrow \pi^0 e^+ e^-$	$(77.9 \pm 0.6)\%$	$(79.7 \pm 0.3)\%$	$(97.7 \pm 0.8)\%$
$B^+ \rightarrow \pi^+ \mu^+ \mu^-$	$(78.3 \pm 0.8)\%$	$(83.1 \pm 0.3)\%$	$(94.2 \pm 1.0)\%$
$B^0 \rightarrow \pi^0 \mu^+ \mu^-$	$(73.3 \pm 0.8)\%$	$(77.8 \pm 0.3)\%$	$(94.2 \pm 1.1)\%$
Efficiency of Fisher and likelihood selection combined:			
$B^+ \rightarrow \pi^+ e^+ e^-$	$(56.0 \pm 0.8)\%$	$(57.0 \pm 0.3)\%$	$(98.2 \pm 1.4)\%$
$B^0 \rightarrow \pi^0 e^+ e^-$	$(55.7 \pm 0.7)\%$	$(57.7 \pm 0.3)\%$	$(96.6 \pm 1.4)\%$
$B^+ \rightarrow \pi^+ \mu^+ \mu^-$	$(54.6 \pm 0.9)\%$	$(57.5 \pm 0.4)\%$	$(95.0 \pm 1.7)\%$
$B^0 \rightarrow \pi^0 \mu^+ \mu^-$	$(48.6 \pm 0.9)\%$	$(50.7 \pm 0.4)\%$	$(95.9 \pm 1.9)\%$

Table 4.11: Fisher and likelihood-ratio efficiencies by mode for data and Monte Carlo (MC). The correction factor C used to correct signal efficiencies in the Monte Carlo samples is taken from the data/MC ratios for the two selection criteria combined.

4.4.4 Systematic effects from model dependence

The simulated signal sample used to evaluate the efficiency is based on kinematics modeling by Ali *et al* [23], and $B \rightarrow \pi$ form-factors are based on Ball & Zwicky [50, 114, 115]. The largest theoretical uncertainty to the branching fraction prediction comes from the form-factor calculations. Thus, it is of interest to estimate how large an effect the form-factor predictions

Mode	Fit region efficiency	Signal region efficiency
$B^+ \rightarrow \pi^+ e^+ e^-$	$(11.92 \pm 0.07)\%$	$(7.17 \pm 0.05)\%$
$B^0 \rightarrow \pi^0 e^+ e^-$	$(8.98 \pm 0.06)\%$	$(5.68 \pm 0.05)\%$
$B^+ \rightarrow \pi^+ \mu^+ \mu^-$	$(6.60 \pm 0.05)\%$	$(4.71 \pm 0.05)\%$
$B^0 \rightarrow \pi^0 \mu^+ \mu^-$	$(4.48 \pm 0.04)\%$	$(3.11 \pm 0.04)\%$
$B^+ \rightarrow \pi^+ e \mu$	$(8.77 \pm 0.05)\%$	$(6.31 \pm 0.04)\%$
$B^0 \rightarrow \pi^0 e \mu$	$(5.45 \pm 0.05)\%$	$(3.70 \pm 0.04)\%$

Table 4.12: Total efficiency for $B \rightarrow \pi \ell^+ \ell^-$ events in the fit region and the signal region after all corrections, based on cut and count procedure. Uncertainties are statistical only.

have on signal efficiencies.

These systematic effects have been evaluated by investigating the change in signal efficiency when different form factor models are used. The alternative models considered are LCSR predictions [114, 115], an alternative set of input parameters from [50] as well as two other form-factor calculations based on the relativistic light-cone quark model (LCQM) [88, 89]. Predictions from lattice QCD are not given for the most relevant form factor $f_T(q^2, \mu)$ (see section 1.2), and are not included in this evaluation. We did attempt to use a couple of lattice QCD models by using a relation between $f_T(q^2, \mu)$ and $f_+(q^2)$ and $f_0(q^2)$ at high values of q^2 given by [87], and this gave a result that matched very well with the other models for the highest values of q^2 , but deviated strongly in the low q^2 region. Since the relation provided and lattice QCD are not reliable for low q^2 , these models were ignored. Figure 4.32 shows the effect of the signal efficiency on the distribution of $m_{\ell^+ \ell^-}$ with different form-factor models. Table 4.13 lists the relative change in signal efficiency for the different models considered.

Mode	Ball'03	B&Z'05 set2	B&Z'05 set4	M'96 set1	M&S'00
$B \rightarrow \pi e^+ e^-$	-0.54%	0.00%	-0.27%	+1.07%	+0.13%
$B^0 \rightarrow \pi^0 e^+ e^-$	+3.31%	0.00%	-0.33%	+2.31%	+0.33%
$B \rightarrow \pi \mu^+ \mu^-$	+4.17%	0.00%	-0.19%	+2.84%	0.00%
$B^0 \rightarrow \pi^0 \mu^+ \mu^-$	+7.31%	0.00%	-0.88%	+2.63%	0.00%

Table 4.13: Relative change in signal efficiencies from choosing different form-factor models. The baseline model is provided by Ball & Zwicky '05 [50], set 2.

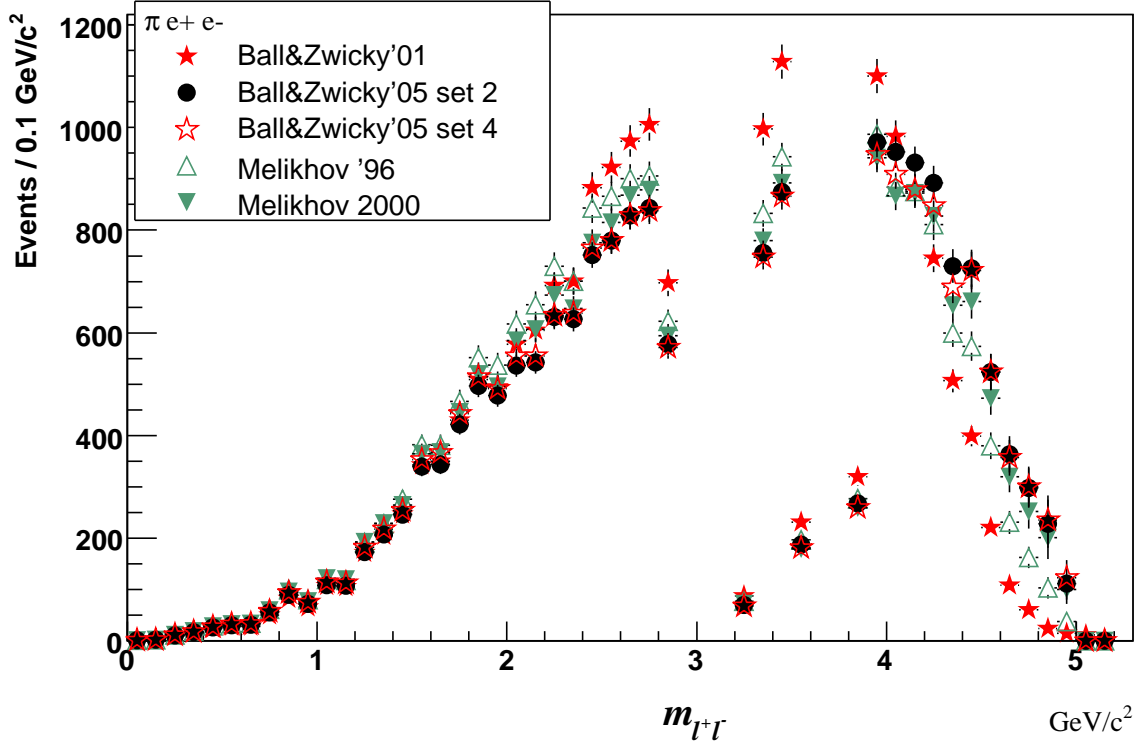


Figure 4.32: $m_{\ell\ell}$ distribution in the $B^+ \rightarrow \pi^+ e^+ e^-$ mode for different form factor models. The dips in the distribution around $m_{J/\psi}$ and $m_{\psi(2S)}$ are due to the charmonium vetoes.

4.5 Estimates of residual peaking background

Peaking backgrounds have been reduced by vetoes of J/ψ , $\psi(2S)$ and D mesons. Some residual background may be left from these modes. In addition, non-reducible backgrounds are expected from non-resonant decays of B mesons, like $B \rightarrow \pi\pi\pi$. This residual background must be estimated and accounted for when computing the branching-fraction upper limit.

We separate peaking background processes into two types: hadronic peaking backgrounds, where the lepton candidates in the $\pi\ell\ell$ final state arise from hadrons misidentified as leptons; and non-hadronic peaking backgrounds, for which the lepton candidates are real leptons.

4.5.1 Hadronic peaking backgrounds

B -meson decays to hadronic final states can mimic the signal if the tracks identified as leptons are misidentified hadrons. Since the number of hadrons passing the electron selection is rather small, this background source is only relevant for muon channels.

These backgrounds are estimated using a control sample of hadronic B decays in *BABAR* data. A sample disjoint from the signal-selection sample is selected by requiring that two out of three tracks fail the muon and electron identification criteria. The remaining track is required to fail the electron identification but it should pass a loose muon identification which has a high rate pion mis-identification ($\sim 8\%$). This selects a sufficiently large control sample of $B \rightarrow \pi\mu h$ events consisting primarily of $B \rightarrow \pi h h$ events, where $h = \pi, K$.

Using this sample, we estimate how many $B \rightarrow \pi h h$ events would pass the $B \rightarrow \pi\mu\mu$ selection, by weighting the events according to each track's probability of passing the tight muon selection. These probabilities are obtained from the high-purity control samples described in section 2.4.3. For instance, the weight applied for a $B^0 \rightarrow \pi^0 h^+ \mu^-$ sample is:

$$w(\mu^+ h^-) = \frac{P(h^+ \rightarrow \mu^+)}{P(h^+ \rightarrow \mu_{loose}^+)(1 - P(h^+ \rightarrow e^+))} \times \frac{P(h^- \rightarrow \mu^-)}{(1 - P(h^- \rightarrow \mu_{loose}^-))(1 - P(h^- \rightarrow e^-))}$$

where

- $P(h^+ \rightarrow \mu^+) [P(h^- \rightarrow \mu^-)]$ is the probability for a positive [negative] hadron species h^+ [h^-] to be misidentified by the muon selection;
- $P(h^+ \rightarrow \mu_{loose}^+) [P(h^- \rightarrow \mu_{loose}^-)]$ is the probability for positive [negative] hadron species h^+ [h^-] to be misidentified by the *loose* muon selection;
- $P(h^+ \rightarrow e^+) [P(h^- \rightarrow e^-)]$ is the probability for positive [negative] hadron species h^+ [h^-] to be misidentified by the electron selection.

The weights given in the control-sample efficiency tables depend on the particle hypothesis assigned to the track. We use the pion identification criteria to classify each event. If a track does not pass these criteria, it is assumed to be a kaon, and the relevant probabilities are picked from the kaon control sample efficiency table (see section 2.4.3). The efficiency loss due to this classification scheme is also included in the weights, *e.g.*:

$$w(\pi^+ \pi^-) = w(\mu^+ h^-) \times \frac{1}{\varepsilon(\pi^+) \varepsilon(\pi^-)}$$

$$w(K^+ \pi^-) = w(\mu^+ h^-) \times \frac{1}{\varepsilon(K^+) \varepsilon(\pi^-)}$$

where $\varepsilon(\pi)$ is the efficiency of a pion to be identified as a pion and $\varepsilon(K)$ is the efficiency of a kaon to fail pion identification.

The expected yield in the signal region is extracted from a one-dimensional χ^2 fit to the weighted m_{ES} distribution, for events within the signal-region of ΔE , as shown in figure 4.33. The PDF consists of an Argus function parameterizing the combinatorial background plus a single Gaussian for the peaking background. The parameters of the Gaussian are fixed to expectations for signal $B \rightarrow \pi\ell^+\ell^-$ events. The slope of the Argus function as well as the relative normalization of the two are floating parameters in the fit.

The m_{ES} distribution with the fitted curve superimposed is shown in Figure 4.33. From this procedure we expect to find $0.027 \pm 0.033 B^\pm \rightarrow \pi^\pm hh$ events and $0.035 \pm 0.022 B^0 \rightarrow \pi^0 hh$ events within the signal region.

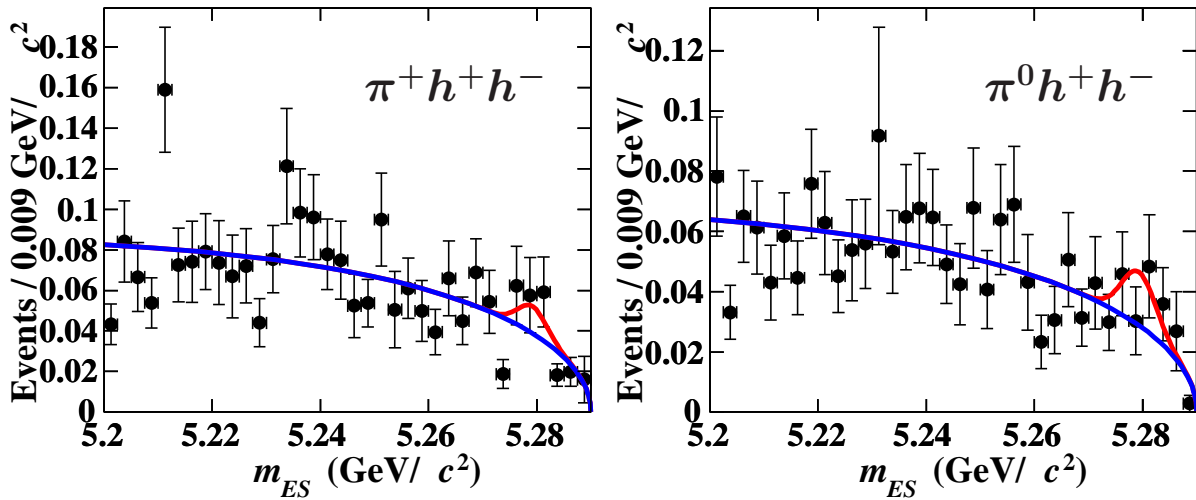


Figure 4.33: m_{ES} fits to extract hadronic peaking background in the signal region. Left: $B^+ \rightarrow \pi^+ h\mu$. Right: $B^0 \rightarrow \pi^0 h\mu$.

4.5.2 Peaking backgrounds with leptons

Peaking background from sources with real leptons are estimated based on high-statistics Monte Carlo samples, with all the same efficiency corrections as were used to evaluate signal efficiencies. Table 4.14 summarizes the contributions from the various samples, and figures 4.34-4.36 show distribution of events from the most important ones in the m_{ES} - ΔE plane. (Note that the plots are *not* normalized to luminosity.) The main contributions come from:

- $K \ell^+\ell^-$ background:

We find that $0.06 \pm 0.02 B^+ \rightarrow K^+ e^+ e^-$ events are expected in the signal region for the $B^+ \rightarrow \pi^+ e^+ e^-$ mode, and this is the largest peaking background contribution to this

reconstruction mode. The contribution from $B^+ \rightarrow K^+ \mu^+ \mu^-$ to the $B^+ \rightarrow \pi^+ \mu^+ \mu^-$ mode is about half of this, and contributions from the K^0 modes are negligible. Most of the events from these decays have too low a ΔE to end up in the $B \rightarrow \pi \ell^+ \ell^-$ signal region, as shown in figure 4.34. From the plot we can see that the core of the distribution falls outside the $\pi \ell^+ \ell^-$ signal region, but the tail of the distribution occupies the low- ΔE half of the signal region.

- $\rho \ell^+ \ell^-$ background:

These events tend to pass most of the selection criteria, but since there is one pion missing from the reconstructed B , both m_{ES} and ΔE tend to be shifted downward. The shift is of order a few MeV in m_{ES} and 200 MeV or more in ΔE . No background events from $B \rightarrow \rho \ell^+ \ell^-$ are expected in the signal region, as seen from figure 4.35 and table 4.14.

- $K^* \ell^+ \ell^-$ background:

These events do not peak anywhere within the fit region, and are only expected to contribute as combinatorial background. Figure 4.36 shows the distribution of $B \rightarrow K^* \ell^+ \ell^-$ events in the fit region.

- Charmonium background:

Any charmonium background events that fail the charmonium veto will appear as peaking background in the data. This background is estimated from exclusive Monte Carlo samples of $B \rightarrow J/\psi \pi$, $B \rightarrow J/\psi K$, $B \rightarrow \psi(2S)\pi$ and $B \rightarrow \psi(2S)K$ events. No such background events are found.

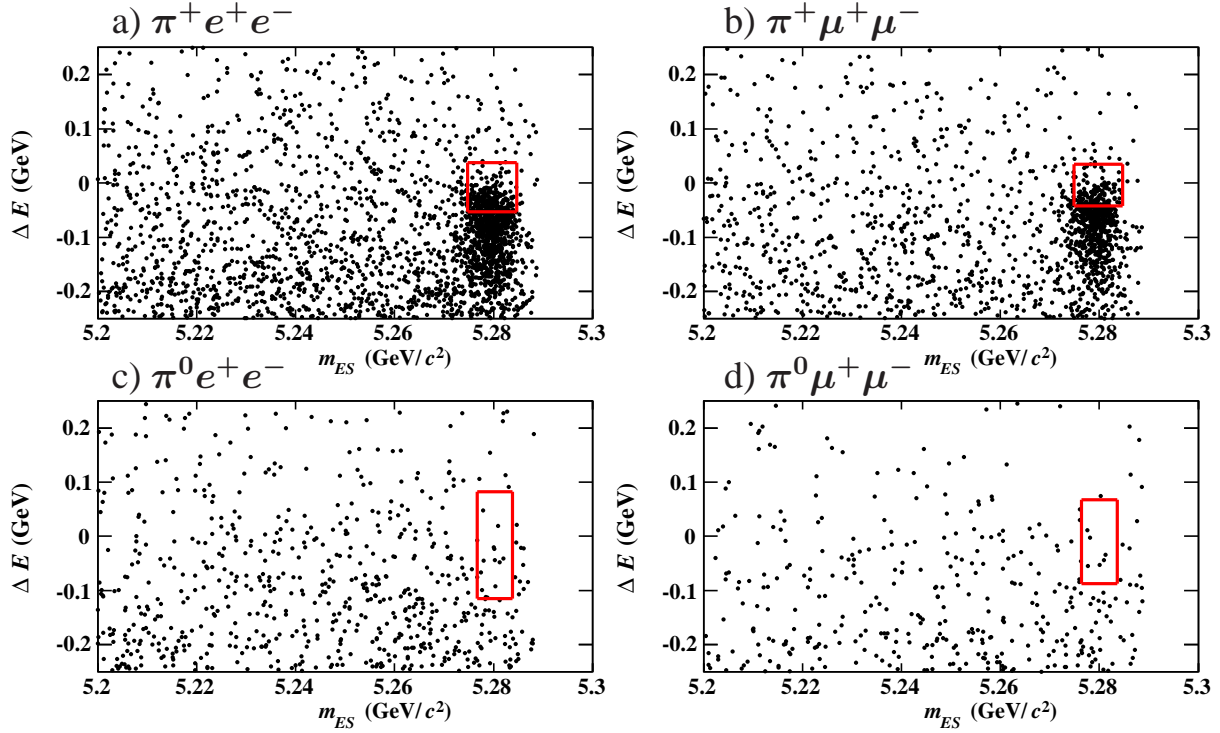


Figure 4.34: Scatter plots of ΔE vs. m_{ES} for $B \rightarrow K\ell^+\ell^-$ Monte Carlo events in the fit region for a) $B^+ \rightarrow \pi^+e^+e^-$, b) $B^+ \rightarrow \pi^+\mu^+\mu^-$, c) $B^0 \rightarrow \pi^0e^+e^-$ and d) $B^0 \rightarrow \pi^0\mu^+\mu^-$ reconstruction modes (*not* scaled to luminosity). The small boxes show the signal regions from which $B \rightarrow \pi\ell^+\ell^-$ candidates will be selected.

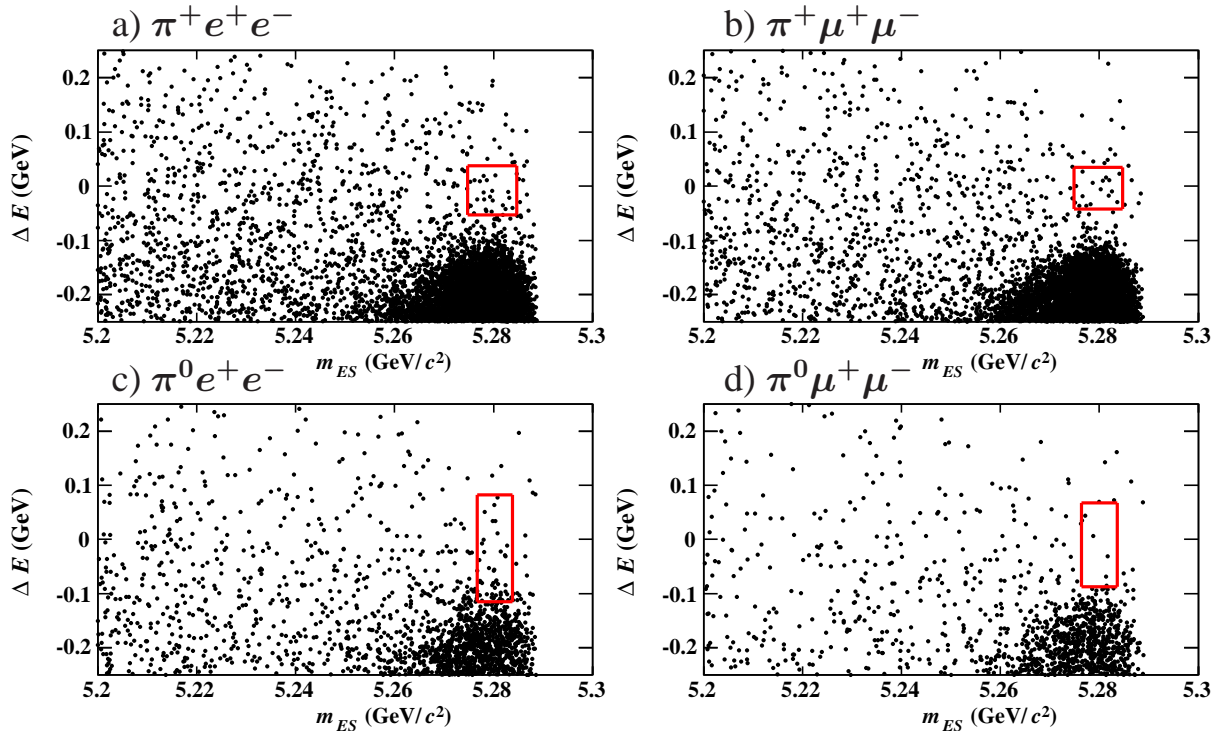


Figure 4.35: Scatter plots of ΔE vs. m_{ES} for $B \rightarrow \rho\ell^+\ell^-$ Monte Carlo events in the fit region for a) $B^+ \rightarrow \pi^+e^+e^-$, b) $B^+ \rightarrow \pi^+\mu^+\mu^-$, c) $B^0 \rightarrow \pi^0e^+e^-$ and d) $B^0 \rightarrow \pi^0\mu^+\mu^-$ (*not* scaled to luminosity). The small boxes show the signal regions from which $B \rightarrow \pi\ell^+\ell^-$ candidates will be selected.

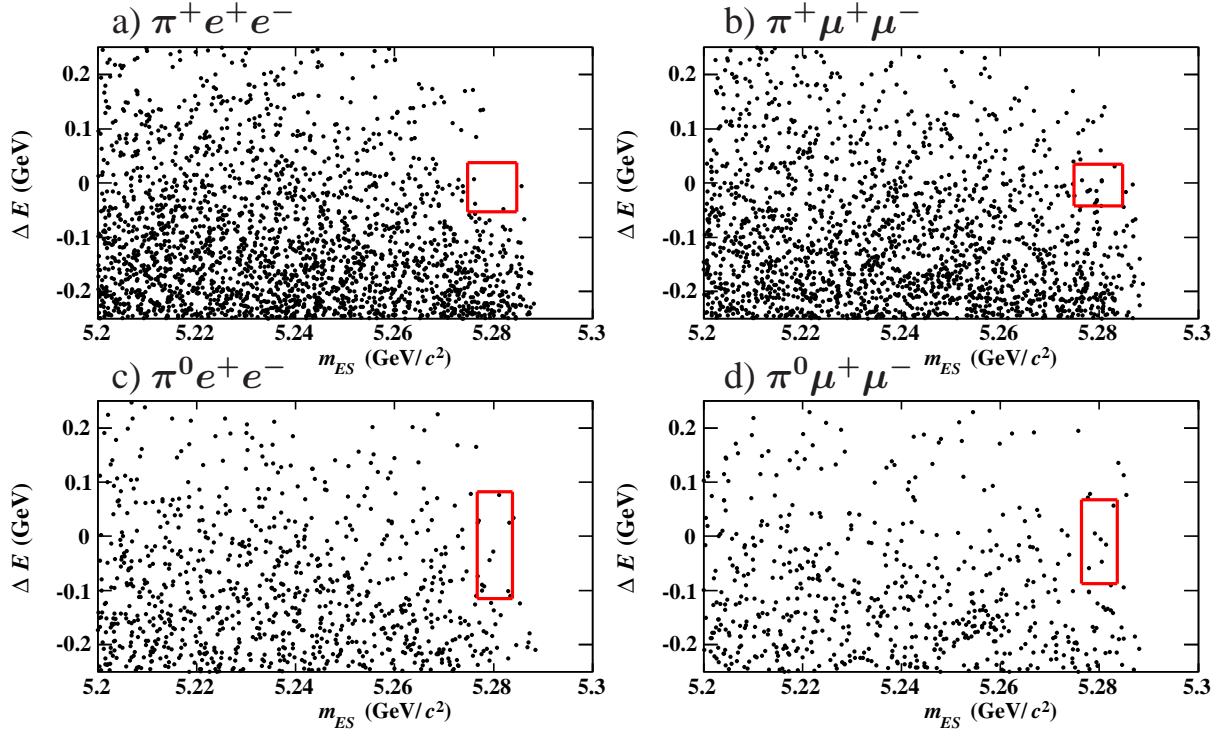


Figure 4.36: Scatter plots of ΔE vs. m_{ES} for $B \rightarrow K^*\ell^+\ell^-$ Monte Carlo events in the fit region for a) $B^+ \rightarrow \pi^+e^+e^-$, b) $B^+ \rightarrow \pi^+\mu^+\mu^-$, c) $B^0 \rightarrow \pi^0e^+e^-$ and d) $B^0 \rightarrow \pi^0\mu^+\mu^-$ (not scaled to luminosity). The small boxes show the signal regions from which $B \rightarrow \pi\ell^+\ell^-$ candidates will be selected.

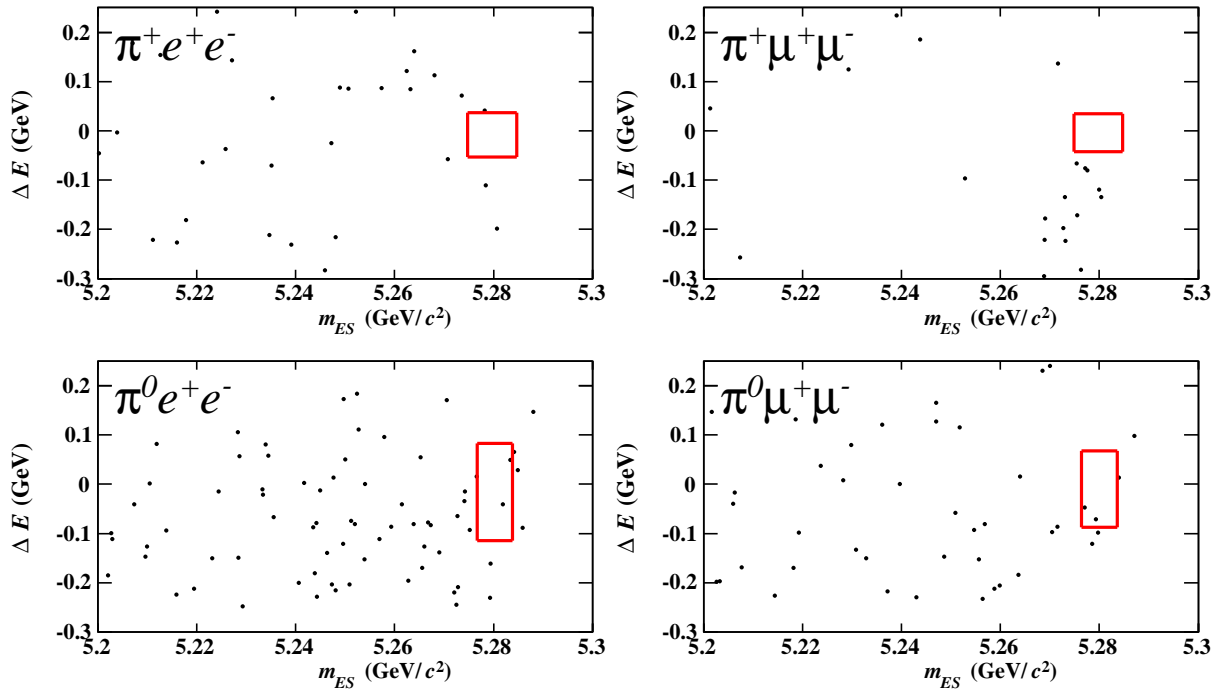


Figure 4.37: Scatter plots of ΔE vs. m_{ES} for inclusive J/ψ and $\psi(2S)$ Monte Carlo events in the fit region for $B^+ \rightarrow \pi^+e^+e^-$, $B^+ \rightarrow \pi^+\mu^+\mu^-$, $B^0 \rightarrow \pi^0e^+e^-$ and $B^0 \rightarrow \pi^0\mu^+\mu^-$ (not scaled to luminosity). The small boxes show the signal regions from which $B \rightarrow \pi\ell^+\ell^-$ candidates will be selected.

Region	sample	$B^+ \rightarrow \pi^+ e^+ e^-$	$B^0 \rightarrow \pi^0 e^+ e^-$	$B^+ \rightarrow \pi^+ \mu^+ \mu^-$	$B^0 \rightarrow \pi^0 \mu^+ \mu^-$	
Fit region:	$K \ell^+ \ell^-$	0.66 ± 0.19	0.17 ± 0.05	0.39 ± 0.11	0.09 ± 0.025	
	$\rho \ell^+ \ell^-$	0.22 ± 0.07	0.09 ± 0.03	0.18 ± 0.06	0.06 ± 0.02	
	$K^* \ell^+ \ell^-$	0.66 ± 0.25	0.25 ± 0.10	0.51 ± 0.20	0.16 ± 0.06	
	$J/\psi \pi$	0.09 ± 0.01	0.05 ± 0.01	0.09 ± 0.01	0.023 ± 0.004	
	$J/\psi K$	0.00 ± 0.00	0.00 ± 0.00	0.46 ± 0.02	0.204 ± 0.009	
	$\psi(2S)\pi$	0.00 ± 0.00	0.00 ± 0.001	0.001 ± 0.0002	0.0005 ± 0.0002	
	$\psi(2S)K$	0.10 ± 0.01	0.00 ± 0.00	0.00 ± 0.00	0.00 ± 0.00	
	hadronic			0.030 ± 0.036	0.048 ± 0.030	
	Total		1.74 ± 0.32	0.56 ± 0.11	1.66 ± 0.24	0.58 ± 0.08
	Signal region:	$K \ell^+ \ell^-$	0.055 ± 0.016	0.003 ± 0.001	0.028 ± 0.008	0.002 ± 0.000
$\rho \ell^+ \ell^-$		0.001 ± 0.000	0.002 ± 0.000	0.001 ± 0.0002	0.000 ± 0.000	
$K^* \ell^+ \ell^-$		0.001 ± 0.000	0.003 ± 0.001	0.011 ± 0.004	0.002 ± 0.001	
$J/\psi \pi$		0.00 ± 0.002	0.000 ± 0.000	0.000 ± 0.000	0.001 ± 0.000	
$J/\psi K$		0.00 ± 0.00	0.000 ± 0.000	0.000 ± 0.000	0.00 ± 0.00	
$\psi(2S)\pi$		0.00 ± 0.00	0.001 ± 0.0002	0.00 ± 0.00	0.000 ± 0.000	
$\psi(2S)K$		0.00 ± 0.00	0.000 ± 0.000	0.00 ± 0.00	0.00 ± 0.00	
hadronic				0.027 ± 0.033	0.035 ± 0.022	
Total			0.057 ± 0.016	0.009 ± 0.002	0.059 ± 0.034	0.040 ± 0.022

Table 4.14: Summary of number of peaking background events expected in the fit and signal regions. Efficiency corrections have been applied like described for signal Monte Carlo.

4.6 Estimate of residual combinatorial background

The combinatorial background is due to random combinations of particles and does not peak in m_{ES} or ΔE . This background is determined from on-resonance data in the fit region before events in the signal region are inspected.

A two-dimensional extended unbinned maximum likelihood fit is performed over a subset of the fit region for which $m_{ES} < 5.2724 \text{ GeV}/c^2$. The yield in the signal region is obtained by extrapolating the best-fit probability-density-function (PDF) into the signal region and integrating the PDF over this region. The statistical uncertainties of this procedure are estimated from the sum in quadrature of the uncertainties induced from the measured background normalization, the measured Argus slope ξ of the m_{ES} function, and the measured ΔE exponent s .

Prior to doing a fit to the on-resonance data sample, the procedure has been tested on simulation samples. This has two purposes. It allows us to make sure that the background has been well understood in terms of luminosity- and sideband-scaled Monte Carlo simulation samples. It also allows us to study the different background shapes for the $B\bar{B}$ component and the continuum component in the data.

4.6.1 Fits and yields in Monte-Carlo simulated data

An extended unbinned maximum likelihood fit of the PDF given in equation 3.8 is performed on a sample of $B\bar{B}$ simulated events and continuum simulated events. After luminosity and sideband scaling, the expected number of events in the fit region ranges from 30 events in the $B^0 \rightarrow \pi^0\mu^+\mu^-$ mode to 107 events in the $B^+ \rightarrow \pi^+e^+e^-$ mode, where the uncertainties in these estimates are in the range 15 – 35%. The numbers for each mode is given in the first column of table 4.15. The uncertainties in the Monte Carlo expectations are dominated by the large uncertainties in data/MC sideband ratios (table 4.9).

The best-fit PDF is then integrated over the signal region to determine the expected number of combinatorial background events in this region. As seen from the third column of table 4.15, based on this Monte Carlo estimate, we expect less than one event in the signal region for each of the modes.

4.6.2 Fits and yields in the *BABAR* data

An unbinned maximum likelihood fit can now be performed on the *BABAR* on-resonance data in the $m_{\text{ES}}-\Delta E$ fit region.

The fit procedure is first performed on the $B^+ \rightarrow \pi^+e\mu$ and $B^0 \rightarrow \pi^0e\mu$ control samples. Figure 4.38 shows the m_{ES} and ΔE distributions for $B \rightarrow \pi e\mu$ events with projections of the best-fit PDF superimposed. The fit yields 167 $B^+ \rightarrow \pi^+e\mu$ events and 65 $B^0 \rightarrow \pi^0e\mu$ events in the fit region. The expectation from fits to simulations of generic $B\bar{B}$ and continuum events were 178 ± 23 and 63 ± 14 events, respectively. With this result, we consider the agreement between number of observed and expected events to be acceptable, we move on to the $B \rightarrow \pi\ell^+\ell^-$ modes.

For the $B \rightarrow \pi\ell^+\ell^-$ modes, the fits are performed on the subregion $m_{\text{ES}} < 5.2724\text{GeV}/c^2$, and yield 128 $B^+ \rightarrow \pi^+e^+e^-$ events, 49 $B^0 \rightarrow \pi^0e^+e^-$ events, 111 $B^+ \rightarrow \pi^+\mu^+\mu^-$ events and 22 $B^0 \rightarrow \pi^0\mu^+\mu^-$ events in the full fit region. This is also consistent with expectations from scaled simulated samples (table 4.15).

By integrating the best-fit PDFs over the signal region, we obtain the observed combinatorial background in the signal region. These expectations are compared with the ones obtained in the same way from simulated data samples in table 4.15.

4.6.3 Bias correction: toy Monte Carlo study

To investigate any potential biases in the signal extraction procedure, toy Monte Carlo experiments are performed. Two sources of bias have been investigated: bias due to low statistics

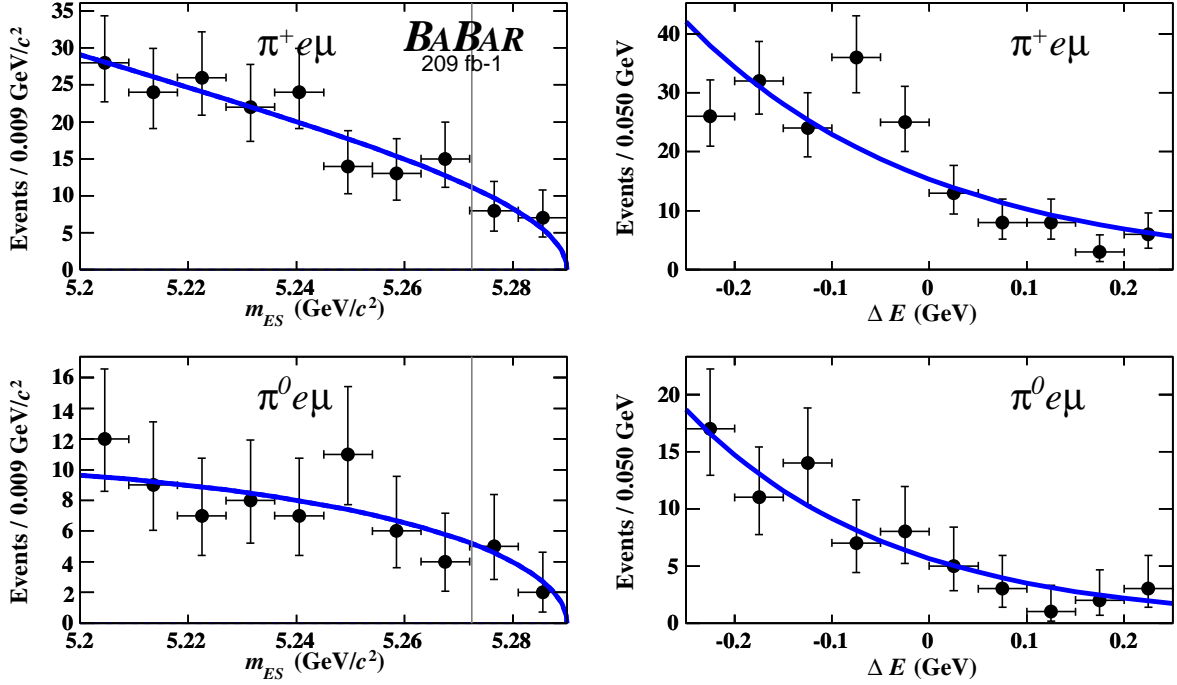


Figure 4.38: Projections of m_{ES} and ΔE with the best fit to the PDF functions from two-dimensional unbinned maximum-likelihood fits to *BABAR* data for the $B \rightarrow \pi e \mu$ modes. The vertical line indicates the edge of the signal region in m_{ES} .

Mode	Fit region expected bkg.	Fit region observed bkg.	Signal region expected bkg.	Signal region observed bkg.
$B^+ \rightarrow \pi^+ e^+ e^-$	107 ± 24	128	0.97 ± 0.22	0.87 ± 0.24
$B^0 \rightarrow \pi^0 e^+ e^-$	34 ± 10	49	0.92 ± 0.27	0.42 ± 0.21
$B^+ \rightarrow \pi^+ \mu^+ \mu^-$	99 ± 17	111	0.77 ± 0.13	0.85 ± 0.24
$B^0 \rightarrow \pi^0 \mu^+ \mu^-$	30 ± 11	22	0.58 ± 0.22	0.17 ± 0.14

Table 4.15: Expected (Monte Carlo) and observed (data) combinatorial background yields and uncertainties in the fit and signal regions.

in the maximum likelihood fit, and bias from fitting a two-component background with a one-dimensional probability density function.

To avoid bias due to low statistics, the *mean* expected background in the signal region is determined from performing the same signal extraction procedure on an ensemble of 10000 toy Monte Carlo experiments. The toy Monte Carlo samples are all generated from the background probability-density-function (equation 3.8) with the best-fit parameters obtained from *BABAR* data. Each of the toy-Monte Carlo experiments is then fitted with the same one-dimensional

probability-density-function with slope parameters and normalization floating, and the signal-region yield is extracted by integrating the resulting PDF over the area of the signal region.

From the distribution of yields from the toy-Monte Carlo experiments, we determine the pull in units of the background uncertainty measured in the real data:

$$\text{pull} = (\text{measured mean} - \text{toy MC mean}) / \text{measured uncertainty}$$

Table 4.16 shows the results of this toy Monte Carlo study. The mean pull is generally negative, *i.e.* the measured values are biased by low statistics toward small values, except for the mode $B^+ \rightarrow \pi^+ e^+ e^-$, where the measured value is larger than the mean of the toy Monte Carlo distributions. The pull distribution width is consistent with unity, except for the low-statistics mode $B^0 \rightarrow \pi^0 \mu^+ \mu^-$, which underestimates errors by 30%.

We correct the observed background in the signal region and its uncertainty, by shifting the central value by the pull mean times the signal region background uncertainty. The signal region background uncertainty is further inflated by a factor equal to the pull width.

Mode	Signal box observed bkg.	Mean toy MC error	pull mean	pull width (σ)	Corr. signal box observed bkg.
$B^+ \rightarrow \pi^+ e^+ e^-$	0.87 ± 0.24	0.26	+0.11	1.00	0.84 ± 0.24
$B^0 \rightarrow \pi^0 e^+ e^-$	0.42 ± 0.21	0.20	-0.08	1.08	0.43 ± 0.23
$B^+ \rightarrow \pi^+ \mu^+ \mu^-$	0.85 ± 0.24	0.23	-0.23	1.06	0.90 ± 0.25
$B^0 \rightarrow \pi^0 \mu^+ \mu^-$	0.17 ± 0.14	0.20	-0.39	1.40	0.23 ± 0.20
$B^+ \rightarrow \pi^+ e \mu$	1.48 ± 0.32	0.33	-0.23	1.04	1.55 ± 0.34
$B^0 \rightarrow \pi^0 e \mu$	1.11 ± 0.39	0.40	-0.34	1.10	1.22 ± 0.43

Table 4.16: Observed combinatorial background yields and uncertainties for 209 fb^{-1} . Tabulated are the baseline fit, the mean error in toy Monte Carlo, the mean pull, the pull distribution width, and the bias corrected signal box yield.

Additionally, there is a potential bias from fitting the on-resonance data with a single PDF function, while the underlying distribution consists of a $B\bar{B}$ component and a continuum component, which may well be different and not well combined as a simple sum. In order to estimate this bias, the on-resonance data has been fitted with a two-component PDF, where one component has all parameters fixed to the shape found for simulated $B\bar{B}$ events, while the other component (modeling the continuum background) has all parameters varying freely in the fit. Toy Monte Carlo studies are then performed based on this two-component parent PDF, and the same procedure as above is used to obtain a bias-corrected signal-region yield. The difference in results from using a two-component PDF compared to a one-component PDF is taken as a systematic uncertainty.

4.6.4 Background shape systematic studies

To gauge the size of the systematic uncertainty due to $m_{\text{ES}}-\Delta E$ correlations in the combinatorial background, the data sample was refitted with a correlated shape as described in section 3.3, and the expected background in the signal region was recomputed.

When the same exercise was performed with simulated $B\bar{B}$ and continuum samples, the $B\bar{B}$ backgrounds exhibit the largest differences while the continuum backgrounds show a negligible difference. The net effect is to decrease the expected background in the signal region by about 10%, which is three to four times smaller than the expected statistical error in this number. The fitted correlation parameters ξ_1 and ξ_2 from equation 3.9 are all statistically consistent with zero.

We also vary the functional form for the ΔE shape, fitting the data with first- and second-degree polynomials in addition to the baseline exponential shape.

The systematic uncertainties determined from these variations in the fitting procedure are given in table 4.17 for each of the modes.

4.7 Results

Once the event selection has been verified by checking that the on-resonance *BABAR* data yields in the fit region agree with expectations, and the total number of *expected* background events in the signal region have been determined, we take a look at the events within the signal region.

4.7.1 Total number of events expected

The total expected background in the signal region is obtained from integrating the PDF from the on-resonance data over this region. The result is summarized in table 4.17. Less than one event is expected in the signal region for each of the penguin modes, with nearly one event expected for the charged modes and 0.3-0.4 events expected in the neutral modes. 1.2-1.5 events are expected in the signal region for the lepton-flavor violating modes.

4.7.2 Total number of events observed

Once we have determined the number of expected background events, we inspect the events in the signal region. Figure 4.39 shows scatter plots of ΔE vs. m_{ES} for all events in the fit region and signal region for all modes. We observe a total of three $B \rightarrow \pi\ell^+\ell^-$ candidates in the signal regions of the $B \rightarrow \pi\ell^+\ell^-$ penguin modes and one candidate in the lepton-flavor violating

Systematic	$\pi^+e^+e^-$	$\pi^0e^+e^-$	$\pi^+\mu^+\mu^-$	$\pi^0\mu^+\mu^-$	$\pi^+e\mu$	$\pi^0e\mu$
$m_{\text{ES}}-\Delta E$ fit	0.824 ± 0.24	0.43 ± 0.23	0.90 ± 0.25	0.23 ± 0.20	1.55 ± 0.34	1.22 ± 0.43
$m_{\text{ES}}-\Delta E$ corr.	± 0.02	± 0.03	± 0.06	± 0.03	± 0.17	± 0.05
ΔE shape	± 0.02	± 0.01	± 0.12	± 0.02	± 0.31	± 0.24
Peaking ($\ell^+\ell^-$)	0.057 ± 0.016	0.009 ± 0.003	0.032 ± 0.008	0.005 ± 0.001	0.0 ± 0.0	0.0 ± 0.0
Peaking (hadronic)	0.0 ± 0.0	0.0 ± 0.0	0.027 ± 0.033	0.035 ± 0.022	0.0 ± 0.0	0.0 ± 0.0
Total	0.90 ± 0.24	0.44 ± 0.23	0.96 ± 0.29	0.27 ± 0.20	1.55 ± 0.49	1.22 ± 0.50

Table 4.17: Estimated number of background events with uncertainties. The uncertainties in the background affect the branching fraction upper limits as additive systematic uncertainties.

$B \rightarrow \pi e\mu$ control modes. As can be seen from the plots, the events are evenly distributed across the fit region, and the number of events observed within the signal regions are consistent with background expectations.

In the $\pi^\pm e^+e^-$ signal region, one event is observed. The background expectation in this mode is 0.90 ± 0.24 events. Two events can be seen just outside the signal region on the low- ΔE side. This is the part of the fit region where $B^+ \rightarrow K^+e^+e^-$ events are expected to accumulate.

In the $\pi^\pm\mu^+\mu^-$ signal region, one event is observed and again this is consistent with the expected 0.96 ± 0.29 background events.

The $B^0 \rightarrow \pi^0\ell^+\ell^-$ modes have smaller statistics. One event is observed in the $\pi^0\mu^+\mu^-$ signal region where 0.27 ± 0.20 background events were expected, and no events are observed in the $\pi^0e^+e^-$ signal region where 0.44 ± 0.23 background events were expected.

Thus, combined for all penguin modes, 2.5 ± 0.5 background events were expected, and 3.0 events were observed. Based on the signal efficiency, tabulated in table 4.12, the signal expected with Standard Model predictions for $\mathcal{B}(B \rightarrow \pi\ell^+\ell^-)$ [47], we expect to have 0.6 ± 0.2 $B^+ \rightarrow \pi^+e^+e^-$ events in the signal region, 0.2 ± 0.1 $B^0 \rightarrow \pi^0e^+e^-$ events, 0.4 ± 0.1 $B^+ \rightarrow \pi^+\mu^+\mu^-$ events and 0.12 ± 0.04 $B^0 \rightarrow \pi^0\mu^+\mu^-$ events in the signal region. Thus, a total of 1.3 ± 0.4 signal events were expected for all modes combined.

No flavor-violating events are expected in the Standard Model, thus for the lepton-flavor violating modes, the Standard Model expectation is to see no events. We have determined that we expect more than one background event in each mode. Since only one event is observed for these modes in total, this is consistent with background and no signal for lepton-flavor-violating modes are seen.

Figure 4.40 shows the m_{ES} and ΔE distributions for the $B \rightarrow \pi\ell^+\ell^-$ events with projections of the best-fit PDF superimposed.

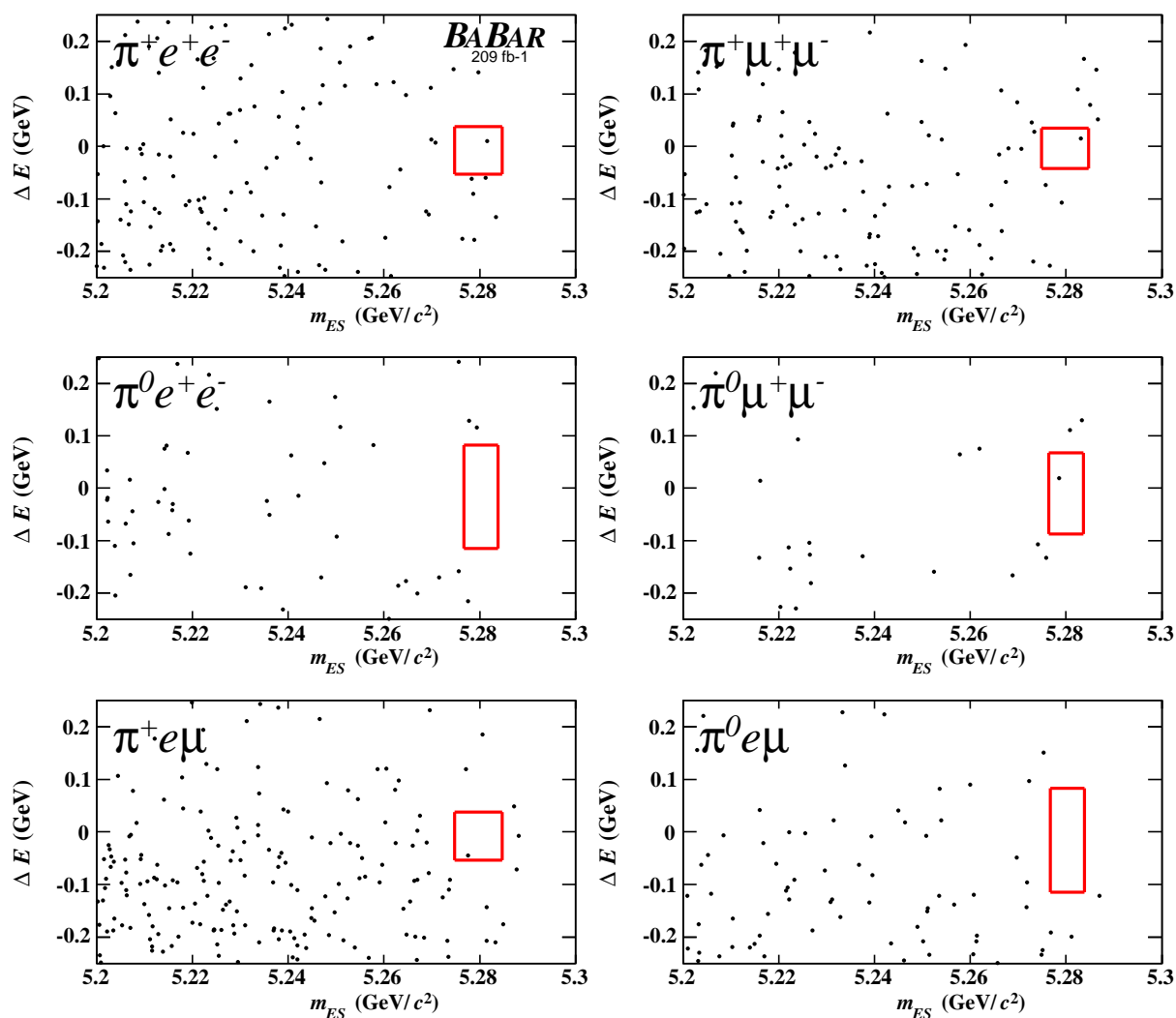


Figure 4.39: Scatter plots of ΔE vs. m_{ES} for all events in the background fit region passing the selection. The small boxes in each of the plots outline the signal region from which signal candidates are selected.

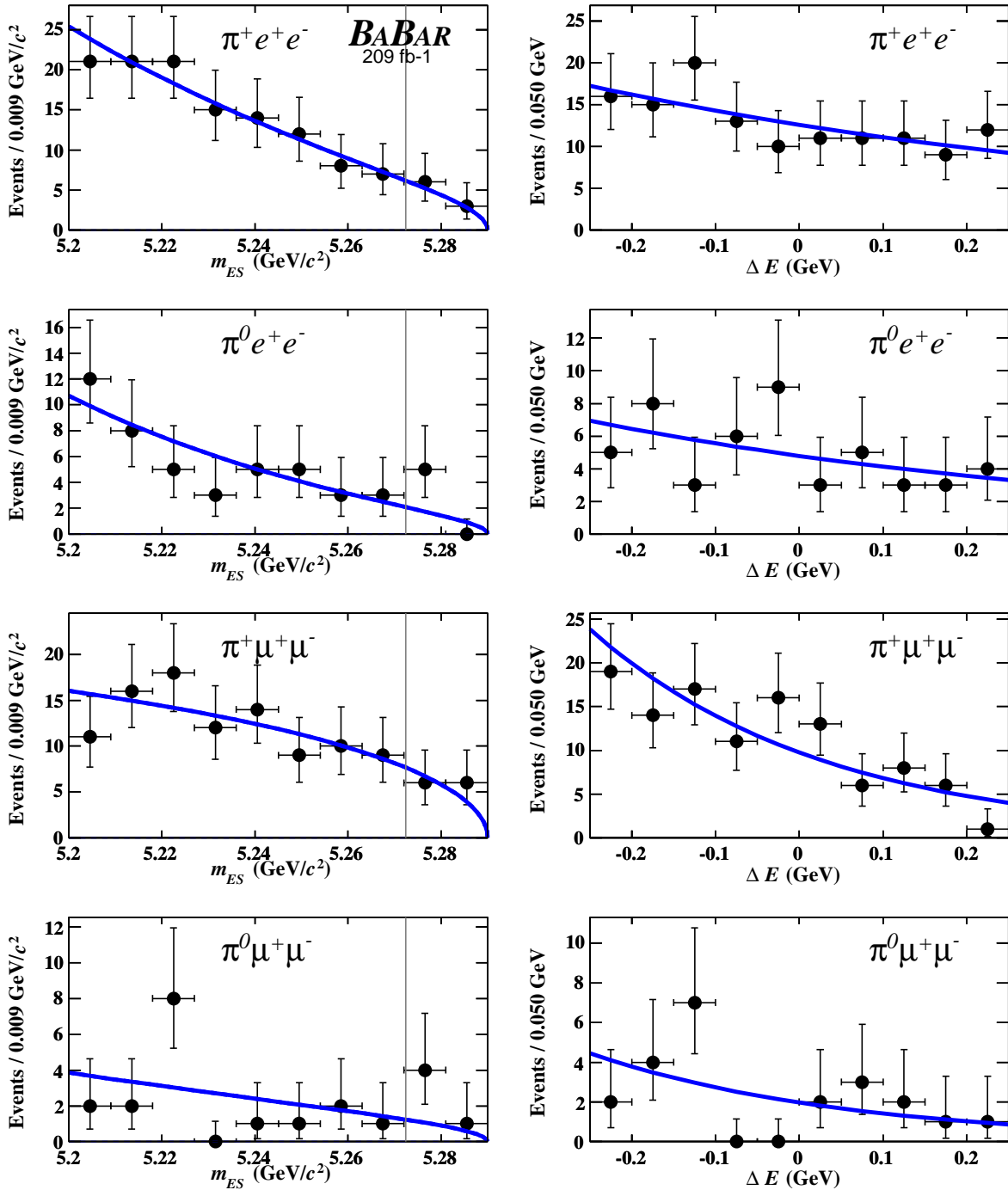


Figure 4.40: Projections of m_{ES} and ΔE of $B \rightarrow \pi \ell^+ \ell^-$ events in the full fit region. Superimposed is the PDF we use to model combinatorial background. The parameters were obtained from two-dimensional unbinned extended maximum-likelihood fits to events outside the signal region, with $m_{\text{ES}} < 5.2724$ (to the left of the grey vertical line).

4.8 Systematic uncertainties

Systematic uncertainties are of two types. The first type consists of multiplicative uncertainties which affect how the observed signal yields are translated into branching fraction measurements. The individual contributions are summarized in section 4.8.1. The second type is uncertainties in the background which additively affect the observed signal yields themselves. These are summarized in section 4.8.2.

4.8.1 Multiplicative systematic uncertainties

Table 4.18 lists the multiplicative systematic uncertainties affecting the signal efficiency. They include the following sources:

- Uncertainty in the tracking efficiency for leptons: after applying the tracking efficiency corrections described in section 2.4.3, we assign a correlated uncertainty of $\pm 0.8\%$ per lepton track.
- Uncertainty in the tracking efficiency for hadron tracks: this is a correlated uncertainty of $\pm 1.4\%$ per hadron track.
- Uncertainty in the efficiency of the electron selection: this is obtained from comparing the electron identification efficiency in data and Monte Carlo based on the charmonium control samples (section 4.4.1). The Monte Carlo is corrected by the data/MC ratio, with the systematic error taken as the uncertainty in this correction, which amounts to $\pm 0.7\%$.
- Uncertainty in the efficiency of the muon selection: this is obtained the same way as the electron systematics (section 4.4.1). The Monte Carlo is corrected by the data/MC ratio, with the systematic error taken as the uncertainty in the correction, which amounts to $\pm 1.9\%$.
- For the uncertainty in the efficiency of the pion selection: we assume an uncertainty of 0.5% for each pion taken, based on a data–MC study of a sample of $B \rightarrow D^0 \pi$ events by [120].
- Uncertainty in the efficiency of π^0 identification: after applying the π^0 efficiency corrections as described in section 2.4.3, the uncertainty is 3.0% per π^0 candidate.

- Uncertainty in the efficiency of the continuum Fisher discriminant selection and the $B\bar{B}$ likelihood-ratio selection is obtained from measuring the efficiency in data and Monte Carlo of these selections combined. The efficiencies are compared using the charmonium control sample, as described in section 4.4.2. The Monte Carlo events are corrected by data/MC ratio, with the systematic error taken as the error on the correction. The size of this uncertainty ranges from 1.4% in the $B \rightarrow \pi e^+ e^-$ modes to 1.9% for the $B^0 \rightarrow \pi^0 \mu^+ \mu^-$ mode.
- Statistical uncertainties in the signal efficiencies originate from the size of the simulated sample used for efficiency evaluation. We have about 260 000 simulated signal events for each mode, so the statistical uncertainty is small (0.1%).
- The estimated number of $B\bar{B}$ events in our data sample has an uncertainty of 1.1%.
- The uncertainties due to the signal efficiency of the m_{ES} and ΔE selection requirements are determined from:
 - The measured mean and width of these distributions in charmonium control samples. For $B^+ \rightarrow \pi^+ \ell^+ \ell^-$, we use samples of $B \rightarrow J/\psi K^+$ events, in which the mean and width are precisely bounded, and we assign a total systematic uncertainty of $\sim 0.7\%$; for $B^0 \rightarrow \pi^0 \ell^+ \ell^-$, we use samples of $B \rightarrow J/\psi \pi^0$ events, which have limited statistics and introduce a total systematic uncertainty of 7%.
 - For the electron modes, we allow for a larger or smaller bremsstrahlung tail in the ΔE distribution, introducing a systematic uncertainty of 1.2-1.3%.
- Uncertainties in signal efficiency resulting from use of different theoretical models to describe the signal arise mainly from the variation of signal efficiency as a function of q^2 . The largest theoretical uncertainty is due to form-factor predictions, and we have investigated the effect of different models in section 4.4.4. The model dependence systematic is taken to be the maximum difference between the alternative models and the baseline model, and ranges from 1.1% for $B^+ \rightarrow \pi^+ e^+ e^-$ to 7.3% for $B^0 \rightarrow \pi^0 \mu^+ \mu^-$.

The total multiplicative systematic uncertainty is the sum in quadrature of these relative uncertainties for the individual sources, with the exception of the tracking efficiency uncertainties for leptons and hadrons, which are taken to be 100% correlated.

Systematic	$\pi^+ e^+ e^-$	$\pi^0 e^+ e^-$	$\pi^+ \mu^+ \mu^-$	$\pi^0 \mu^+ \mu^-$	$\pi^+ e \mu$	$\pi^0 e \mu$
Trk eff.	± 3.0	± 1.6	± 3.0	± 1.6	± 3.0	± 1.6
Electron ID	± 0.7	± 0.7			± 0.4	± 0.4
Muon ID			± 1.9	± 1.9	± 1.0	± 1.0
Pion ID	± 0.5		± 0.5		± 0.5	
π^0 ID		± 3.0		± 3.0		± 3.0
Fisher and $B\bar{B}$ likelihood	± 1.4	± 1.4	± 1.7	± 1.9	± 1.4	± 1.4
MC statistics	± 0.1	± 0.1	± 0.1	± 0.1	± 0.1	± 0.1
$B\bar{B}$ counting	± 1.1	± 1.1	± 1.1	± 1.1	± 1.1	± 1.1
signal m_{ES} model	± 0.3	± 5.1	± 0.4	± 4.9	± 0.3	± 5.1
signal ΔE model	± 0.6	± 5.1	± 0.5	± 5.4	± 0.5	± 5.2
signal ΔE radiative tail	± 1.2	± 1.3			± 1.0	± 1.4
Model dependence	± 1.1	± 3.3	± 4.2	± 7.3	± 3.0	± 3.0
Total	± 4.0	± 8.9	± 5.9	± 11.2	± 4.9	± 8.9

Table 4.18: The sources of systematic uncertainty in the upper limit on the branching fraction due to signal efficiency (%).

4.8.2 Background systematic uncertainties

Uncertainties in background expectations affect the branching fraction upper limit in an additive way. The additive systematic uncertainties considered here have been summarized in table 4.17 and include the following components:

- Uncertainty due to the shape assumed for combinatorial backgrounds:
 - Uncertainties from the $m_{\text{ES}}-\Delta E$ fit is the dominant systematic effect. They are evaluated by varying each of the parameters of the fit by $\pm 1\sigma$, for each change recomputing the signal-region expectation and finally adding the deviations from each in quadrature. On top of this, a small correction is applied from the bias studies described in section 4.6.3.
 - Uncertainties due to $m_{\text{ES}}-\Delta E$ correlations are evaluated by performing a background estimation fit which allows the m_{ES} Argus slope to depend on ΔE (see section 4.6.4).
 - ΔE shape uncertainties are evaluated from using alternative probability density functions (linear, quadratic), described in section 4.6.4.
- Uncertainties in peaking background estimates:
 - The uncertainty in hadronic peaking background yields are taken from the uncertainty of the yield obtained from the one-dimensional m_{ES} χ^2 -fit in section 4.5.1.

- The uncertainty in peaking background with real leptons (section 4.5.1), estimated from simulated background samples, are due to uncertainties in the branching fraction assumed [54].

The total additive systematic uncertainty is the sum in quadrature of the absolute uncertainties listed, as summarized in table 4.17.

4.9 Branching fraction upper limit

The branching fraction \mathcal{B} is generally calculated by

$$\mathcal{B}(B \rightarrow \pi \ell^+ \ell^-) = \frac{N_{\text{observed}} - N_{\text{background}}}{N_B \times \varepsilon} \quad (4.4)$$

with N_{observed} and $N_{\text{background}}$ being the observed number of events and expected background in the signal region, respectively. N_B is the number of B -mesons in the *BABAR* data sample (given in table 2.1), and ε is the efficiency for detecting $B \rightarrow \pi \ell^+ \ell^-$ decays.

With the observed events consistent with background, no evidence for a $B \rightarrow \pi \ell^+ \ell^-$ signal is found. Thus we set an upper limit on the $B \rightarrow \pi \ell^+ \ell^-$ branching fraction using a frequentist method which takes into account both the uncertainties in the signal sensitivity ($N_B \times \varepsilon$) and the expected background ($N_{\text{background}}$) [121, 122]. The signal efficiency varies by mode and is given in table 4.19. The number of B -meson decays is $N_{B^\pm} = N_{B^0(\overline{B}^0)} = 230.15$ million.

The upper limit is computed at 90% confidence level, meaning that in the one-sided confidence interval there is 10% probability or less that the true value of the parameter (\mathcal{B}) is above this interval. This is basically a conventional frequentist limit, following an approach due to Neyman [123]. The uncertainties in sensitivity and background estimates introduces a Bayesian viewpoint. However, the main source of uncertainty – the Poisson statistics of the number of events – is treated in a frequentist fashion.

A toy Monte Carlo technique is used to compute the confidence limits. For a given number of observed events (n), background expectation ($N_{\text{bkg.}} \pm \sigma_{N_{\text{bkg.}}}$) and sensitivity ($S \pm \sigma_S$), a Poisson distribution is constructed. Here, both background and sensitivity are assumed to have Gaussian uncertainties. Based on this Poisson probability-density-function, ensembles of toy Monte Carlo experiments are generated. The branching fraction upper limit at 90% confidence level corresponds to the value for which the toy Monte Carlo experiments yield higher branching fractions in less than 10% of the experiments. By setting the sensitivity to unity, we similarly obtain the upper limit on the number of signal events at 90% confidence level, given as 'Events

Mode	Observed Events	Expected Background	Events U.L. 90% C.L.	Signal Efficiency	\mathcal{B} U.L. 90% C.L. (10^{-7})
$B^+ \rightarrow \pi^+e^+e^-$	1	0.90 ± 0.24	3.01 (2.99)	$7.1 \pm 0.3\%$	1.84 (1.83)
$B^0 \rightarrow \pi^0e^+e^-$	0	0.44 ± 0.23	1.89 (1.86)	$5.7 \pm 0.5\%$	1.44 (1.42)
$B^+ \rightarrow \pi^+\mu^+\mu^-$	1	0.96 ± 0.29	2.96 (2.93)	$4.7 \pm 0.3\%$	2.74 (2.71)
$B^0 \rightarrow \pi^0\mu^+\mu^-$	1	0.27 ± 0.20	3.64 (3.62)	$3.1 \pm 0.3\%$	5.12 (5.10)
$B^+ \rightarrow \pi^+e\mu$	1	1.55 ± 0.49	2.43 (2.34)	$6.3 \pm 0.3\%$	1.69 (1.63)
$B^0 \rightarrow \pi^0e\mu$	0	1.22 ± 0.50	1.21 (1.08)	$3.7 \pm 0.3\%$	1.42 (1.28)
$B^+ \rightarrow \pi^+\ell^+\ell^-$					1.16 (1.15)
$B^0 \rightarrow \pi^0\ell^+\ell^-$					1.16 (1.15)
$B \rightarrow \pi\ell^+\ell^-$					0.946 (0.936)
$B \rightarrow \pi e\mu$					0.920 (0.83)

Table 4.19: Results of the $B \rightarrow \pi\ell^+\ell^-$ analysis: The table includes observed signal candidate events, expected background, signal yield upper limit at 90% confidence level, signal efficiency, and the branching fraction upper limit at 90% confidence level. The numbers in parentheses are limits evaluated without the inclusion of systematic uncertainties. The combined limits at the bottom are derived from simultaneous limits calculated from the individual modes.

U.L.’ in table 4.19. This number corresponds to the number of events for which 10% of the toy experiments yield a larger number of events.

To evaluate the effect of the uncertainties in signal sensitivity and background, we have computed the upper limits without uncertainties as well. The numbers are given in parentheses in table 4.19. As expected, the upper limits decrease when uncertainties are removed.

To combine results from the individual modes, we use the quark-model isospin relation between π^\pm and π^0 as well as the world average [54] of B -meson lifetime ratio $\tau_{B^+}/\tau_{B^0} = 1.071 \pm 0.009$ as a constraint:

$$\mathcal{B}(B \rightarrow \pi\ell^+\ell^-) \equiv \frac{1}{2} \left\{ \mathcal{B}(B^+ \rightarrow \pi^+\ell^+\ell^-) + 2\frac{\tau_{B^+}}{\tau_{B^0}} \mathcal{B}(B^0 \rightarrow \pi^0\ell^+\ell^-) \right\} \quad (4.5)$$

The most significant upper limit is obtained from the $B^+ \rightarrow \pi^+e^+e^-$ channel, which yields $\mathcal{B}(B^+ \rightarrow \pi^+e^+e^-) < 1.84 \times 10^{-7}$ at 90% confidence level. The upper limit from the $B^+ \rightarrow \pi^+\mu^+\mu^-$ channel is considerably less restrictive due to the much lower detection efficiency of this mode. Here we obtain $\mathcal{B}(B^+ \rightarrow \pi^+\mu^+\mu^-) < 2.74 \times 10^{-7}$ at 90% confidence level.

The best limit in the neutral modes is obtained from the $B^0 \rightarrow \pi^0e^+e^-$ channel, where no events were observed. Here we find $\mathcal{B}(B^0 \rightarrow \pi^0e^+e^-) < 1.44 \times 10^{-7}$ at 90% confidence level. Since the branching fraction for the neutral modes are expected to be half of the corresponding

charged mode, this limit is really less sensitive than the one obtained for the charged mode. The background expectation is also low in this mode, contributing to a higher limit. The $B^0 \rightarrow \pi^0 \mu^+ \mu^-$ channel is the least restrictive of the $B \rightarrow \pi \ell^+ \ell^-$ channels with $\mathcal{B}(B^0 \rightarrow \pi^0 \mu^+ \mu^-) < 5.12 \times 10^{-7}$ at 90% confidence level. Here the background expectation is lowest and we do see one event.

Assuming the partial widths of $B \rightarrow \pi \ell^+ \ell^-$ to electrons and muons are equal, the limits for the two decay modes can be simply combined to provide a combined limit of 1.16×10^{-7} for $B^+ \rightarrow \pi^+ \ell^+ \ell^-$ and 1.16×10^{-7} for $B^0 \rightarrow \pi^0 \ell^+ \ell^-$.

Taking isospin symmetry into account (equation 4.5), the four $B \rightarrow \pi \ell^+ \ell^-$ modes are combined, yielding

$$\mathcal{B}(B \rightarrow \pi \ell^+ \ell^-) < 0.95 \times 10^{-7} \quad \text{at 90\% C.L.}$$

For the lepton-flavor violating modes, the most sensitive limit is again obtained from the charged mode which has a branching fraction of a factor two larger than the neutral mode due to isospin. The $B^+ \rightarrow \pi^+ e \mu$ channel has a higher detection efficiency and larger background expected than the neutral mode. Thus, this limit is the most restrictive despite the one event observed. The limit obtained is $\mathcal{B}(B^+ \rightarrow \pi^+ e \mu) < 1.69 \times 10^{-7}$ at 90% confidence level. The limit obtained from the $B^0 \rightarrow \pi^0 e \mu$ channel where no events are seen is $\mathcal{B}(B^0 \rightarrow \pi^0 e \mu) < 1.42 \times 10^{-7}$ at 90% confidence level.

A combined limit is obtained for the lepton-flavor violating modes $B \rightarrow \pi e \mu$, assuming isospin symmetry analogous to equation 4.5. The combined limit is

$$\mathcal{B}(B \rightarrow \pi e \mu) < 0.92 \times 10^{-7} \quad \text{at 90\% C.L.}$$

Chapter 5

Conclusion

Electroweak penguin processes constitute an exciting laboratory for searching for effects of physics beyond the Standard Model. Already $b \rightarrow s\gamma$ measurements have become precision measurements, and the $B \rightarrow K^*\ell^+\ell^-$ analysis is beginning to yield sufficiently large sample of events that allow for measurements of forward-backward asymmetries, branching fraction ratios and other model-independent quantities that test the Standard Model are put constraints on models of new physics. So far, no measurements have been in disagreement with the Standard Model, but they also allow for many new physics scenarios.

The rare semileptonic penguin decay $B \rightarrow \pi\ell^+\ell^-$ constitute another test of the Standard Model. This mode has never been observed, and is expected to have a branching fraction of about 3.3×10^{-8} [47]. A search for this B -meson decay mode has been performed using a sample of $(230.1 \pm 2.5) \times 10^6$ $B\bar{B}$ pairs produced at the $\Upsilon(4S)$ resonance in the *BABAR* experiment. No excess of events is seen in the signal region, and an upper limit is set for the lepton-flavor-averaged branching fraction at 90% confidence level:

$$\mathcal{B}(B \rightarrow \pi\ell^+\ell^-) < 9.5 \times 10^{-8},$$

This upper limit is more than four orders of magnitude lower than the previous limits set for these decay modes [78]. This is about a factor of 3 ± 1 above the Standard Model prediction. A branching fraction of 4.1×10^{-8} has been predicted in the two-Higgs doublet model [47], and our result does not put any constraint on this model yet. Larger discrepancies may possibly occur in other models, but have not been explored theoretically in the $b \rightarrow d\ell^+\ell^-$ transition yet.

In addition, an upper limit on the branching fraction of the lepton-flavor-violating modes

$B \rightarrow \pi e \mu$ is set at 90% confidence level:

$$\mathcal{B}(B \rightarrow \pi e \mu) < 9.2 \times 10^{-8}.$$

This is the first search for $B \rightarrow \pi \ell^+ \ell^-$ events performed by the B factory experiments. With anticipated final samples of order 1 ab^{-1} , and with the small backgrounds observed in this analysis, it may be possible in the future to achieve an experimental sensitivity comparable to the Standard Model prediction. Figure 5.1 shows a projection of the current upper limit result for $\mathcal{B}(B \rightarrow \pi \ell^+ \ell^-)$, assuming no more events are seen despite the increasing luminosity. Figure 5.2 shows a similarly naive extrapolation of the significance, expressed as S/\sqrt{B} , based on the current results. Here we assume that signal and background both scale proportional to luminosity.

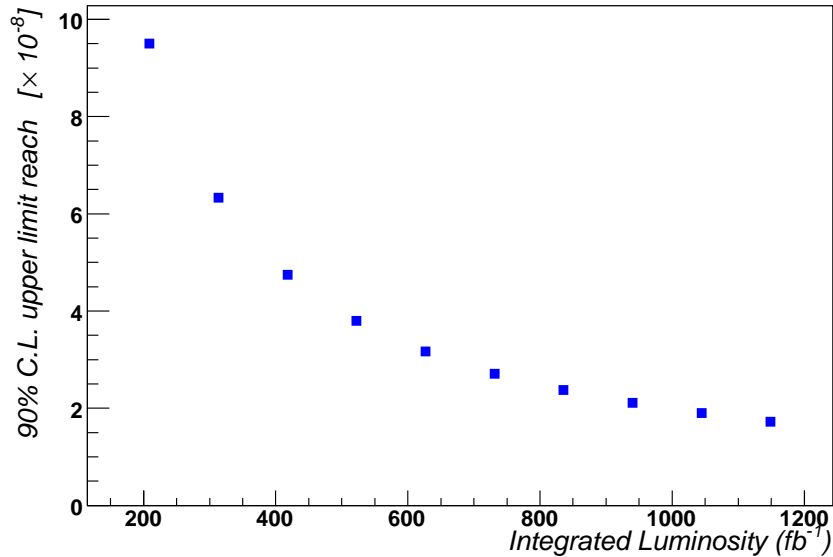


Figure 5.1: Branching-fraction upper limit vs. integrated luminosity projected for the search for $\mathcal{B}(B \rightarrow \pi \ell^+ \ell^-)$ events in the future. A data sample of 1000 fb^{-1} is expected by the end of *BABAR*.

Based on the estimate given in figure 5.1, the upper limit reach with 1 ab^{-1} is comparable to the Standard Model prediction of 3.3×10^{-8} . If there is also new physics present which contribute constructively to these decays, an observation may be at hand.

Additionally, possible improvements to the analysis are within reach. For the *BABAR* data collected during 2005 and later, a new muon detection system is used. This may improve the significance of the muon modes. Improved background rejection would also improve the statistical significance compared to the estimate in figure 5.2. With increased statistics, one can also do a

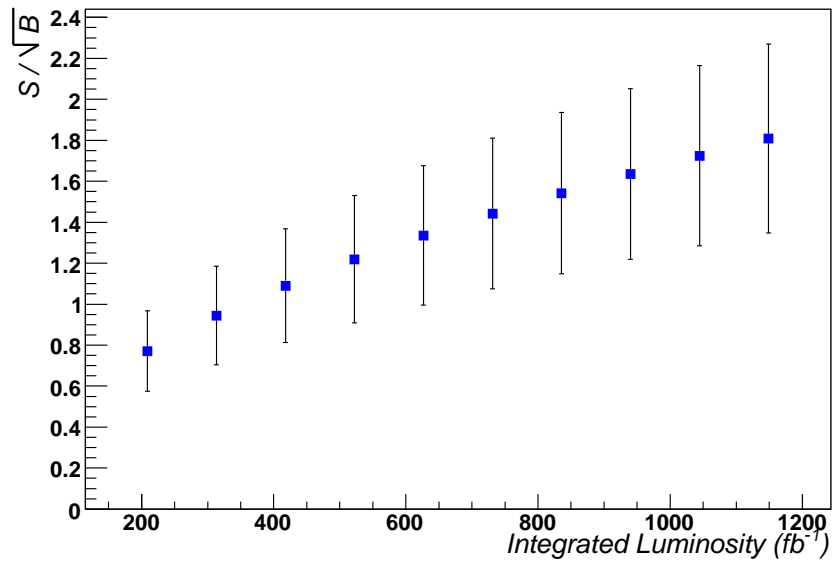


Figure 5.2: Significance (S/\sqrt{B}) vs. integrated luminosity projected for a future $\mathcal{B}(B \rightarrow \pi\ell^+\ell^-)$ measurement. A data sample of 1000 fb^{-1} is expected by the end of *BABAR*.

maximum likelihood fit and improve somewhat from this method. Thus, with some reachable improvements to the analysis, it is very likely that *BABAR* is able to detect $B \rightarrow \pi\ell^+\ell^-$ events before PEP-II switches off in 2008.

Bibliography

- [1] R. P. Feynman, Phys. Rev. **76**, 769 (1949); Phys. Rev. **84**, 108 (1951).
J. S. Schwinger, Phys. Rev. **74** (1948) 1439; Phys. Rev. **75** (1948) 651; Phys. Rev. **76** (1949) 790.
S. I. Tomonaga, Phys. Rev. **74**, 224 (1948).
F. J. Dyson, Phys. Rev. **75** (1949) 1736; Phys. Rev. **85** (1952) 631.
- [2] S. Glashow, Nucl. Phys **22** (1961) 579
S. Weinberg, Phys. Rev. Lett. **19** (1967) 1264
A. Salam, *in*: Elementary Particle Physics, relativistic groups and analyticity, Nobel Symp. No 8, ed. N. Svartholm (Almqvist and Wiksell, Stockholm 1968) p. 367.
- [3] D. J. Gross and F. Wilczek, Phys. Rev. Lett. **30**, 1343 (1973).
H. D. Politzer, Phys. Rev. Lett. **30**, 1346 (1973).
D. J. Gross and F. Wilczek, Phys. Rev. D **8**, 3633 (1973).
H. D. Politzer, Phys. Rept. **14**, 129 (1974).
- [4] For an introduction to the Standard Model, see *e.g.*
I. Ofte, Cand. Scient. thesis, University of Bergen (2001).
- [5] For an introduction to gauge theories, see *e.g.*
A. W. Borgland, Dr. Scient thesis, University of Bergen (1999)
- [6] H. Yukawa, Proc. Phys. Math. Soc. Jap. **17** (1935) 48.
- [7] M. Gell-Mann, Phys. Lett. **8**, 214 (1964).
M. Gell-Mann, Phys. Rev. Lett. **12**, 155 (1964).
R. P. Feynman, M. Gell-Mann and G. Zweig, Phys. Rev. Lett. **13** (1964) 678.
- [8] G. Arnison *et al.* [UA1 Collaboration], Phys. Lett. B **126**, 398 (1983).
G. Arnison *et al.* [UA1 Collaboration], Phys. Lett. B **122**, 103 (1983).
M. Banner *et al.* [UA2 Collaboration], Phys. Lett. B **122**, 476 (1983).
- [9] S. Myers and E. Picasso, Sci. Am. **263** (1990) 34.
R. Assmann, M. Lamont and S. Myers, Nucl. Phys. Proc. Suppl. **109B** (2002) 17.
- [10] J. D. Lykken, arXiv:hep-ph/0609274.

- [11] P. W. Higgs, Phys. Lett. **12**, 132 (1964).
P. W. Anderson, Phys. Rev. **130** (1963) 439.
- [12] R. N. Cahn, Rev. Mod. Phys. **68**, 951 (1996).
- [13] J. Wess and B. Zumino, Phys. Lett. B **49**, 52 (1974).
- [14] P. F. Harrison and H. R. Quinn [BABAR Collaboration], *The BaBar physics book: Physics at an asymmetric B factory*, SLAC-R-0504, Oct 1998. 1056pp.
- [15] C. Jarlskog (Ed.) *CP violation*, Singapore: World Scientific (1989) 723 p (Advanced Series on Directions in High Energy Physics, 3).
- [16] A. Bondar [BELLE Collaboration], Nucl. Instrum. Meth. A **408** (1998) 64.
- [17] H. A. Gustafsson, Nucl. Phys. A **774** (2006) 361.
and references therein.
- [18] N. Cabibbo, Physical Review Letters **10** (1963), 531;
M. Kobayashi and K. Maskawa, Progress of Theoretical Physics **49** (1973), 652.
- [19] L. Wolfenstein, Physical Review Letters 51 (1983), 1945.
- [20] S. L. Glashow, J. Iliopoulos and L. Maiani, Phys. Rev. D **2**, 1285 (1970).
- [21] G. Burdman, Phys. Rev. D **52**, 6400 (1995).
- [22] J. L. Hewett and J. D. Wells, Phys. Rev. D **55**, 5549 (1997).
- [23] A. Ali, E. Lunghi, C. Greub and G. Hiller, Phys. Rev. D **66**, 034002 (2002)
[arXiv:hep-ph/0112300].
- [24] G. Eilam, J. L. Hewett, and T. G. Rizzo, Phys. Rev. D **34**, 2773 (1986);
T. M. Aliev, A. Ozpineci, and M. Savci, Eur. Phys. J. **C29**, 265 (2003).
- [25] S. Davidson, D. C. Bailey, and B. A. Campbell, Z. Phys. C **61**, 613 (1994).
- [26] B. Aubert [BABAR Collaboration], Phys. Rev. D **73**, 092001 (2006)
- [27] Belle Collaboration, M. Iwasaki *et al.*, Phys. Rev. D **72**, 092005 (2005);
BABAR Collaboration, B. Aubert *et al.*, Phys. Rev. Lett. **93**, 081802 (2004);
Belle Collaboration, A. Ishikawa *et al.*, Phys. Rev. Lett. **91**, 261601 (2003).
- [28] G. Buchalla, A. J. Buras and M. E. Lautenbacher, Rev. Mod. Phys. **68** (1996) 1125
- [29] A. J. Buras, arXiv:hep-ph/9806471.
- [30] R. Ammar *et al.* [CLEO Collaboration], Phys. Rev. Lett. **71**, 674 (1993).

- [31] M. S. Alam *et al.* [CLEO Collaboration], Phys. Rev. Lett. **74**, 2885 (1995).
S. Ahmed *et al.* [CLEO Collaboration], arXiv:hep-ex/9908022.
- [32] CLEO Collaboration, P. Avery *et al.*, Phys. Lett. B **183** (1987) 429.
- [33] CLEO Collaboration, A. Beam *et al.*, Phys. Rev. D **35** (1987) 3533.
- [34] ARGUS Collaboration, W. Schmidt-Parzefall. Nucl. Phys. B (Proc. Suppl.) **3** (1988) 257.
- [35] J. Kaneko *et al.* [Belle Collaboration], Phys. Rev. Lett. **90**, 021801 (2003)
- [36] B. Aubert *et al.* [BABAR Collaboration], Phys. Rev. Lett. **93**, 081802 (2004)
- [37] K. G. Wilson and W. Zimmermann, Commun. Math. Phys. **24**, 87 (1972).
- [38] W. A. Bardeen, A. J. Buras, D. W. Duke and T. Muta, Phys. Rev. D **18**, 3998 (1978).
- [39] C. Bobeth, M. Misiak and J. Urban, Nucl. Phys. B **574**, 291 (2000)
- [40] M. Gell-Mann and F. E. Low, Phys. Rev. **95** (1954) 1300.
G. 't Hooft, Nucl. Phys. B **61** (1973) 455.
S. Weinberg, Phys. Rev. D **8**, 3497 (1973).
- [41] A. J. Buras and M. Munz, "Effective Hamiltonian for $B \rightarrow X(s) e^+ e^-$ beyond leading logarithms in Phys. Rev. D **52**, 186 (1995)
- [42] K. Adel and Y. P. Yao, Phys. Rev. D **49**, 4945 (1994)
- [43] A. J. Buras, M. Misiak, M. Munz and S. Pokorski, Nucl. Phys. B **424**, 374 (1994)
- [44] C. Greub and T. Hurth, Phys. Rev. D **56**, 2934 (1997)
- [45] A. J. Buras, A. Kwiatkowski and N. Pott, Nucl. Phys. B **517**, 353 (1998)
- [46] F. Kruger and L. M. Sehgal, Phys. Rev. D **55**, 2799 (1997)
- [47] T. M. Aliev and M. Savci, Phys. Rev. D **60**, 014005 (1999)
- [48] N. Isgur and M. B. Wise, Adv. Ser. Direct. High Energy Phys. **10**, 549 (1992).
- [49] M. Neubert, Phys. Rept. **245**, 259 (1994)
- [50] P. Ball and R. Zwicky, Phys. Rev. D **71**, 014015 (2005)
- [51] I. I. Balitsky, V. M. Braun and A. V. Kolesnichenko, Nucl. Phys. B **312**, 509 (1989).
V. L. Chernyak and I. R. Zhitnitsky, Nucl. Phys. B **345** (1990) 137.

- [52] T. Onogi, eConf **C0304052**, WG112 (2003)
J. Shigemitsu *et al.*, Nucl. Phys. Proc. Suppl. **140**, 464 (2005)
M. Okamoto *et al.*, Nucl. Phys. Proc. Suppl. **140**, 461 (2005)
- [53] D. Becirevic, arXiv:hep-ph/0211340.
- [54] Particle Data Group, W.-M. Yao *et al.*, J. Phys. G **33**, 1 (2006)
- [55] B. Aubert *et al.* [BABAR Collaboration], Phys. Rev. D **70**, 112006 (2004)
- [56] M. Nakao *et al.* [BELLE Collaboration], Phys. Rev. D **69**, 112001 (2004)
- [57] T. E. Coan *et al.* [CLEO Collaboration], Phys. Rev. Lett. **86**, 5661 (2001)
- [58] S. W. Bosch and G. Buchalla, Nucl. Phys. B **621**, 459 (2002)
- [59] A. Ali and A. Y. Parkhomenko, Eur. Phys. J. C **23**, 89 (2002)
- [60] B. Aubert *et al.* [BABAR Collaboration], Phys. Rev. Lett. **97**, 171803 (2006)
- [61] B. Aubert *et al.* [BABAR Collaboration], Phys. Rev. D **72**, 052004 (2005)
- [62] P. Koppenburg *et al.* [Belle Collaboration], Phys. Rev. Lett. **93**, 061803 (2004)
- [63] S. Nishida *et al.* [BELLE Collaboration], Phys. Rev. Lett. **93**, 031803 (2004)
- [64] S. Chen *et al.* [CLEO Collaboration], Phys. Rev. Lett. **87**, 251807 (2001)
- [65] T. E. Coan *et al.* [CLEO Collaboration], Phys. Rev. Lett. **86**, 5661 (2001)
- [66] E. Barberio *et al.* [Heavy Flavor Averaging Group (HFAG)], arXiv:hep-ex/0603003.
- [67] M. Misiak and M. Steinhauser, arXiv:hep-ph/0609241.
M. Misiak *et al.*, arXiv:hep-ph/0609232. (Submitted to Phys.Rev.Lett.)
- [68] A. J. Buras, A. Czarnecki, M. Misiak and J. Urban, Nucl. Phys. B **631**, 219 (2002)
- [69] T. Becher and M. Neubert, arXiv:hep-ph/0610067.
- [70] E. Lunghi, arXiv:hep-ph/0205135.
- [71] H. H. Asatrian, H. M. Asatrian, C. Greub and M. Walker, Phys. Lett. B **507**, 162 (2001);
Phys. Rev. D **65**, 074004 (2002)
- [72] A. Ali, G. Hiller, L. T. Handoko and T. Morozumi, Phys. Rev. D **55**, 4105 (1997)
- [73] M. Iwasaki *et al.* [Belle Collaboration], Phys. Rev. D **72**, 092005 (2005)
- [74] A. Ali, arXiv:hep-ph/0210183.

- [75] K. Abe *et al.*, Phys. Rev. Lett. **96**, 221601 (2006)
- [76] B. Aubert *et al.* [BABAR Collaboration], arXiv:hep-ex/0607099.
- [77] A. Ali, E. Lunghi and A. Y. Parkhomenko, Phys. Lett. B **595**, 323 (2004)
- [78] A. Weir *et al.*, Phys. Rev. D **41**, 1384 (1990).
- [79] G. Hiller and F. Kruger, Phys. Rev. D **69**, 074020 (2004)
- [80] P. Ball and R. Zwicky, JHEP **0604**, 046 (2006)
- [81] [CDF - Run II Collaboration], Phys. Rev. Lett. **97**, 062003 (2006)
- [82] For an introduction to $B_s^0 - \overline{B}_s^0$ mixing formalism, see *e.g.*
A. W. Borgland, Dr. Scient thesis, University of Bergen (1999)
- [83] T. M. Aliev, D. A. Demir, E. Iltan and N. K. Pak, Phys. Rev. D **54**, 851 (1996)
- [84] F. Kruger, L. M. Sehgal, N. Sinha and R. Sinha, Phys. Rev. D **61**, 114028 (2000)
Erratum-ibid. D **63**, 019901 (2001)
- [85] F. Kruger and L. M. Sehgal, arXiv:hep-ph/9711301.
- [86] F. Kruger and L. M. Sehgal, Phys. Rev. D **56**, 5452 (1997)
Erratum-ibid. D **60**, 099905 (1999)
- [87] P. Colangelo *et al.*, Phys. Rev. D **53**, 3672 (1996)
Erratum: P. Colangelo *et al.*, Phys. Rev. D **57**, 3186 (1998)
- [88] D. Melikhov and N. Nikitin, arXiv:hep-ph/9609503.
D. Melikhov, Phys. Lett. B **380**, 363 (1996)
D. Melikhov, Phys. Rev. D **53**, 2460 (1996)
- [89] D. Melikhov and B. Stech, Phys. Rev. D **62**, 014006 (2000)
- [90] G. Buchalla, G. Hiller and G. Isidori, Phys. Rev. D **63**, 014015 (2001)
- [91] A. Ali, P. Ball, L. T. Handoko and G. Hiller, Phys. Rev. D **61**, 074024 (2000)
- [92] G. Erkol and G. Turan, JHEP **0202**, 015 (2002)
- [93] B. Aubert *et al.* [BABAR Collaboration], Nucl. Instrum. Meth. A **479**, 1 (2002)
- [94] "PEP-II: An Asymmetric B Factory. Conceptual Design Report," SLAC-418, LBL-5379,
June 1993
- [95] J. Seeman *et al.*, SLAC-PUB-11727

- [96] M. H. Kelsey [BABAR Collaboration], Nucl. Instrum. Meth. A **535**, 206 (2004).
- [97] P. Billoir, Nucl. Instrum. Meth. A **225** (1984) 352.
- [98] I. Adam *et al.* [BABAR-DIRC Collaboration], Nucl. Instrum. Meth. A **538**, 281 (2005).
- [99] A. Drescher *et al.*, Nucl. Instrum. Meth. A **237**, 464 (1985).
- [100] R. Sinkus and T. Voss, Nucl. Instrum. Meth. A **391**, 360 (1997).
F. Zernike, Physica 1, 689 (1934).
- [101] T. Brandt, Ph.D. thesis, Der Technischen Universität Dresden (2001)
<http://hep.phy.tu-dresden.de/~tbrandt/thesis>
BABAR analysis document No. 391.
- [102] M. Kocian [BABAR Collaboration], SLAC-PUB-10170 *Presented at 10th International Conference on Calorimetry in High Energy Physics (CALOR 2002), Pasadena, California, 25-30 Mar 2002*
- [103] R. Santonico and R. Cardarelli, Nucl. Instrum. Meth. **187** (1981) 377.
- [104] J. D. Bjorken and S. D. Drell, "Bremsstrahlung." 7.6 in *Relativistic Quantum Mechanics*. New York: McGraw-Hill, pp. 120-127, 1964.
The phenomenon was first discovered by Nikola Tesla during research conducted between 1888 and 1897.
- [105] T. Sjostrand, L. Lonnblad and S. Mrenna, "PYTHIA 6.2: Physics and manual,"
arXiv:hep-ph/0108264.
- [106] G. C. Fox and S. Wolfram, Nucl. Phys. **B149** (1979) 413
- [107] Legendre, A. M. "Sur l'attraction des Sphroides." Mm. Math. et Phys. presents l'Ac. r. des. sc. par divers savants 10, 1785.
- [108] S. Brandt, Ch. Peyrou, R. Sosnowski and A. Wroblewski, Phys. Lett. **12** (1964) 57;
E. Fahri, Phys. Rev. Lett. **39** (1977) 1587
- [109] R. Brun and F. Rademakers, ROOT - An Object Oriented Data Analysis Framework, Proceedings AIHENP'96 Workshop, Lausanne, Sep. 1996, Nucl. Inst. & Meth. in Phys. Res. A 389 (1997) 81-86. See also <http://root.cern.ch/>.
- [110] W. Verkerke and D. Kirkby, "The RooFit toolkit for data modeling," eConf **C0303241**, MOLT007 (2003) See also <http://roofit.sourceforge.net/>
- [111] T. Skwarnicki, Ph.D Thesis, Institute of Nuclear Physics, Cracow, 1986, DESY Report No. DESY F31-86-32.
- [112] ARGUS collaboration, Z.Phys. C48,543 (1990)

- [113] A. Roodman, eConf **C030908**, TUIT001 (2003)
- [114] P. Ball and R. Zwicky, JHEP **0110**, 019 (2001)
- [115] P. Ball, *Invited talk at 2nd Workshop on the CKM Unitarity Triangle, Durham, England, 5-9 Apr 2003*. eConf **C0304052**, WG101 (2003)
- [116] S. Agostinelli *et al.* [GEANT4 Collaboration], Nucl. Instrum. Meth. A **506**, 250 (2003).
- [117] D. J. Lange, Nucl. Instrum. Meth. A **462** (2001) 152.
- [118] The branching fraction for $B \rightarrow \psi(2S)\pi$ has not yet been measured, and we have estimated it to be $\mathcal{B}(B^+ \rightarrow \psi(2S)\pi^+) = 2 \times \mathcal{B}(B^0 \rightarrow \psi(2S)\pi^0) = 3 \times 10^{-5}$ under the naive assumption that $\frac{\mathcal{B}(B^+ \rightarrow \psi(2S)\pi^+)}{\mathcal{B}(B^+ \rightarrow \psi(2S)K^+)} = \frac{\mathcal{B}(B^+ \rightarrow J\psi\pi^+)}{\mathcal{B}(B^+ \rightarrow J/\psi K^+)}$
- [119] R. A. Fisher *The Use of Multiple Measurements in Taxonomic Problems*, Annals of Eugenics, 7 Part II, 179-188, 1936.
- [120] B. Aubert *et al.* [BABAR Collaboration], Phys. Rev. Lett. **96**, 011803 (2006)
- [121] R. Barlow, Comput. Phys. Commun. **149**, 97 (2002)
- [122] R. D. Cousins and V. L. Highland, Nucl. Instrum. Meth. A **320**, 331 (1992).
- [123] J. Neyman, Phil. Trans. Royal Soc. London, Series A, **236**, 333 (1937), reprinted in *A Selection of Early Statistical Papers on J. Neyman* (University of California Press, Berkeley, 1967).

Appendix A

Beam-background detectors

Beam background hitting the detector will over time cause damage to the detector components and electronics. The main known sources of beam background are: synchrotron radiation (X -rays) in the vicinity of the interaction region; interaction between the beam particles and the residual gas in either ring; and electromagnetic showers generated by beam-beam collisions.

The synchrotron radiation is effectively reduced through the design of the interaction region, so this source is expected to be low. Beam-gas scattering is most severe when vacuum is poor, and is usually reduced after some time of beam operation. This is the primary source of radiation damage in the SVT and the dominant source of background in all detector systems except the DIRC. The third component, electromagnetic showers generated by beam-beam collisions, is directly proportional to the luminosity and is expected to be the dominant background over time. This is already the main source of background seen by the DIRC.

During my work with detector operations for the EMC subsystem, I did a study of the total leakage currents of the EMC readout diodes since the start of *BABAR* data collection 1999 (see figure A.1, which shows the average leakage current per diode in each of the channels, where channel 8 and 9 correspond to the forward end cap). The currents were recorded when none of the beams were in operation, although residual background radiation may be present. The leakage currents of the diodes are seen to increase over time, which was expected. However, the increase is far larger than expected from photon/electron radiation alone, and there is suspicion that the damage is due to neutrons [1]. In any case, it remains important to reduce the radiation damage as much as possible.

2002/05/23 18.07

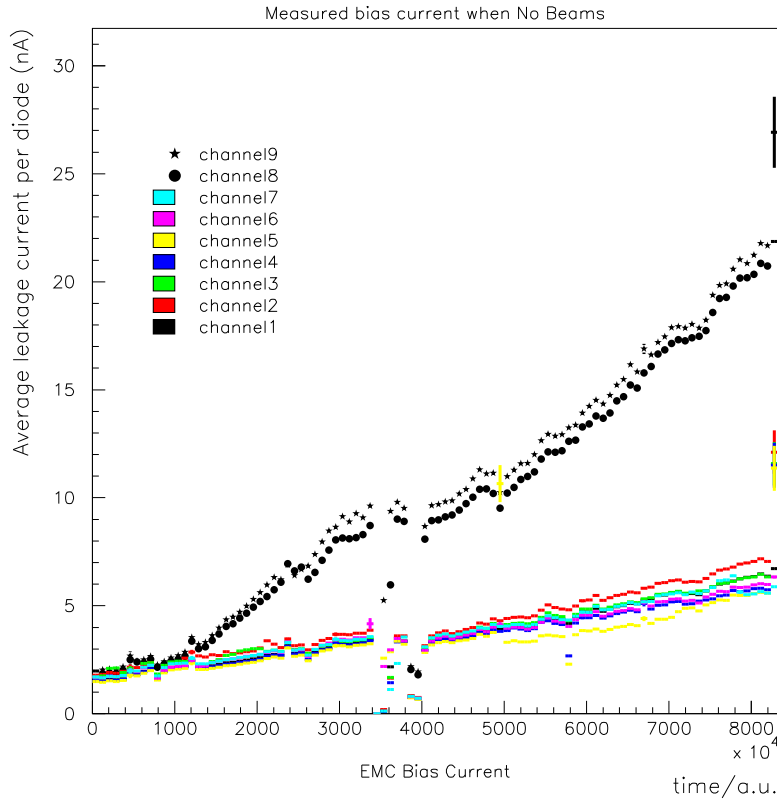


Figure A.1: Average leakage current per diode, October 1999 through May 2002. The total measured current per quadrant with no beams present, divided by the number of diodes in the quadrant, is shown versus time in seconds.

A.1 EMC CsI(Tl)/PIN-diode Radiation Sensors

In order to protect *BABAR* against excessive radiation, especially during the beginning of the PEP-II collision run in 1999, a protection system was designed to measure instantaneous radiation close to the beam pipe inside *BABAR*. The EMC group made four sensors from materials left over from building the EMC. The sensors are thus miniature calorimeters, consisting of a small piece of CsI(Tl) crystal with a PIN-diode for electronic readout, and were installed along the inner wall of the forward end cap of the EMC.

In the summer of 2002, PEP-II and *BABAR* had a major shutdown to improve cooling to the bellows close to the interaction point, which was needed for running with higher luminosity. By this time, the signal from these sensors had become unstable, which was taken as a sign of radiation damage. We made use of the shutdown opportunity to replace the four radiation sensors. The same mechanical setup was used as before, but the CsI(Tl) crystal and the PIN-diodes were

replaced.

A.2 Preparation and assembly

The active part of the sensors consists of an approximately $4 \times 4 \times 1$ cm³ block of Thallium doped CsI crystal with a PIN diode attached with optical grease. The PIN diodes¹ draw currents of less than one nA when un-irradiated, and the current increases linearly with increasing radiation incident on the diode surface. CsI(Tl) crystal is a scintillator whose purpose it is to increase the signal gain for the light-sensitive PIN diodes.

The old packages were removed from *BABAR* and taken apart. The mechanical housing was the only part which was reused. The housing is a solid aluminum piece with an approximately $2 \times 4 \times 4$ cm³ carved cavity in which the instrumentation of the sensors sits. The 4×4 cm² opening is covered by a thin aluminum lid. The old piece of CsI(Tl) crystal was taken out and inspected. It had acquired a slightly pink color, which could amount to some 10% loss of light yield.

Four new pieces of CsI(Tl) crystals were prepared (figure A.2), first machine cut by Light Fabrication at SLAC, then hand polished in a fume hood (to minimize breathing of toxic thallium dust).



Figure A.2: New CsI(Tl) crystals in the process of being polished. The crystals are $4 \times 4 \times 1$ cm³ blocks of scintillating material providing high photon yield for PIN-diode readout.

¹HAMAMATSU S3590-01 Si PIN diodes

The finished crystals were finally wrapped with a diffuse reflector (165 μm TYVEK paper) with a $1 \times 1 \text{ cm}^2$ cut at one side where the PIN diode was attached. A thin layer of optical grease between the PIN diode and the CsI(Tl) crystal ensures smooth light transmission from the crystal to the diode. Cables² were soldered onto the anode and cathode of the PIN diode. For later convenience, the cables were equipped with connectors³ about 1-2 meters from the sensor, so that they can be taken out without unmounting the whole cable system. A piece of Kapton(R) tape covers the soldering joints to ensure that they are insulated from the aluminum lid. The PIN-diodes are connected to the crystals by mechanical pressure from the lid of the aluminum box, increased by a strip of foam stuck to the lid. Once the lid had been closed, the packages were wrapped in black tape, calibrated and installed along the copper cooling pipes on the inner cylinder of the end cap. The calibration will be described in detail later. A picture of an almost assembled sensor is seen in figure A.3, and figure A.4 shows two of the newly installed sensor packages.

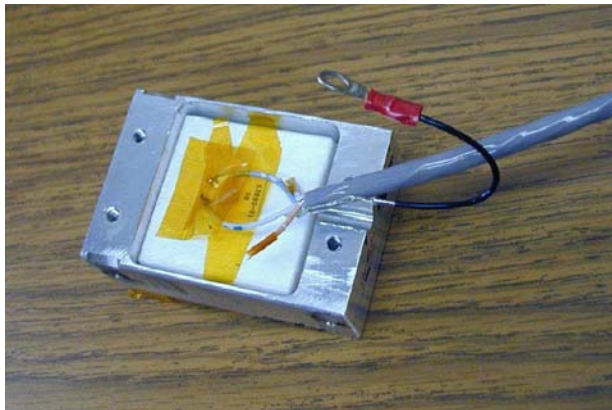


Figure A.3: Assembled background EMC PIN-diode sensor without the aluminum lid.

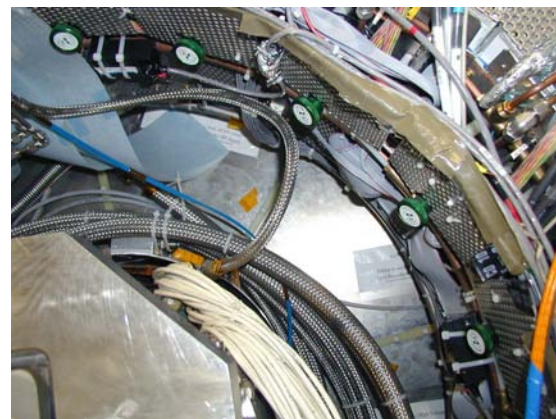


Figure A.4: Two sensors installed at 12 o'clock and 3 o'clock positions.

A.3 The electronic readout

The currents from the four EMC PIN-diode background detectors are fed into a preamplification board (figure A.5) located at the south-east side of *BABAR* where the signals are amplified, summed and converted into a voltage signal. The voltage is output to the CAMAC Beam Abort Module (figure A.6) located in the IR-2 alcove.

²BELDEN 88103, with a length of approximately 15 meters.

³Burndy Trim Trio



Figure A.5: Two pre-amplifier boards in a mobile crate attached to the east side of the *BABAR* detector.



Figure A.6: CAMAC Beam Abort Module in the IR-2 alcove.

The CBAM was designed for the *BABAR* Protection System and is connected to the PEP-II beam abort system. The *BABAR* Protection System as a whole was designed to be capable of dumping the beams or inhibiting injection if the radiation dose rate was above a certain level. The output of the CBAM module is read in by EPICS [2], the slow-control system for *BABAR*, where the signal from the four EMC PIN-diode sensors are labelled EMC.TOTL.

A threshold is set on the CBAM, which corresponds to a level where the beams should be dumped. For the EMC-diode signal, this beam-dump mechanism has been disabled, but at a signal 70% of the threshold setting, the injection rate will be reduced.

A.4 Calibration of the new sensors

The sensors were calibrated using a 5.6 Ci Cobalt 60 source well facility available at the Radiation Physics / OHP department at SLAC. The well is a narrow shaft with a bucket containing a radioactive Co60 source. The bucket can be raised or lowered in the well and thus providing different radiation intensities due to the distance between the source and the diodes. The lowest radiation dose provided (with the bucket at the bottom of the well) is 3 mrad/min and the highest radiation dose provided (with the bucket high up in the well) is 200 mrad/min.

The goal of the calibration is to be able to understand the output voltage from the CBAM in terms of radiation incident on the sensors. Ideally this should have been done by calibrating the sensors and its full readout chain as one unit. However, due to time constraints only the sensors and preamplification boards were calibrated. Estimates of further amplification stage in

the CBAM were based on the schematics, as well as some test measurements after installation.

The calibration had to be done in two steps due to initial problems with figuring out the grounding scheme on the preamplification boards. The sensors themselves had to be installed before the SVT cables were reattached after the shutdown, and thus there was a time constraint in having the sensors calibrated. Therefore, the sensors were calibrated first, to understand the currents induced as a function of radiation. The electronics was calibrated later to understand the combined voltage as a function of input currents.

A.4.1 Calibration setup

The setup consisted of all four EMC background sensors on the Plexiglas on top of the source well. The cables connecting the sensors to the preamplification board, ran out into the adjoining room where the electronics was set up for reading out the resulting voltages. The output of the preamplification board was read out with an oscilloscope, either with all channels connected or with single channels connected.

In the following, the four sensors are named according to their position along the cooling pipes on the inner cylinder of the end cap: “12 o’clock” position (top), readout channel 0; “3 o’clock”-position (east), readout channel 1; “6 o’clock”-position (bottom), readout channel 2; “9 o’clock”-position (west), readout channel 3.

The output voltage from the preamplification board was measured at about 5-10 different radiation intensities between the lowest and the highest position of the bucked in the well. The



Figure A.7: Calibration in Co60 Source well, “aerial view”. Four sensors are seen on a sheet of Plexiglas on the top of the well. The radiation level is measured with a radiation meter (Radcal).

(ASP-1) [rad/h]	(Radcal) [mrad/min]	12 o'clock Ch. 0 [nA]	3 o'clock Ch. 1 [nA]	6 o'clock Ch. 2 [nA]	9 o'clock Ch. 3 [nA]
0.0	0.0	0.24	0.27	0.25	0.43
0.2	3.0	0.53	0.58	0.50	0.70
1.6	25	2.50	2.80	2.25	3.00
2.6	50	4.90	5.00	3.80	5.30
4.6	75	7.50	7.60	5.80	8.00
6.0	100	9.50	10.00	7.50	10.5
7.5	125	12.40	12.80	9.60	13.20
9.1	150	14.50	15.00	11.00	15.50
12.0	175	17.40	17.90	13.30	18.40
14.0	200	19.60	20.50	15.20	21.00

Table A.1: Calibration data from the new EMC PIN-diode sensors biased at 30 V.

dose rate at the calibration points were measured with a radiation meter.

A.4.2 Calibration of individual sensors

The voltage regulator on the original preamplification board turned out to be damaged, and until the damage could be repaired, we first tested the sensors using the spare preamplification board. The currents read out from the individual channels showed a linear response, indicating that the sensors were working as they should.

Most importantly, we calibrated the diode currents directly without the amplification stage using a pico-amperemeter. This required the diodes to be reverse-biased due to the low currents. For this we used a 30-V voltage supply, $1M\Omega$ resistor, the diode and a BNC pico-amperemeter. This gave a reliable relation between currents drawn by the individual diodes and radiation incident on the sensors. The results can be found in table A.1 and plotted in figure A.8.

Normally the diodes are operated without reverse bias voltage, since a bias voltage may increase the radiation damage to the diodes. A bias voltage only increases the stability and linearity of the diodes, but the currents are the same with and without reverse bias voltage.

For this measurement, two radiation meters were used: Radcal 9010 and ASP-1. The former is the reliable one, but this one was unfortunately not available for the later measurements. The discrepancy between the two meters are seen from the first and second column of table A.1. The tables in this appendix contains the raw, uncorrected readings from the ASP-1 (measured in rad/h), but the plots have the corrected numbers.

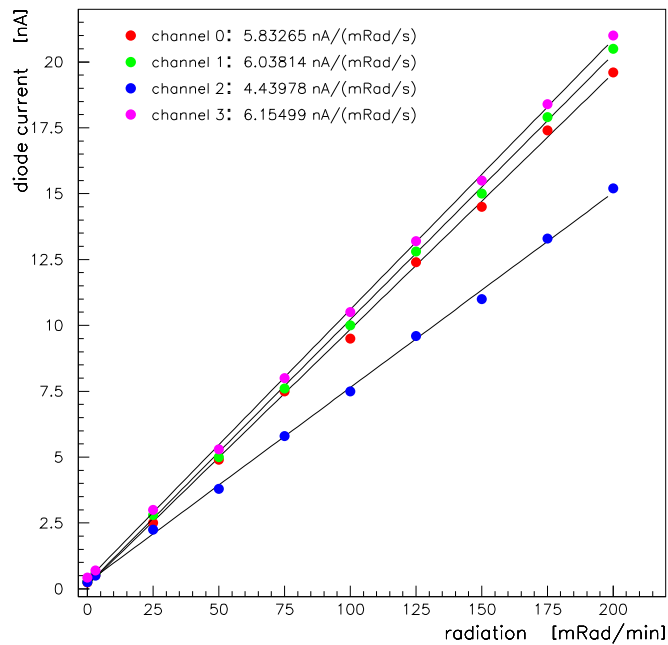


Figure A.8: Measured leakage current vs. radiation for the new EMC PIN-diode sensors biased at 30 V.

A.4.3 Calibration of the preamplification boards

After the original preamplification board was repaired and the grounding understood, both of the preamplification boards were calibrated to understand the relation between output voltage and input currents. It was difficult to obtain any device supplying currents of a few nA, so in this calibration we made use of some old radiation detectors made by the DCH group to provide currents of approximately the right magnitude.

These old DCH diodes first must be calibrated in the same way as the EMC diodes, biased at 30 V and read out by a pico-ammeter. These diodes were smaller and had some radiation damage, but they still provided a reliable input current of the right order of magnitude when irradiated. These measurements are shown in table A.2 and plotted in figure A.9. This data serves as a reference for combining the currents from the EMC diodes with the voltage of the pre-amplifier boards.

The pre-amplifier boards were then connected to the DCH diodes, and the measurements were done again for individual channels and all channels combined with DCH diodes at the source well. The raw data from these measurements are given in tables A.3 and A.4 and con-

(ASP-1) [rad/h]	12 o'clock Ch. 0 [nA]	3 o'clock Ch. 1 [nA]	6 o'clock Ch. 2 [nA]	9 o'clock Ch. 3 [nA]
0.0	2.30	0.62	1.00	0.60
1.0	2.50	1.00	1.50	1.00
3.0	3.40	1.80	2.40	1.80
6.0	5.00	3.10	4.00	3.20
10.0	7.20	4.90	6.10	5.00
15.0	8.90	6.30	7.80	6.45

Table A.2: Calibration data for old DCH diodes biased at 30 V. The diagram shows data for each sensor plotted vs. radiation.

stitutes a calibration of the boards as a function of radiation. Using data from table A.2, we can translate voltage vs. radiation into voltage vs. input currents. To do this, we assume that the currents are the same whether the diodes are biased or not. Figure A.10 shows this relation for individual channels, and figure A.11 shows the output voltage as a function of input currents when all channels are connected to irradiated sensors.

(ASP-1) [rad/h]	12 o'clock Ch. 0 [mV]	3 o'clock Ch. 1 [mV]	6 o'clock Ch. 2 [mV]	9 o'clock Ch. 3 [mV]	Sum [mV]
3.0	182	165	206	164	736
6.0	468	392	492	396	1760
10.0	850	692	860	712	3240
15.0	1190	990	1200	1020	4520

Table A.3: Calibration data for the original preamplification board.

(ASP-1) [rad/h]	12 o'clock Ch. 0 [mV]	3 o'clock Ch. 1 [mV]	6 o'clock Ch. 2 [mV]	9 o'clock Ch. 3 [mV]	Sum [mV]
1.0	60	48	60	60	222
3.0	214	172	204	188	800
6.0	500	412	492	424	2000
10.0	870	710	850	728	3300
15.0	1200	980	1160	1000	4480

Table A.4: Calibration data for the spare preamplification board.

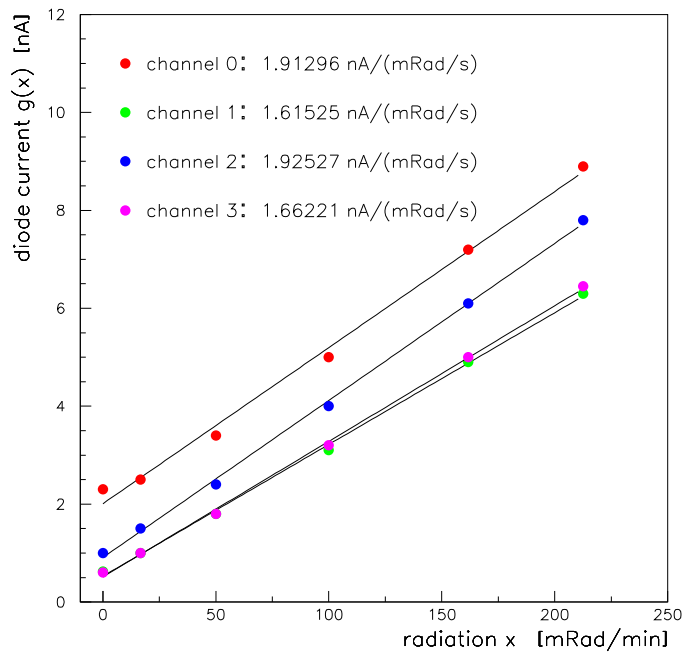


Figure A.9: Measured leakage current vs. radiation for each of the old DCH PIN-diode sensors biased at 30 V.

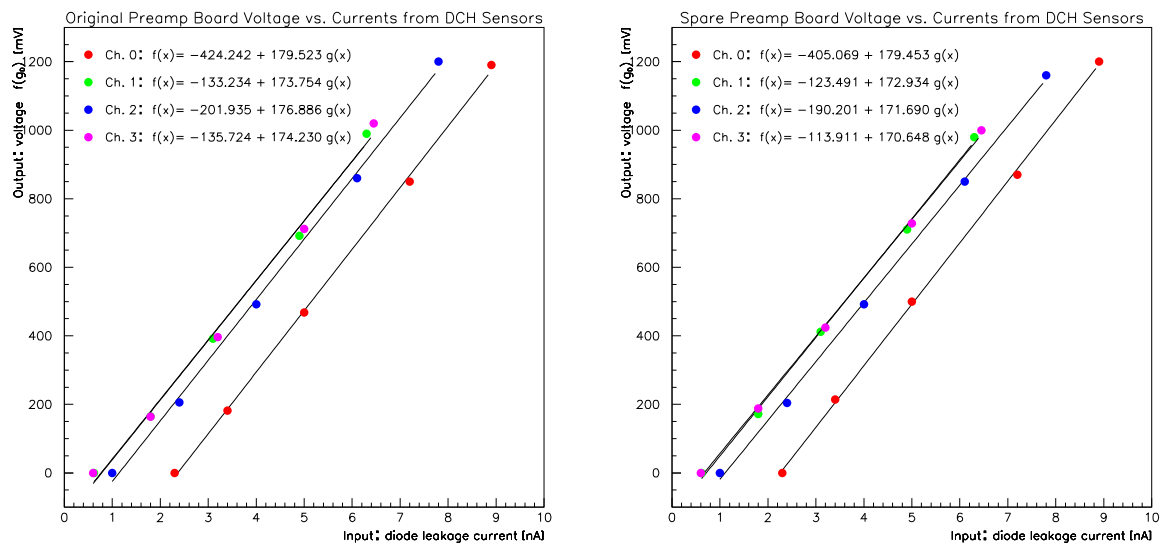


Figure A.10: Measured single channel output voltage of original (left) and spare (right) preamplification board vs. input currents.

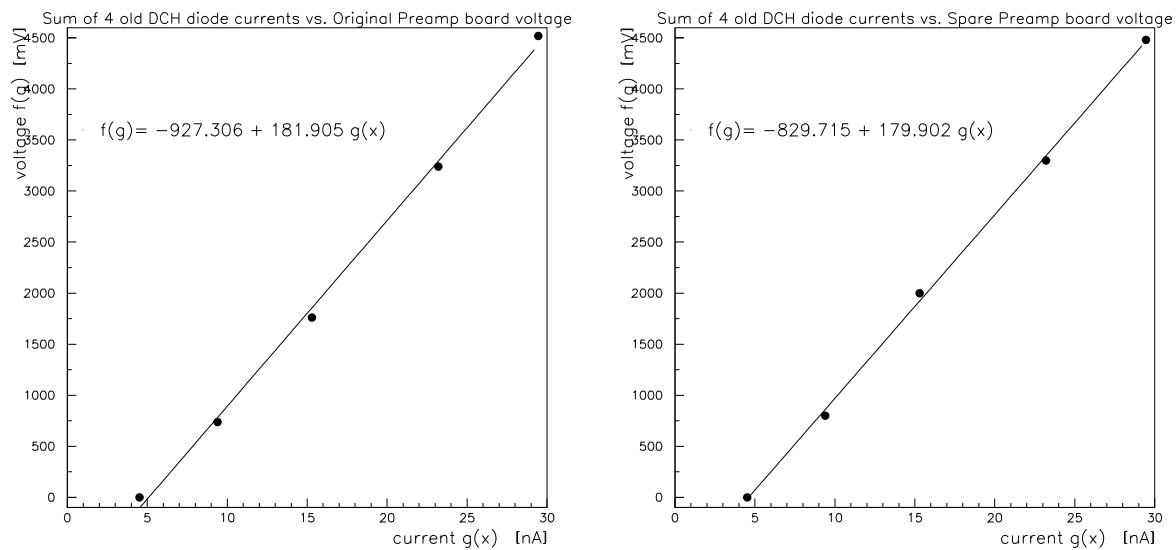


Figure A.11: Plotted here are the sum of input (DCH-diode) currents versus total output voltage with all channels connected. To the left: voltage readings from the original board, and to the right: voltage readings from the spare preamplification boards.

A.5 Radiation Dose-Rate Calculations

In order to extrapolate voltage f vs. current g or radiation x to larger currents suitable for the EMC diodes, the data points in figures A.10 and A.11 are fitted to a first-order polynomial $f(g)$, expressing output voltage in terms of the input current g . g in turn is a function of radiation x , $g(x)$. The function $f(g)$ is specific for the preamplification board (f_o and f_s , representing voltage from the “original” and the “spare” preamplification boards, respectively), and $g(x)$ is specific for the diode sensors (g_D and g_E , representing currents from the DCH and EMC diodes, respectively).

We see from the figures that all the fits to $f(g)$ have almost the same slope. The slope for the total output voltage is systematically a bit higher than the slopes for the individual channels. This mirrors the fact that the total voltage with all channels connected were also systematically higher than the sum of voltages from single channels connected (tables A.3 and A.4).

The constant term in f differs a bit depending on the diodes’ dark current, since the preamplification board has been tuned to give 0 V at 0 mrad/min. The dark current for the old diodes are much higher (2.3 nA, 0.62 nA, 1.00 nA and 0.60 nA) than what they are for the new EMC PIN diodes (0.24 nA, 0.27 nA, 0.25 nA and 0.43 nA), therefore the constant term is larger for

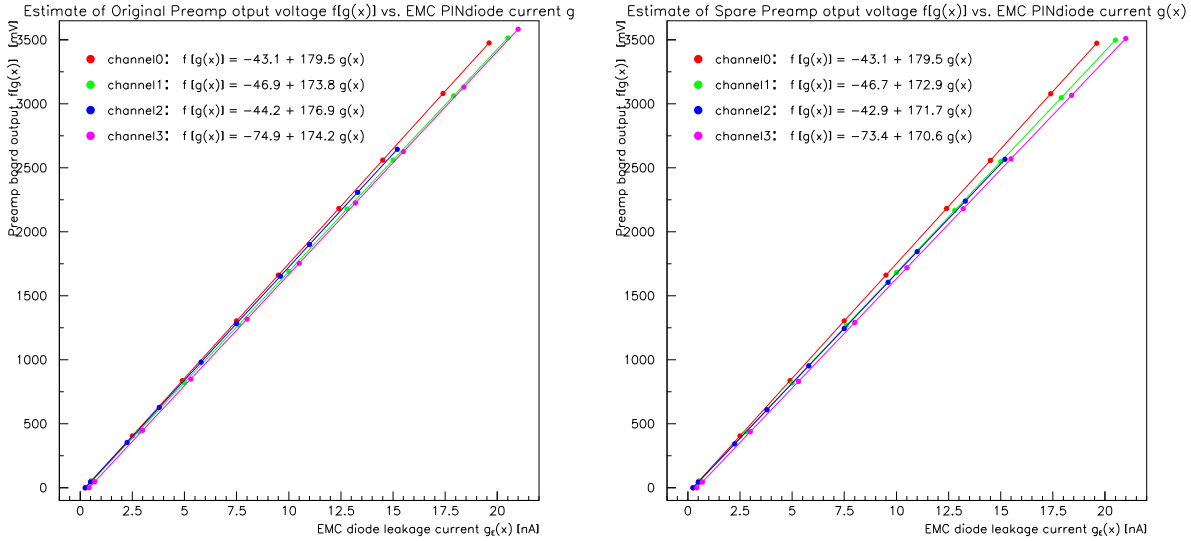


Figure A.12: Estimate of preamplification board output voltage vs. currents for single EMC PIN diodes (original preamplification board to the left, spare preamplification board to the right).

$f(g_D)$ than for $f(g_E)$.

The constant term is not of any major interest in these calibrations because the baseline current (dark current) will inevitably change with time as the diodes are exposed to radiation, and the trimming potentiometers on the preamplification board and the CBAM will need to be adjusted so that the output voltage show 0 V when beams are off.

For the single-channel slopes, figure A.12 gives an estimate of the output voltage from the preamplification board with respect to currents from single new EMC diodes by merely using the same slope as obtained from figure A.10, but adjusting the constant according to dark current (requiring 0 V at 0 mrad/min). The constant term here is found from the product: $(-1) \times$ the slope \times the diode dark current. We can do the same for total voltage with respect to the sum of all four input currents. This is shown in figure A.13.

To obtain the output voltage from a given preamplification board as a function of radiation, $f(x)$, we substitute the current $g(x)$ with the measured old DCH diode currents, $g_D(x)$, or the measured new EMC diode currents, $g_E(x)$, as obtained from the calibration of individual diode sensors at 30 V. For f^D this should agree with the curves obtained from the preamplification board calibrations in tables A.3 and A.4. These curves have been plotted in figure A.14. The calculated $f(x)$ is given in table A.5. Comparing the functions $f^D(x)$ in the table with the curves in figure A.14 shows that they mostly agree; the largest discrepancy is for the slope in channel

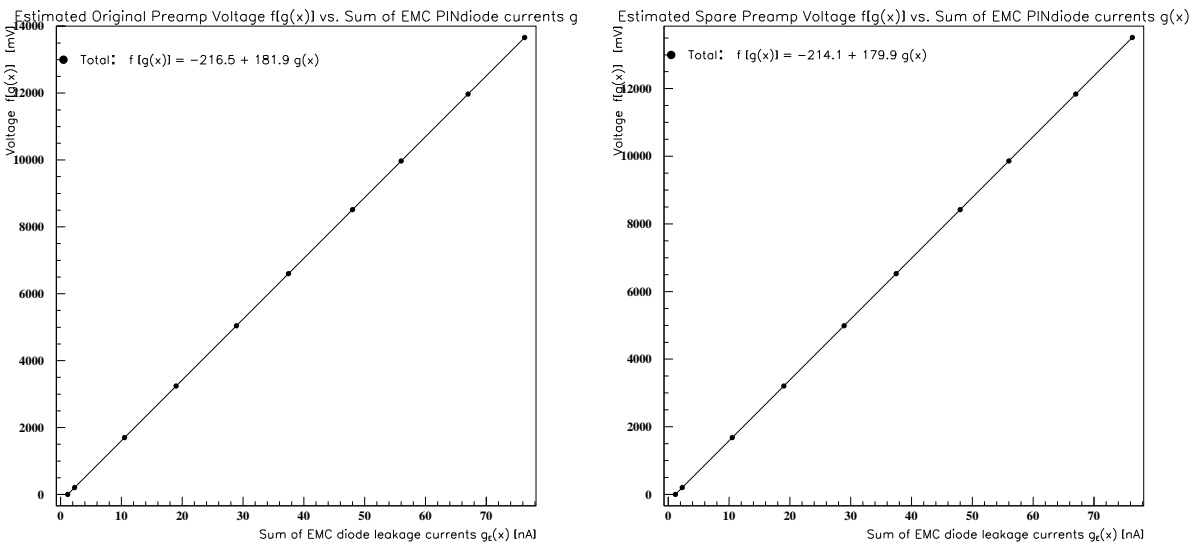


Figure A.13: Estimate of total preamplification board output voltage vs. the sum of the EMC PIN diode currents (original preamplification board to the left, spare preamplification board to the right).

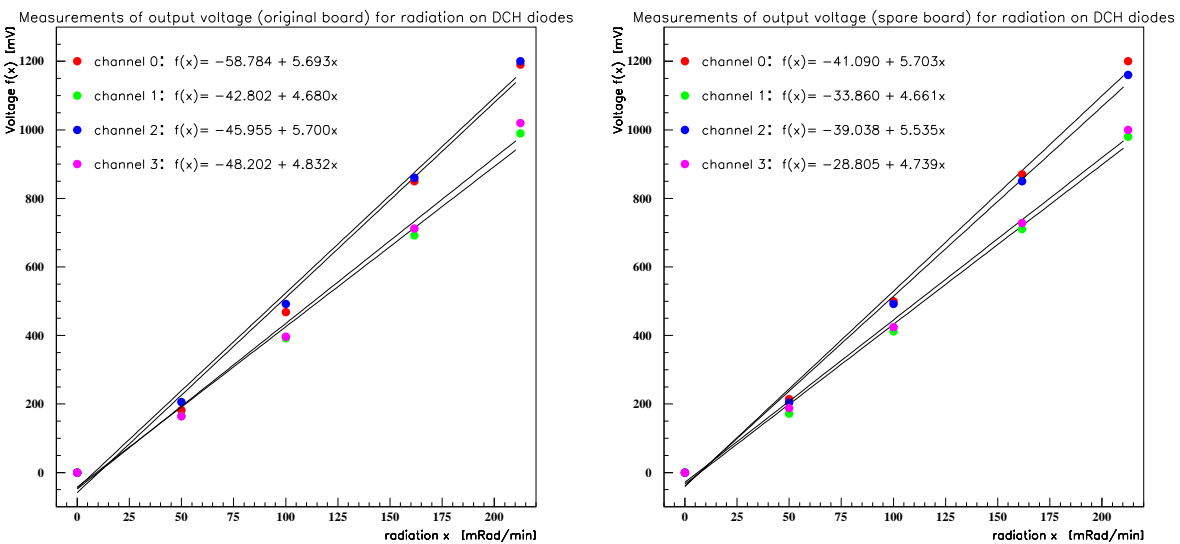


Figure A.14: Original Pre-Amplifier Board output vs. radiation (measured), to be compared with the $f_o(x)$ entries for channels 0 - 3 for the old DCH sensors in table A.5.

channel	old DCH sensors	new EMC sensors
0	$g_D(x) = 2.032 + 0.032 x$ $f_o[g(x)] = -424.2 + 179.5 g(x)$ $f_s[g(x)] = -405.1 + 179.5 g(x)$ $f_o^D(x) = -59.5 + 5.7 x$	$g_E(x) = 0.129 + 0.097 x$ $f_o[g(x)] = -43.1 + 179.5 g(x)$ $f_s[g(x)] = -43.1 + 179.5 g(x)$ $f_o^E(x) = -19.9 + 17.4 x$
1	$g_D(x) = 0.516 + 0.027 x$ $f_o[g(x)] = -133.2 + 173.8 g(x)$ $f_s[g(x)] = -123.5 + 172.9 g(x)$ $f_o^D(x) = -43.5 + 4.7 x$	$g_E(x) = 0.159 + 0.101 x$ $f_o[g(x)] = -46.9 + 173.8 g(x)$ $f_s[g(x)] = -46.7 + 172.9 g(x)$ $f_o^E(x) = -19.3 + 17.6 x$
2	$g_D(x) = 0.877 + 0.032 x$ $f_o[g(x)] = -201.9 + 176.9 g(x)$ $f_s[g(x)] = -190.2 + 171.7 g(x)$ $f_o^D(x) = -46.8 + 5.7 x$	$g_E(x) = 0.239 + 0.074 x$ $f_o[g(x)] = -44.2 + 176.9 g(x)$ $f_s[g(x)] = -43.0 + 171.7 g(x)$ $f_o^E(x) = -1.9 + 13.1 x$
3	$g_D(x) = 0.497 + 0.028 x$ $f_o[g(x)] = -135.7 + 174.2 g(x)$ $f_s[g(x)] = -113.9 + 170.6 g(x)$ $f_o^D(x) = -49.1 + 5.9 x$	$g_E(x) = 0.340 + 0.103 x$ $f_o[g(x)] = -74.9 + 174.2 g(x)$ $f_s[g(x)] = -73.4 + 170.6 g(x)$ $f_o^E(x) = -15.7 + 17.9 x$
total	$g_D(x) = 3.92 + 0.119 x$ $f_o[g(x)] = -927.3 + 181.9 g(x)$ $f_s[g(x)] = -829.7 + 179.9 g(x)$ $f_o^D(x) = -214.3 + 21.6 x$ $f_s^D(x) = -124.5 + 21.4 x$	$g_E(x) = 0.867 + 0.375 x$ $f_o[g(x)] = -216.5 + 181.9 g(x)$ $f_s[g(x)] = -214.1 + 179.9 g(x)$ $f_o^E(x) = -58.8 + 68.2 x$ $f_s^E(x) = -58.1 + 67.5 x$

Table A.5: The equations for calculating voltage output from the preamplification board from diodes leakage currents at different radiation dose rates. Each of the four channels measured with DCH diodes, then based on measured dark current, calculated for EMC diodes. The units are: $[x] = \text{mrad/min}$, $[g] = \text{nA}$, $[f] = \text{mV}$.

3. In the case of f^E , we do not have this direct measurement, and the curve to obtain f^E we need to rely on the calculations, given in the last column in table A.5.

Table A.5 summarizes the measured and calculated relations between radiation x , current g and voltage f for the “original” and “spare” preamplification boards and the four “old DCH diodes” and the four “new EMC diodes”. The equations $g_E(x)$ and $g_D(x)$ are obtained directly from the fit to data in tables A.1 and A.2. $f_o[g(x)]$ and $f_s[g(x)]$ in the “old DCH sensor” column are obtained from fits to the data in tables/figures A.3 and A.4. The same functions in the “new EMC sensor” column inherits the slope from the “DCH” measurements, but have constant term adjusted according to different diode dark currents. The equations for $f_o(x)$ and $f_s(x)$ are the results of substituting $g_D(x)$ or $g_E(x)$ in $f_o[g(x)]$ and $f_s[g(x)]$, respectively. The functions $g(x)$ in the “total” row are a sum of the currents in each individual channel, $g(x) = \sum_i g_i(x)$.

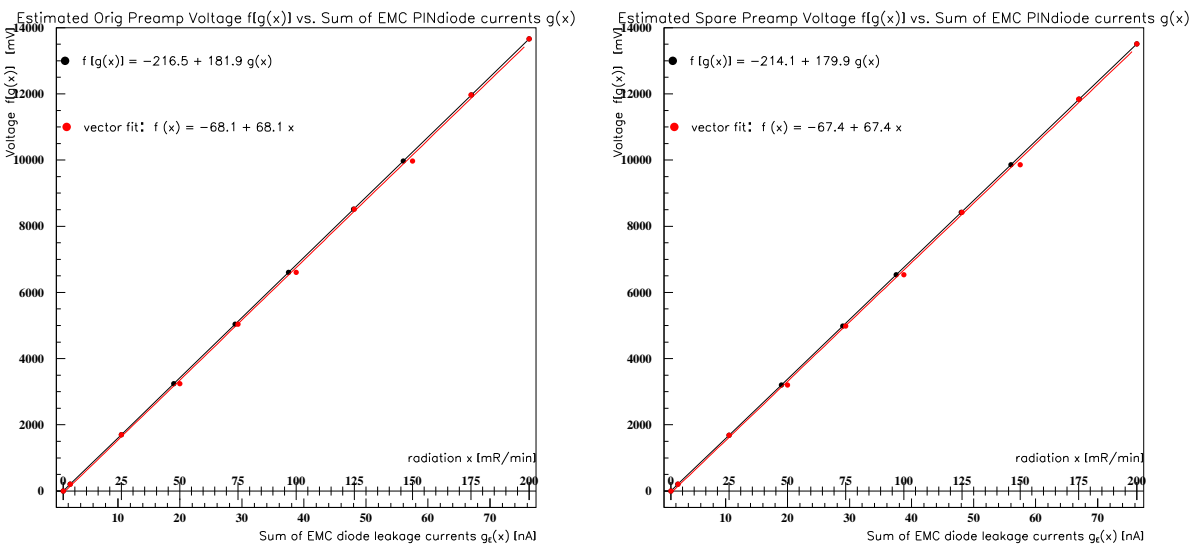


Figure A.15: Final estimate of preamplification boards output w.r.t input currents from the EMC PIN-diode sensors, and w.r.t radiation, for the original preamplification board (left) and the spare preamplification board(right).

In figure A.15, the estimate of output voltage from the preamplification boards with respect to total current in from the new EMC diodes ($f[g_E(x)]$) are plotted. In the same picture, the radiation incident on the EMC PIN-diode sensors is given as an alternative x-axis, making this also a curve of the estimated $f^E(x)$. As already noted, the constant terms in the fits are arbitrary.

The CBAM comes on top of this, but as this is only an inverter, the slope will be the same, and only the constant term will be affected.

A.6 Cross-checks

As an independent cross check, four packages of various types of dosimeters were installed close to the PIN-diode sensors. Most of these dosimeters (opti-chromic types) have very high dose absorption, and need to stay in for some length of time before we can see any measurable effect. In each package there is also one ordinary TLD (Thermoluminescent Dosimeter), which only measures doses precisely up to about 50 rad, and so should be read out at an earlier stage. These ordinary TLDs also have the nice feature that they can distinguish between neutron radiation and other forms of radiation.

After nearly one year of running after the PIN diode sensors were calibrated and installed,

the dosimeters were taken out, and accumulated radiation dose checked. This radiation dose was compared to the integrated voltage signal recorded in EPICS. The analysis of EPICS data is presented in section A.6.1. The results of the dosimeter readout is presented in section A.6.2.

A.6.1 Cross-check with EPICS data

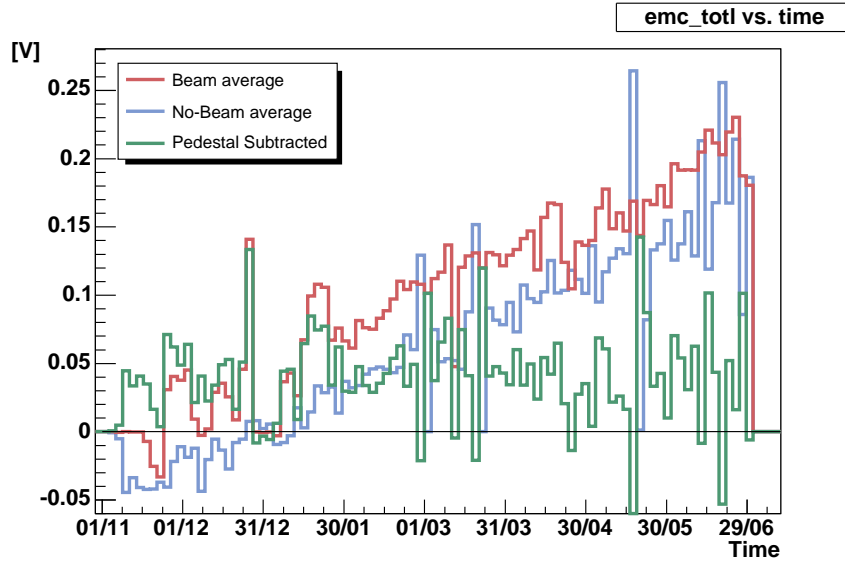


Figure A.16: Voltage (EMC_TOTL signal) plotted as a function of time, from Nov 5, 2002 until June 30, 2003, averaged over periods with beam, without beam, and the difference between the two (pedestal subtracted voltage).

The result of the calibration with the Co-60 source can be summarized in a single equation expressing the voltage, U , as a function of dose rate, x :

$$U(x) = 1.137x, \quad (\text{A.1})$$

with $[U] = V$ and $[x] = \text{mrad/s}$. Note that the unit used for x is now mrad/s, while the figures in earlier sections quote mrad/min. Turning the equation around gives us the dose rate as a function of voltage, which is more convenient for finding the integrated dose rate:

$$\text{Rate} = x(U) = \frac{\Delta \text{Dose}}{\Delta t} = 0.88 U, \quad (\text{A.2})$$

and so by integrating the voltage over time, we get the accumulated dose:

$$\int d(Dose) = 0.88 \int U(t)dt \quad (A.3)$$

The voltage read out from CBAM into EPICS is stored in the Ambient database, and this information can be retrieved. In figure A.16, the voltage is plotted as a function of time for all of the Run 3 period. The plot shows three curves, one representing voltage readings in periods with beams on, one representing voltage readings in periods with beams off, and the third one representing the difference of the two. Thus, the third line is the pedestal subtracted voltage. Assuming equation A.3 obtained from the Co-60 calibration, is the correct relation between voltage and dose, a numerical integration of the pedestal subtracted histogram in figure A.16 gives total absorbed energy dose

$$D_{4 \text{ PIN-diodes}} = 816402 \text{ mrad} = 816.4 \text{ rad}/8\text{months} = 102 \text{ rad/month} \quad (A.4)$$

Since the dose D [rad] is per unit mass, it would be more correct to interpret the average dose seen by the four detectors:

$$D_{\text{PIN-diode}} = 204.1 \text{ rad}/8\text{months} = 25.5 \text{ rad/month}. \quad (A.5)$$

Given that dosimeters were installed in all four locations it would also have been of interest to compare dosimeter and PIN-diode sensor in each location, but we do not have the signal for each of the PIN-diode sensors read out, only the sum of the four signals.

A.6.2 Thermoluminescent dosimeter cross-check

There were 4 TLDs present from Nov 5, 2002 until August 18, 2003, each located close to one of the background sensors. Each TLD was replaced once during the total period. The total dose absorbed in each location is calculated as a simple sum.

Each TLD consists of four elements, in table A.6 given as E1-4. E3 and E4 are $CaSO_4$ phosphor with plastic and lead filters respectively. The response on these elements are almost purely due to γ radiation. E1 and E2 also see β and n radiation.

On recommendation from H. Tran at ES&H Radiation Protection at SLAC, we use the signal from E2 as the total accumulated dose and the signal from E4 as the accumulated dose due to photons. Thus we have accumulated from November 5, 2002 - August 18, 2003 (approximately 9.5 months):

TLD Id		Time range	E1 [rad]	E2 [rad]	E3 [rad]	E4 [rad]	Photon ED [rem]	Neutron ED [rem]	E2/E4	E3/E4
3h	1082	Nov5-Jan24	67.58	60.07	37.80	40.97	37.06	25.93	1.5	0.9
6h	1350	Nov5-Jan24	89.20	82.43	91.95	83.94	76.68	9.24	1.0	1.1
12h	3676	Nov5-Jan24	91.65	85.28	116.50	85.28	77.70	10.74	1.0	1.4
9h	1165	Nov5-Mar27	143.05	139.32	103.66	112.73	101.85	39.43	1.2	0.9
3h	6000672	Jan24-Aug18	282.22	244.87	207.29	234.70	208.60	52.07	1.0	0.9
6h	6000713	Jan24-Aug18	331.53	304.28	302.38	232.03	211.55	104.06	1.3	1.3
9h	6001013	Mar27-Aug18	124.47	117.92	81.29	77.45	70.69	49.96	1.5	1.0
12h	6001585	Jan24-Aug18	314.13	290.32	369.12	294.82	269.09	32.94	1.0	1.3

Table A.6: Summary of results from dosimeter (TLD) cross-check.

- 3h: 304.94 rad total, 275.69 rad due to photons, 29.27 rad due to neutrons.
- 6h: 386.71 rad total, 315.97 rad due to photons, 70.74 rad due to neutrons.
- 9h: 259.24 rad total, 190.18 rad due to photons, 69.06 rad due to neutrons.
- 12h 375.60 rad total, 380.10 rad due to photons, -4.5 rad due to neutrons.

Uncertainties in the measurements of the TLD readings were not supplied, but we state the result as an average of the four locations, and give the measurement error as the spread in values, giving:

$$D_{\text{TLD (total)}} = (331.6^{+72.4}_{-55.1}) \text{ rad}/9.5\text{months} = 34.9^{+7.6}_{-5.8} \text{ rad/month} \quad (\text{A.6})$$

$$D_{\text{TLD (photons)}} = (290.5^{+89.6}_{-100.3}) \text{ rad}/9.5\text{months} = 30.6^{+9.5}_{-10.6} \text{ rad/month} \quad (\text{A.7})$$

$$D_{\text{TLD (neutrons)}} = (41.1^{+29.6}_{-45.6}) \text{ rad}/9.5\text{months} = 4.3^{+3.1}_{-4.8} \text{ rad/month} \quad (\text{A.8})$$

These numbers must be compared to equation A.5. Given rather large uncertainties, it looks like the result obtained integrating the EMC_TOTL signal is consistent with the photon dose measured by the TLDs.

We have compared the values read out from the diodes and stored in the ambient database, with the dose accumulated by nearby dosimeters. Since the crystal-PIN-diode detectors are used as input in the evaluation of beam quality, it is important that their measurements are reliable, at least on a relative scale.

A.7 Concluding remarks

This study suggests that crystal-PIN-diode sensors have measured about 74% of the total dose accumulated by the TLDs in approximately the same positions. If we assume the crystal-PIN-diode sensors are sensitive to photon radiation only, the discrepancy is smaller (83% of the TLD result). The discrepancy may be much larger, however, if the crystal-PIN-diode sensors are sensitive to neutrons as well, as this would not have been included in the calibration, since no neutron radiation was present during calibration. There is a strong suspicion that this is the case [1].

Until now the EMC PIN-diode background detectors have only been used as a relative measurement of background radiation from the beams, in order to protect against excessive radiation during poor injections. The calculation of dose-rate from the EMC_TOTL voltage is only meant to support decisions on where to set the limits as to what is damaging radiation for the EMC (see also [1]).

The sensors might need to be replaced (at least) once more during the life of the *BABAR* experiment. My suggestions in case of this, is that we reconsider the choice of cables, as the ones used now are not really low-noise and the diode signal is very weak. The electronics is also very sensitive to variations in temperature and humidity, and the only method used until now for stabilizing this has been to insulate the pre-amplifier crate with foam. Perhaps there are ideas for better solutions out there and if so, perhaps it would be worthwhile trying to implement the temperature corrections with thermistors once again. I would also advice in favor of thinking about a better mechanical setup for the diode in the box, to ensure that it does not move with respect to the crystal and that there is no air gap between the two. Another possibly large source of error is the baseline subtraction in the EMC_TOTL integration. Some better averaging / histogramming algorithm may be able to improve this.

The study as described only makes a simple average over the full time range. Also, the time range considered for the crystal-PIN-diode detectors are not the exact same as the time range the TLD's were accumulating doses, and the time range of each TLD also differ a bit, and it is possible that these were saturated towards the end of the time span.

With the uncertainties discussed taken into account, this study shows that the crystal-PIN-diode sensors do measure approximately correct dose rate in the forward end cap of the *BABAR* calorimeter.

Bibliography

- [1] I. Eschrich, Investigation of Increased Leakage Currents in the EMC Readout Diodes.
BABAR Note No. 554, v2.
- [2] Experimental Physics and Industrial Control System
<http://www.aps.anl.gov/epics/>

Errata

This version of the thesis has been modified with respect to the original, printed, version. The following mistakes have been corrected:

- A half sentence has been removed from the caption of Fig 4.1. The text was mistakenly not commented out in the source file.
- In Table 4.5, the entries in the last column ($S/\sqrt{S+B}$) has been corrected. These originally incorrectly listed the values for S/\sqrt{B} .